Development of a Cell Cross Flow System

by

Jessica Chung
B.Eng., Carleton University, 2008

A Thesis Submitted in Partial Fulfillment of the
Requirements for the Degree of

MASTER OF APPLIED SCIENCE

in the Department of Mechanical Engineering

Supervisory Committee

Development of a Cell Cross Flow System

by

Jessica Chung
B.Eng., Carleton University, 2008

Supervisory Committee

Dr. Nikolai Dechev, Co-Supervisor
Department of Mechanical Engineering, University of Victoria, Victoria, BC, Canada

Dr. Edward J. Park, Co-Supervisor
Department of Mechanical Engineering, University of Victoria, Victoria, BC, Canada
School of Engineering Science, Simon Fraser University, Burnaby, BC, Canada

Dr. David Sinton, Departmental Member
Department of Mechanical Engineering, University of Victoria, Victoria, BC, Canada

Abstract

Supervisory Committee

Dr. Nikolai Dechev, Co-Supervisor
Department of Mechanical Engineering, University of Victoria, Victoria, BC, Canada

Dr. Edward J. Park, Co-Supervisor
Department of Mechanical Engineering, University of Victoria, Victoria, BC, Canada
School of Engineering Science, Simon Fraser University, Burnaby, BC, Canada

Dr. David Sinton, Departmental Member
Department of Mechanical Engineering, University of Victoria, Victoria, BC, Canada

Single cell analysis devices have become important tools to obtain unique information on cells to improve current medical techniques, such as tissue engineering, or diagnosis of cancer at an early stage. This thesis documents the development of a "cell cross flow system" (CFS), which aims to capture magnetically tagged (MT) cells from a heterogeneous population of cells, and array these cells in pre-determined locations using magnetic force. The CFS integrates a “magnetic single cell micro array” (MSCMA), and a gasket assembly to achieve this. Current single cell technology, relevant fluid and magnetic theory, CFS design process, finite element method (FEM) simulation, and cross flow experiments are detailed in this thesis. The CFS was successful in capturing MT Jurkat cells, and the experimental results were consistent with the FEM simulation analysis. It was found that the CFS was capable of capturing MT Jurkat cells up to a ratio of 1 to 10^3 (MT to non-magnetically tagged cells) using a cell concentration of 10^5 *cells/mL*. Although these results are promising, non-magnetically tagged Jurkat cells were found to adhere to the chip and could not be easily removed. Several recommendations were suggested for future iterations, including changing the gasket assembly design, optimizing the flow rate and cell concentration, and using smaller trap sizes for the MSCMA design.

Table of Contents

Supervisory Committee ii
Abstract iii
Table of Contents iv
List of Tables vii
List of Figures ix
Acronyms xiv
Nomenclature xv
Acknowledgement xvii
Dedication xix
Chapter 1: Introduction 1
Chapter 2: Background 6
  2.1 Single Cell Analysis Technologies 7
    2.1.1 Cell Manipulation Methods 7
    2.1.2 Single Cell Analysis Techniques 10
  2.2 Technology Similar to the CFS 15
    2.2.1 Active Magnetic Separators 16
    2.2.2 Passive Magnetic Separators 18
  2.3 Motivation for the CFS 21
Chapter 3: Magnetic Theory 22
  3.1 Magnetic Terminology and Concepts 22
    3.1.1 Maxwell's Equation 23
    3.1.2 Magnetic Material 24
    3.1.3 Magnetic B – H Curve 25
  3.2 Force on a Magnetically Tagged Cell 27
    3.2.1 Immunomagnetic Labelling 28
    3.2.2 Total Magnetic Force on a Cell 29
    3.2.3 Factors That Influence the Magnetic Force on a Cell 32
Chapter 4: Fluid Flow Theory 34
  4.1 Fluid Flow Terminology 34
    4.1.1 Continuum Assumption 34
    4.1.2 Fluid Flow Governing Equations 36
    4.1.3 Reynolds Number 37
  4.2 Fluid Force on a Spherical Object 39
Chapter 5: CFS Design and Properties 41
  5.1 Design Requirements and Methodology 41
  5.2 Description of Final Design 44

5.2.1 Base Plate 45
5.2.2 Magnet Cover 45
5.2.3 Magnetic Microarray 46
5.2.4 Gasket Assembly 47
5.2.5 Top Plate 50
5.2.6 Final Assembly 50

5.3 Material Properties 52

5.3.1 Magnetic Properties 52
5.3.2 Biocompatibility Properties 55

5.4 Fluid Delivery System 56
5.5 Design Summary 56

Chapter 6: FEM Analysis of CFS 58

6.1 COMSOL Subdomain and Boundary Conditions 59

6.1.1 Magnetic FEM Model 59
6.1.2 Fluid Flow FEM Model 60

6.2 Large Scale Magnetic Model 61

6.2.1 LSM Model Setup 62
6.2.2 LSM Model Results 63

6.3 Large Scale Fluid Flow Model 65

6.3.1 LSFF Model Setup 66
6.3.2 LSFF Model Results 67

6.4 Smaller Boundary Magnetic/Fluid FEM Model 69

6.4.1 Information Extracted from Large Scale Models 70
6.4.2 SBMF Model Setup 71
6.4.3 SBFM Model Assumptions 72
6.4.4 SBFM Sinusoidal and Sawtooth Model Results 73

6.5 Predicted Cell Path Simulation 79

6.5.1 Simulation Process 79
6.5.2 Assumptions 80
6.5.3 Predicted Cell Path Simulation Results 84
6.5.4 Force Trends 86

6.6 Simulation and FEM Results 90

6.6.1 Optimal CFS Design 90
6.6.2 Optimal Experiment Methodology 91

Chapter 7: Cross Flow Experiment 96

7.1 Experimental Objective 96
7.2 Experimental Setup and Procedure 96

7.2.1 DIC versus Brightfield Setup 97

    - 7.2.2 Brightfield Experimental Setup....100
    - 7.2.3 Experimental Procedure....101
    - 7.2.4 Post-Experimental Procedure....102
    - 7.2.5 Cleaning Procedure....102
    - 7.2.6 Cell Preparation....102
    - 7.2.7 Methods to Analyze Experimental Results....103
  - 7.3 Establishment of Experimental Parameters....106
  - 7.4 Methods to Minimize Non-magnetically Tagged Cells....108
    - 7.4.1 High Initial Flow Rate Test....109
    - 7.4.2 Cell Removal Tests....110
  - 7.5 Rare Cell Experiments....114
    - 7.5.1 Rare Cell Experiment Counting Procedure....115
    - 7.5.2 Rare Cell Experiment Results....117
    - 7.5.3 Summary of Cross Flow Experiments....121
- Chapter 8: Discussion and Recommendation....123
  - 8.1 Key Findings....123
    - 8.1.1 MT Cells....123
    - 8.1.2 NMT Cells....130
  - 8.2 Predicted Cell Path Recommendations....133
    - 8.2.1 Verifying Current Simulation....133
    - 8.2.2 Methods to Improve the Current Simulation....135
  - 8.3 Cell Experiment Recommendations....136
    - 8.3.1 Methods to Increase the MT Cell Capture Efficiency....136
    - 8.3.2 Methods to Decrease the NMT Cell Capture Efficiency....145
  - 8.4 Summary of CFS Findings and Recommendations....148
- Chapter 9: Conclusion....150
- References....154
- Appendix A: Magnetic Single Cell Micro Array Fabrication Process....162
- Appendix B: Magnetic Information for Permalloy Strips....164
- Appendix C: Dimensions for Large Scale Fluid Flow Model....166
- Appendix D: Predicted Cell Path Simulation Steps....167
- Appendix E: Dynabead Magnetic Characteristics....169
- Appendix F: Entire Trap Area vs. Trap Region....171

List of Tables

Table 5.1: Material for each component of the CFS. 52
Table 5.2: Physical properties of materials in the CFS. 52
Table 5.3: Magnetic properties of materials in the CFS. (Conversion between χ_v to μ_r is $\mu_r = 1 + \chi_v$. Other relevant conversions are shown in equations 5.3 and 5.4.) 53
Table 5.4: Biocompatibility of materials that come into contact with the cells 56
Table 6.1: COMSOL magnetic boundary conditions [93] 60
Table 6.2: Boundary conditions for fluid flow model [94] 61
Table 6.3: Subdomain equations and relevant coefficients for the LSM model 63
Table 6.4: Boundary conditions and relevant coefficients for the LSM model 63
Table 6.5: Fluid inlet velocity and average fluid velocity through the centre of the culture chamber assuming a constant flow rate 67
Table 6.6: Subdomain equations and relevant coefficients for the LSFF model 67
Table 6.7: Boundary conditions and relevant coefficients for the LSFF model 67
Table 6.8: Magnetic information extracted from large LSM model 70
Table 6.9: Fluid flow information extracted from LSFF model 70
Table 6.10: Subdomain equations and relevant coefficients for SBMF FEM Model. 71
Table 6.11: Boundary conditions and relevant coefficients for SBMF FEM Model using boundary numbers in Figure 5.10. 72
Table 6.12: Total time for cell to travel from an initial (x, y, z) position of (160, 240, 50) μm to the trap with varying percentages of magnetic force. 82
Table 6.13: Total time for cell to reach trap initial (x, y, z) position of (160, 240, 50) μm to the trap. 85
Table 6.14: Horizontal distance a cell travels due to settling velocity. 93
Table 7.1: Parameter establishment test summary. 108
Table 7.2: Efficiency analysis for parameter establishment test. 108
Table 7.3: High initial flow rate test summary. 110
Table 7.4: Efficiency analysis for high initial flow rate test. 110
Table 7.5: Cell removal test summary. 112
Table 7.6: Efficiency analysis for cell removal test. 112
Table 7.7: Change in traps after cell removal tests shown in Figure 7.11. 114
Table 7.8: Rare cell experiment parameters assuming a total cell concentration of 10^5 *cells/mL*. 115

Table 7.9: Rare cell test summary (fixed cells only). 121
Table 7.10: Rare cell test summary (live cells only). 121
Table 7.11: Efficiency analysis for rare cell test (fixed cells only). 121
Table 7.12: Efficiency analysis for rare cell test (live cells only) 121
Table 8.1: Increasing cell concentration test summary. 144
Table 8.2: Efficiency analysis for increasing cell concentration. 144

Table A.1: Electroplating bath recipe [102]. 163
Table A.2: Magnetic information for permalloy strips [88] 164
Table A.3: Area perpendicular to flow and volume according to Figure A.3. For Area D (culture chamber) was taken at the largest part of the culture chamber, which is at the centre. 166
Table A.4: Constants used in predicted cell path simulation. 167
Table A.5: Magnetic characteristics of Dynabead magnetic nanoparticles 170

List of Figures

Figure 2.1: Spiral micro-electromagnet device. (A) Schematic view of micro machined magnetic bead separator. (B) Separation results of magnetic beads after 300 *mA* applied on the right conductor for 10s. [55] 17

Figure 2.2: Ring micro-electromagnet array. (A) Schematic of gold wire ring traps topped with an insulating layer. (B) Close up of the gold wire ring traps. [56] 17

Figure 2.3: Magnetic pin holder device. (A) Magnetic cells on a culture dish on top of the pin holder. (B) Close up of micro-pillars [57] 19

Figure 2.4: Magnetically active bead-patterned hydrogel. (A) Cell experiment using magnetic bead clusters. (B) Close-up of cell capture experiment. [58]....... 19

Figure 2.5: Multitarget magnetic activated sorter schematic showing different sizes of cells being sorted into various channels. [59] 20

Figure 2.6: Magnetic bead microarray using hydrodynamic focusing. Beads are captured by putting them in different inlets that are separated by a buffer flow. [52] 21

Figure 3.1: Generalized B-H curves for various magnetic materials................................ 26

Figure 3.2: B - H curve nomenclature for a typical ferromagnetic material.................... 27

Figure 3.3: Immunomagnetically labelled cell [65]... 28

Figure 3.4: Factors that influence the number of magnetic particles attached to the surface of a cell. [65] 33

Figure 5.1: Edge of the culture chamber cannot be viewed due to the cone of light that enters the culture chamber from the objective. 44

Figure 5.2: Base Plate. (1) Tapped 10-32 holes to secure upper components to the base. (2) M6 clearance holes to secure base to Newport URS150PP microscope stage. (3) Hole for viewing cells using DIC Microscope. (4) Recessed hole for MSCMA. (5) Magnet holder. (6) Hole to easily remove the MSCMA. 45

Figure 5.3: (A) Magnet cover. (B) Top view. (C) Bottom view.................................... 46

Figure 5.4: MSCMA with permalloy strips on a glass substrate with dimensions in *mm* (overall dimensions are 10 *mm* x 18 *mm* x 1.1 *mm*). 46

Figure 5.5: MSCMA trap dimensions for both sawtooth and sinusoidal design (all dimensions in μm). Light yellow/brown regions are the permalloy and blue regions are the area between the permalloy (glass). 47

Figure 5.6: (A) Gasket assembly. (B) Exploded gasket assembly.................................. 48

Figure 5.7: Mould and gasket for (A) culture chamber gasket and (B) square gasket. 49

Figure 5.8: (A) Top plate. (B) Bottom view of top plate... 50

Figure 5.9: Final SMCS assembly on the Newport URS150PP microscope stage with barbed fitting and tubing to introduce flow into the CFS. 51

Figure 5.10: CFS assembly. (A) Base plate. (B) Add MSCMA. (C) 4 N52 magnets on each side placed into the base. (D) Magnet cover placed on top of base to prevent the magnets from moving. (E) Thumb screws secure the base plate and magnet cover to the microscope stage. (F) Gasket assembly is placed over the MSCMA. (G) The upper plate is placed over the gasket assembly. (H) Thumb screws secure the upper plate to the base plate and barbed fittings are used to provide an inlet/outlet. 51

Figure 5.11: B-H curve of electroplated NiFe 81/19 permalloy, 12 μm and 35 μm thick. [87] 54

Figure 5.12: B-H curve of electroplated NiFe permalloy layers 3 μm thick. [88]........... 54

Figure 5.13: Thickness of the permalloy layers versus the relative permeability. [87].... 55

Figure 6.1: (A) Magnetic components of the CFS (B) LSM Model Set-up 62

Figure 6.2: Magnetic flux density of the permalloy strips.. 64

Figure 6.3: Magnetic potential at several locations. (A) Edge of the permalloy strips, x = -7.5 *mm*. (B) Centre of Permalloy strips, x = 0 *mm*. (C) Edge of the permalloy strips, x = 7.5 *mm*. 64

Figure 6.4: (A) Magnetic flux lines (*B*-field). (B) Magnetic field lines (*H*-field). 65

Figure 6.5: (A) Fluid flow through the CFS. (B) SCM fluid geometry with dotted black line showing direction of flow. (1) Barbed fitting (2) Top Plate (3) Inlet/outlet arms of gasket (4) Culture chamber of gasket assembly. 66

Figure 6.6: Velocity streamlines through the CFS. (A) Streamlines equally spaced from one another. (B) Streamlines through the centre of the culture chamber (1 *mm* from bottom of chamber). 68

Figure 6.7: Culture chamber fluid plots showing (A) Velocity and (B) Pressure. 69

Figure 6.8: Velocity profile at the centre of the culture chamber. 69

Figure 6.9: Smaller Boundary Magnetic/Fluid FEM Models. (A) Sinusoidal design. (B) Sawtooth design. Grey region represents the permalloy. 70

Figure 6.10: Smaller boundary extracted from larger models. 71

Figure 6.11: Boundary walls for predicted cell path simulation model........................... 72

Figure 6.12: 2D versus 3D model showing *B*-field at top of the permalloy traps. (A) Sinusoidal permalloy trap design. (B) Sawtooth permalloy trap design....... 73

Figure 6.13: Magnetic flux density between permalloy traps at z = 0 for (A) sinusoidal and (B) sawtooth permalloy design. Grey region is the permalloy. 74

Figure 6.14: *B*-field gradient plot for sinusoidal and sawtooth permalloy design. 75

Figure 6.15: Magnetic flux density for the sinusoidal (left) and sawtooth (right) permalloy traps. (A) Between the permalloy traps z = 0. (B) z = 6 *µm* (C) z = 2.5 *µm* (D) z = 5 *µm*. 76

Figure 6.16: Fluid flow for both sinusoidal (left) and sawtooth (right) permalloy designs. (A) Slice plot throughout the boundary. (B) Fluid flow streamlines throughout the entire boundary. 77

Figure 6.17: Sinusoidal streamline plots at (A) z = 3 *µm* and (B) z = 6 *µm*. 78

Figure 6.18: Predicted cell path simulation cycle. 80

Figure 6.19: Predicted cell path with varying percentages of magnetic force starting at an (x, y, z) position of (160, 240, 50) *µm* for (A) sinusoidal and (B) sawtooth permalloy design. 82

Figure 6.20: Predicted Cell Path with varying flow rates starting at an (x, y, z) position of (160, 240, 50) *µm* for (A) Sinusoidal and (B) Sawtooth permalloy design... 85

Figure 6.21: Magnetic force in the X Direction at z = 12.1 *µm*. 86

Figure 6.22: Magnetic force in the Y direction at z = 12.1 *µm*. 87

Figure 6.23: Magnetic force in the Z direction at z = 12.1 *µm*. 87

Figure 6.24: Magnetic force with varying z-coordinate at the location with greatest *B*-field. (A) X-direction, (B) Y-direction, (C) Z-direction and (D) total magnitude. 88

Figure 6.25: Maximum *B*-field location for (A) sinusoidal and (B) sawtooth. 89

Figure 6.26: Force magnitude for the sinusoidal and sawtooth permalloy design for flow rate of (A) 0 *mL/min* and (B) 10 *mL/min*. 90

Figure 6.27: Flow over MSCMA with overall culture chamber dimensions and distance to traps. 93

Figure 6.28: Distance cell travels at specified initial heights with varying flow rates 94

Figure 7.1: Experimental setup and computer used to view and extract images. 97

Figure 7.2: (A) RoboSCell Setup. (B) Cells viewed using DIC setup, where the black areas are the permalloy strips, and the shiny circles are cells. 98

Figure 7.3: (A) Mixed population of cells viewed using the DIC setup. (B) Same image as (A), but only showing the fluorescently tagged cells. 99

Figure 7.4: Experiment setup using a brightfield microscope. Dotted lines show the tubing and the direction of flow in the tubing. (1) A 5 *mL* syringe contains the medium, which is introduced into the CFS using the syringe pump. (2) The medium goes through tubing and a 3-way stopcock that also has a 3 *mL* syringe, which contain the cells and the cells/medium enter the CFS via the inlet. (3) Fluid exits out of the CFS via the outlet into the waste container. 100

Figure 7.5: (A) Cells that were imaged were categorized as being on the permalloy, between the permalloy, or in traps. (B) This image shows a sample of the

images used to analyze the device where the blue circles show cells that are considered to be in traps. The total cell count results in 13 cells on the permalloy, 4 cells in a trap, and 3 cells between the permalloy. 104

Figure 7.6: Parameter establishment results using two flow rates and two concentrations. The graph shows the number of cells found on the permalloy, in a trap, or between the permalloy for (A) NMT Cells only and (B) MT cells only. 107

Figure 7.7: Parameter establishment results with the number of traps with MT cells.... 107

Figure 7.8: High initial flow rate tests using both MT and NMT cells. (A) Number of cells on chip. (B) Number of traps with MT cells. 109

Figure 7.9: Number of cells on the chip for the cell removal test for (A) NMT and (B) MT cells using different flow rates to remove cells.................................... 111

Figure 7.10: Cell removal tests showing the number of traps with a single cell, 2 cells, or 3+ cells before and after the cell removal test. 111

Figure 7.11: Distribution of captured MT cells before and after cell removal test for (A) Test 1 and (B) Test 2.. 113

Figure 7.12: Traps that either had cells removed or added after cell removal tests for (A) Test 1 and (B) Test 2.. 113

Figure 7.13: Heterogeneous population of cells showing the contrast between MT and NMT cells. (A) Fixed NMT cells were dyed using Trypan Blue 116

Figure 7.14: (A) MT Cells at a concentration of 3e5 *cells/mL*. (B) NMT Cells at a concentration of 3e5 *cells/mL*. 117

Figure 7.15: Cells that appear pink are shown in a pink circle and are known to be MT cells. Cells shown in a green circle are not pink, but are assumed to be MT due to position. Cells shown in a red circle are not assumed to be MT even though they are in a trap.. 117

Figure 7.16: Comparison between MT and NMT cells for rare cell tests. (A) Using fixed cells and (B) live cells... 118

Figure 7.17: Rare cell test results showing the number of MT cells on the chip for (A) fixed cells and (B) live cells.. 119

Figure 7.18: Rare cell test results showing the number of traps with a single cell, two cells, or 3+ cells for (A) fixed cells and (B) live cells. 119

Figure 7.19: Rare cell test results showing the number of NMT cells on the chip for (A) fixed cell and (B) live cells. 120

Figure 8.1: (A) *B*-field in traps. (B) predicted cell path results. 124

Figure 8.2: (A) *B*-field along permalloy strip. (B) Cell capture distribution................ 125

Figure 8.3: Live MT cell capture distribution along the chip showing (A) the side closest to the inlet, (B) the middle of the chip, and (C) the side closest to the outlet. 125

Figure 8.4: (A) Force magnitude for the sawtooth design. (B) Test showing traps with cells added or removed. ... 126

Figure 8.5: Dimensions of trap area (black) versus culture chamber (green)... 128

Figure 8.6: Images taken at various z-heights. (A) Starting at the substrate where $z = 0$. (B) $z \approx 1$ *mm*. (C) $z \approx 2$ *mm*. ... 129

Figure 8.7: (A) Image of chip after initial cell deposit using a flow rate of 0.04 *mL/min*. The cells land randomly on the chip. (B) Image of chip after cell removal test using flow rates of 1.0 *mL/min* and 2.5 *mL/min*... 132

Figure 8.8: FEM model showing flow rate around the traps ... 133

Figure 8.9: Cells attached to (A) features found on the trap and (B) to the end of the permalloy strips. ... 137

Figure 8.10: Culture chamber gasket ... 138

Figure 8.11: MSCMA viewed (A) normally and (B) through 2 cm of PDMS. ... 139

Figure 8.12: Magnetic flux density between the permalloy ($z = 0$). Comparison between (A) Sawtooth with small features and (B) Sawtooth with large features... 141

Figure 8.13: Magnetic flux at various heights. (A) Between the permalloy $z = 0$. (B) $z = 6$ *μm*. (C) $z = 10$ *μm*. (D) $z = 30$ *μm*. ... 141

Figure 8.14: Number of traps with live MT cells with increasing cell concentrations... 143

Figure 8.15: Live MT cell capture distribution for different concentrations. (A) 1e5 *cells/mL*. (2) 3e5 *cells/mL*. (3) 3e6 *cells/mL*. ... 144

Figure 8.16: Live NMT cell distribution for different concentrations. (A) 1e5 *cells/mL*. (B) 3e5 *cells/mL*. (C) 3e6 *cells/mL*. ... 145

Figure 8.17: NMT cells become attach to entire surface of the MSCMA. (A) Above the trap area. (B) In the trap area. ... 147

Figure A.1: MSCMA fabrication steps [23]. ... 163

Figure A.2: Permalloy magnetic information (A) Relative permeability vs. magnetic field. (B) BH curve... 165

Figure A.3: Large scale fluid flow model. (1) Barbed fitting. (2) Top plate after the fluid exits the barbed fitting. (3) Inlet/Outlet arms. (4) Culture chamber. ... 166

Figure A.4: Magnetization versus Applied Field for magnetic Dynabead particles. (A) MyOne Dynabead (B) M-270 Dynabead (C) M-280 Dynabead (D) M-450 Dynabead ... 170

Figure A.5: Trap region which only includes the green triangle shown... 171

Figure A.6: Image analysis used 15 images of the entire chip. Entire trap area which includes 2 ½ strips (1a and 1b) and 15 full strips (2 - 16). Each ½ strip contains 40 traps, and each full strip contains 80 traps for a total of 1280 traps. ... 172

Acronyms

ABC : Antibody Binding Capacity
AM : Automated Microscopy
FBS : Fetal Bovine Serum
CE% : Capture Efficiency
CFS : Cross Flow System
DIC : Differential Interference Contrast
DW : Deionised Water
DNA : Deoxynucleic Acid
FC : Flow Cytometry
FEM : Finite Element Method
LSC : Laser Scanning Cytometry
LSFF : Large Scale Fluid Flow
LSM : Large Scale Magnetic
MEMS : Microelectromechanical System
MSCMA : Magnetic Single Cell Micro Array
MT : Magnetically Tagged
MT-CE% : Magnetically Tagged Cell Capture Efficiency
MP : Magnetic Particle
NA : Numerical Aperture
NMT : Non-Magnetically Tagged
NMT-CE% : Non-Magnetically Tagged Cell Capture Efficiency
PBS : Phosphate Buffer Solution
PDMS : Polydimethylsiloxane
POM : Polyoxymethylene
RNA : Ribonucleic Acid
SCTE% : Single Cell Trapping Efficiency
SBMF : Small Boundary Magnetic/Fluid
TE% : Trapping Efficiency

Nomenclature

Symbol	Description	Units
A	Area	m^3
B	Magnetic flux density	T
B_r	Remanent flux density	T
B_s	Saturation magnetic flux density	T
D_H	Hydraulic diameter	m
F_b	Buoyancy Force	N
F_d	Stokes drag	N
F_g	Force due to gravity	N
F_m	Magnetic force on a magnetic nanoparticle	N
$F_{m,total}$	Total magnetic force	N
g_x, g_y, g_z	Gravitational constant depending on the orientation of gravity	m/s^2
H	Magnetic field	A/m
H_c	Coercive magnetic field	A/m
H_s	Saturation magnetic field	A/m
L	Characteristic linear dimension	m
L_p	Point length scale	m
L_t	Transport length scale	m
J_f	Free current density	A/m
J_d	Displacement current density	A/m
M	Magnetization	A/m
m	Magnetic moment	Am^2
n_x	Number of binding sites on a cell	
P	Perimeter	m
p	Pressure	N/m
Q	Flow Rate	m^3/s
r	Sphere radius	m
Re	Reynolds number	
Re_{NCD}	Reynolds number for flow in a non-circular duct	
Re_{XF}	Reynolds number for a sphere in a fluid	
U	Mean fluid velocity	m/s
U_f	Velocity of fluid	m/s
U_s	Velocity of sphere	m/s
u	Fluid velocity in the x-direction	m/s
V	Volume	m^3
V_m	Volume of magnetic particle	
v	Fluid Velocity in the y-direction	m/s
w	Fluid velocity in the z-direction	m/s
β	Number of magnetic particles bound to each primary antibody	
η	Dynamic Viscosity	$Pa \cdot s$

Symbol	**Description**	**Units**
$\boldsymbol{\theta_x}$	Fraction of antigen on the cell surface bound by antibodies	
$\boldsymbol{\lambda}$	Valence of the antibody	
$\boldsymbol{\mu}$	Magnetic permeability	N/A^2
$\boldsymbol{\mu_o}$	Permeability of free space	N/A^2
$\boldsymbol{\mu_r}$	Relative magnetic permeability	
$\boldsymbol{\rho}$	Density	kg/m^3
$\boldsymbol{\tau}$	Shear stress	Pa
$\boldsymbol{\chi}$	Magnetic susceptibility (mass or volume [dimensionless])	m^3/kg
$\boldsymbol{\psi}$	Magnetic Potential	A

NOTE: If no unit present, the unit is dimensionless

Acknowledgement

There are many people that have helped me get to where I am. First and foremost, I would like to thank both my supervisors, Dr. Nikolai Dechev and Dr. Edward Park for their guidance, support, and knowledge. This thesis shows the work that you have both helped me with, and for that I am grateful. Thanks to both Kelly Sakkaki, and Hadi Esmaeilsabzali, even though you were across the pond, having other students to talk to helped more than you know. To Stephanie Gibson and Dr. Robert Burke, thank you for your cell knowledge and support, all those beautiful Jurkat cells made my life so much easier. I would also like to thank Dr. David Sinton’s lab for letting me use and hog the syringe pump, your understanding was greatly appreciated.

My academic career has been hard and long, but I drew strength from my parents love and I have to thank them for pushing me to be the best that I can be. Like my Dad says, "you can do anything". Thank you to my sister Angela, for always being a phone call away, for listening to me with patience and love regardless of the time or long distance charges. Thank you to my brother Tony, for protecting me that one time on the bus and watching two movies with me in one day, you have inspired me in ways you could not possibly imagine. A girl cannot survive without some good ol’ estrogen, Charleen and Chelsey, thank you for being amazing far-away friends, for all your love and support back in Ottawa. It is because of you two that I want to come back!

I would also like to thank the Kerrigan clan, because you provided me a home away from home, always made me feel loved and a part of the family. Dawn thank you for your amazing heart, Shawn thank you for your constant support, and Sara thanks for all the laughs. Last, but definitely not least I want to thank the one person who truly shared every moment of this experience with me. Brett, thank you for always lending an ear, providing a shoulder to lean on and opening your arms for a great big hug, you always knew which one I needed. We have done everything together, from our undergrad, to Pratt, to our Masters, and I cannot wait to do everything else together as well. I love you.

Dedication

This is dedicated to my grandma Young Lye Kim, for her never ending love and support.

I will love you forever.

I wish you were here.

사랑해 외할머니

Chapter 1: Introduction

The cell is the basic building block of any living organism and the knowledge obtained by understanding the behaviour and characteristics of cells has great potential. Knowledge of single cells is especially beneficial as it can unlock individual processes that result from cell mutations, reveal details of cell development and differentiation, show reactions to various cell stimuli, or determine environments that support and sustain cell viability. Single cell analysis devices aim to unlock all this information to improve medical techniques currently used such as the use of stem cells to improve tissue engineering capabilities, or to diagnose birth defects or cancer at an early stage.

Current techniques to obtain information from cells are usually done by taking an average value from a population of cells. These techniques are generally referred to as bulk techniques; they are used because they are simple and well-established. However, averaged values obtained from bulk techniques tend to mask the individual behaviour/response of cells, which can yield important information. Hence, average values can be misleading as they cannot accurately represent single cells unless every cell within the population is identical and at equilibrium [1].

Due to the presence of non-uniform environments, heterogeneity of cells, and randomly timed cell signalling in populations, it is important to outline the limitations of gathering data with bulk techniques [2]. For example, the western blot is a bulk technique that is used to detect specific proteins in cells. It does this by separating protein from a population of cells and then detects this protein using specific antibodies that target the protein [3]. Using this technique has as few drawbacks. For example if that experiment is conducted several times the results will vary since the results only detect the levels of protein at one instance of time, and the protein levels measured are not that of an individual cell but of the entire population [3]. Every cell in a population will not be in equilibrium since the start and duration of the life span will differ for every cell [4]. This means that physiology and gene expressions will differ for each cell as a function of time. It is also difficult to see the interaction between two cells with bulk techniques, since the interaction signals will not be coincident for all cells and this information is often masked by other dominant signals [5].

Cell signals and interactions can be further altered if every cell is not exposed to the same environment. A non-uniform environment can result if there are too many cells within a specific area, which results in a lack of nutrients in one area. Cells that are in areas of low nutrition will die at a faster rate compared to cells in an area with adequate nutrition. It has also been shown that exposing cells to different environments can significantly affect the cells. For example, the structural and functional properties of cardiac constructs will vary in different environments, [6] and bacteria grown in different media will differ in their protein, ribonucleic acid (RNA), deoxyribonucleic acid (DNA), lipid, carbohydrates, and even their size [7]. Also, an optimal environment is needed to ensure the viability of all cells and to potentially dictate what cells become. For example, stem cells need an optimal environment, also referred to as a “niche”, to grow successfully and differentiate [8-9].

Another factor that will contribute to misleading bulk average values is cell heterogeneity, which can be defined as every cell in a population being different. These differences can be categorized as genetic differences, biochemical differences, physiological differences, and behavioural differences [10, 11]. Genetic differences between cells include the presence/absence/copy of genetic material (e.g. DNA and RNA). Biochemical differences are the differences in the macromolecular composition of the cell (e.g. proteins, carbohydrates, and lipids). Physiological differences are primarily morphological differences such as cell size, shape, surface, or internal characteristics. Lastly, behavioural differences are a result of all other factors mentioned previously and include how each cell will interact with its environment or other cells. There are several examples that clearly demonstrate cell heterogeneity. Embryonic and adult stem cells are heterogeneous in their transcription factors and gene expressions that dictate the cells ability to self-renew and what each cell can or will differentiates into [12]. Differences in gene expression have also been seen in bacteria cells that result in heterogeneity in division time, rate of growth, and cell size at division [13]. Lastly, heterogeneity in the composition of the nucleus, specifically the nuclear lamins has been seen in the cells of rat tissue [14].

To rectify the problems seen with bulk techniques, single cell analysis can serve as an important tool for cellular research. Information obtained for individual single cells can be used to detect abnormal cells at an early stage, which could be used to diagnose and possibly prevent physical ailments, such as cancer or birth defects [15]. Specific examples include the identification of the process that results in a stem cell becoming a cancerous cell [16], and a better understanding of the progression of monoclonal b-cell lymphocytosis into chronic lymphocytic leukemia [17].

Single cell analysis can also be used for applications such as tissue engineering, which includes growing cells under specific conditions to artificially grow tissues and organs [15]. Examples of tissue engineering include studying different environments that will successfully sustain osteoblastic cells for bone cell growth research [18], and the study of ventricular cardiac myocytes for cardiac tissue engineering [6]. Stem cells also have huge potential in tissue engineering as they can develop into specific cell types depending on stem cell interaction with its environment and other cells. Information gathered from the study of single stem cells may determine how they can differentiate into specific cells [15]. Also, a stem cell niche created using single cell manipulation techniques potentially has the ability to grow stem cells and control what these cells differentiate into [19-20].

The true goal of any single cell analysis device is to understand the function and structure of cells more thoroughly and use this knowledge for further research or to develop new medical therapies. Therefore, a system capable of performing in vitro single cell analysis should incorporate a number of functions, which include:

1. Ability to physically isolate single cells from each other, and then to obtain unique information from these isolated cells.
2. Ability to control the environment to ensure cell viability over duration of time.
3. Ability to alter the environment such as temperature and pH to potentially trigger certain characteristics.
4. Ability to replenish the culture medium and introduce new reagents as required by the analysis.
5. Ability to perform these functions with less equipment, by integrating traditional cell analysis hardware into a single system.

This thesis research has been done to develop a system that will possess these generally proposed functions, and integrate them all into a single design called the “cell cross flow system" (CFS). The research presented shows the design, analysis and testing of the CFS. The goal of the CFS is to capture and array single cells using magnetic force and fluid dynamic concepts, while ensuring the CFS is compatible with automated cell analysis instrumentation. The CFS makes use of a previously developed technology, a microelectromechanical systems (MEMS) chip called a "magnetic single cell micro array" (MSCMA) for capturing magnetically tagged (MT) cells [21] [22]. Additionally, the CFS has been designed to operate within RoboSCell which is an automatic system that visually analyses and probes cells [23].

This thesis covers the following sections. First, the current technologies used for single cell analysis is reviewed, followed by a summary of devices that perform functions similar to the CFS. Next, basic magnetic and fluid concepts used in this work are discussed and will include basic magnetic and fluid terminology and concepts used in this thesis, along with the magnetic and fluid forces exerted on a cell. Next the design, construction, and properties of both the CFS and MSCMA are discussed. Using the CFS design, a finite element method (FEM) analysis is done on both the magnetic and fluid aspects of the system. This information is then used to conduct a simulation to predict the path a single MT cell will follow in response to simultaneous magnetic and fluid forces. The FEM analysis and the simulation are used to optimize experimental methodology. Next, experiments to test the capabilities of the CFS are done, including establishing test parameters, methods to remove unwanted cells, and tests with mixed ratios of MT to non-magnetically tagged (NMT) cells. Lastly, the experimental results will be compared to the FEM analysis and key findings of the CFS will be discussed including several recommendations to the overall design.

Chapter 2: Background

Single cell analysis is an emerging field that has gained popularity in the last ten years. Devices used for single cell analysis can be categorized based on the method used to manipulate cells, and the technique used to further analyze single cells. The methods used to manipulate cells vary depending on the device and include fluid, optic, electric, magnetic and mechanical manipulation methods. The techniques used to capture and analyze cells will differ for each device and can be categorized as high-throughput, microfluidic, high-content separation and array-based techniques.

The CFS manipulates cells with magnetic and fluid forces using an array-based technique. The CFS has two main parts, which are: (i) MSCMA chip that uses an externally applied magnetic field to capture MT cells, and (ii) a gasket assembly, which is a fluid platform to control the movement of the cells using a syringe pump. The MSCMA is what classifies the CFS as an array-based technique as it includes several strips of magnetic traps that use an externally applied magnetic field to capture MT cells. This MSCMA allows the cells to be arrayed, or placed in pre-defined locations using magnetic force. The cells are also manipulated using a fluid force applied by a gasket assembly, which flow cells and fluid over the MSCMA.

The proposed CFS has been designed to capture cells from a heterogeneous population. This increases the versatility and speed of cell analysis, since the population does not need to be processed to only include one type of cell. Secondly, the CFS is designed to array single cells in pre-defined locations within a single chamber, which exposes each cell to the same environment. Also, arraying cells in pre-defined locations simplifies the automatic machine vision task of RoboSCell for locating the cells once all the cells have been captured. Being able to quickly locate cells will reduce processing time and computational power needed to obtain information on single cells. This chapter will first review the techniques and methods used in other single cell analysis technologies, and then discuss some specific devices that are similar to the CFS.

2.1 Single Cell Analysis Technologies

There are a variety of methods to manipulate cells, and many techniques use these methods to further analyze single cells.

2.1.1 Cell Manipulation Methods

Single cells can be manipulating using fluid, optic, electric, magnetic and mechanical forces [24]. This section will briefly discuss these methods including advantages and disadvantages of each.

2.1.1.1 Fluid Manipulation Method

Fluid manipulation methods are commonly used to control cells that are suspended in a fluid. Cells in a fluid suspension can be manipulated using pumps that move the fluid by either electrically induced or pressure gradient induced methods. Electrically induced pumping is based on electroosmotic pumping [25]. When the surface of a channel is charged using cathodes placed at either sides of a channel, ions of opposite charge to that of the surface are attracted towards the surface, while ions of like charges are repelled. This causes the positive ions of water to be drawn towards the charged surface whereas the negative water ions are drawn towards the negative cathode and this creates a net flow towards the cathode.

Another method to move fluid is by creating a pressure gradient. This can be done using a pump external to the device or integrated into the device. Examples of external pumps include syringe and peristaltic pumps. Syringe pumps use a stepper motor to linearly actuate a syringe at a specific rate, and peristaltic pumps use a roller attached to a rotor to compress flexible tubing creating a pressure difference in the tubing to move the fluid. Internal pumps use micro-valves to apply pressure gradients within the device and these valves are actuated through pressure, magnetism, electromagnetism and thermal expansion [26].

Cells are easily manipulated using a fluid force, which can be used on all types of cells as long as they are in a fluid suspension. One major drawback to using an electroosmotic pump is that large voltages are needed to move the liquid, and this can have negative effects such as heating and bubble formation [27-28]. Another drawback to using fluid manipulation methods is that generally a closed system is needed to create the necessary pressure gradient to move cells. Hence, it is not easy to physically access the cells within a fluid manipulation system.

2.1.1.2 Optical

Optical manipulation use optical forces from radiation pressure, and are used in optical traps [29]. Radiation pressure is the pressure exerted on the cell surface that is exposed to visible or infrared laser light. The force depends on the optical properties (e.g. refractive index and absorption) and geometric properties (e.g. shape, composition, and surface charge) of the cell [24]. Optical traps use optical manipulation by focusing a laser beam onto a cell, which provides an attractive or repulsive force depending on the difference in the refractive index between the cells and the medium. This method is non-invasive but the use of optical force poses the risk of increasing the cell temperature due to cell absorption of light [24]. Also, the setup needed for optical manipulation can be costly and labour intensive. [30]

2.1.1.3 Electric

Electric manipulation includes methods such as dielectrophoresis (DEP) and electrotation. DEP manipulates dielectric particles using non-uniform electric fields and electrotation manipulates electrically polarized particles by controlling the phase and magnitude of the electric field [24]. Both of these methods have been used to non-invasively manipulate cells (translation and rotation) and determine the electric characteristics of cells [31-32]. These methods are non-invasive but can only be used on particles that can be manipulated by an electric field, such as dielectric or polarized cells. Also, the current needed to manipulate the cell can cause current-induced heating. [33]

2.1.1.4 Magnetic

Magnetic manipulation uses a magnetic field to manipulate magnetic particles. In order for this manipulation method to be used with cells, the cell must first be magnetically tagged. These tags consist of magnetically susceptible particles (i.e. iron) that are coated with dextran, which attach to antibodies. These antibodies then attach to molecules on the surface of the cell, also referred to as antigens, through an antibody/antigen interaction. This technique can be used for the study of cellular properties, sorting of cells, capture of cells, and isolation of cells [34-35]. Magnetic manipulation is a non-invasive technique and the magnetic field used causes no harm on cell health and behaviour for extended periods. However it can only be used if an immunomagnetic tag can be attached to a cell, and this can only occur if there is an antibody that can successfully bind to a specific antigen on the desired cell [24].

2.1.1.5 Mechanical

Mechanical manipulation methods use contact forces such as suction from a pipette or micro-grippers [36]. Several mechanical methods have been automated to improve the reproducibility and success rate, which is not possible with human manipulation. Mechanical manipulation has the advantage of being reproducible and predictable, but there is the obvious drawback of harming the cell by exerting too much force on the cell since this method is very invasive.

2.1.2 Single Cell Analysis Techniques

Single cell analysis techniques can be categorized into four groups as follows: (i) high-throughput, (ii) microfluidic, (iii) high content separation and (iv) array-based techniques [3]. All these techniques use one or more of the manipulation methods discussed previously. This section will outline each group and discuss specific examples.

2.1.2.1 High-Throughput Techniques

High-throughput techniques scan a large number of cells in a short amount of time and include flow cytometry (FC), laser scanning cytometry (LSC), and automated microscopy (AM) [37]. The most common high-throughput technique is FC, which passes cells in suspension in a high speed stream at a rate of 1000 *cells/s* through an illumination zone. Dyes are used that bind to specific molecules such as DNA, RNA, or proteins found on or in cells. Cells are transported using flow past laser detectors that measure the magnitude of an emitted light pulse that shows the light that becomes scattered as the cell passes by the light source. The magnitude of the emitted light can show the quantity of the specific molecule of interest. This method is capable of analysing a large number of cells in a short period of time, but it is not possible to observe the spatial location of the molecules. Further, cells remain anonymous, since there is no way to individually identify them or track them over time. [10, 37-38]

LSC is similar to FC, except that the cells are fluorescently dyed and a laser is used to excite the dye. The fluorescence that is emitted from the cell is measured at multiple wavelengths with high sensitivity and accuracy. Images are taken of each cell and this allows for the spatial analysis of fluorescence in each cell to be analyzed. Another advantage of LSC is that it is possible to analyze cells that are not in a fluid stream (as with FC), but instead are stationary cells grown on a solid substrate, which can be analyzed. The overall time needed to analyze cells is greater than FC and therefore LSC has a lower throughput. [3, 39-40]

AM uses computational power to take hundreds of images over a period of time of cells that are stationary. These images are used to analyze useful parameters such as the cell shape, nuclear shape, and protein distribution within the cell. Specific parts of cell can also be fluorescently labelled so that if the cell is exposed to fluorescent light, those parts will emit light. This can be used to observe the change of these parts over a period of time. The number of images that can be taken is only limited by the power of the computer. Further processing of these images can be used to obtain more information in comparison to FC, but it is more time consuming. [3, 41-42]

To summarise, devices that use high-throughput techniques have several advantages: (i) FC is capable of analyzing single cell at a high-speed; (ii) LSC allows for spatial analysis of fluorescence of cells that are in a fluid flow and on a solid substrate; and (iii) AC methods can analyze cells over a period of time, but yield a lower throughput. There are also some disadvantages, including high apparatus cost and high cost of labour due to the complex procedures. [10]

2.1.2.2 Microfluidic Techniques

Microfluidic techniques are micron sized pumps, valves, channels and chambers that are patterned onto a polymer substrate. Microfluidic-based techniques can dynamically control reagents and cells using fluid manipulation methods. They commonly use external pumps to apply a pressure gradient across the channels and chambers to move fluid and cells through the device. Integrated pumps are also used such as micro-valves used to create a peristaltic effect or electroosmotic pumps [25-26].

The most common polymer used to make microfluidic devices is polydimethylsiloxane (PDMS), which is a silicon based organic polymer. PDMS is commonly used due to its advantages [43]. One advantage is the ability to produce micron scale features that are the same size of a single cell making cell manipulation simpler. PDMS also provides optical clarity, which allows for cells and reagents to be viewed clearly using a microscope. It is possible to cure PDMS at room temperature, which reduces the number of other devices needed to fabricate a device. It is also biocompatible with cells and will not adversely affect their health. Lastly it is possible to reversibly seal to itself and other materials, or permanently seal to materials using an air plasma device. The use of PDMS also allows for soft lithography and rapid prototyping fabrication methods. Soft lithography uses an elastomeric structure with patterns embedded into it to create a mould, whereas rapid prototyping uses a computer-aided design (CAD) program to transfer a design onto a silicon wafer via contact photolithography [43].

Microfluidic techniques have been designed to reproduce the functionality of FC using a simpler and less expensive platform but still demonstrate lower throughput compared to FC [3]. They are also able to observe changes in cells over time and observer the cells interaction with reagents. Microfluidic devices are capable of monitoring multiple parameters over time and can analyze hundreds of single cells in parallel, but this creates a more complex device [44]. A more complex device will result in lower throughput and higher device cost [45].

2.1.2.3 High-content Separation Techniques

Chemical cytometry is commonly known as a high-content separation based technique and specific examples include mass spectrometry and capillary electrophoresis. Chemical cytometry is a destructive method that acts to break down a cell through a process called lysis after which the components of the cell are separated and analyzed [46]. Lysis refers to "breaking open" of a cell using enzymatic, osmotic, or mechanical mechanisms that compromise the integrity of the cell membrane [47]. It is done to avoid shear forces exerted on the cell that could degrade molecules such as proteins, RNA, and DNA. Examples of lysis include using specific enzymes to target the cell wall (enzymatic lysis), lowering the ionic strength of the surrounding medium, which causes the cell to swell and burst (osmotic lysis), and using minute glass beads that collide and destroy the cell membrane (mechanical lysis) [46].

Single cell mass spectrometry involves selecting a single cell, inducing cell lysis, separating the desired components from the cell, and inserting these components into a mass spectrometer. The mass spectrometer measures the mass-to-charge ratio of charged particles to determine the mass and chemical composition of the components [48].

Capillary electrophoresis involves injecting intact single cells into narrow capillaries. The cell is then lysed and the cell components are separated using an electroosmotic flow through a size selective matrix. The components are fluorescently dyed and analyzed using a laser-induced fluorescence to determine the amount that has been separated [49].

Although these techniques are not able to obtain dynamic or localized cellular information, they are capable of obtaining a large quantity of information from a single cell (e.g. DNA, RNA, and protein) [3]. These techniques involve a number of steps including (i) injecting individual cells into an external apparatus, (ii) performing cell lysis, and (iii) separating desired molecules from the cell. These three steps are time consuming and increases the overall analysis time [50]. Also, since the process is destructive, these techniques can only be used as an analysis tool.

2.1.2.4 Array-based Techniques

Array-based single cell analysis techniques include a variety of techniques that array and isolate single cells while exposing each cell to the same environment. This allows for greater control of environmental factors and minimizes unwanted cell-to-cell interactions. This technique commonly uses MEMS technology, which have micron-sized geometrical features that facilitate the array process. MEMS-based arraying devices have features that are sized at the same scale as the cell, which allows for easier characterization of a single cell. If the cells are organized and well distributed into predefined arrays, imaging and cell gathering processes are simplified since the cells are easier to locate. [3]

Array-based devices use a variety of cell manipulation methods such as mechanical confinement, magnetic, electromagnetic, chemical or thermal forces.

Mechanical confinement arrays rely on either gravity or fluid manipulation methods for cells to fall/flow out of suspension and into a physical trap [51]. Magnetic arrays rely on soft magnetic materials magnetized by an external magnetic field (e.g. permanent magnet) to capture MT cells [21]. Electromagnetic arrays are similar to magnetic arrays, but the arrays are capable of producing their own magnetic field [52]. Chemical arrays use chemicals patterned onto a substrate that are adherent to cells [3]. Lastly, thermal arrays use heat to actuate traps to capture cells [53].

Array-based devices are capable of arraying a large number of individual cells in parallel. They can use a variety of methods to manipulate cells, which increases their versatility. The throughput is lower compared to FC or LSC and the construction can be complex and expensive. Since cells are viewed in parallel it is difficult to obtain real-time dynamic information from multiple cells at once. Although array-based techniques place cells in pre-defined locations, the ability to track the progress of each cell over time becomes a function of external hardware. This includes items such as the microscope system, motion stage to move the sample under the microscope, and the algorithm used to identify the cell, and therefore the computational power. [3]

2.2 Technology Similar to the CFS

The CFS uses an array-based technique to manipulate cells with both fluid and magnetic methods. Cells can be separated from a heterogeneous population of cells using magnetic force as long as the desired cell exhibits magnetic characteristics. If the desired cell does not demonstrate intrinsic magnetic characteristics, the cell needs to be immunomagnetically tagged using a surface antigen (section 3.2.1). [54]

There are many single cell devices that use similar techniques to the CFS. Using magnetic force as the main manipulation method to isolate cells can be classified as passive or active [52]. Active separators use integrated micro-electromagnets that are capable of producing their own magnetic gradient. Passive separators use soft magnetic material magnetized by an externally applied magnetic field. This next section will review various devices that use active or passive magnetic separation method.

2.2.1 Active Magnetic Separators

Active magnetic separators use micro-electromagnets, which produce their own magnetic field gradients to manipulate magnetic particles. Most of these devices also use a fluid platform to position the cells as needed. This section will discuss the following active magnetic separators: (i) the spiral electromagnet separator, and (ii) the ring electromagnetic array.

The first active magnetic particle separator is a spiral electromagnet developed by J. Choi et al. from the University of Cincinnati (Cincinnati, Ohio). This device separates magnetic nanoparticles using a planar bio-magnetic bead separator on a glass chip, and is shown in Figure 2.1. The separator includes a micro-machined semi-encapsulated spiral electromagnet and microfluidic channels, which are fabricated separately then bonded together. The magnetic particles are suspended in a fluid, which flows over the separator using the microfluidic channels. A DC current of $300\,mA$ is applied to the electromagnet, which results in a magnetic field that attracts the magnetic particles. This device was successful in separating magnetic particles from the fluid flow, but it has not been tested with cells. [55]

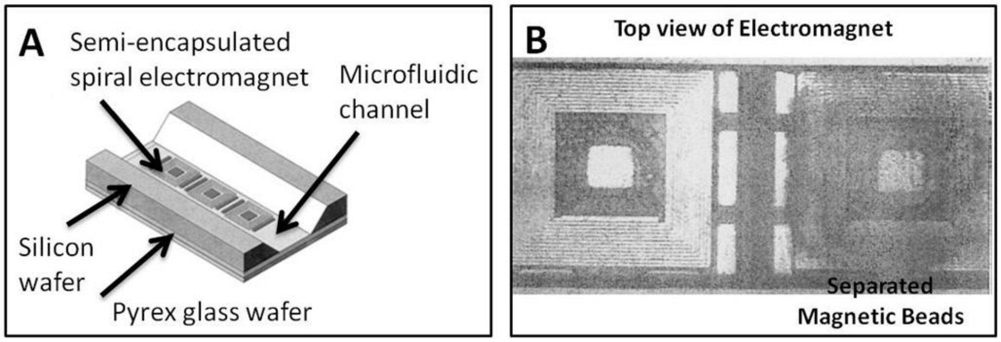

Figure 2.1: Spiral micro-electromagnet device. (A) Schematic view of micro machined magnetic bead separator. (B) Separation results of magnetic beads after 300 *mA* applied on the right conductor for 10s. [55]

A ring electromagnetic array developed by H. Lee et al. from Harvard University (Cambridge, Massachusetts) is another example of an active magnetic separator. Micro-electromagnet rings positioned in an array are used to generate a local magnetic field to control magnetic particles. The ring trap is a circular gold wire topped with an insulating layer and current is passed through the wire to control the magnetic field above the trap, and is shown in Figure 2.2. This device is capable of trapping magnetic particles within the ring traps and the orientation of the particle is controlled by changing the phase of the current applied to each trap. Although this device could trap and control magnetic particles, it has not been tested using cells. [56]

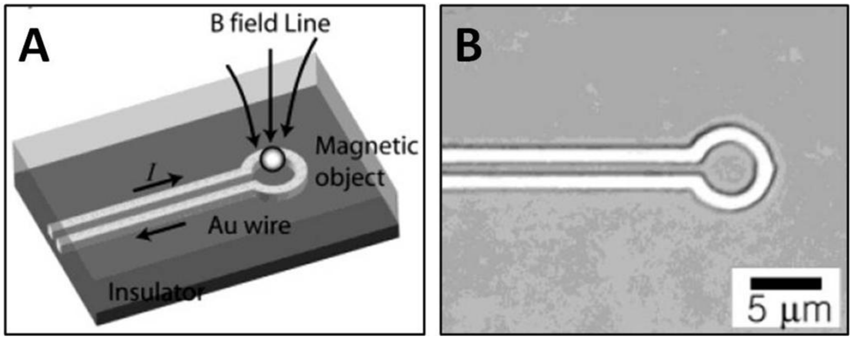

Figure 2.2: Ring micro-electromagnet array. (A) Schematic of gold wire ring traps topped with an insulating layer. (B) Close up of the gold wire ring traps. [56]

These active separator devices are potentially capable of separating and arraying MT cells from a fluid flow. They have the advantage of being able to locally manipulate magnetic particles without the use of an externally applied magnetic field. However, the fabrication process of all of these devices is quite complex, which increases the cost of these devices. Also, a constant current source is needed to manipulate the magnetic particles, which increases the number of external devices needed. The magnetic field created by these devices is generally smaller in comparison to passive magnetic separator devices. This is due to the small size of the traps, which results in small amounts of conducting material, and therefore a lower magnetic field.

2.2.2 Passive Magnetic Separators

Passive magnetic separators use soft magnetic materials in various shapes that require an externally applied magnetic field. This applied magnetic field is created using either a permanent magnet or an electromagnet. They also commonly use fluid platforms to deposit cells over the devices. This section will discuss the following passive magnetic separator devices: (i) magnetic pin holder, (ii) bead-patterned hydrogel, (iii) multitarget magnetic activated cell sorter, and (iv) a hydrodynamic focusing magnetic bead microarray.

A magnetic pin holder device was created by researchers I. Kosuke et al. from Nagayo University (Nagoya, Japan). This device is made from iron and measures approximately 20 x 20 x 20 mm^3 and contains 6000 pillars, each measuring 0.1 x 0.1 x 0.3 mm^3, as shown in Figure 2.3. A culture dish containing cells is placed on the pin holder, which in turn is placed onto a cylindrical neodymium magnet. This device is able to array and isolate single MT cells. Several factors influence the rate of capture, such as the distance between the cell and the pin holder, the ratio between the cell and the pillar, and the concentration of cells used. [57]

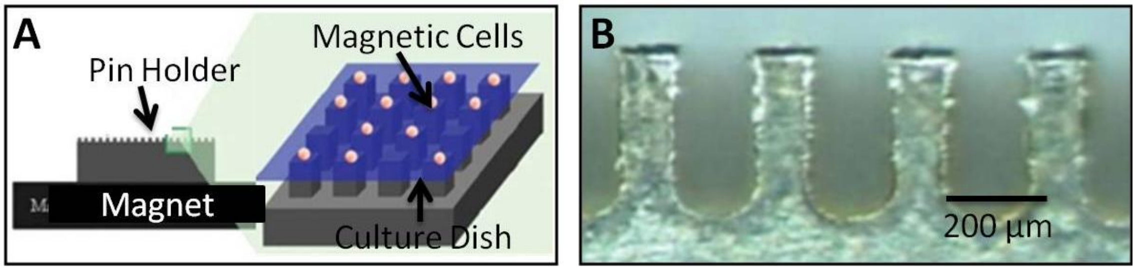

Figure 2.3: Magnetic pin holder device. (A) Magnetic cells on a culture dish on top of the pin holder. (B) Close up of micro-pillars [57]

The second passive device is a magnetically and biologically active bead-patterned hydrogel, as shown in Figure 2.4 developed by D. C. Pegibon et al. at the Massachusetts Institute of Technology (Cambridge, Massachusetts). Magnetic beads are patterned as clusters in polyethylene glycol hydrogel that are covalently linked to a glass surface. MT cells in a fluid flow are passed over the device using a microfluidic channel, and the MT cells were successfully captured by the magnetic clusters. Once captured the cells could be easily released by removing the magnetic field. [58]

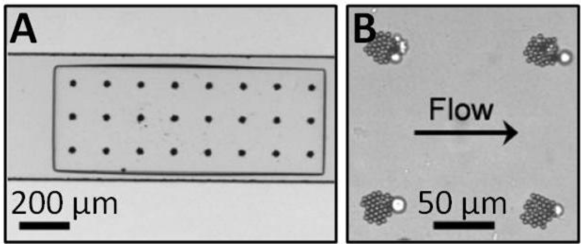

Figure 2.4: Magnetically active bead-patterned hydrogel. (A) Cell experiment using magnetic bead clusters. (B) Close-up of cell capture experiment. [58]

Another passive magnetic separator is a multi-target magnetic activated cell sorter developed by J. D. Adams et al. from the University of California (Santa Barbara, California). This device is fabricated using a glass/PDMS system, which uses external magnets and a fluid system to sort cells, as shown in Figure 2.5. This device uses microfabricated ferromagnetic strips (MFS) to generate large and reproducible magnetic fields that act at a pre-determined angle. Multiple types of cells can be sorted from a heterogeneous population of cells by using the difference in the Stokes drag on cells with different sizes. The cell's Stokes drag is calculated and the angle of the MFS is matched to that cell to direct it towards a specific channel. This device was capable of separating different types of cells from the fluid flow based on the relationship between the Stokes drag and the MFS angle. [59]

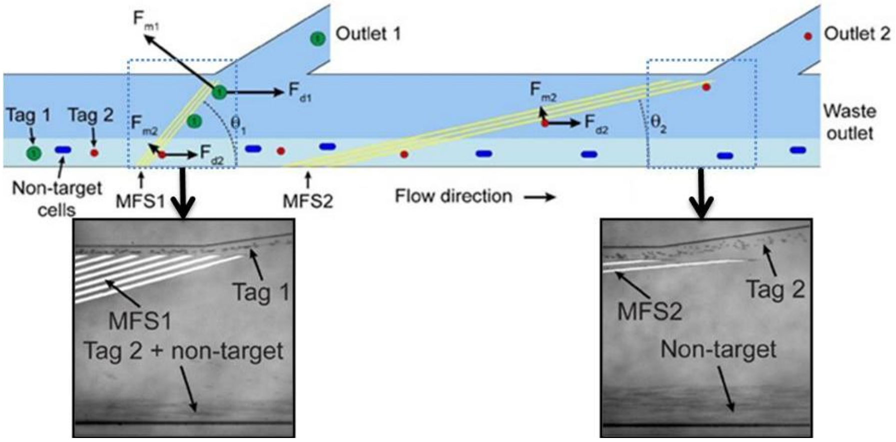

Figure 2.5: Multitarget magnetic activated sorter schematic showing different sizes of cells being sorted into various channels. [59]

Another device also capable of separating two different types of magnetic beads was developed by K. Smistrup et al. from the Technical University of Denmark (Kogens Lyngby, Denmark). This device consists of a microfluidic channel measuring 0.1 x 0.12 x 0.013 mm^3 with three inlets and one outlet, as shown in Figure 2.6. Magnetic elements that measure 0.05 x 0.04 x 0.0049 mm^3 are placed symmetrically along the sides of the microfluidic channel every 0.35 *mm*. The device is capable of capturing different magnetic beads by using hydrodynamic focusing. Two solutions with different beads are introduced into the device by the two outer inlets. A buffer stream is flowed into the centre inlet, which separates the two outer solutions and forces them towards the outer edges of the channel. This allows for different magnetic beads to be captured at opposite sides of the microfluidic channel. Currently, this device has not been tested with cells. [52]

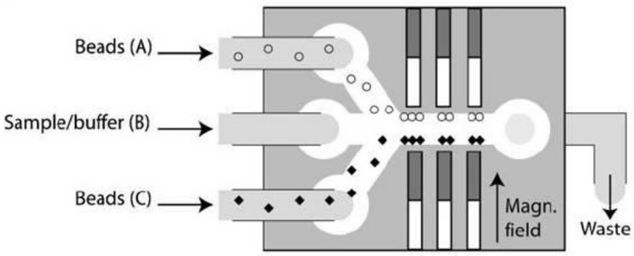

Figure 2.6: Magnetic bead microarray using hydrodynamic focusing. Beads are captured by putting them in different inlets that are separated by a buffer flow. [52]

All of the passive devices mentioned in this section use magnetic manipulation integrated with a cross flow device to potentially separate cells from a fluid flow. The fabrication process for passive devices is generally simpler in comparison to active devices. They require an externally applied magnetic field and exhibit higher magnetic properties when compared to active devices, but they lack the ability to independently control cells. The simplicity of the passive devices combined with their high magnetic properties greatly outweighs the disadvantage of requiring an externally applied magnetic field and not being able to independently control each trap.

2.3 Motivation for the CFS

The CFS was developed to isolate and capture rare single MT cells, and has several integrated components to control the fluid flow over the MSCMA. The MSCMA is a passive magnetic separator that uses a MEMS-based design to create an array of traps to separate and isolate single cells. The main component that introduces a fluid flow over the MSCMA is a gasket assembly. This gasket assembly was integrated to easily deliver cells over the MSCMA and promote single cell capture from a heterogeneous population. It can also be used to deliver medium and nutrients to the cell once they have been arrayed allowing for greater environmental control. The next two chapters will discuss the magnetic and fluid theories which were used to analyze and develop the CFS.

Chapter 3: Magnetic Theory

The CFS uses both magnetic and fluid forces to manipulate cells. The MSCMA captures and arrays MT cells using magnetic force and a gasket assembly exerts fluid force on the cells using an externally integrated syringe pump. To analyze and develop the CFS, it is essential to understand the magnetic theory, which drives the MSCMA. This next chapter will discuss the magnetic theory used and it will include an overview on magnetic terminology, concepts and the magnetic force exerted on a single cell.

3.1 Magnetic Terminology and Concepts

To understand the MSCMA it is important to first define some magnetic concepts. A magnetic field always surrounds a permanent magnetic material, and this can be shown by the force exerted on a magnetic particle that is in the presence of a magnetic field. There are two terms used for magnetic fields: magnetic flux density (*B*-field) and applied magnetic field (*H*-field). The *H*-field is the magnetic field that would be present in a vacuum and is measured in amps per meter (*A/m*). The *B*-field is the magnetic field that occurs in a region and consists of the *H*-field times the magnetic permeability of that region, and is measured in Tesla (*T*). [60]

If a magnetic material is placed in an *H*-field, the overall response is the *B*-field and can be defined as:

$$\vec{\boldsymbol{B}} = \boldsymbol{\mu_o}\left(\vec{\boldsymbol{H}} + \vec{\boldsymbol{M}}\right) \qquad \textbf{3.1}$$

$$\vec{\boldsymbol{M}} = \frac{\vec{\boldsymbol{m}}}{\boldsymbol{V}} \qquad \textbf{3.2}$$

Where μ_o is the permeability of free space and is a constant with the value of $4\pi\,\mathrm{x}10^{-7}$ N/A^2. Magnetization, *M*, is the magnetic moment per unit volume, where *m* is the magnetic moment on a volume, V, of material and is measured in amps per meter (*A/m*). Another way to define magnetization is by the volumetric magnetic susceptibility, χ, as follows:

$$\boldsymbol{\vec{M}} = \chi \boldsymbol{\vec{H}} \tag{3.3}$$

The magnetic susceptibility can also be related to the magnetic permeability using the following equation:

$$\boldsymbol{\mu} = \boldsymbol{\mu_o}(\mathbf{1} + \boldsymbol{\chi}) \tag{3.4}$$

$$\boldsymbol{\mu_r} = \frac{\boldsymbol{\mu}}{\boldsymbol{\mu_o}} \tag{3.5}$$

Both the magnetic susceptibility and the magnetic permeability, μ, measure the degree of magnetization present in a material due to the response to an H-field. Many materials are characterized by the relative permeability, μ_r, which is the ratio between the magnetic permeability of the object and the magnetic permeability of free space. [60]

3.1.1 Maxwell's Equation

Using the magnetic terminology and concepts mentioned before, the Maxwell's equation can be defined. The Maxwell's equation is a set of four equations that relate the electric and magnetic field to their sources, charge density and current density. The four Maxwell's equations are: (i) Gauss's law, (ii) Gauss's law for magnetism, (iii) Faraday's law of induction, and (iv) Ampère's law with Maxwell's correction. Only equations (ii) and (iv) are relevant to permanent magnets.

Gauss's law for magnetism states that there are no magnetic charges (also referred to as magnetic monopoles) in a material. Instead the magnetic field is generated by a configuration of dipoles. Each dipole has no magnetic charge but resembles a positive and negative charge bound together. Since there are no magnetic charges, the B-field lines coming out of a closed surface will be the same as the *B*-field lines going back into the closed surface. This also implies that all *B*-field lines form a closed loop and that they do not have a beginning or an end. Therefore the net flux of *B*-field lines through an enclosed volume is zero: [61]

$$\boldsymbol{\nabla} \cdot \vec{\boldsymbol{B}} = \boldsymbol{0} \tag{3.6}$$

Ampère's law with Maxwell's correction relates the magnetic source to its electric current source and can be summarised as (where J_f is the free current density):

$$\boldsymbol{\nabla} \times \vec{\boldsymbol{B}} = \boldsymbol{\mu_o} \vec{\boldsymbol{J}}_{\boldsymbol{f}} \tag{3.7}$$

If there is no current present, then equation 3.7 equals zero (equation 3.8) and it can be used to define the magnetic potential (ψ). The magnetic potential is a useful tool in describing the *B*-field when there is no current present, such as a permanent magnet. It is measured in amps (*A*) and will always exist in the presence of a *B*-field and can be defined as [62]:

$$\boldsymbol{\nabla} \times \vec{\boldsymbol{B}} = \boldsymbol{0} \tag{3.8}$$

$$\vec{\boldsymbol{B}} = -\boldsymbol{\mu_o} \boldsymbol{\nabla} \boldsymbol{\psi} \tag{3.9}$$

3.1.2 Magnetic Material

All magnetic materials fall into one of the following groups: ferromagnetic, antiferromagnetic, ferrimagnetic, diamagnetic and paramagnetic. Ferromagnetic materials exhibit magnetic characteristics when they have been magnetized, and will continue to exhibit these characteristics even when there is no *H*-field present [63]. This occurs because ferromagnetic materials have unpaired electrons, and the electrons' intrinsic magnetic moments tend to align parallel with the *H*-field and with one another. When the *H*-field is removed, the electrons in the material remain in a parallel orientation allowing the material to exhibit magnetic characteristics without an *H*-field. Antiferromagnetic materials on the other hand, do not exhibit any magnetic characteristics [63]. The electrons' magnetic moments still have a tendency to align with the *H*-field, but they are pointed in opposite direction with equal amounts pointing in each direction. This implies that the net magnetic moment in antiferromagnetic materials is zero, meaning no *H*-field is produced from antiferromagnetic materials. Ferrimagnetic materials are similar to both ferromagnetic and antiferromagnetic materials [63]. For ferrimagnetic materials, the electrons' magnetic moments point in opposite directions, but are unequal in magnitude, which results in a net magnetization that is weaker than the magnetization found in ferromagnetic materials. [64]

Diamagnetic materials have core electrons in filled shells and when an *H*-field is present, these electrons resist any tendency to align. Therefore diamagnetic materials slightly reduce the *B*-field present and have a negative magnetic susceptibility in the range of -10^{-6} to -10^{-3}. Paramagnetic materials have an imbalance in electrons due to unfilled bands and therefore a weak magnetic effect is seen when the electrons align with the *H*-field. They have a positive magnetic susceptibility in the range of 10^{-6} to 10^{-1}. Paramagnetic and diamagnetic materials lose their magnetic properties when the *H*-field is removed. [64]

3.1.3 Magnetic B – H Curve

All of the magnetic groups mentioned can be characterized by their *B* – *H* curves as can be seen in Figure 3.1. Paramagnetic and diamagnetic materials exhibit a linear relationship, where the increase in the *H*-field will result in a linear increase in the *B*-field. Paramagnetic materials will always result in a *B*-field slightly higher than the relative permeability since the magnetic susceptibility is always positive. Diamagnetic materials will always have a *B*-field slightly less than the relative permeability since the magnetic susceptibility is always negative. Ferromagnetic materials on the other hand do not exhibit a linear relationship and the relationship is called a hysteresis curve. [64]

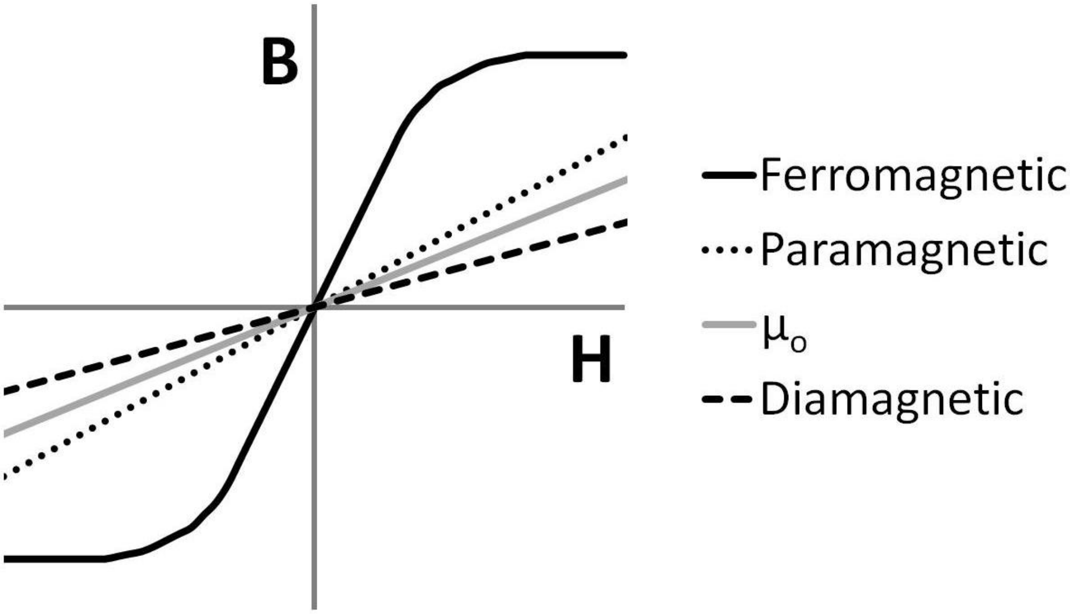

Figure 3.1: Generalized B-H curves for various magnetic materials.

The nomenclature for a typical ferromagnetic hysteresis curve is shown in Figure 3.2. An increase in the *H*-field will result in a non-linear increase of the *B*-field up to the saturation point. At this point an increase in the *H*-field will no longer increase the *B*-field and this is called magnetic saturation. Magnetic saturation is represented by the saturation flux density, B_s, and the saturation field, H_s. Once a ferromagnetic material has reached saturation, if the *H*-field is removed the material will still exhibit a *B*-field. The magnitude of the *B*-field as the *H*-field reaches zero is known as the remanent flux density, B_r. Remanent flux density is commonly seen in permanent magnets, where the greater the magnitude of the remanent flux density the stronger the magnet. Another term used to describe ferromagnetic materials is coercivity, which measures the resistance of a ferromagnetic material to become demagnetized. The coercive field, H_c, is the intensity of the H-field needed to reduce the B-field of the material to zero. Materials with a high coercive field are called hard ferromagnetic material and are used to make permanent magnets. Materials with a low coercive field are known as soft ferromagnetic materials and are commonly used in magnetic MEMS devices.

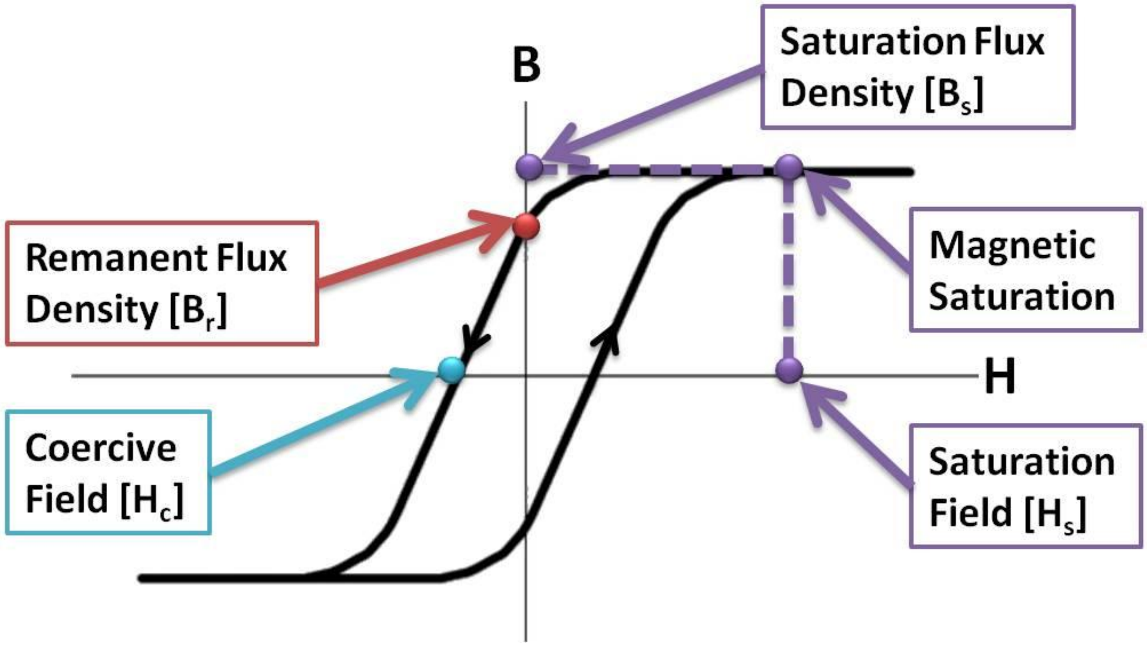

Figure 3.2: B - H curve nomenclature for a typical ferromagnetic material.

3.2 Force on a Magnetically Tagged Cell

The MSCMA, which is a magnetic MEMS device, uses magnetic force to manipulate MT cells. To use magnetic manipulation methods on cells, they need to exhibit magnetic characteristics. Some cells exhibit intrinsic magnetic characteristics, whereas other cells require external modification. This modification is called immunomagnetic labelling, which attaches magnetic nanoparticles to the cell through the use of antibody/antigen interactions. The next section will discuss the process used to modify cells so that they exhibit magnetic characteristics through the use of immunomagnetic labelling and the equations that dictate the magnetic force.

3.2.1 Immunomagnetic Labelling

The ability to manipulate a cell using an externally applied field will depend on the type of cell being manipulated. There are two types of cells; cells with an intrinsic magnetic moment, and non-magnetic cells. Cells with an intrinsic magnetic moment do not require any modification for magnetic manipulation and only include two types: (i) red blood cells and (ii) magnetotactic bacteria cells. All other cells are non-magnetic and require a magnetic label in order for magnetic manipulation to occur. To magnetically label a cell, an immunomagnetic label is applied to a cell using a two step process as shown in Figure 3.3. [65]

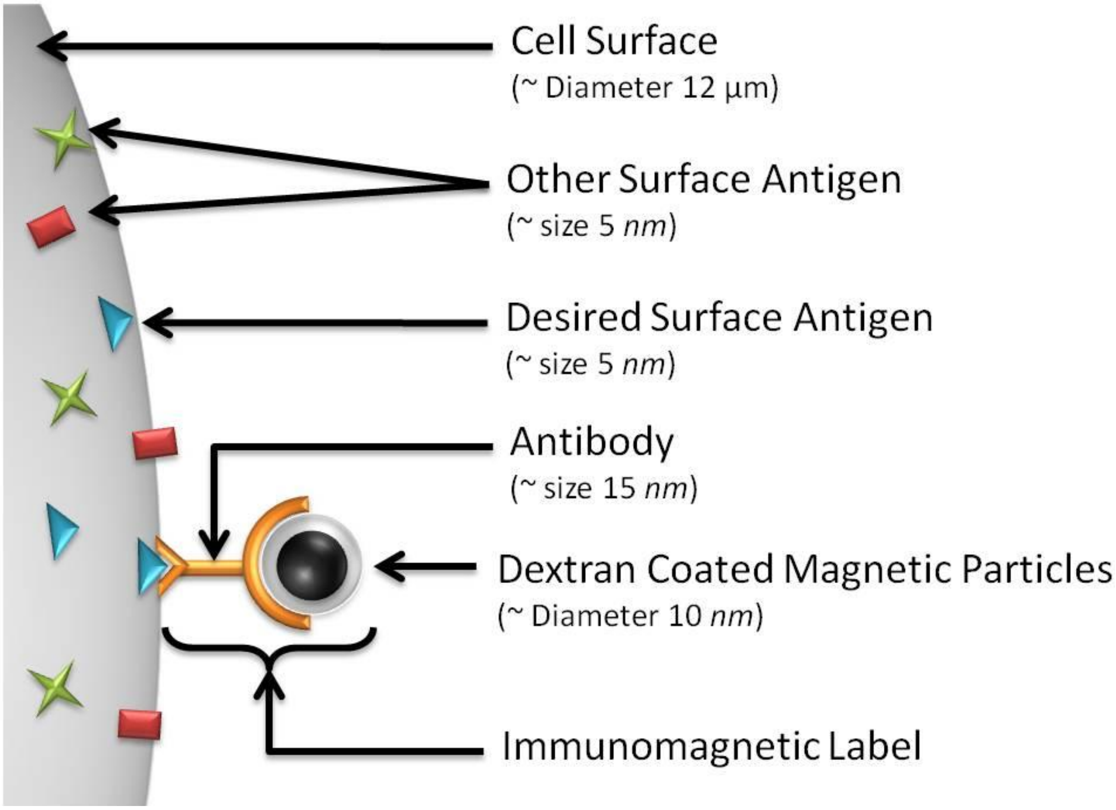

Figure 3.3: Immunomagnetically labelled cell [65]

All cell experiments shown in this thesis use human T-lymphocyte cells, also known as Jurkat cells, which are approximately 12 μm in diameter. The first step in immunomagnetically labelling cells is to mix them with a mixture that contains antibodies. These antibodies will have two free ends and are approximately 15 *nm* in size. One free end of the antibody will only attach to a specific antigen on the surface of the desired cell, and these antigens are roughly 5 *nm* in size. The desired antigen is unique to each cell, and the CD3+ antigen is used to positively identify Jurkat cells. The other free end of the antibody will only attach to a dextran coated magnetic particle that is approximately 10 *nm* in diameter. Therefore, the second step to immunomagnetically label cells is to add the dextran coated magnetic particles to the cell solution. This two step process is generally conducted multiple times to ensure that each cell has several immunomagnetic tags attached to it.

There are several unknowns in the immunomagnetic labelling process such as the amount of antigens on each cell, the actual number of antibodies that attach to each cell, the number of secondary antibodies that attach to each primary antibody, and the number of magnetic particles that attach to each antibody. The size of the antibody (~15 *nm*) and magnetic particle (~10 *nm*) are significantly smaller than the size of the cell (~12 μm). Due to the discrepancy in size, it is impossible to physically see the immunomagnetic labels attached to the surface of each cell. Although it is possible to immunomagnetically label specific cells, it is impossible to determine the amount and location of the magnetic particles that are physically attached to each cell. The next section will discuss the parameters that determine the total magnetic force on a cell in more detail.

3.2.2 Total Magnetic Force on a Cell

If a two-step immunomagnetic labelling process is used the total magnetic force acting on an immunomagnetically labelled cell is:

$$\vec{\boldsymbol{F}}_{\boldsymbol{m,total}} = (\boldsymbol{ABC})\boldsymbol{\beta}\vec{\boldsymbol{F}}_{\boldsymbol{m}} \tag{3.10}$$

Where the antibody binding capacity, *ABC*, is the number of primary antibodies that have attached to the cell and can be defined as follows [66]:

$$\boldsymbol{ABC} = \boldsymbol{n_1}\boldsymbol{\theta_1}\boldsymbol{\lambda_1} \tag{3.11}$$

Where n_1 is the number of primary binding sites per cell, θ_1 is the fraction of antigen molecules on the cells surface that are actually bound by the primary antibody, and λ_1 is the valence of the primary antibody. For example, it is known that one antibody binds two CD_4 antigen molecules making the valence 1/2 [67].

The secondary antibody binding amplification factor, β, is the number of magnetic nanoparticles that bind to each primary antibody on the cell and can be described using the following equation:

$$\boldsymbol{\beta} = \boldsymbol{n_2}\boldsymbol{\theta_2}\boldsymbol{\lambda_2}\boldsymbol{n_3} \tag{3.12}$$

Where n_2 is the number of binding sites on the primary antibody recognized by the secondary antibody, θ_2 is the fraction of binding sites on the primary antibodies bounded by a secondary antibody, λ_2 is the valence of the secondary antibody, and n_3 is the number of magnetic particles attached to the secondary antibody. The multiplication of ABC and β results in the total number of magnetic nanoparticles bound to each cell and is referred to as the magnetic particle binding capacity. [66]

The last term in equation 3.10, F_m is the magnetic force acting on one paramagnetic particle. Magnetic particles (MP) used in immunomagnetic labelling are paramagnetic and they only exhibit magnetic characteristics in the presence of an *H*-field. When the *H*-field is non-uniform, the magnetic particle will experience a gradient force that moves towards areas of higher magnetic flux [68]. It is important to note that a magnetic flux gradient is needed for a magnetic force to be exerted on a MP, whereas a uniform field will result in torque force but not in translational force. The derivation of the force on an individual MP starts with the definition of the magnetic force acting on a point-like magnetic dipole:

$$\vec{F}_m = (\vec{m} \cdot \nabla)\vec{B} \tag{3.13}$$

If the MP is suspended in a weak diamagnetic medium such as water, the total magnetic moment on the particle can be summarized as:

$$\vec{m} = V_m \vec{M} \tag{3.14}$$

$$\vec{M} = \Delta\chi \vec{H} \tag{3.15}$$

$$\Delta\chi = \chi_{MP} - \chi_w \tag{3.16}$$

Where V_m is the volume of the magnetic particle and $\Delta\chi$ is the difference in the magnetic susceptibility between the MP and the medium. [60]

If it is assumed that the MP is in pure water, the overall response of the MP plus the water can be summarized as:

$$\vec{B} = \mu_o \mu_r \vec{H} \tag{3.17}$$

Using these equations, the magnetic force on an individual MP becomes:

$$\vec{F}_m = \frac{V_m \Delta\chi}{\mu_o}(\vec{B} \cdot \nabla)\vec{B} \tag{3.18}$$

Also, since there are no time-varying electric fields or currents in the medium the Maxwell equation (equation 3.8) can be applied as follows [60]:

$$\nabla(B \cdot B) = 2B \times (\nabla \times B) + 2(B \cdot \nabla)B = 2(B \cdot \nabla)B \tag{3.19}$$

$$\vec{F}_m = V_m \Delta\chi \, \nabla\left(\frac{\vec{B}^2}{2\mu_o}\right) = \frac{V_m \Delta\chi}{2\mu_o} \nabla(\vec{B}^2) \tag{3.20}$$

This implies that the magnitude of the magnetic force on a single MP is based on the volume of the MP, the difference in the susceptibility between the MP and the medium and the magnetic flux gradient. Paramagnetic materials (i.e. MP) will also align in a magnetic field so that the direction of its magnetic dipoles is in the same direction of the field. Also the direction of the magnetic force exerted on paramagnetic material will be towards the magnetic field maximum (*H*-field or *B*-field since they are linearly related) [69].

3.2.3 Factors That Influence the Magnetic Force on a Cell

The ability of a device to manipulate an immunomagnetically labelled cell will depend on the number of the magnetic particles that bind to each cell, and the magnitude of the magnetic flux gradient. The magnetic flux gradient will be directly related to the type of magnetic device used to manipulate the cells. The number of magnetic particles that attach to each cell will be influenced by the properties of the cell, magnetic particle, and the medium. The four main parameters that will influence the number of MP on each cell are the ABC, secondary antibody binding amplification factor, the diameter of the MP and the cell. [65]

These factors are summarised in Figure 3.4 and an increase in the ABC, secondary antibody binding amplification factor, MP size, and the cell size will increase the total magnetic force on a cell. A cell with a larger number of surface antigens will have a larger ABC and therefore will have more MP on the cell. As the secondary binding amplification factor increases, more magnetic particles will attach to each primary antibody, which will increase the total number of MP attached to a cell. A larger MP will have a larger magnetic susceptibility, which will increase the overall magnetic force on each MP. The cell diameter will also affect the total magnetic force since a larger cell will have more antigens for binding magnetic particles. [65]

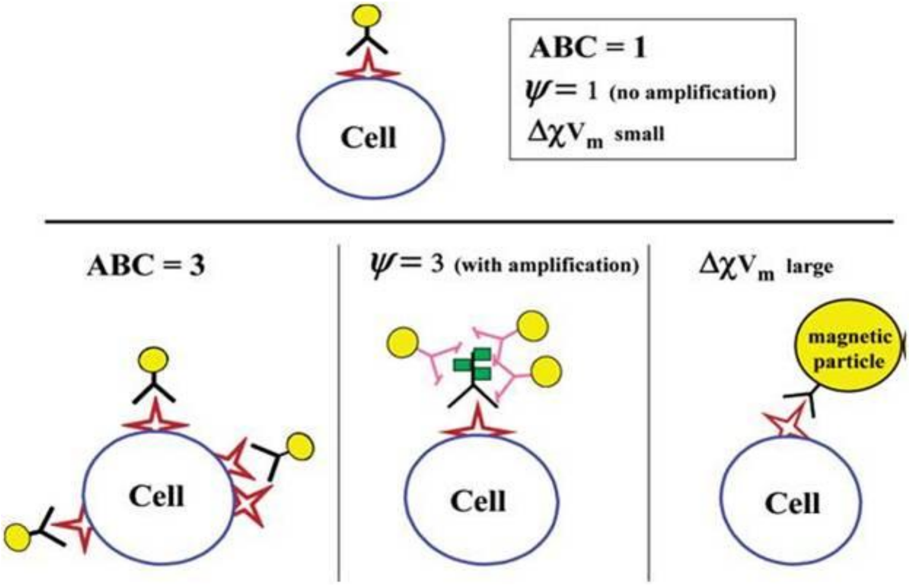

Figure 3.4: Factors that influence the number of magnetic particles attached to the surface of a cell. [65]

Chapter 4: Fluid Flow Theory

Although magnetic manipulation is the main method used to manipulate the cells in the CFS, fluid forces are also present. Integrating a gasket assembly delivers the cells over the MSCMA and also enables the CFS to capture rare cells from a heterogeneous population of cells. The following chapter will outline the fluid flow theory behind the CFS, including some basic fluid flow terminology as well as the fluid force exerted on a cell.

4.1 Fluid Flow Terminology

The movement of an object through a fluid depends on the properties of the fluid and the flow. These properties can be categorized as kinematic (e.g. velocity and acceleration), transport (e.g. viscosity and thermal conductivity), thermodynamic (e.g. pressure, temperature, and density) or miscellaneous properties (e.g. surface tension and vapour pressure) [70].

4.1.1 Continuum Assumption

The properties of a fluid and a flow can be modelled as a collection of individual interacting molecules or as a continuum [71]. In order for a fluid to be modelled as a continuum, all aspects of the fluid must be continuous within the specified boundary. Length scales are used to determine whether a fluid is continuous or not and will depend on the property categories mentioned before (kinematic, transport, thermodynamic, or miscellaneous). Kinematic and thermodynamic properties can be treated as point quantities and the length scale can be determined by assuming that there must be a minimum of 10^4 molecules in the sample volume for properties to be considered continuous. The point length scale is:

$$\boldsymbol{L_p = \sqrt[3]{\frac{10^4}{Number\ Density}}} \qquad \textbf{4.1}$$

Where the number density is the total number of water molecules per volume. For water the number density is $2\text{x}10^{28}$ m^{-3} and therefore the point length is 0.08 μm. This implies that the kinematic and thermodynamic properties can only be considered continuous if the sample volume has a minimum length of 0.08 μm. [70]

Transport properties can be treated as a continuum as long as the molecules interact more with themselves than with the flow boundaries. This can be calculated assuming that the sides of the volume are 10 times larger than the molecules' interaction length scale. For a liquid, the molecules are usually in a state of interaction so the molecular diameter is a good estimation of the interaction length scale. The transport length is as follows:

$$\boldsymbol{L_t = 10 \times (molecular\ diameter)} \qquad \textbf{4.2}$$

The molecular diameter for water is roughly 0.3 *nm* and therefore the sample volume can only have a minimum length of 0.003 μm in order for the transport properties to be considered continuous. [70]

Since all properties of the fluid needs to be continuous the smaller of the two lengths must be used. For a sample volume with water to be considered continuous, the volume must be roughly $2.7\text{x}10^{-8}$ μm^3, with a minimum sample volume length of 0.003 μm. As long as the sample volume length is greater than this minimum values, it can be assumed that the fluid is continuous. [70]

4.1.2 Fluid Flow Governing Equations

The equations that govern a fluid flow will depend on the type of fluid being considered. A Newtonian fluid is a fluid whose stress versus strain curve is linear and follows the equation:

$$\boldsymbol{\tau = \eta \frac{dU}{dy}} \tag{4.3}$$

Where τ is the shear stress, η is the dynamic viscosity, and U is the fluid velocity. Another way to describe a Newtonian fluid is that the fluid continues to flow regardless of the any external forces acting on it, such as water. [72]

If the changes in temperature and pressure within a fluid are sufficiently small the changes in density can be considered negligible. If this is true, then the fluid can be modelled as an incompressible fluid and the change of density, ρ, with respect to time, t, is assumed to be zero [73]:

$$\boldsymbol{\frac{d\rho}{dt} = 0} \tag{4.4}$$

Also for incompressible flows, the divergence of the velocity can also be considered to be zero [73] :

$$\boldsymbol{\vec{U}(x, y, z) = u + v + w} \tag{4.5}$$

$$\boldsymbol{\nabla \cdot \vec{U} = \frac{du}{dx} + \frac{dv}{dy} + \frac{dw}{dz} = 0} \tag{4.6}$$

The governing equations for fluids that are continuous, incompressible and viscous fluids are known as the Navier-Stokes equations. Assuming that the fluid velocity has components in the x, y, and z components, the Navier-Stokes equations are as follows:

$$\rho g_x - \frac{\partial p}{\partial x} + \eta\left(\frac{\partial^2 u}{\partial x^2} + \frac{\partial^2 u}{\partial y^2} + \frac{\partial^2 u}{\partial z^2}\right) = \rho \frac{du}{dt} \qquad 4.7$$

$$\rho g_y - \frac{\partial p}{\partial y} + \eta\left(\frac{\partial^2 v}{\partial x^2} + \frac{\partial^2 v}{\partial y^2} + \frac{\partial^2 v}{\partial z^2}\right) = \rho \frac{dv}{dt} \qquad 4.8$$

$$\rho g_z - \frac{\partial p}{\partial z} + \eta\left(\frac{\partial^2 w}{\partial x^2} + \frac{\partial^2 w}{\partial y^2} + \frac{\partial^2 w}{\partial z^2}\right) = \rho \frac{dw}{dt} \qquad 4.9$$

Where g is gravitational constant and p is the pressure. The gravitational constants g_x, g_y, and g_z will depend on the orientation of gravity with respect to the chosen coordinate system. [72]

4.1.3 Reynolds Number

Another concept that is readily used to define a fluid flow is the Reynolds number, which is the ratio between inertial and viscous forces, where L is the characteristic linear dimension:

$$Re = \frac{\rho U L}{\eta} \qquad 4.10$$

The Reynolds number, Re, can be defined based on specific situations. Two situations that are applicable to the CFS is the Reynolds number of the flow in a non-circular duct, and the Reynolds number for a sphere in a fluid. The Reynolds number for flow in a non-circular duct can be defined as:

$$Re_{NCD} = \frac{4\rho D_H}{\eta} \qquad 4.11$$

Where the characteristic linear dimension is the hydraulic diameter, D_H, which is defined as 4 times the duct area, A, divided by the perimeter, P, of the duct [74].

$$D_H = \frac{4A}{P} \qquad 4.12$$

For a sphere in a fluid, the characteristic linear dimension is the diameter of the sphere, the characteristic velocity is that of the sphere relative to the fluid some distance away from the sphere, and the density and viscosity are those of the fluid. The Reynolds number of a sphere in a fluid can therefore be defined as: [75]

$$\boldsymbol{Re_{SF} = \frac{\rho\left(U_f - U_s\right)D}{\eta}} \qquad \textbf{4.13}$$

Where D is the diameter of the sphere, U_f is the velocity of the fluid and U_s is the velocity of the sphere.

Two important properties that are determined by the Reynolds number are whether a fluid flow is laminar or turbulent and if either inertial or viscous forces are dominant. Turbulent flow is characterized by recirculation and eddies whereas laminar flow will not exhibit any of these characteristics. The transition from laminar to turbulent flow regimes occurs in the range of Re_{NCD} = 2100 – 2500 for flow in non-circular ducts [76]. For spheres in a fluid, purely laminar flow can only exist up to Re_{SP} = 0.1 [75].

The Reynolds number can also be used to determine if either the inertial or viscous forces are dominant. Generally speaking, if Re is significantly less than 1 (i.e. $Re \ll 1$), the inertial forces can be neglected compared to viscous forces [77]. Where inertial forces is an apparent force that acts on objects in a non-inertial frame of reference and viscous forces is a measure of the resistance of a fluid that is being deformed by either shear stress or tensile stress. These concepts will be used in the next section to determine the governing equations on a cell in a fluid flow.

4.2 Fluid Force on a Spherical Object

The movement of a spherical object, such as a cell, in a fluid will be governed by three main forces: (i) buoyancy, (ii) gravitational and (iii) drag force. The gravitational and buoyancy force on a cell will be constant and relatively small since the weight of a single cell is small. The gravitational and buoyancy force equations are as follows (equation 4.14 and 4.15 respectively), where V_m is the volume of the cell, ρ_c is the density of the cell and ρ_m is the density of the medium:

$$\vec{F}_g = V_m \rho_c \vec{g} \tag{4.14}$$

$$\vec{F}_b = V_m \rho_m \vec{g} \tag{4.15}$$

The main fluid force on a cell is the viscous force and is known as Stokes drag. If $Re << 1$, the viscous forces are dominant compared to inertial forces and therefore the dominating force is the Stokes force. Stokes drag is derived by solving the Navier-Stokes equations for small Reynolds numbers, and can be defined as:

$$\vec{F}_d = 6\pi\eta r \vec{U} \tag{4.16}$$

Where r is the radius of the cell and U is the velocity of a cell, which can generally be taken as the difference between the fluid velocity and the cell velocity. The direction of the Stokes drag is in the same direction of the flow.

If the cell is falling through a viscous fluid and the only forces acting on the cell is gravity, the cell will reach a terminal velocity. Terminal velocity is reached when the Stokes drag plus the buoyancy force are exactly the same as the gravitational force.

$$\vec{F}_g = \vec{F}_d + \vec{F}_b \tag{4.17}$$

$$V_m \rho_c \vec{g} = 6\pi\eta r \vec{U} + V_m \rho_m \vec{g} \tag{4.18}$$

For all calculations, it is assumed that the cell is spherical in shape, and therefore the volume and terminal velocity for a cell is:

$$\boldsymbol{V_m = \frac{4}{3}\pi r^3} \tag{4.19}$$

$$\boldsymbol{\vec{U}_T = \frac{2}{9}\frac{(\rho_c - \rho_m)}{\eta}\vec{g}r^2} \tag{4.20}$$

The main fluid forces that will act on a cell in a fluid are the buoyancy force (equation 4.14), gravitational force (equation 4.15), and stokes drag (equation 4.16). If the cell exhibits magnetic characteristics (i.e. a MT cells), when an externally applied magnetic field is applied, the MT cells will experience an additional magnetic force (equation 3.20).

Chapter 5: CFS Design and Properties

A major aspect of this thesis has been the design of the CFS. The CFS has been designed to facilitate the separation of desired cells (magnetically tagged) from a heterogeneous population of cells, and array them in pre-defined locations. The CFS consists of several components that all work together to flow cells over the MSCMA. This chapter will discuss the design methodology used, which outlines several requirements that were followed when designing the CFS and reasons for these requirements. Each component of the CFS will also be shown, and how these components meet the requirements.

5.1 Design Requirements and Methodology

When designing the CFS, several requirements were used as guideline and are summarised as follows:

1. Flow cells suspended in media over the MSCMA in a reproducible manner.
2. Ability to control the flow rate of the fluid and maintain fluid pressure.
3. Designed to work with both a differential interference contrast (DIC) and brightfield microscope platform.
4. Allow active trap area of the MSCMA to be viewable at all times, with both microscope platforms.
5. Ensure all materials used in the CFS that the cells come into contact with are biocompatible.
6. Ensure materials used in the CFS have minimal magnetic interference (i.e. a relative permeability close to 1.0).

7. Enable CFS to withstand Autoclaving to keep it sterilized between uses.
8. Incorporate disposable PDMS gaskets into design, again for sterility.
9. Allow for easy replacement of the MSCMA chip.
10. Easy removal and assembly of all components.
11. Secure and separate the magnets from the rest of the device.
12. Design to fit into the RoboSCell platform.
13. Ensure that all components can be fabricated using a computer numerical controlled (CNC) machine.

Requirement 1 and 2 are important to ensure that a majority of heterogeneous cells are delivered in close proximity to the traps, which increases the probability of capturing MT cells. Reproducibility of the flow also allows for experimental results to be easily compared, which becomes important when optimizing testing parameters. Requirement 2 also specifies control over the fluid aspect of the CFS for application such as the fluid force exerted on the cells, ability to control the introduction of reagents, and potential removal of unwanted cells. The ability to clearly see the cells using both the DIC and brightfield setup will allow for easier experiment analysis and were the main driving force behind requirement 3 and 4.

Requirement 5 and 6 outline the biocompatible and magnetic properties of the materials used in the CFS. The main component that allows for MT cells to be captured and arrayed is the interaction between permanent magnets and the MSCMA chip. Ensuring that the other materials in the CFS do not alter the magnetic interaction between these two components will result in a larger *B*-field, and therefore larger magnetic force exerted on each MT cell. This was done by selecting materials that do not exhibit any magnetic characteristics, and possess a relative permeability close to 1. The other material property that was important was biocompatibility. Materials that demonstrate biocompatibility will not alter or degrade the health of cells over a period of time. This is also emphasized in requirements 7 and 8 as sterility of the material will deter bacteria growth and will act to maintain the viability and health of the cells.

Requirements 9 and 10 allow for easy and quick experiment setup and allows for easy replacement of the MSCMA between experiments if necessary. This also makes troubleshooting problems encountered during experiments quicker and more efficient. Due to the strength of the magnets used, requirements 11 was necessary to ensure that the magnets do not become dislodged or displaced during or between experiments. Requirement 12 was an important consideration for the design. It placed an overall ‘size restriction’ on the CFS, to ensure that it could be integrated into the RoboSCell platform. In this way, the various automatic functions envisioned for this work could be achieved. Requirement 13 is important for many aspects of the CFS design to ensure ease of fabrication. This included accounting for machine tolerances, fits, alignments between parts, and surface finish of components.

Some additional points can be made regarding the influence of requirement 3 on the CFS system. The field of view, resolution, and image quality of both the DIC and brightfield microscope system will depend on the numerical aperture (NA) of the objective lens. The NA defines the angle of a cone of light entering the objective, from the viewable regions, as shown in Figure 5.1. The NA for the DIC microscope (corresponds to the RoboSCell setup) is 0.7, which makes the half angle for the cone of light (θ) to be 45°. When designing the culture chamber dimensions, an additional area needs to be added to the perimeter of the culture chamber to ensure that the entire active trap area of the chip can be viewed. The parameter *x*, shown in Figure 5.1 indicates the distance from the chamber edge will yield poor images. Although it can be viewed the image becomes progressively darker and unfocused towards the chamber edge, due to the occlusion of the light cone. This cone of light will depend on (θ) (equation 5.1) and the depth of the culture chamber (equation 5.2). The implications of adding this extra space, defined by *x*, around the trap area is that many cells can flow past without being captured by the MSCMA. This is discussed in the results section of the thesis.

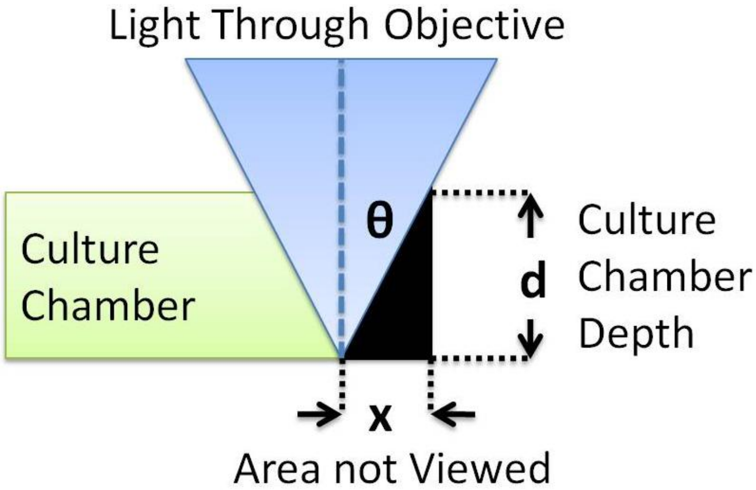

Figure 5.1: Edge of the culture chamber cannot be viewed due to the cone of light that enters the culture chamber from the objective.

$$\mathbf{NA = n \cdot \sin\theta} \qquad 5.1$$

$$\mathbf{x = d \cdot \tan\theta} \qquad 5.2$$

5.2 Description of Final Design

The 13 requirements previously discussed were used as general guidelines when designing the CFS. This section will discuss the components of the CFS, which include a base, magnet cover, MSCMA, gasket assembly, and top plate.

5.2.1 Base Plate

The base plate is the main support of the CFS and has an outer diameter of 132 *mm* with a thickness of 6.35 *mm.* It is made of aluminum to meet requirement 6 (magnetic permeability equal to 1) and requirement 7 (autoclaving), and can be seen in Figure 5.2. The MSCMA is inserted into a recessed area on the base plate, at location 3. There is a viewing hole from the bottom that allows the chip to be viewed using an inverted transmission illumination DIC or brightfield microscope platform. The base also has a recessed area to place the magnets (location 5) to keep the magnets separated from the MSCMA and gasket assembly. There are also through holes that secure the entire CFS to a microscope platform (location 2) and tapped holes that secure all upper components to the base plate (location 1). These tapped holes act to ensure enough pressure can be applied to the gasket assembly, to minimize any leaks.

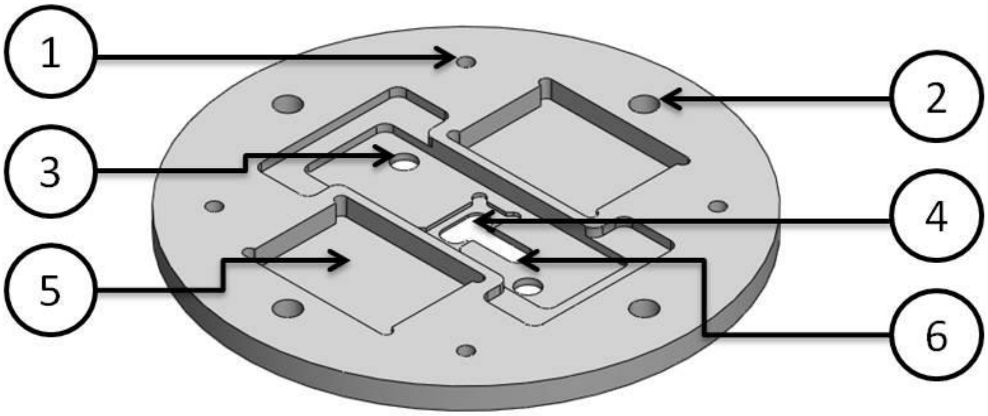

Figure 5.2: Base Plate. (1) Tapped 10-32 holes to secure upper components to the base. (2) M6 clearance holes to secure base to Newport URS150PP microscope stage. (3) Hole for viewing cells using DIC Microscope. (4) Recessed hole for MSCMA. (5) Magnet holder. (6) Hole to easily remove the MSCMA.

5.2.2 Magnet Cover

Eight N52 neodymium magnets are used in the CFS with 4 on each side of the MSCMA on the base plate. These magnets are very strong and the magnet cover is used to prevent the magnets from moving and damaging the rest of the device and the microscope. The magnet cover has an outer diameter of 132 *mm* with a thickness of 3.175 *mm* and is made from aluminum, as shown in Figure 5.3.

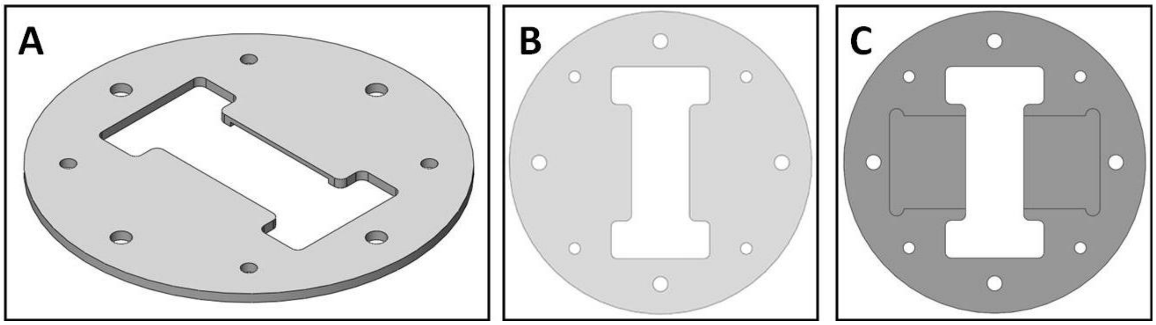

Figure 5.3: (A) Magnet cover. (B) Top view. (C) Bottom view.

5.2.3 Magnetic Microarray

The MSCMA, which was previously developed by W. Liu et al. [21], as illustrated in Figure 5.4, will be briefly discussed here. The basic design consists of permalloy strips that have been electroplated using a microfabrication technique, onto a glass substrate that measures 18 x 10 x 1.1 mm^3. It contains 16 permalloy strips on the top surface of the glass substrate, with sawtooth or sinusoidal shaped edges along the strips. The valleys on the edges form the magnetic trap sites, with each strip containing 80 traps (40 on each side of the strip) for a total of 1280 traps per chip. The MSCMA is fabricated using a mask electroplating process and is detailed in Appendix A.

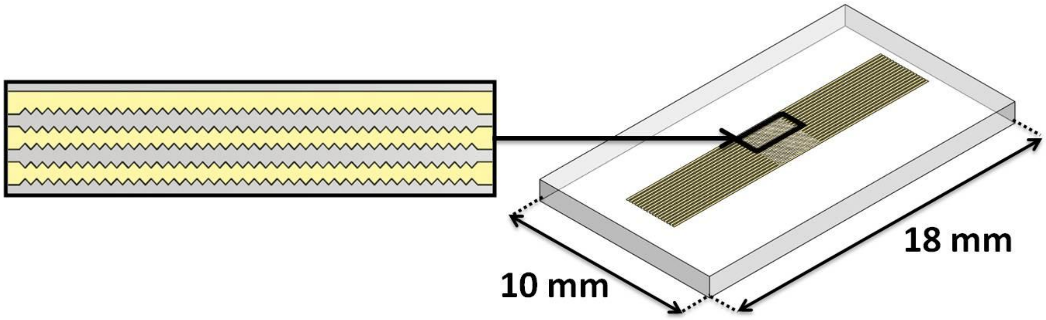

Figure 5.4: MSCMA with permalloy strips on a glass substrate with dimensions in *mm* (overall dimensions are 10 *mm* x 18 *mm* x 1.1 *mm*).

Permalloy is a nickel-iron alloy that has a high magnetic permeability and low coercivity and is considered a soft ferromagnetic material. It is possible to magnetize the permalloy so that MT cells are attracted to it when an externally *H*-field is applied. Two different permalloy designs were analysed, sinusoidal and sawtooth, which have similar dimensions as can be seen from Figure 5.5. The permalloy strips seen as the yellow/gold regions in Figure 5.5 are spaced in rows 170 μm from one another (pitch distance). Each permalloy strip has an overall width of 110 μm. Each trap site has a width of 60 μm (peak to peak) and a depth of 30 μm.

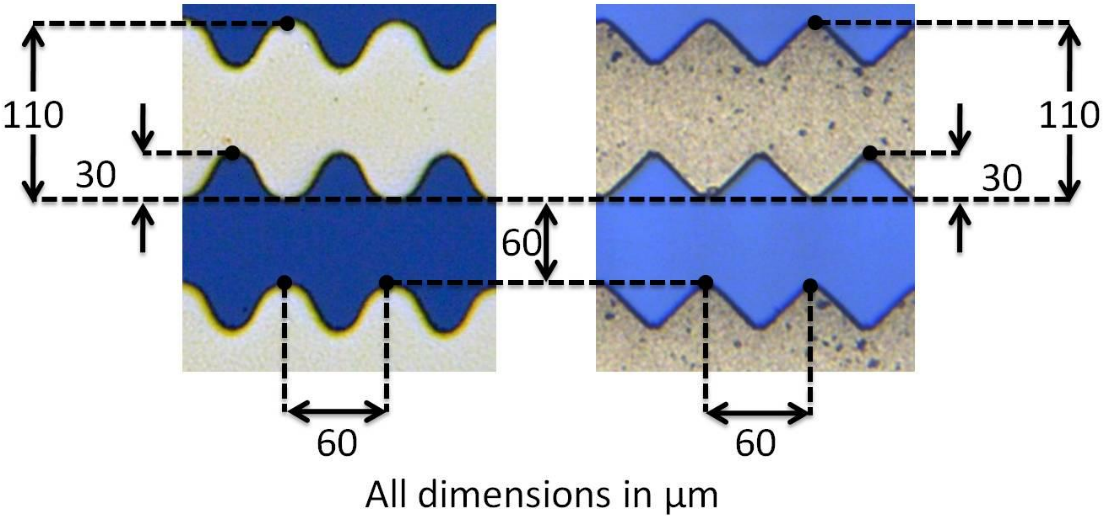

Figure 5.5: MSCMA trap dimensions for both sawtooth and sinusoidal design (all dimensions in μm). Light yellow/brown regions are the permalloy and blue regions are the area between the permalloy (glass).

5.2.4 Gasket Assembly

The main component of the CFS is the “culture chamber” concept, which passes cells suspended in a fluid flow over the MSCMA. The culture chamber and inlet/outlet channels is formed by the design of two polymer gaskets and a glass cover slip, as shown in Figure 5.6. The three parts include: (i) the polymer culture chamber gasket, which is placed over the MSCMA chip; (ii) a microscope cover slip measuring 30 x 22 mm^2 with a thickness of 0.13 – 0.17 *mm* (standard #1) is placed on top of the culture chamber gasket to provide an upper boundary to the culture chamber; and (iii) the last component is the square gasket, which is placed on top of the culture chamber gasket and cover slip.

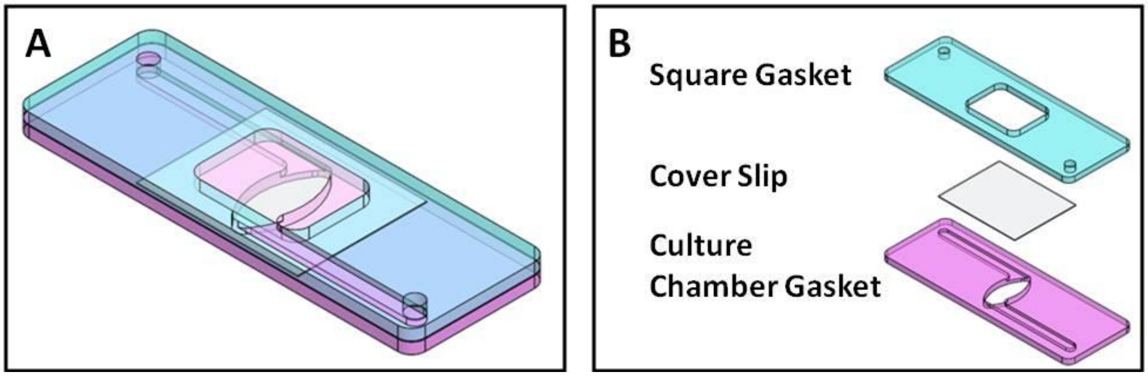

Figure 5.6: (A) Gasket assembly. (B) Exploded gasket assembly.

Both the square gasket and the culture chamber gaskets are made using a polymer called PDMS (polydimethylsiloxane). Since the design requirements dictate that the gaskets are to be disposable, a fabrication method was developed. The method consisted of making negative moulds into which PDMS was poured, and allowed to cure at room temperature. The negative moulds are made from polyoxymethylene (POM, which is a thermoplastic commonly known under DuPont's trade name Delrin). The culture chamber gasket has both inlet and outlet channels that lead to and from the culture chamber, as can be seen in Figure 5.7 A. The culture chamber size and dimensions were designed to include the magnetic trap area, an additional 1 *mm* beyond the traps (x value of Figure 5.1) to account for the area not viewable. There are two different MSCMA designs with trap area sizes that measured 5 x 5 mm^2, or 2.5 x 2.5 mm^2. The bigger of the two trap areas was used for the culture chamber design to accommodate both chip designs.

The square gasket has inlet and outlet holes that mate with the beginning of the inlet and outlet channels on the lower gasket, as can be seen in Figure 5.7 B. It also creates the upper boundary of the inlet/outlet channels. The centre of the square gasket contains a viewing hole which allows light to be passed through the culture chamber so that cells can be easily viewed using either microscope setup (DIC or brightfield). Due to the deformable nature of PDMS, when mechanical pressure is applied to the square gasket with the top plate (section 5.2.5), the PDMS deforms and seals around the cover slip to minimize potential leaks.

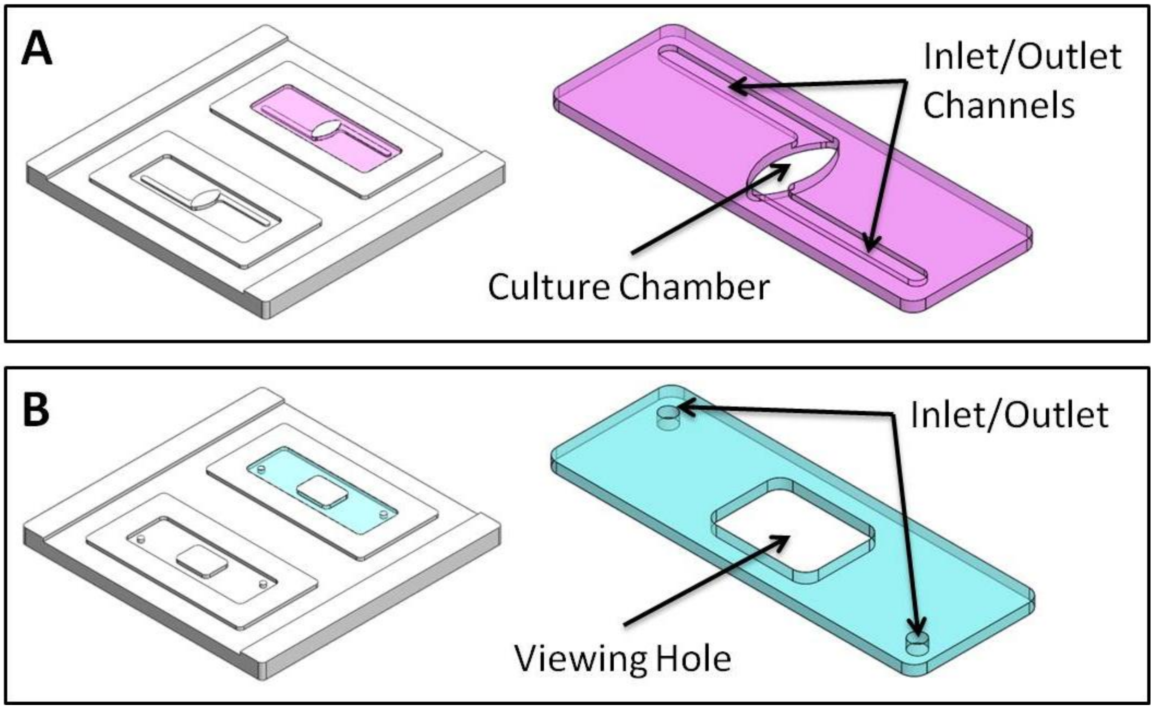

Figure 5.7: Mould and gasket for (A) culture chamber gasket and (B) square gasket.

A cover slip was used as the top portion of the culture chamber due to its optical clarity, and minimal thickness. The optical clarity was very important, as it ensured that the cells could be easily viewed using either microscope setup. For the DIC setup, the light source comes from below the MSCMA, through the glass of the MSCMA, through the water in the culture chamber, and then through the cover slip. Ensuring that all materials have similar refractive index will increase the optical clarity. The refractive index of water and glass is 1.33 and 1.46 respectively [78]. The small thickness of the cover slip will also minimize any leaks that occur due to the interface between the cover slip and the square gasket.

5.2.5 Top Plate

The last part of the CFS is the top plate, as shown in Figure 5.8, which has an outer diameter of 132 *mm* with a thickness of 9.525 *mm* and is made of Delrin. The top plate is secured to the base plate using four #10-32 thumbscrews. This allows for pressure to be applied to the gasket assembly to eliminate leaks when fluid is allowed to flow through the system.

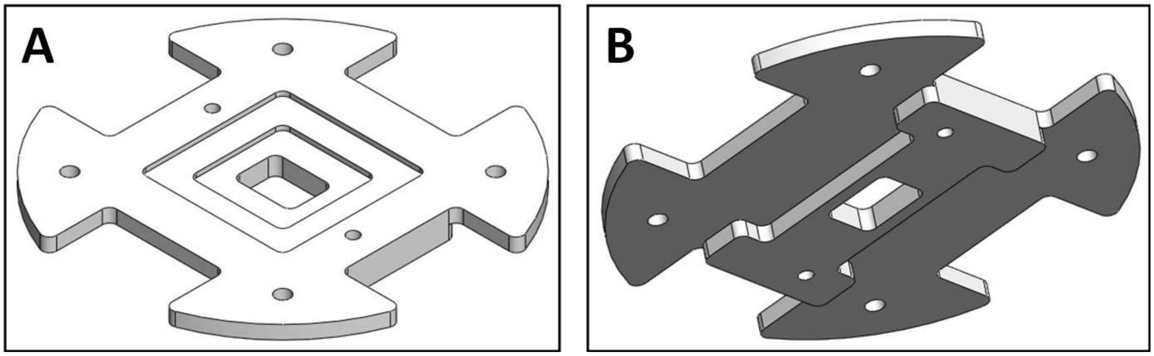

Figure 5.8: (A) Top plate. (B) Bottom view of top plate.

5.2.6 Final Assembly

The complete CFS assembly is illustrated in Figure 5.9, where it is shown attached to the rotational stage of the RoboSCell. The assembly sequence of the CFS is illustrated in Figure 5.10. Barbed fittings are attached to the top plate, which creates the inlet and outlet into the culture chamber and over the MSCMA. Ether-based polyurethane tubing is used to deliver cells to and from the CFS.

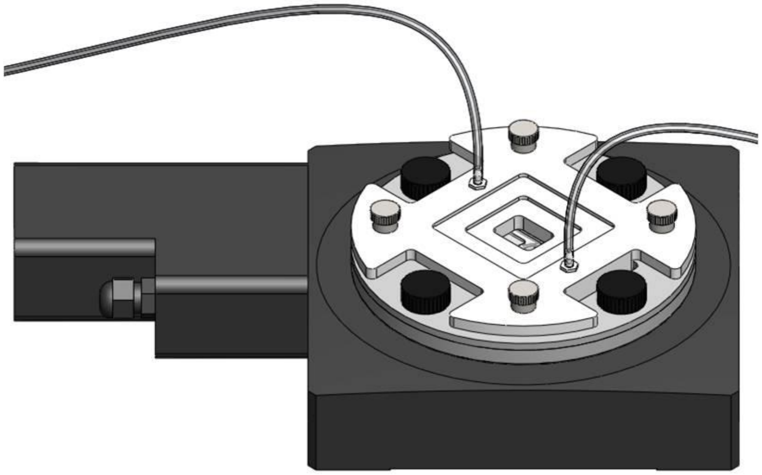

Figure 5.9: Final SMCS assembly on the Newport URS150PP microscope stage with barbed fitting and tubing to introduce flow into the CFS.

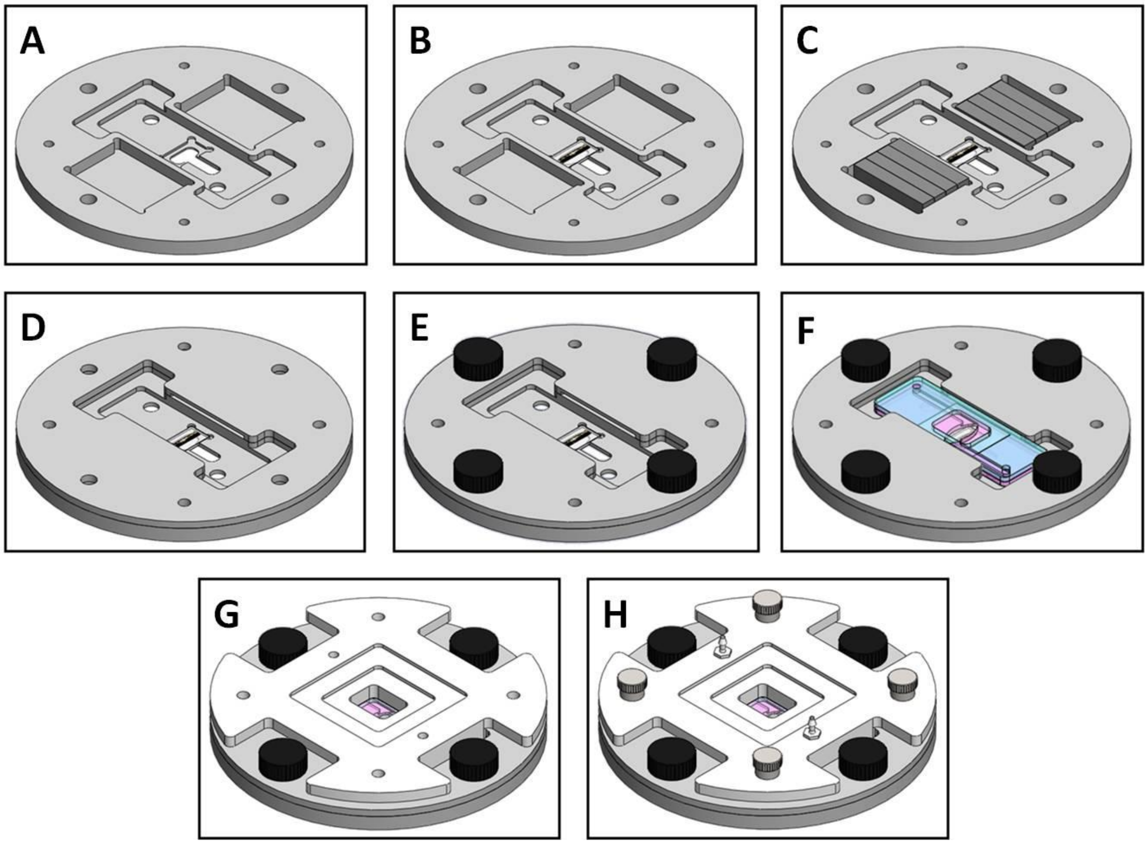

Figure 5.10: CFS assembly. (A) Base plate. (B) Add MSCMA. (C) 4 N52 magnets on each side placed into the base. (D) Magnet cover placed on top of base to prevent the magnets from moving. (E) Thumb screws secure the base plate and magnet cover to the microscope stage. (F) Gasket assembly is placed over the MSCMA. (G) The upper plate is placed over the gasket assembly. (H) Thumb screws secure the upper plate to the base plate and barbed fittings are used to provide an inlet/outlet.

5.3 Material Properties

The materials used in the CFS were chosen meet design requirements 5, 6, and 7 to ensure minimal magnetic interference, and biocompatibility. A summary of the materials used for each component can be found in Table 5.1. This next section will discuss the magnetic and biocompatible properties of materials included in the CFS.

Table 5.1: Material for each component of the CFS.

Component	Material
Base Plate	• Aluminum
Magnet Cover	• Aluminum
Gasket Assembly	• PDMS (culture chamber and square gasket) • Glass (microscope cover slip)
MSCMA	• Glass (base) • Permalloy (magnetic strips)
Top Plate	• Delrin
Thumb Screws	• 18-8 stainless steel
Barbed Fittings	• Nylon
Tubing	• Polyurethane

5.3.1 Magnetic Properties

Table 5.2 and Table 5.3 show the physical and magnetic properties of materials used in the CFS (excluding the permalloy, which will be discussed in more detail later), that could potentially exhibit magnetic characteristics. Both nylon and polyurethane were not included in this list, as plastics do not exhibit magnetic characteristics. As can be seen from Figure 5.4, the relative permeability of all the materials is approximately 1 and therefore will not affect the magnetic properties of the device.

Table 5.2: Physical properties of materials in the CFS.

Material	Molar mass [$\times 10^{-3}$ kg/mol] [79]	Density [$\times 10^{3}$ kg/m^3]
Aluminum	26.98	2.70 [80]
Delrin	30.03	1.42 [81]
Glass	60.08	2.40 [82]
PDMS	NA	0.97 [83]

Table 5.3: Magnetic properties of materials in the CFS. (Conversion between χ_v to μ_r is $\mu_r = 1 + \chi_v$. Other relevant conversions are shown in equations 5.3 and 5.4.)

Material	**Molar Magnetic Susceptibility (χ_{mol}) [x10^{-10} m^3/mol]**	**Mass Magnetic Susceptibility (χ_{mol}) [x10^{-9} m^3/kg]**	**Volume Magnetic Susceptibility (χ_v) [x10^{-5}]**	**Relative Permeability (μ_r)**
Aluminum	2.07 [84]	7.67	2.07	1.00002
Delrin	1.77 [85]	5.89	0.839	1.00001
18-8 Stainless Steel	NA	NA	NA	1.02 [86]
Glass	3.72 [84]	6.19	1.49	1.00001
PDMS	NA	0.60 [83]	0.0058	1.0000001

$$\chi_m = \frac{\chi_{mol}}{Molar\ Mass} \qquad 5.3$$

$$\chi_v = \chi_m \cdot \rho \qquad 5.4$$

5.3.1.1 Permalloy Magnetic Properties

The main mechanism that allows the MSCMA to capture MT cells is the permalloy layer. Permalloy is an Iron/Nickel magnetic alloy of approximately 80% Ni and 20% Fe (80/20 Ni/Fe), which has high magnetic permeability and low coercivity. Therefore, it exhibits strong magnetic properties when an *H*-field is present and no magnetic characteristics when the *H*-field is removed. The magnetic properties of a thin permalloy layer are affected by many factors such as the thickness of the permalloy layer, the composition of the electroplating bath used to deposit the permalloy, and the current density used in the electroplating bath.

The B-H curve for an electroplated NiFe 81/19 permalloy with a thickness of 12 μm or 35 μm, which is shown in Figure 5.11. The saturation flux density is the same regardless of the permalloy thicknesses with a value of 1.18 *T*, and the maximum relative permeability will change with the thickness. A thickness of 12 μm will result in a maximum relative permeability of 310, and a thickness of 35 μm will result in a maximum relative permeability of 105. [87] Another conventional NiFe permalloy with a thickness of 3 *μm* is shown in Figure 5.12. This permalloy was plated at 10 *mA/cm*^{2} and has a saturation flux density value of approximately 0.9 – 1.08 *T*, with a maximum relative permeability of 1500 – 2000, and a coercivity ranging from 55.70 – 119.37 *A/m* (0.7 – 1.5 *Oe*). The *B*-field (magnetic induction) versus the *H*-field (applied field) for this 3 *μm* NiFe permalloy is shown in Figure 5.12. [88]

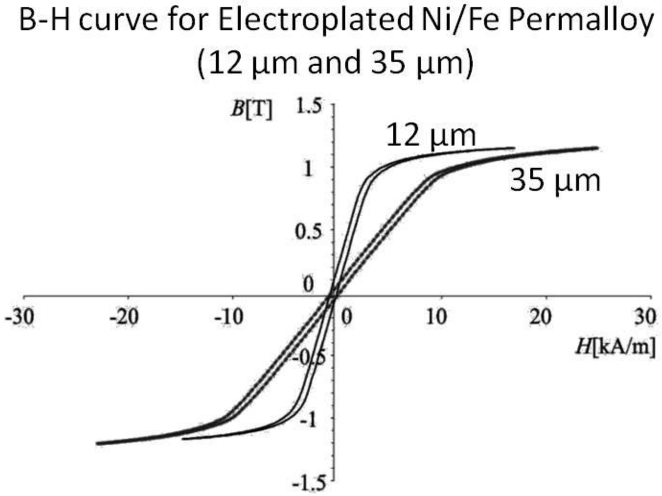

Figure 5.11: B-H curve of electroplated NiFe 81/19 permalloy, 12 *μm* and 35 *μm* thick. [87]

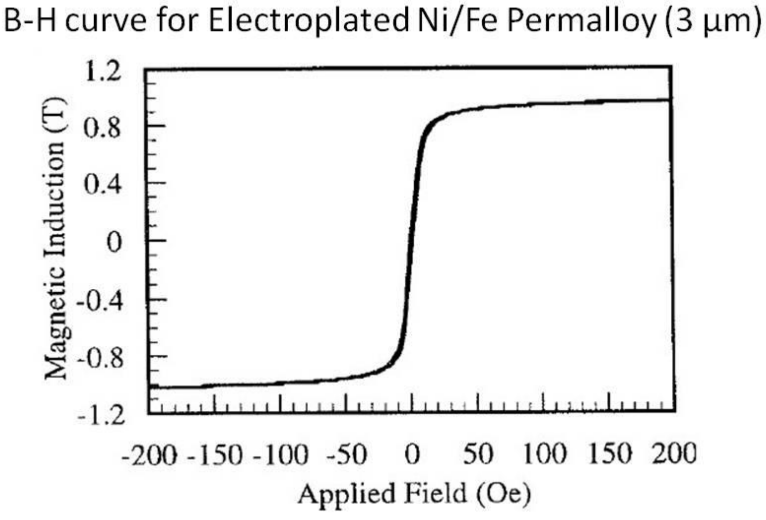

Figure 5.12: B-H curve of electroplated NiFe permalloy layers 3 *μm* thick. [88]

The permalloy layer in the MSCMA is an 80/20 NiFe composition that is roughly 6 *μm* thick. From this data, the maximum relative permeability should be greater than

310 (corresponding to a thickness of 12 μm), but should be less than 2000 (corresponding to a thickness of 3 μm). This is verified by Figure 5.13, which shows that the maximum relative permeability of a permalloy layer that is 6 μm is roughly 710.

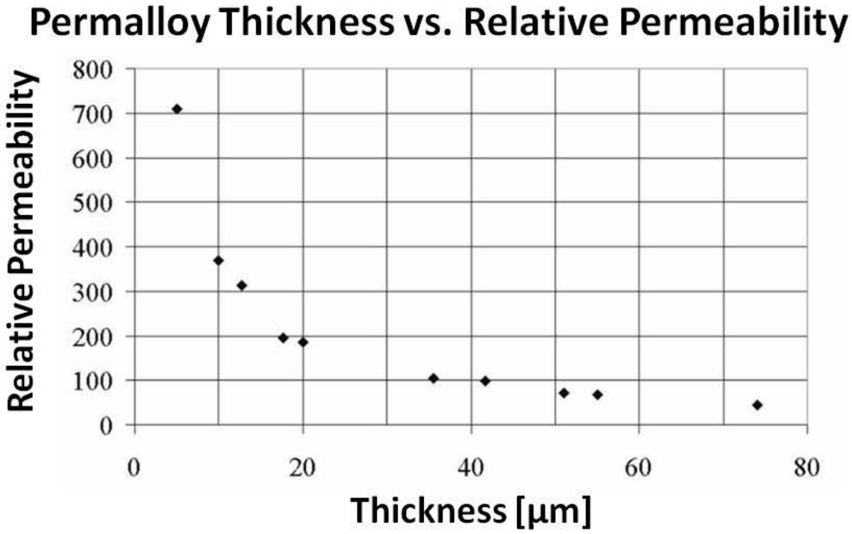

Figure 5.13: Thickness of the permalloy layers versus the relative permeability. [87]

5.3.2 Biocompatibility Properties

Another important material property is biocompatibility, which implies that the material will not adversely affect the health of the cell over an extended period of time. The only components of the CFS that the cells physically come into contact with are the tubing (polyurethane), barbed fitting (nylon), top plate (Delrin), gasket assembly (glass and PDMS), and the MSCMA (permalloy and glass). Since the permalloy is not biocompatible, a gold layer is deposited overtop the permalloy, as described in section 5.2.3. When cells come into contact with the MSCMA, they will interact with the gold layer that is deposited on top of the permalloy and glass. Table 5.4 outlines the biocompatibility of the materials used in the CFS that cells will come into contact with, and shows that the material used will not affect the cell's health.

Table 5.4: Biocompatibility of materials that come into contact with the cells

Material	Medical Applications	Publications of Biocompatibility
Polyurethane	Substrate for Cell Culture	Demonstrates good biocompatibility [89]
Nylon	Tendon repair material	Demonstrates good inertness in the human body [90]
Delrin	Joint Prostheses	Delrin 150 did not exhibit local or systematic toxicity [91]
PDMS	Cell Culture (microfluidic devices)	Demonstrates good biocompatibility [43]
Gold	Nanomedicine	Biocompatible properties [92]

5.4 Fluid Delivery System

In order to move fluid through the CFS, a fluid pumping system was required. After conducting various systems, it was decided that a syringe pump system would best satisfy the design requirements. Initial tests were conducted by flowing water through the CFS. No leaks were seen and the syringe pump was successfully integrated. The syringe pump acts to accurately, and reproducibly flow cells over the MSCMA, while allowing the fluid dynamics to be easily altered using settings on the pump. Also, integrating the syringe pump to saturate all lines removed any bubbles seen and clear images of the trap area were seen. Additional information on the CFS design, including experimental setup and results will be discussed in Chapter 7 and Chapter 8.

5.5 Design Summary

The requirements defined in the design methodology were used to design the CFS. The CFS is composed of several parts that all work together to deliver cells to the MSCMA to capture and array single cells. The materials chosen act to minimize the magnetic interference, and also ensure biocompatibility. The gasket assembly is capable of guiding the cells overtop of the MSCMA, with fluid pressure supplied by a syringe pump that is externally integrated. The use of the syringe pump allows for easy fluid control over a wide range of flow rates, which can be used to flow cells and fluid over the MSCMA. This allows for applications such as cell delivery, removal of unwanted cells and cell media delivery. The next chapter will detail the FEM models and analysis used to design the CFS. In addition, they will describe the simulation models developed to predict the path of a cell subjected to both fluid and magnetic forces within the culture chamber.

Chapter 6: FEM Analysis of CFS

FEM modeling is a common tool used to determine reaction forces in various Engineering applications. It is a useful tool to optimize a device and show a proof of concept without having to physically build the device. There are many software packages that aim to quickly compute reaction forces based on user-defined inputs and functions. One of these programs is COMSOL, which has multiple pre-defined modules.

The two modules used to model the CFS are the AC/DC and fluid dynamics (incompressible Navier-Stokes) modules. The AC/DC module can be used to evaluate magnetostatic problems where there is no current involved, such as modeling a permanent magnet. The fluid dynamics module can be used to predict the fluid flow properties through a volume. COMSOL can also combine multiple modules using a single multiphysics function. This function was used to combine the AC/DC with a fluid flow module to create FEM models of the CFS.

Magnetic and fluid models are completed with the goal of modelling the interaction between a MT cell and permalloy traps, with a constant flow rate applied over the traps. Large scale fluid flow and magnetic FEM models are completed to define a smaller volume located within the culture chamber. This smaller volume model is used to determine the x, y, and z displacement of a single cell due to its interaction with the MSCMA and fluid flow. This chapter will discuss the FEM models used to model the CFS including: (i) a large scale magnetic (LSM) model, (ii) a large scale fluid flow (LSFF) model, (iii) a smaller boundary magnetic/fluid (SBMF) model, and (iv) predicted cell path simulation. This chapter will also conclude with the FEM and cell path simulation results and how they can be used to optimize the experimental methodology.

6.1 COMSOL Subdomain and Boundary Conditions

To fully define an FEM model, conditions have to be set to both the subdomain and boundaries of the model. Subdomains are 3D volumes, such as a cube or a sphere, and conditions applied to a subdomain are applicable throughout the entire volume. Boundaries, on the other hand, are any outer surfaces formed by the subdomains, and conditions applied to the boundaries only apply to that particular surface. This next section will discuss the subdomain and boundaries for both magnetic and fluid models.

6.1.1 Magnetic FEM Model

Two magnetic models are created in COMSOL modelling the interaction between the MSCMA and permanent magnets. This interaction is used to determine how a MT cell will interact with a magnetized MSCMA chip.

6.1.1.1 Magnetic Subdomain Equations

All magnetic models are created using a magnetostatic with no current module, which is a sub-module of the AC/DC module in COMSOL. This sub-module is commonly used to model magnetic elements that do not require a current source to produce a *B*-field, such as a permanent magnet. Magnetostatic with no current models are solved with one of the following equations applied to any subdomain:

$$\vec{B} = \mu_0 \mu_r \vec{H} \tag{6.1}$$

$$\vec{B} = \mu_0 \mu_r \vec{H} + \vec{B}_r \tag{6.2}$$

These equations define the magnetic characteristics based on specific properties such as relative permeability and the remanent *B*-field. Equation 6.1 is the basic constitutive relation that describes the macroscopic properties of the defined medium and equation 6.2 adds a constant that accounts for any remanent *B*-field present. [93]

6.1.1.2 Magnetic Boundary Conditions

One of the following boundary conditions are used to define the magnetic FEM model: magnetic insulation, magnetic potential, magnetic shielding, and continuity. A description of these boundary conditions can be found in Table 6.1. [93]

Table 6.1: COMSOL magnetic boundary conditions [93]

Boundary Condition	**Description**
Magnetic Potential	• Specify the magnetic potential at the boundary
Magnetic Insulation	• Sets the normal component of the *B*-field equal to zero • Boundary condition is useful at boundaries confining a surrounding region of air • *H*-field and *B*-field streamlines run parallel with the boundary
Magnetic Shielding	• Describes a thin layer of permeable medium that shields the magnetic field • User defines the thickness and relative permeability of the layer
Continuity	• Natural boundary condition ensuring continuity of the normal component of the *B*-field

6.1.2 Fluid Flow FEM Model

A fluid flow model was created that includes the interaction between the MSCMA and the fluid flow. This interaction is used to determine how a cell will interact with a constant fluid flow that is applied over the MSCMA.

6.1.2.1 Governing Subdomain Equations and Conditions

The incompressible Navier-Stokes module is used for all fluid flow models. COMSOL uses a generalized version of the Navier-Stokes equations to allow for variable viscosity as follows:

$$\boldsymbol{\rho}\frac{\partial \boldsymbol{U}}{\partial \boldsymbol{t}} - \nabla \cdot \left[\boldsymbol{\eta}\left(\nabla \boldsymbol{U} + (\nabla \boldsymbol{U})^{\boldsymbol{T}}\right)\right] + \boldsymbol{\rho}(\boldsymbol{U}\cdot\nabla)\boldsymbol{U} + \nabla \boldsymbol{p} = \boldsymbol{F} \qquad \textbf{6.3}$$

This equation is another version of the Navier-Stokes equations shown in equations 4.7 – 4.9, and it also assumes that the fluid is continuous (equation 4.6). The density, ρ, dynamic viscosity, η, and volume force vector, F, can be specified, where the volume force vector, $F = (F_x, F_y, F_z)$, describes a distributed force field such as gravity and the unit is force/volume. [94]

6.1.2.2 Boundary Conditions

One of the following boundary conditions is defined for each boundary: wall, inlet/outlet, or symmetry. Each boundary condition has additional conditions and a description of the boundary conditions that are used can be seen in Table 6.2. [94]

Table 6.2: Boundary conditions for fluid flow model [94]

Boundary Condition		Description
Wall	No Slip	• Fluid is not moving at the wall
	Sliding Wall	• Wall assumed to behave like a conveyor belt • Surface is sliding tangentially with respect to the wall • Velocity equal to the given vector projected into the boundary plane
Inlet/ Outlet	Velocity	• Specify the velocity at the inlet/outlet • Set the velocity equal to a given vector • Specify a normal inflow velocity
	Pressure, no viscous stress	• Allows total control of the pressure along the entire boundary • Assumed that there is no viscous stress acting at the inlet/outlet
Symmetry	Symmetry	• Assumes that the boundary acts like a mirror and properties on either side of that boundary are identical

6.2 Large Scale Magnetic Model

A LSM model is created in COMSOL and contains all components of the CFS that affect the magnetic characteristics of the system, which includes the permanent magnets and the MSCMA. All other parts of the CFS are not included in the magnetic model since they all have a relative permeability approximately equal to 1 and they also do not exhibit any remanent *B*-field, as was shown in section 5.3. This next section will discuss the LSM model setup and results.

6.2.1 LSM Model Setup

The LSM model includes the MSCMA chip, two permanent magnets and a medium around everything, as can be seen in Figure 6.1. A total of 8 N52 magnets (4 on each side) are used in the CFS. Each magnets measures 38.1 x 6.35 x 6.35 *mm*^{3} and they are placed 6.2 *mm* from either edge of the permalloy strips. The magnets are modelled as two larger magnets (measuring 38.1 x 25.4 x 6.35 *mm*^{3}), since each magnet has the same relative permeability and remanent *B*-field, it is assumed that a single larger magnet will have the same magnetic properties as 4 smaller magnets.

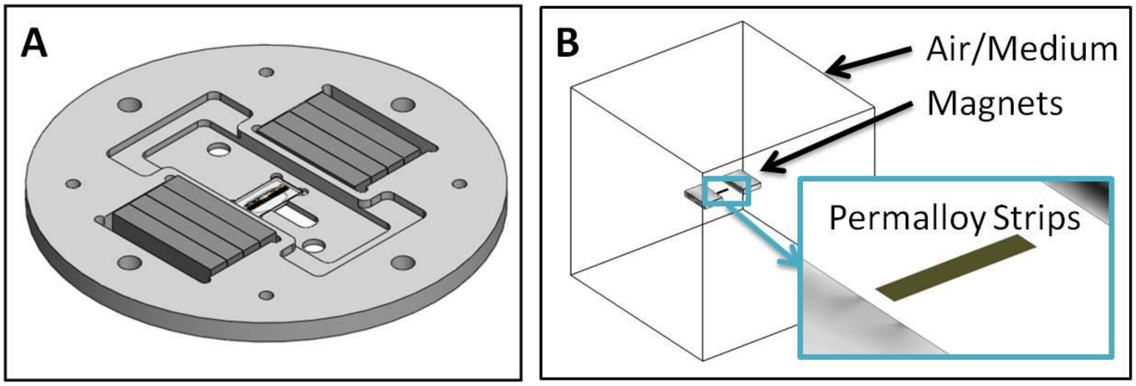

Figure 6.1: (A) Magnetic components of the CFS (B) LSM Model Set-up

The MSCMA chip contains 16 permalloy strips with 80 traps per strip, for a total of 1280 traps per chip. To reduce the complexity of the large scale magnetic model, it is assumed that the MSCMA contained 16 rectangular strips measuring 15 x 0.11 x 0.006 *mm*^{3}. The relative permeability is defined as a function of the *H*-field. This function is determined for the permalloy strips using information extracted from Figure 5.12, and is shown in Appendix B. The B-H curve shown in Figure 5.12 is converted into a relative permeability function using the following equation:

$$\mu_r = \frac{B}{H \cdot \mu_o} \tag{6.4}$$

A large volume is also placed around the magnets and permalloy strips measuring 500 x 500 x 500 mm^3, which acts as the medium for the model. It is assumed that the medium is air with a relative permeability equal to 1. Only the air medium and the 2 permanent magnets are modelled as subdomains. The permalloy strips are treated as boundaries, applying a magnetic shielding boundary condition to them. The subdomain and boundary conditions used for the LSM model are defined in Table 6.3 and Table 6.4 respectively.

Table 6.3: Subdomain equations and relevant coefficients for the LSM model

Subdomain	Governing Equation	Relevant Coefficients
Magnet	$\vec{B} = \mu_o \mu_r \vec{H} + \vec{B}_r$	μ_r = 1.5 B_r = -1.45 T [95]
Medium	$\vec{B} = \mu_o \mu_r \vec{H}$	μ_r = 1

Table 6.4: Boundary conditions and relevant coefficients for the LSM model

Boundary	Boundary Condition	Relevant Coefficients
Magnet	Continuous	
Medium	Magnetic Insulation	
Permalloy Strips	Magnetic Shielding	μ_r = function shown in Appendix C thickness = 6 μm

6.2.2 LSM Model Results

This next section will show the results of the LSM model. Figure 6.2 shows the *B*-field of the permalloy strips, where the maximum and minimum *B*-field occur at the edge (0.161 *T*) and centre of the strips (0.111 *T*) respectively. The *B*-field of the permalloy strips is found to increase due to the following: (i) if the magnet are placed closer to the permalloy strips, (ii) the magnet size is increased, and (iii) the magnets remanent *B*-field is increased. Also, multiple relative permeability functions were used to define the permalloy (corresponding to Figure 5.11), and it was found that different function did not significantly affect the *B*-field.

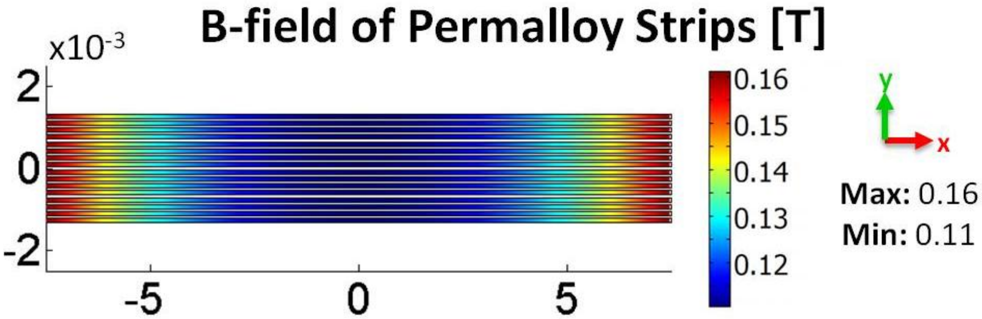

Figure 6.2: Magnetic flux density of the permalloy strips

The magnetic potential is plotted for three different planes, as shown in Figure 6.3. The magnetic potential increases as you get closer to either magnet and decreases as you move away from them. The closer the permalloy is to a permanent magnet, the greater the magnetic potential is, and therefore, the greater the magnitude of the *H*-field and *B*-field will be. Since the permalloy strip is placed in the centre of the two magnets, the magnetic potential has similar absolute values at planes x = ±7.5 *mm*. At the plane x = 0 *mm*, the lowest difference in the magnetic potential is seen, since this plane is the farthest away from either magnet.

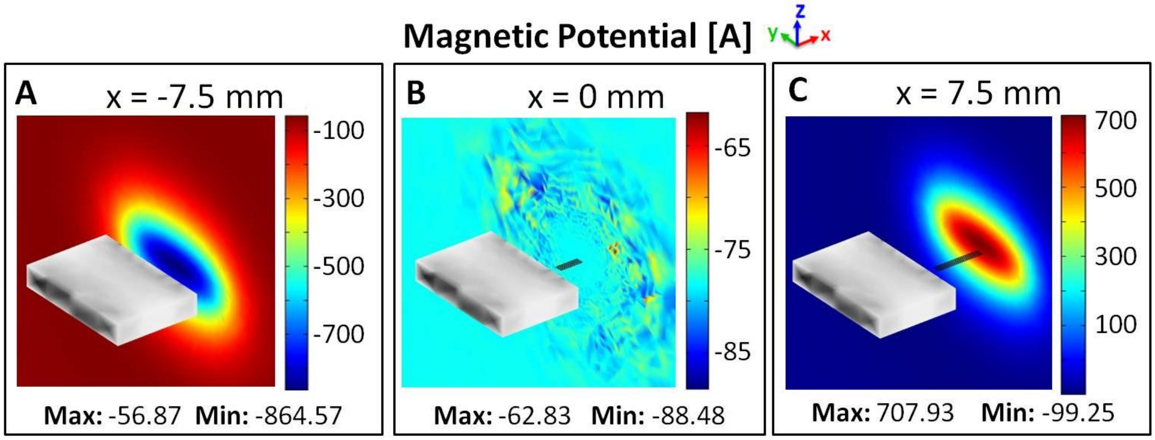

Figure 6.3: Magnetic potential at several locations. (A) Edge of the permalloy strips, x = -7.5 *mm*. (B) Centre of Permalloy strips, x = 0 *mm*. (C) Edge of the permalloy strips, x = 7.5 *mm*.

The direction of the *H*-field and *B*-field lines is an important factor when trying to define a smaller boundary. The boundary conditions of the smaller boundary need to be correctly defined to ensure that the direction and general patterns of the *H*-field and *B*-field lines are consistent with the larger scale models. Figure 6.4 show the *H*-field and *B*-field lines due to the permalloy strips and the permanent magnets. These images are consistent with Gauss's law for magnetism (equation 3.6) as the field lines (for both *H*-field and *B*-field) are closed loops. These images also show that close to the MSCMA, the field lines run parallel to the surface of the permalloy strips.

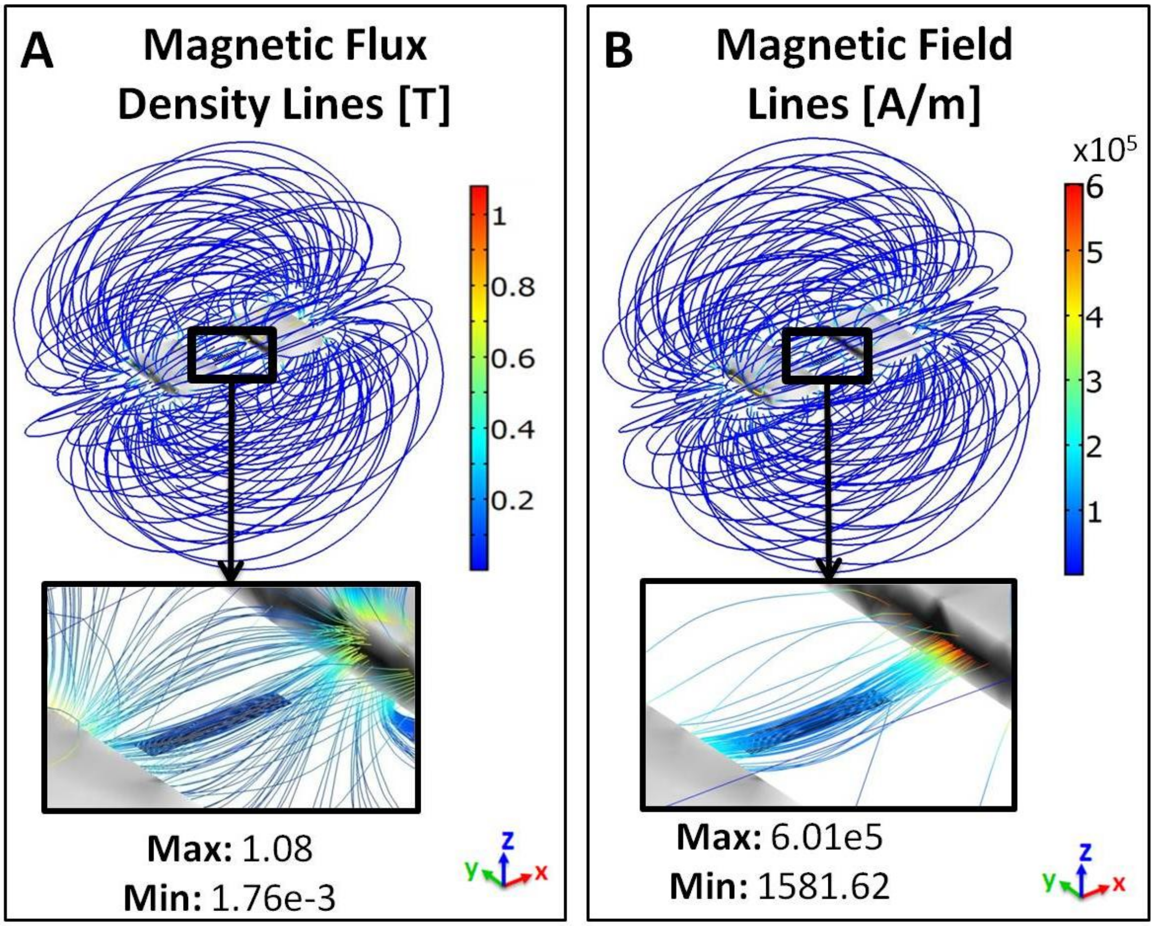

Figure 6.4: (A) Magnetic flux lines (*B*-field). (B) Magnetic field lines (*H*-field).

6.3 Large Scale Fluid Flow Model

A LSFF model was created that contains all components of the CFS, which affects the fluid properties of the system. The fluid flow path through the CFS starts in the external tubing, goes through the barbed fitting attached to the top plate, through the gasket assembly (over the MSCMA), through the outlet barbed fitting, and then exiting through more tubing into a waste container. This section will discuss the LSFF model setup and results.

6.3.1 LSFF Model Setup

To fully define the LSFF model, it is assumed that the flow rate through the CFS is always constant. The volumetric flow rate, Q, through the entire system was assumed to be constant using the following equation:

$$\boldsymbol{Q = AU} \tag{6.5}$$

$$\boldsymbol{A_{inlet}U_{inlet} = A_{Culture\ Chamber}U_{Culture\ Chamber}} \tag{6.6}$$

A desired flow rate is assumed in the culture chamber, and using the constant flow rate assumption, the inlet velocity is determined. The LSFF model only includes fluid contained within the CFS (up to the top plate) and is divided into the following areas, as can be seen in Figure 6.5: (1) barbed fitting that thread into the top plate, (2) top plate as the fluid exits the barbed fitting, (3) inlet/outlet arms of the gasket, and (4) the culture chamber of the gasket assembly.

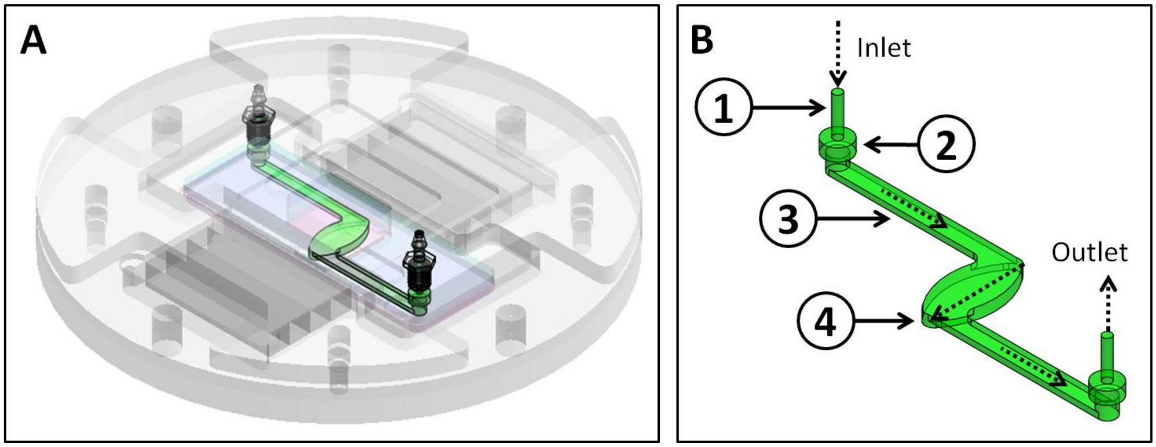

Figure 6.5: (A) Fluid flow through the CFS. (B) SCM fluid geometry with dotted black line showing direction of flow. (1) Barbed fitting (2) Top Plate (3) Inlet/outlet arms of gasket (4) Culture chamber of gasket assembly.

Three different LSFF models are completed with flow rates of 1 *mL/min*, 5 *mL/min* and 10 *mL/min*. The dimensions used to determine the inlet flow rate (equation 6.6) can be found in Appendix C, and the resulting inlet flow rates can be found in Table 6.5. The inlet velocity is assumed to be constant and the pressure at the outlet is assumed to be zero. This will ensure that the flow will always travel from the inlet to the outlet. Also, the fluid is assumed to be water with corresponding density and viscosity. The subdomain and boundary conditions and properties used can be found in Table 6.6 and Table 6.7 respectively.

Table 6.5: Fluid inlet velocity and average fluid velocity through the centre of the culture chamber assuming a constant flow rate

Q [*mL/min*]	**1**	**5**	**10**
Fluid Inlet Velocity [m/s]	0.015	0.076	0.15
Average Fluid Velocity through centre of culture chamber [m/s]	0.001	0.005	0.01

Table 6.6: Subdomain equations and relevant coefficients for the LSFF model

Subdomain	**Governing Equation**	**Relevant Coefficients**
Fluid Flow	Equation 6.3	$\rho = 1000\ kg/m^3$ $\eta = 1 \times 10^{-3}\ Pa \cdot s$

Table 6.7: Boundary conditions and relevant coefficients for the LSFF model

Boundary	**Boundary Condition**	**Relevant Coefficients**
Inlet	Velocity	Normal Inflow Velocity specified to obtain a specific flow rate (values found in Table 6.5)
Outlet	Pressure, no viscous stress	$p = 0$

6.3.2 LSFF Model Results

The fluid flow through the LSFF model will determine how the cell interacts with different flow rates. Although different fluid models were created for each flow rate, only the results for 1 *mL/min* are shown. All additional flow rates showed similar fluid behaviours, but the fluid velocity corresponded to the flow rates (i.e. higher flow rates showed higher fluid velocities). Figure 6.6 shows the fluid streamline direction and magnitudes through the CFS. The fluid behaves as expected, travelling from the inlet to the outlet with no visible turbulence. The maximum velocity is seen at the centre of the inlet/outlet since this area has the smallest cross sectional area. The minimum velocity is at the centre of the culture chamber since it has the largest cross sectional area.

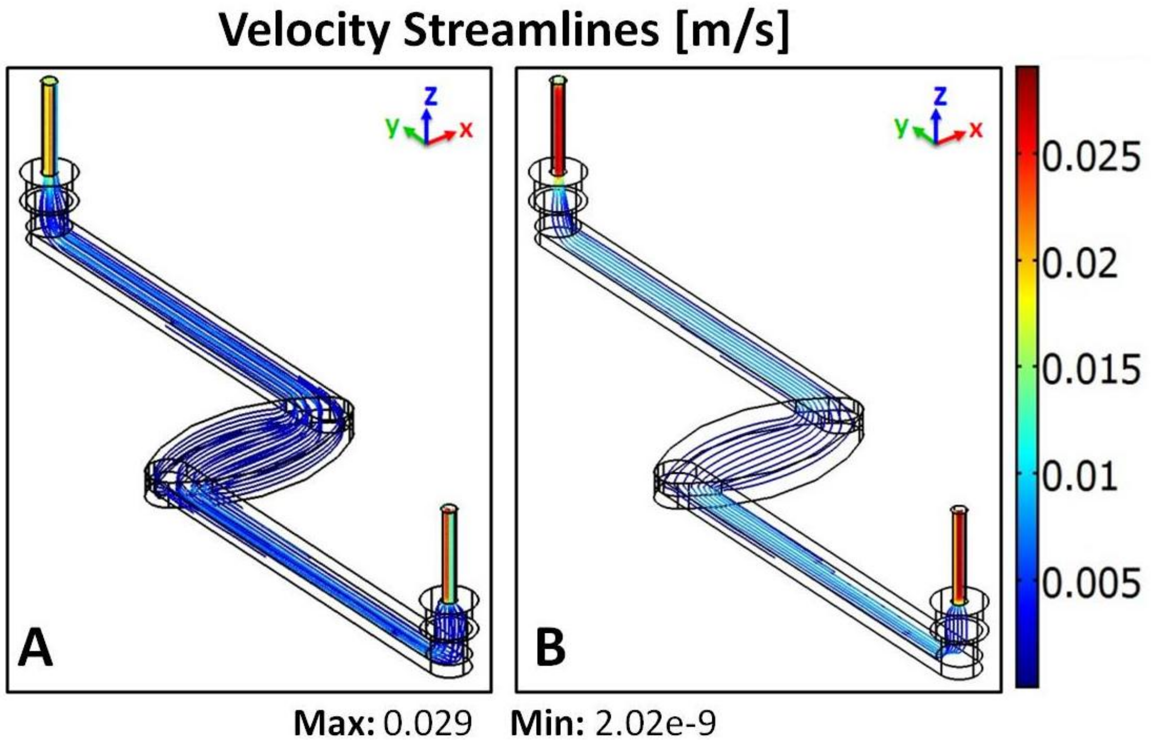

Figure 6.6: Velocity streamlines through the CFS. (A) Streamlines equally spaced from one another. (B) Streamlines through the centre of the culture chamber (1 *mm* from bottom of chamber).

The flow through the culture chamber is the most important aspect of the cross flow system. This area is where the cells will flow over the traps, and the relationship between the fluid and the cell will determine how different flow rates affect MT cell capture. Due to the no-slip boundary condition that was applied, the fluid velocity at the walls is zero, and the velocity increases as you travel towards the centre of the chamber, as seen in Figure 6.7 (A). Also, the pressure decreases as the fluid flow travels from the inlet to the outlet as is expected, as can be seen in Figure 6.7 (B). The velocity profile with respect to the direction of flow at the centre of the culture chamber (where the width is the greatest) is parabolic, which is characteristic of a laminar flow, as can be seen in Figure 6.8. The maximum flow rate also occurs at the centre of the culture chamber (z = 1 *mm*).

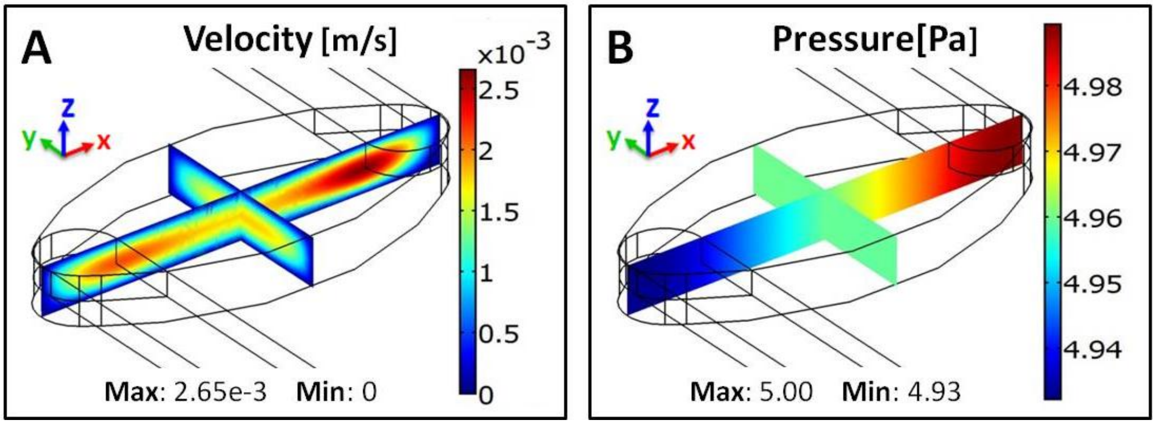

Figure 6.7: Culture chamber fluid plots showing (A) Velocity and (B) Pressure.

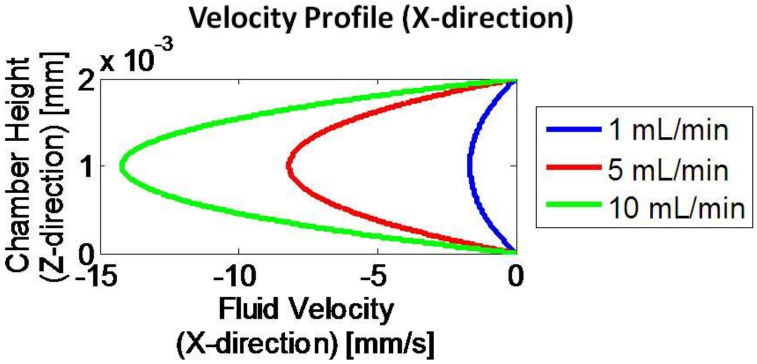

Figure 6.8: Velocity profile at the centre of the culture chamber.

6.4 Smaller Boundary Magnetic/Fluid FEM Model

To predict the path a MT cell will follow a SBMF FEM model was created. This model uses the multiphysics module of COMSOL, integrating the magnetic and fluid flow modules. Two SBMF models are completed, one with a sinusoidal design and another with a sawtooth design. Both models contain 1 full row and 2 half rows of permalloy traps, with 8 traps per full row (total of 16 traps), with a medium around the traps, as shown in Figure 6.9. The permalloy traps are the grey regions seen in Figure 6.9, with a height of 6 μm from the MSCMA substrate, which is represented by the bottom of the model. The medium volume around the SBMF model measures 0.24 x 0.34 x 0.24 mm^3 in the x, y, and z direction respectively.

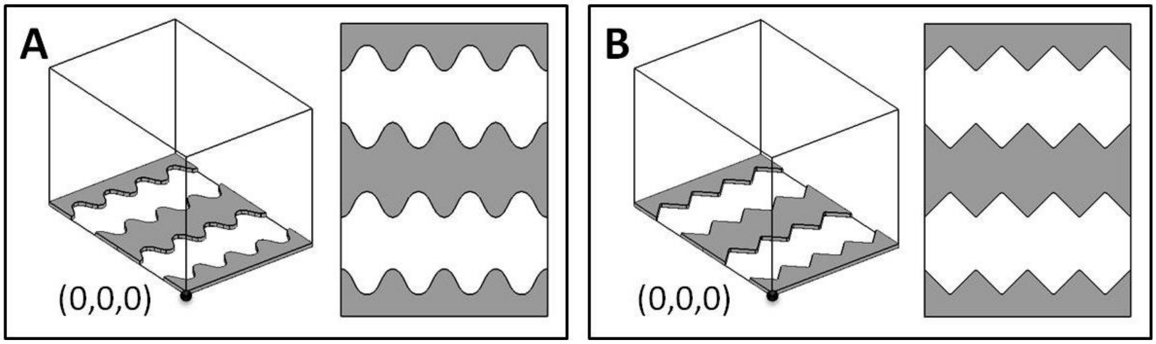

Figure 6.9: Smaller Boundary Magnetic/Fluid FEM Models. (A) Sinusoidal design. (B) Sawtooth design. Grey region represents the permalloy.

6.4.1 Information Extracted from Large Scale Models

Magnetic and fluid flow information is extracted from the large scale models shown in sections 6.2 and 6.3 respectively. The location and relative size of the smaller boundary in comparison to the larger scale models can be seen in Figure 6.10. The magnetic and fluid flow information is extracted from five points on boundary 1 – 3, and the values are averaged. The magnetic information is summarised in Table 6.8, where the magnetic potential is extracted from the LSM model at boundaries 1 and 3. The fluid information is summarised in Table 6.9, where the pressure is extracted from the LSFF model at boundaries 1 and 3, and the velocity at boundary 2.

Table 6.8: Magnetic information extracted from large LSM model

Boundary	1	2	3
Magnetic potential [A/m]	-5.3753	NA	16.3179

Table 6.9: Fluid flow information extracted from LSFF model

Flow Rate [*mL/min*]	Boundary 1 Pressure [*Pa*]	Boundary 2 Velocity [*mm/s*]	Boundary 3 Pressure [*Pa*]
1	4.4763	-0.6999	4.4771
5	28.5831	-3.4537	28.5855
10	74.7314	-5.9968	74.7353

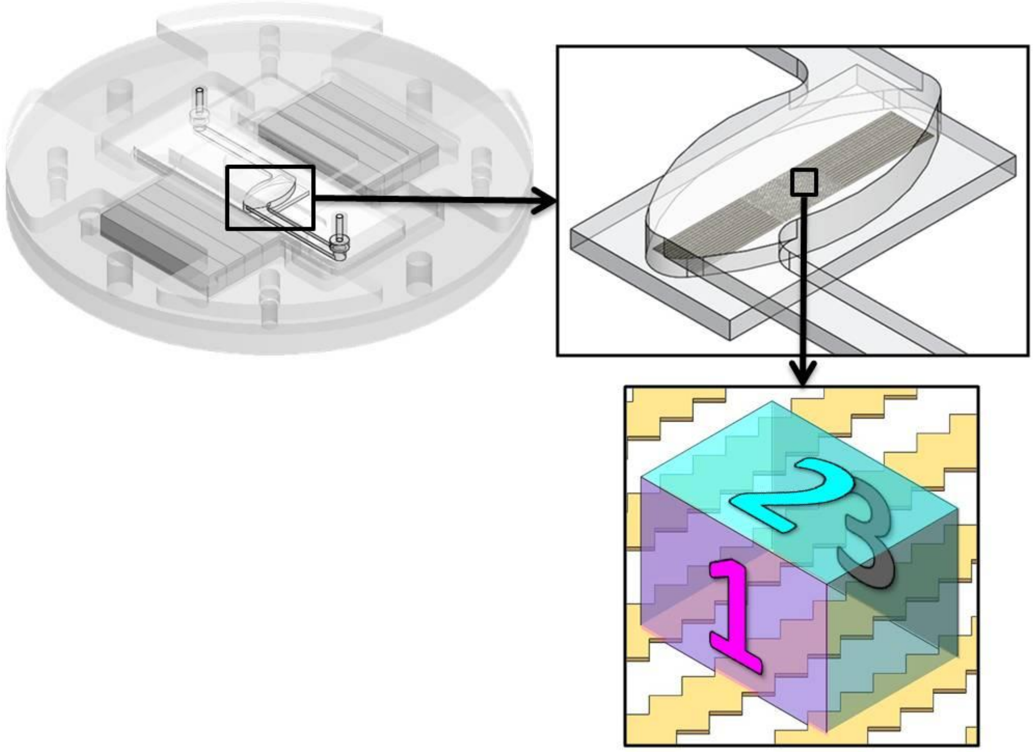

Figure 6.10: Smaller boundary extracted from larger models.

6.4.2 SBMF Model Setup

The information extracted from the large scale model is used to define the subdomain and boundaries for the SBMF model. The 3D permalloy strips are assumed to have a constant relative permeability. Since they are treated as solid 3D objects, the fluid can only flow around them. The volume around the permalloy trap is assumed to be water, with corresponding density and viscosity. The same subdomain and boundary conditions are applied to both models (sinusoidal and sawtooth) and can be found in Table 6.10 and Table 6.11 respectively.

Table 6.10: Subdomain equations and relevant coefficients for SBMF FEM Model.

Model	Subdomain	Governing Equation	Relevant Coefficients
Magnetic	Fluid Flow	$B = \mu_o \mu_r H$	$\mu_r = 1$
	Permalloy Traps	$B = \mu_o \mu_r H$	$\mu_r = 725$
Fluid	Fluid Flow	Equation 6.3	$\rho = 1000\ kg/m^3$ $\eta = 1\text{x}10^{-3}\ Pa \cdot s$
	Permalloy Traps	Solid area where fluid does not flow	

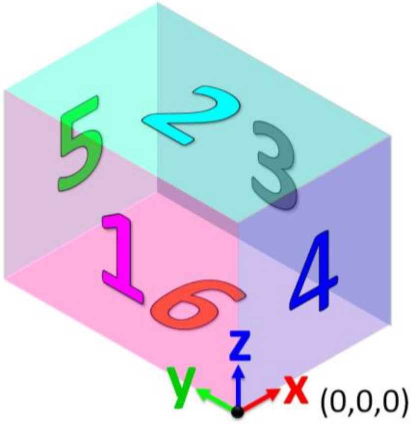

Figure 6.11: Boundary walls for predicted cell path simulation model

Table 6.11: Boundary conditions and relevant coefficients for SBMF FEM Model using boundary numbers in Figure 5.10.

Model	Boundary	Boundary Condition	Relevant Coefficients
Magnetic	1	Magnetic Potential	V_m = -5.3753
	3	Magnetic Potential	V_m = -16.3179
	2, 4, 5, 6	Magnetic Insulation	
	Permalloy	Continuous	
Fluid	1	Inlet, Pressure, no viscous force	Pressure defined according to Table 6.9 (Boundary 1 column)
	2	Wall, Sliding Wall	Sliding wall velocity defined according to Table 6.9 (Boundary 2 column)
	3	Outlet, Pressure, no viscous force	Pressure defined according to Table 6.9 (Boundary 3 column)
	4, 5	Symmetry	
	6, Permalloy	Wall, No Slip	

6.4.3 SBFM Model Assumptions

Several assumptions are made for the SBMF models, and will be discussed in this section. The first assumption used for the SBMF model, is that the fluid medium used is water. The cells are actually kept in a phosphate buffer solution (PBS) medium, which has similar fluid properties to water [96]. Secondly, the permalloy traps are modelled as 3D volumes with a constant relative permeability throughout the entire volume. This was done as opposed to modelling the permalloy strips as a 2D surface and applying a magnetic shielding boundary condition, where the 2D model represents the top surface of the 3D volume. When using the magnetic shielding boundary condition, a relative permeability function can be used to define the permalloy strips (Appendix B).

Figure 6.12 shows the comparison between the 2D and 3D models for both the sinusoidal and sawtooth design. As can be seen in both figures, the magnetic flux density is very similar between the 2D and 3D designs, with the 2D models having slightly lower values. Since the two models are very similar, this shows that assuming a 3D model with constant permeability is a safe assumption. Also, since the fluid flow can travel around the 3D traps, this will allow the fluid properties to be more accurately modelled using the 3D model.

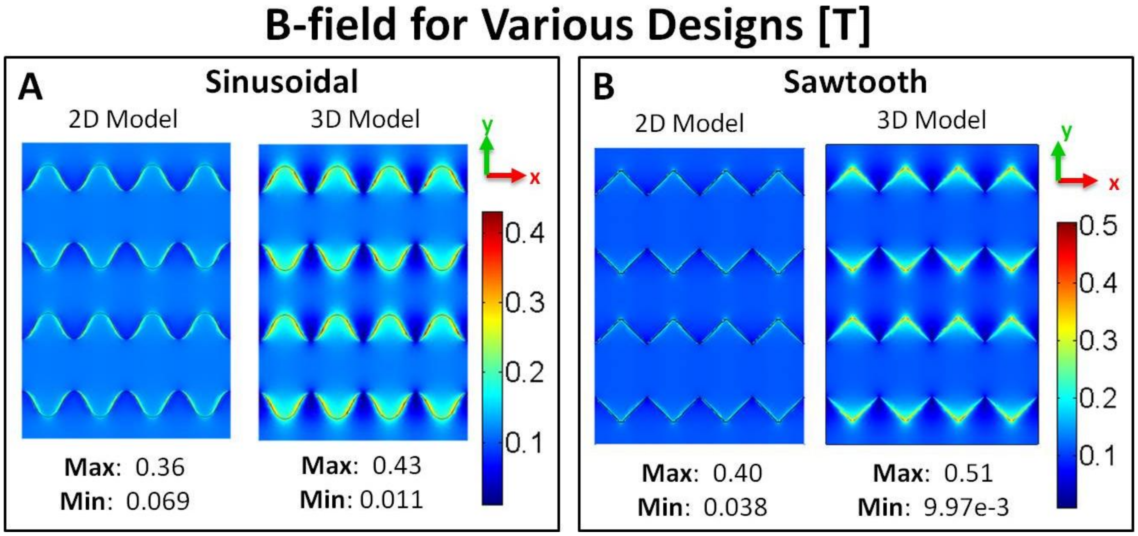

Figure 6.12: 2D versus 3D model showing *B*-field at top of the permalloy traps. (A) Sinusoidal permalloy trap design. (B) Sawtooth permalloy trap design.

6.4.4 SBFM Sinusoidal and Sawtooth Model Results

The magnetic and fluid properties of the sinusoidal and sawtooth design are evaluated and will be shown in this section. The path that the cell will travel will depend mainly on the magnetic force and stokes drag acting on the cell. The direction a MT cell travels in response to a *B*-field gradient will be towards the maximum *B*-field. As can be seen in Figure 6.13, the maximum *B*-field for both designs is seen within the traps, which is beneficial since this implies that a cell will be drawn towards the traps. The sinusoidal design creates two *B*-field maximums at either side of each trap with a maximum of 0.238 *T*. The sawtooth design, on the other hand, creates a single *B*-field maximum located at the centre of the trap with a maximum of 0.374 *T*. Another aspect that is important is the strength of the magnetic force.

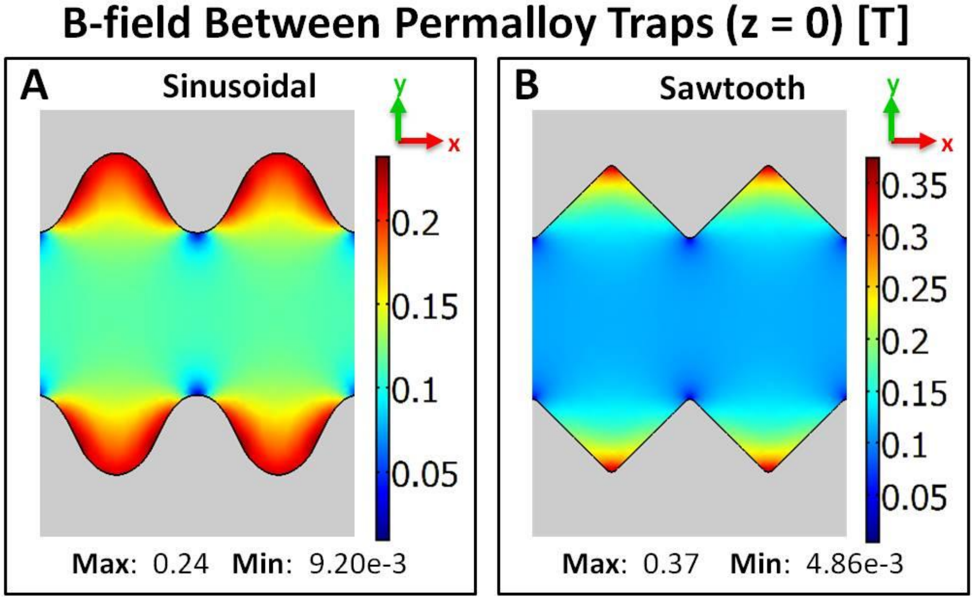

Figure 6.13: Magnetic flux density between permalloy traps at z = 0 for (A) sinusoidal and (B) sawtooth permalloy design. Grey region is the permalloy.

The strength of the magnetic field will depend on the *B*-field gradient. A plot of the *B*-field gradient for both the sinusoidal and sawtooth designs at a distance of 12.1 μm from the top of the glass can be seen in Figure 6.14. The *B*-field gradient increases as you get closer to the magnetic traps and the maximum occurs at the region of maximum *B*-field (either side of trap for sinusoidal, and centre of trap for sawtooth), as can be seen in Figure 6.13. The sawtooth pattern has the greatest *B*-field gradient with a maximum of 8.14×10^4 *T/m*, whereas the sinusoidal pattern has a maximum of 3.07×10^4 *T/m*. The *B*-field gradient is greater for the sawtooth design close to the traps, whereas the *B*-field away from the traps is similar for both designs.

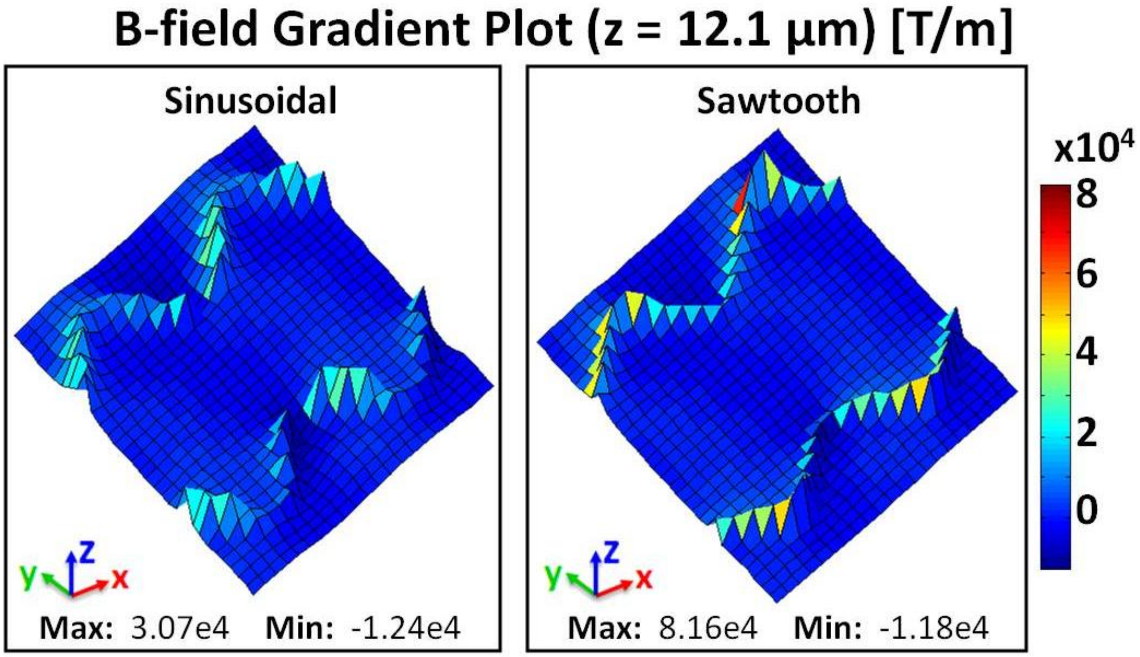

Figure 6.14: ***B*-field gradient plot for sinusoidal and sawtooth permalloy design.**

Another important aspect of the permalloy traps is their ability to draw a cell into a trap, which will depend on the *B*-field patterns seen as you move away from the traps. Figure 6.15 (A) through (D) shows the *B*-field at varying heights for both the sinusoidal (left images of Figure 6.15) and sawtooth (right images of Figure 6.15) permalloy designs. In general, the sawtooth design has a larger *B*-field maximum in comparison to the sinusoidal design for all heights. The *B*-field reaches a maximum at the top surface of the permalloy (z = 6 μm) for both the sinusoidal and sawtooth design (0.430 T and 0.507 T respectively). As you move away from the permalloy in the positive *z*-direction, the *B*-field decreases until you no longer see a distinction (*B*-field gradient approaches zero). This occurs at a distance of 50 μm from the glass substrate of the MSCMA. This is shown in Figure 6.15 (D), as the difference between maximum and minimum is only 0.001 T. The magnetic force on a cell is dependent on the *B*-field gradient. When the *B*-field distinction approaches zero, this implies that the *B*-field gradient also approaches zero, and therefore, the magnetic force approaches zero at a height greater than 50 μm.

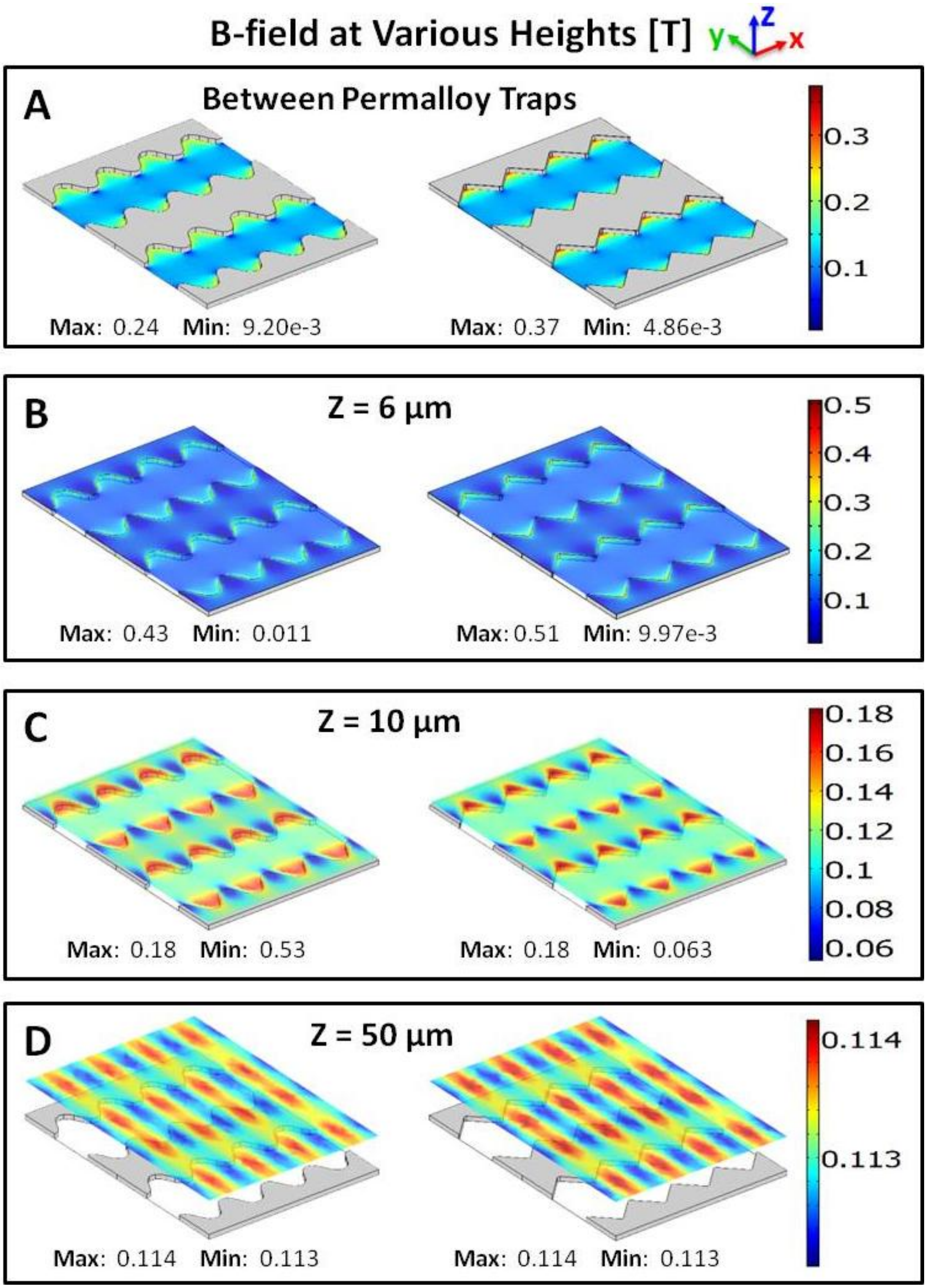

Figure 6.15: Magnetic flux density for the sinusoidal (left) and sawtooth (right) permalloy traps. (A) Between the permalloy traps z = 0. (B) z = 6 μm (C) z = 2.5 μm (D) z = 5 μm.

Another important aspect of the SBMF model is the fluid flow properties throughout the volume. For both models, the fluid flow is in the negative x-direction and all images show the results for a flow rate of 1.0 *mL/min*. As was seen in section 6.3.2, all flow rates results are similar, but with corresponding fluid velocities. Both permalloy designs show similar fluid properties throughout the entire boundary. The velocity on the surface of the substrate and permalloy traps is always zero (i.e. no slip assumption) and increases to a maximum of 0.7 *mm/s* at the top of the model, as shown in both the slice plot and streamline plot of Figure 6.16.

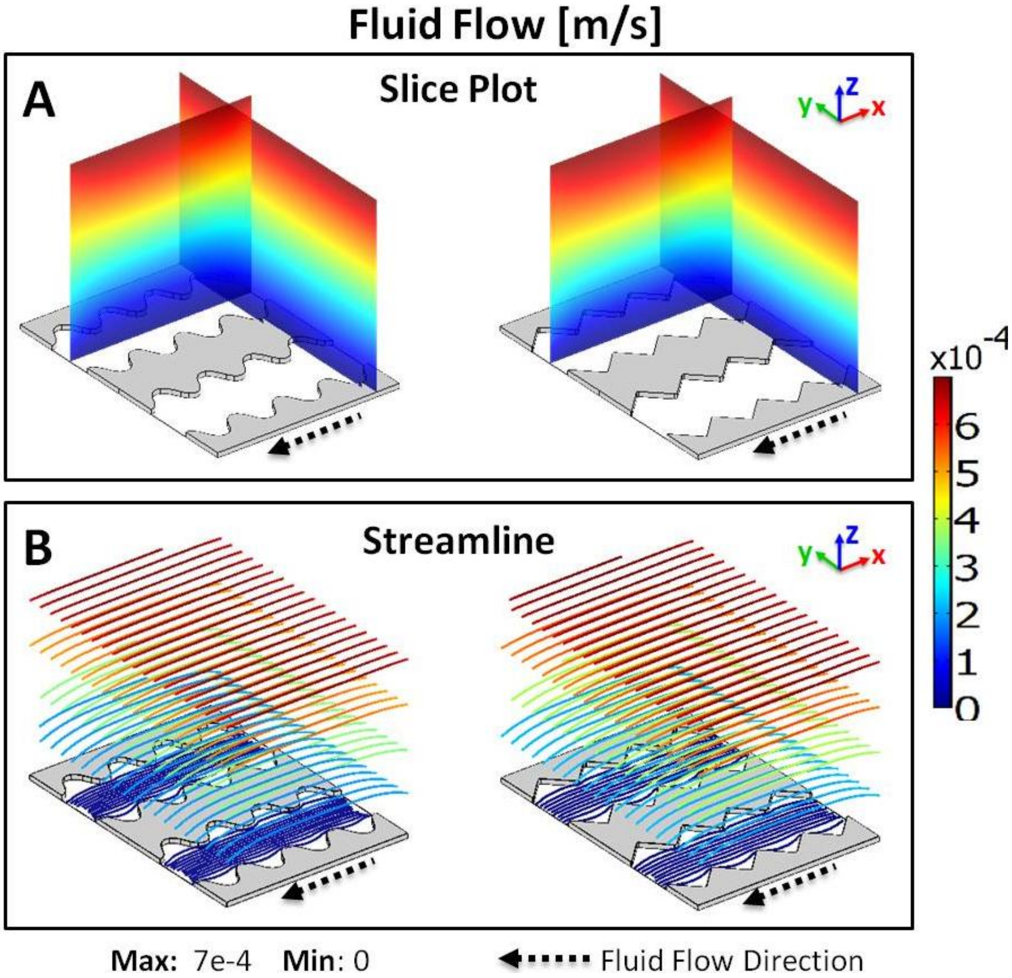

Figure 6.16: Fluid flow for both sinusoidal (left) and sawtooth (right) permalloy designs. (A) Slice plot throughout the boundary. (B) Fluid flow streamlines throughout the entire boundary.

The streamline plot for two different heights can be seen in Figure 6.17. Where Figure 6.17 (A) shows the streamline plots between the permalloy traps (z = 3 μm), and Figure 6.17 (B) shows the streamline plots at the top of the permalloy (z = 6 μm). For both heights, the fluid velocity is the greatest directly between the permalloy traps in the y-direction. As you move closer to the permalloy traps, the fluid velocity tends to decrease. This implies that stationary cells that are in or close to a trap region will experience a smaller Stokes drag compared to cells that are directly between the permalloy lines, since the Stokes drag is a function of the fluid velocity.

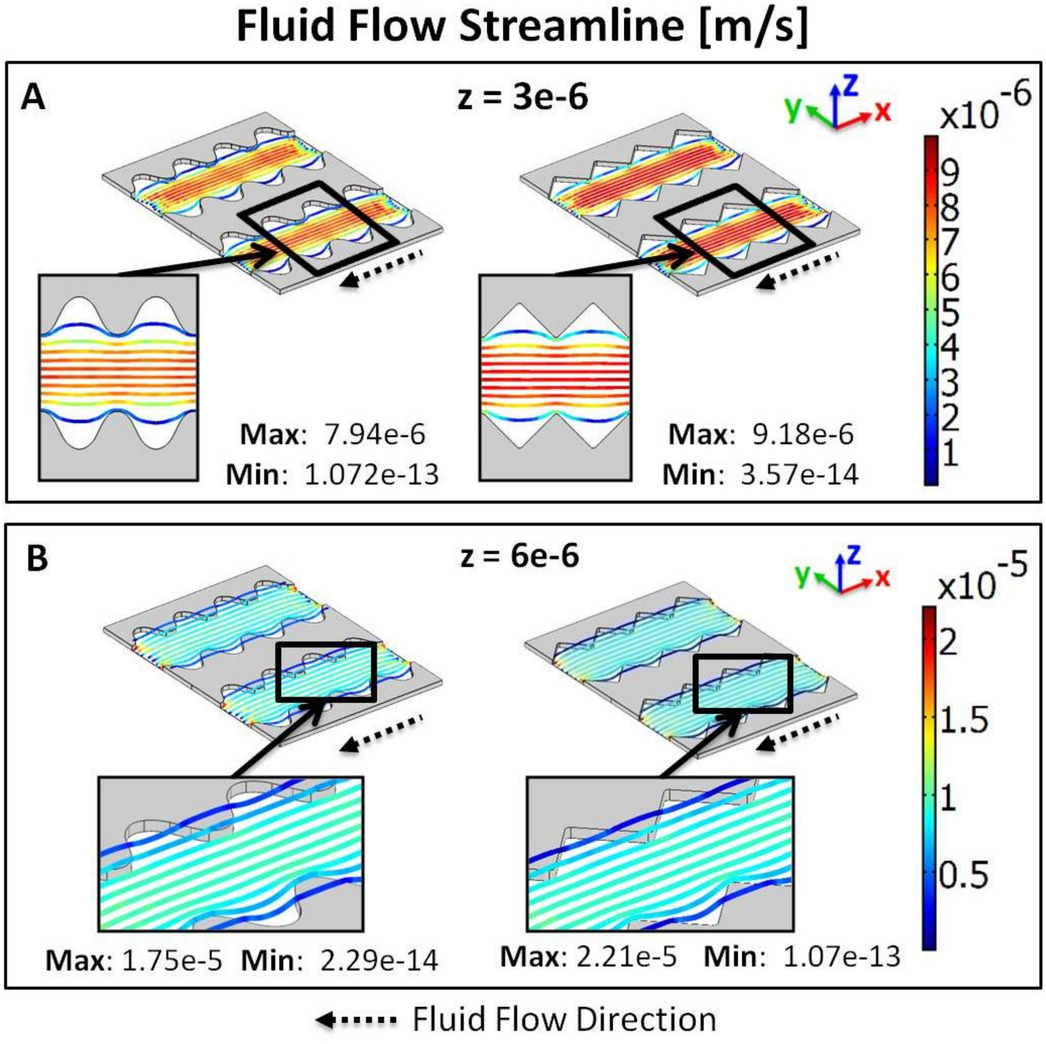

Figure 6.17: Sinusoidal streamline plots at (A) z = 3 μm and (B) z = 6 μm.

6.5 Predicted Cell Path Simulation

The SBMF multiphysics FEM model was created using information extracted from larger scale magnetic and fluid flow models. The multiphysics models will be used to predict the path a MT cell will follow due to magnetic and fluid forces. This simulation is used to optimize the CFS design and experimental methodology. The next section will discuss the simulation process, assumptions, cell path simulation results, and force trends.

6.5.1 Simulation Process

A cell path simulation is completed using information extracted from COMSOL and input into Matlab using a COMSOL/Matlab integration program. A simplified simulation cycle can be seen in Figure 6.18, and a more detailed simulation cycle can also be found in Appendix D. The simulation is an iterative solution, where the time step is defined by the user prior to each simulation. Each simulation starts by solving the SBMF model in COMSOL, which is only solved once for the duration of the simulation. The magnetic characteristics are kept constant between each simulation. However, the fluid flow that is introduced into the boundary will differ for each simulation.

For the first iteration, the position of the cell is defined by the user, and the velocity of the cell is assumed to be the same as the fluid velocity. Using the initial cell position, information is extracted from the COMSOL SBMF model, and input into Matlab to calculate the forces on a single cell. The four dominating forces that are considered in this simulation are the magnetic force (F_m), stokes drag (F_d), buoyancy force (F_b), and gravitational force (F_g). All other relevant calculations are also completed in Matlab. The acceleration of the cell is then found by summing the forces and dividing by the mass of a single cell (*F* = *ma*). Then the final velocity and position of the cell are found using the initial position, velocity and acceleration. The final cell position and velocity are then used as the initial cell position and velocity for the next iteration. This cycle continues until the cell touches the permalloy traps. To maximize the versatility of this simulation, parameters such as the permalloy design and fluid velocity can easily be altered to test different configurations.

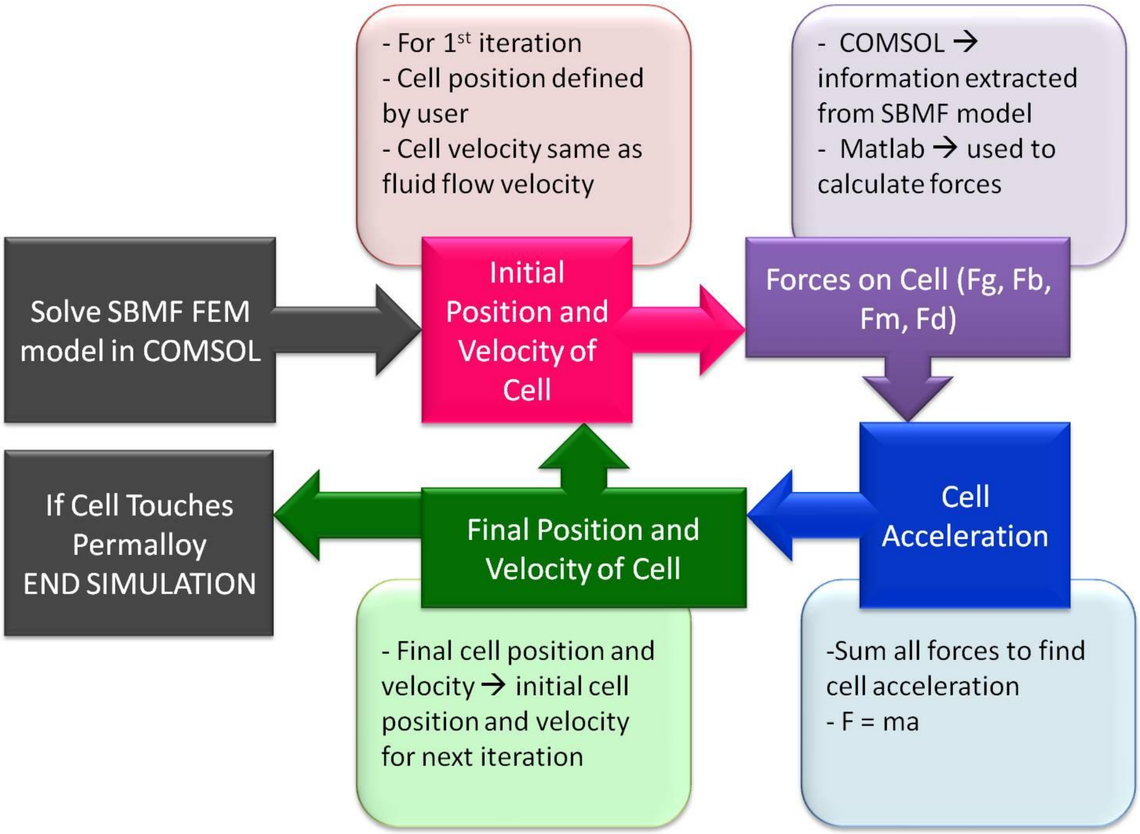

Figure 6.18: Predicted cell path simulation cycle.

6.5.2 Assumptions

To reduce the complexity and therefore the solve time of the simulation, it is necessary to make several assumptions. This next section will outline the magnetic and fluid flow assumptions that are made.

6.5.2.1 Magnetic Force Assumptions

The magnetic force on a cell (as derived in section 3.2) depends on four main factors: (i) the number of magnetic tags on a cell, (ii) the difference in the volume magnetic susceptibility between the cell and the surrounding fluid, (iii) the *B*-field gradient around the particle, and (iv) the volume of the particle. Of these 4 factors, factors 2, 3, and 4 can be estimated, but factor 1 is unknown, and the number of magnetic tags on a cell will ultimately determine the total magnetic force on the cell. Due to this lack of information, it is assumed that instead of having magnetic particles attached to the outside of the cell, the entire cell is treated as a magnetic particle. The relative permeability for the cell is assumed to have the same relative permeability provided by the manufacture of Dynabeads (Appendix E). It is also assumed that the magnetic force always acts at the centre of the cell. There is an obvious discrepancy between the sizes of a magnetic particle ($\sim 10^{-9}\ m$) versus the size of a cell ($\sim 10^{-6}\ m$). To account for the difference in size, and the unknown number of magnetic particles on the cell, a percentage of the total magnetic force is used for the simulations.

Three simulations were completed using varying magnetic force percentages (100%, 10% and 1%), as can be seen in Figure 6.19. Each simulation follows the simulation process defined in Appendix D and no flow rate is applied. Changing the percentage of the magnetic force did not change the path the cell followed, but instead changed the time it took a cell to reach the traps. The time shown is the total time required for a cell to travel from the starting position to the permalloy trap. As the magnetic force percentage changes from 100% to 10%, and again from 10% to 1%, the time decreases by a factor of 10 in each case, as can be seen in Table 6.12.

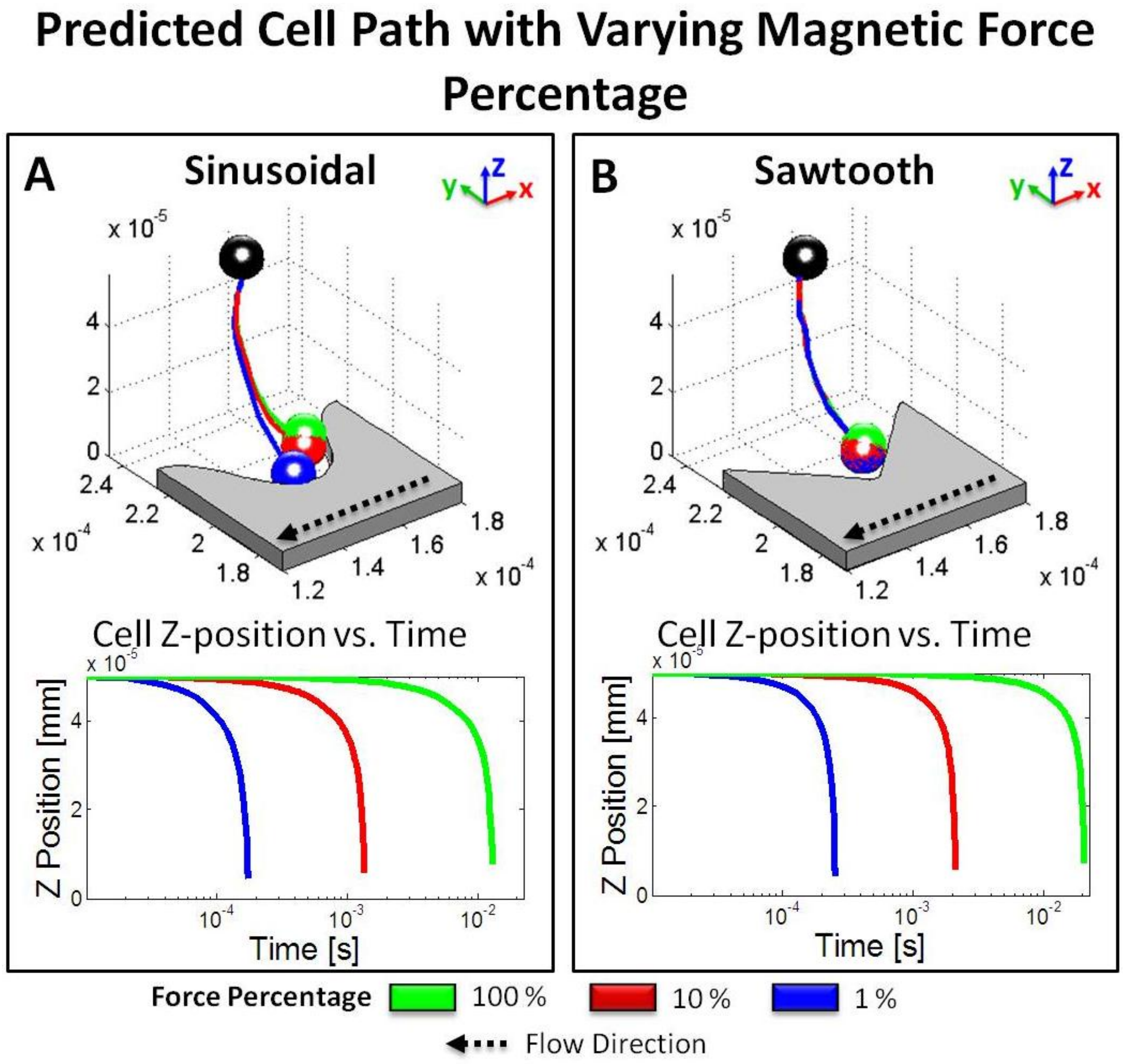

Figure 6.19: Predicted cell path with varying percentages of magnetic force starting at an (x, y, z) position of (160, 240, 50) *μm* for (A) sinusoidal and (B) sawtooth permalloy design.

Table 6.12: Total time for cell to travel from an initial (x, y, z) position of (160, 240, 50) *μm* to the trap with varying percentages of magnetic force.

Magnetic Force %	Sinusoidal Total Time [s]	Sawtooth Total Time [s]
100	0.000175	0.000253
10	0.0014	0.0021
1	0.0131	0.0204

The implications of using a percentage of the magnetic force for the cell path simulation, is that there will always be a set number of magnetic particles that are evenly distributed on the surface of each cell. The magnetic force percentage can be equated to the number of magnetic particles attached to each cell using the following equations:

$$\vec{F}_m = \frac{V_c \Delta\chi}{2\mu_o} \nabla(\vec{B}^2) \tag{6.7}$$

$$1\% \frac{V_c \Delta\chi}{2\mu_o} \nabla(\vec{B}^2) = \#MP \frac{V_m \Delta\chi}{2\mu_o} \nabla(\vec{B}^2) \tag{6.8}$$

$$1\% (V_c) = \#MP (V_m) \tag{6.9}$$

Where V_c is assumed to be the volume of the cell and V_m is the volume of the magnetic particle. Equation 6.7 is the total magnetic force exerted on a single cell, assuming that the entire cell is treated as a magnetic particle. Equation 6.8 shows how many magnetic particles would be needed to equal 1% of the magnetic force. Now assuming that $\Delta\chi$ and the B-field gradient are constant, the only factors that still remain are the volume of the cell, the volume of the magnetic particle, and the number of magnetic particles (equation 6.9).

A single Jurkat cell has a diameter of 12 μm, with a corresponding volume of 905 μm^3 (9.05×10^{-16} m^3). Assuming that a standard magnetic particle is approximately 10 nm in diameter, this corresponds to a volume of 5.24×10^{-7} μm^3 (5.24x10-^{25} m^3). This means that a total of 17.27×10^6 magnetic particles are needed to equal 1% of the cell magnetic force (1% force = 9.05 μm^3). Although this number does seem quite high, another way of quantifying a 1% magnetic force is calculating what additional volume of magnetic material around the cell is equivalent to that force, as shown in the following equation:

$$1\% (V_c) = \frac{4}{3}\pi(r_c + t_m)^3 - V_c \tag{6.10}$$

Where r_c is the radius of the cell, and t_m is the thickness of the magnetic material. Using this equation, a 1% magnetic force is equivalent to the entire surface of the cell being coated with a 20 *nm* layer of magnetic materials. Since each magnetic particle is approximately 10 nm in diameter, a 20 nm layer of evenly coated magnetic material on the surface of the cell is a fairly reasonable estimate. Although using 1% of the magnetic force is probably a high estimate, it is still a good starting point for cell path simulations.

6.5.2.2 Fluid Flow Assumptions

For the fluid flow, it was assumed that the fluid through the SBMF model is continuous. In order to assume this the volume had to be greater than $2.7\text{x}10^{-18}$ mm^3 ($3\text{x}10^{-6}$ x $3\text{x}10^{-6}$ x $3\text{x}10^{-6}$ mm^3) (section 4.1.1). The volume length used in the simulation has a total volume of 0.0196 mm^3 (0.24 x 0.24 x 0.34 mm^3) and therefore the continuum assumption can be used. The COMSOL model does not include the cell, and therefore, the cell will not affect the fluid flow. This assumption will neglect any affects that a moving sphere will impose on the surrounding fluid. It is also assumed that the cell is a rigid sphere that does not deform. This assumption will neglect any shear forces that would be exerted on a deformable cell.

6.5.3 Predicted Cell Path Simulation Results

Four simulations were completed for both the sawtooth and sinusoidal designs with the following flow rates: 0 *mL/min* (no flow rate applied), 1.0 *mL/min*, 5.0 *mL/min* and 10.0 *mL/min*. The results of these simulations can be seen in Figure 6.20 and Table 6.13. Changing the flow rate did not drastically change the overall path that the MT cell followed, but there is a slight difference between each flow rate.

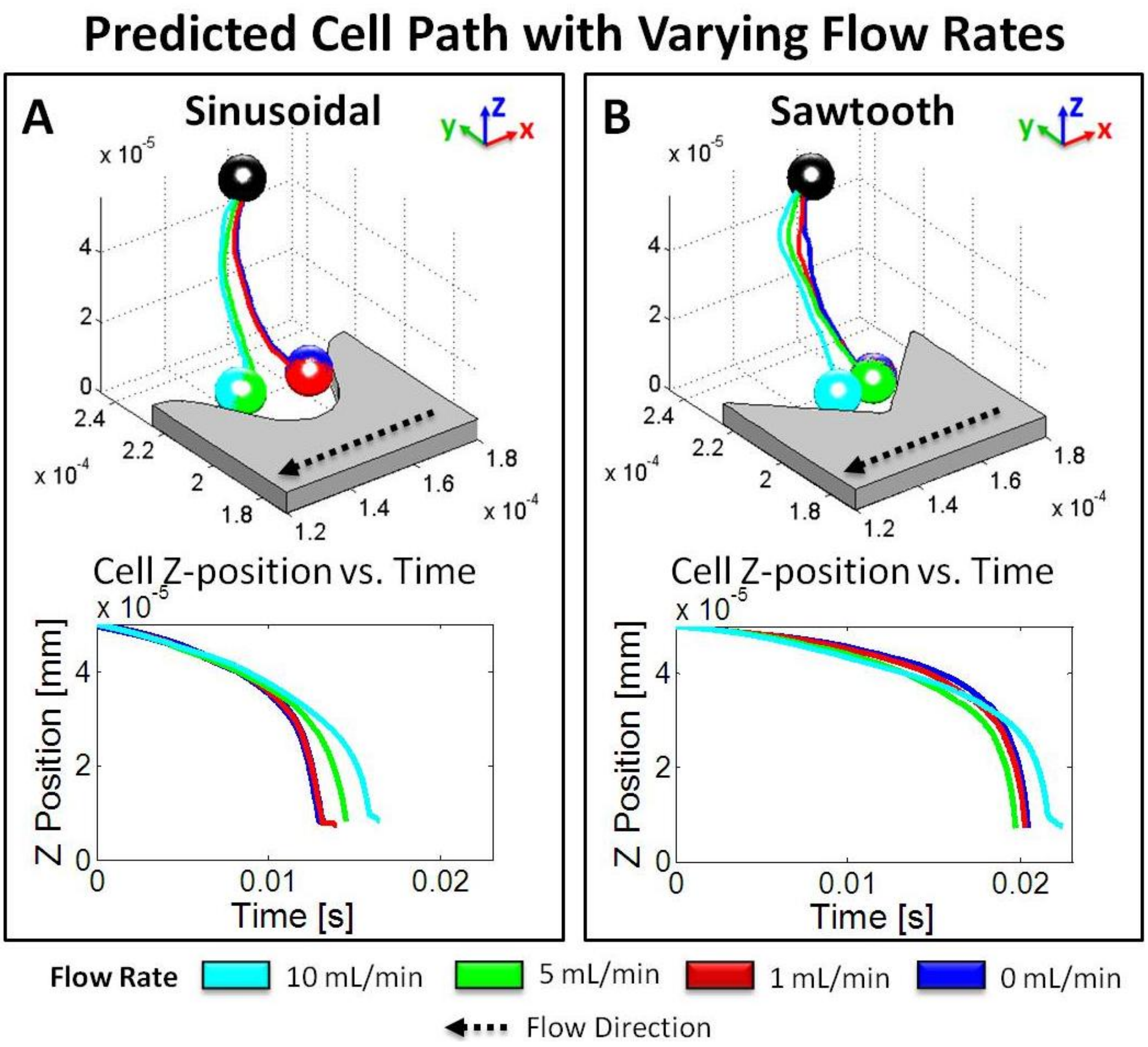

Figure 6.20: Predicted Cell Path with varying flow rates starting at an (x, y, z) position of (160, 240, 50) *µm* for (A) Sinusoidal and (B) Sawtooth permalloy design.

Table 6.13: Total time for cell to reach trap initial (x, y, z) position of (160, 240, 50) *µm* to the trap.

Flow Rate [*mL/min*]	Sinusoidal Total Time [*s*]	Sawtooth Total Time [*s*]
10	0.0165	0.0224
5	0.0146	0.0197
1	0.0139	0.0203
0	0.0132	0.0205

For the sinusoidal design, the cell is drawn to each side of the trap since the maximum *B*-field is seen at these points. The predicted cell path is similar for a flow rate of 0 *mL/min* and 1.0 *mL/min* and a distinct difference is not seen until the flow rate reaches 5.0 *mL/min*. For the sawtooth design, the cell is drawn into the centre of the trap, where the maximum *B*-field is found and little difference is seen between all four flow rates. The time for the cell to travel from the original position to the trap increases with increasing flow rates and it is greater for the sawtooth design for all flow rates.

6.5.4 Force Trends

To better understand the trends seen in the previous section the force trends will also be analyzed. Figure 6.21, Figure 6.22, and Figure 6.23 show both the magnetic force in the x, y, and z direction at a *z*-height of 12.1 *µm* from the substrate (i.e. the bottom of the model). At this height, the magnetic force was always greater for the sawtooth design (right images) in comparison to the sinusoidal design (left images). These three images show that for this specified height, the magnetic force always tends to draw cells towards the areas of maximum *B*-field seen within the traps.

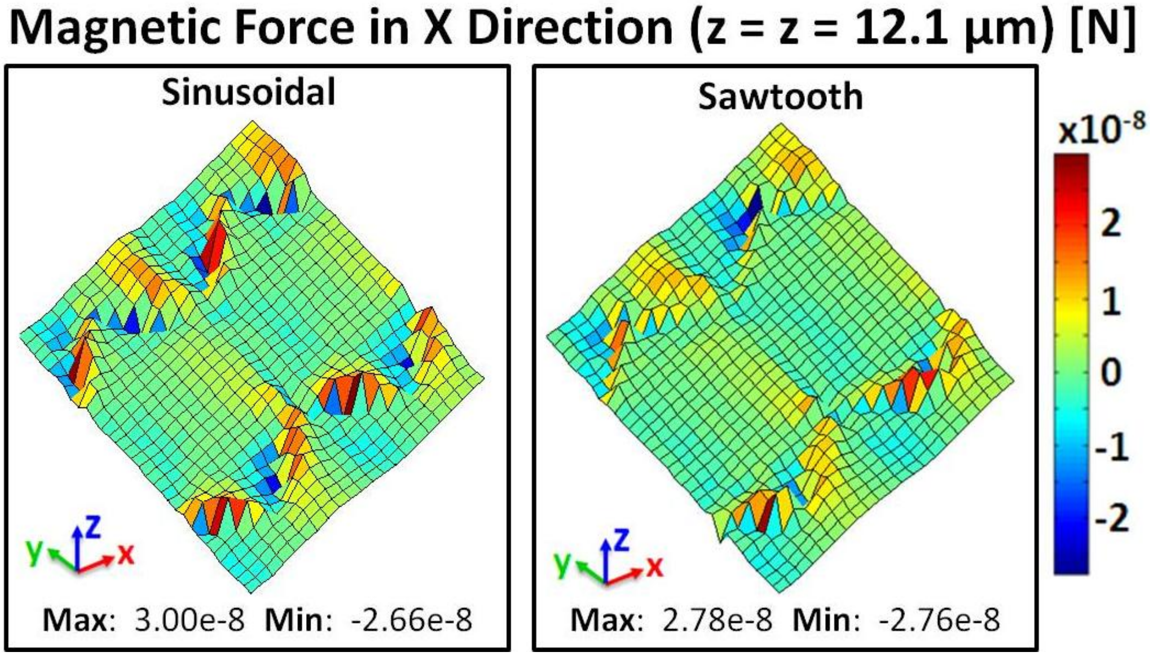

Figure 6.21: Magnetic force in the X Direction at z = 12.1 *µm*.

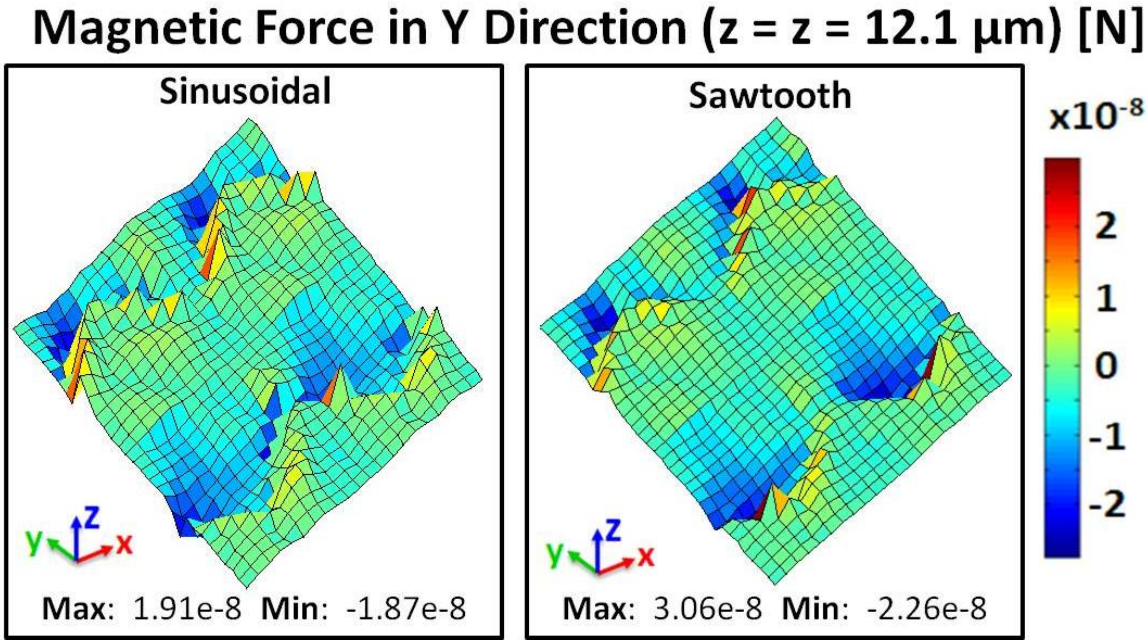

Figure 6.22: Magnetic force in the Y direction at z = 12.1 μm.

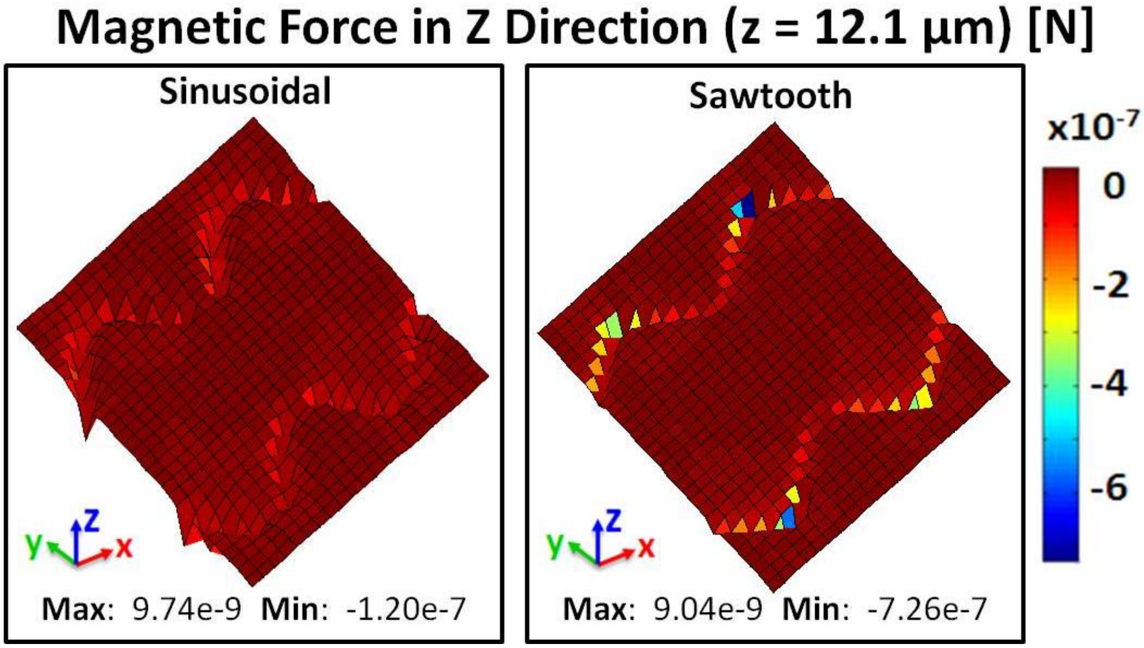

Figure 6.23: Magnetic force in the Z direction at z = 12.1 μm.

Although at a height of 12.1 μm from the substrate, the magnetic force in the x, y, and z direction is greater for the sawtooth design, this is not true for all heights, as can be seen in Figure 6.24. The magnetic force was calculated at various heights when the centre of the cell was closest to the maximum *B*-field, as can be seen in Figure 6.25. At a height greater than 18 *μm* the sinusoidal design exhibits a slightly larger magnetic force magnitude. However, at a height less than 18 *μm*, the sawtooth design exhibits a significantly larger magnetic force magnitude. This implies that the sinusoidal design will affect cells at a faster rate farther away from the permalloy in the *z*-direction. However, once the cells are within the trap region, the sawtooth design will exert a considerably larger magnetic force onto each cell.

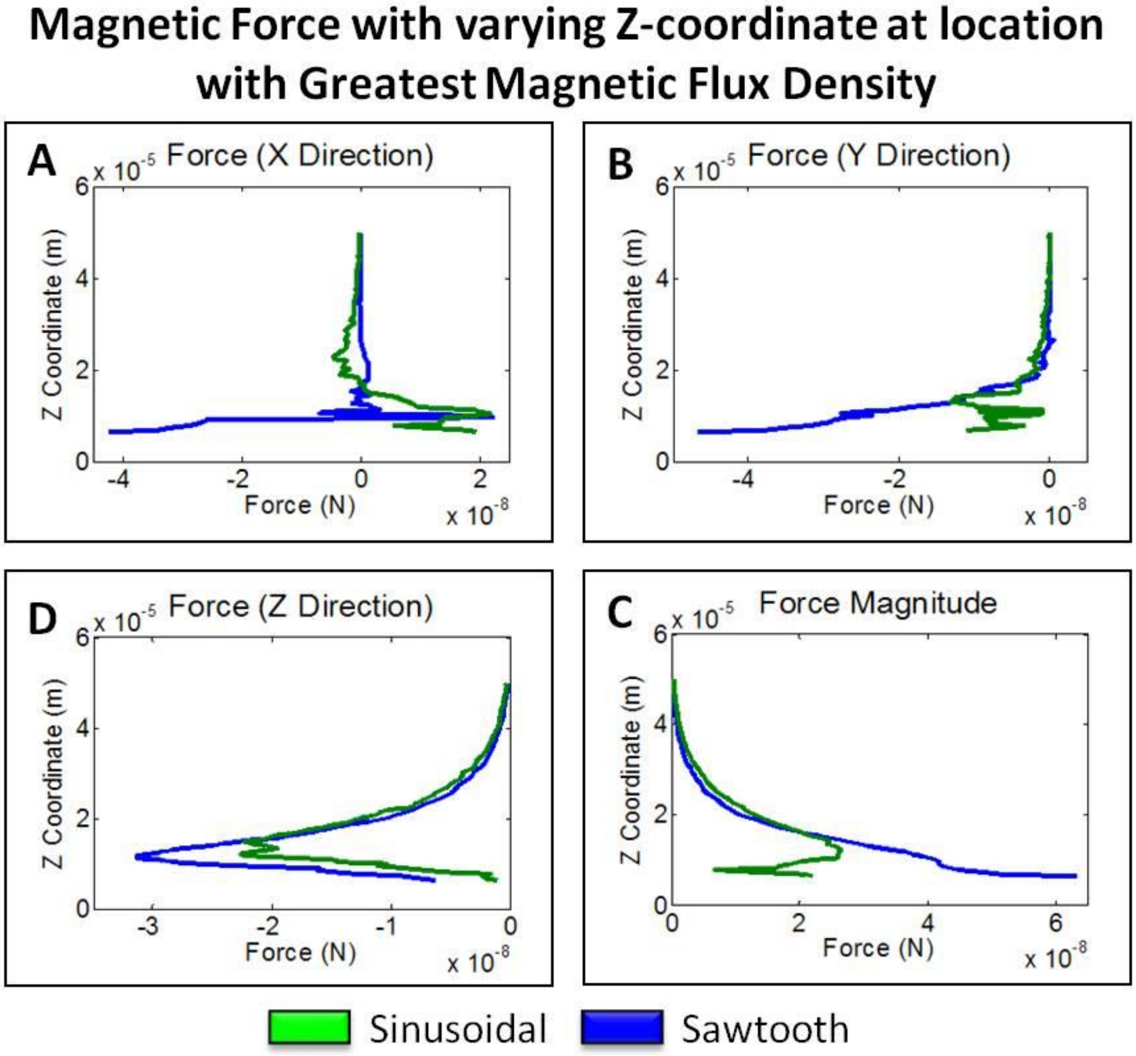

Figure 6.24: Magnetic force with varying z-coordinate at the location with greatest *B*-field. (A) X-direction, (B) Y-direction, (C) Z-direction and (D) total magnitude.

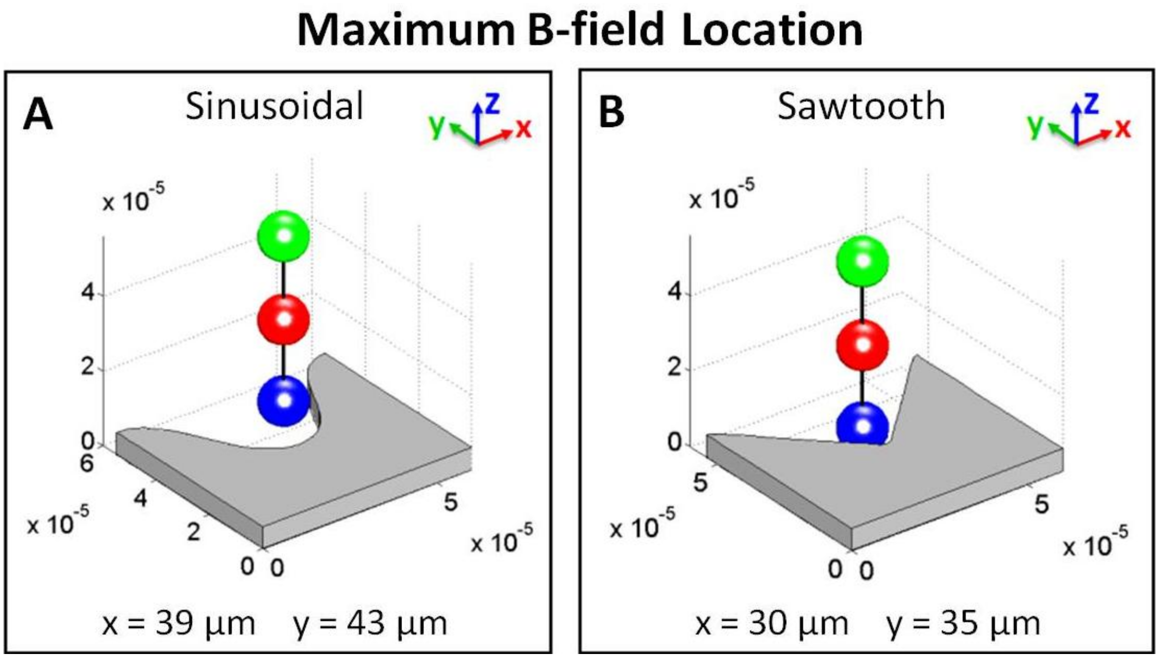

Figure 6.25: Maximum *B*-field location for (A) sinusoidal and (B) sawtooth.

Looking at all the forces exerted on the cell during the simulation, to draw cells into the traps, the dominant force needs to be the magnetic force. Figure 6.26 shows the force magnitude trends for a flow rate of 0 *mL/min* and 10 *mL/min* for both the sawtooth and sinusoidal designs. The dominating force for both flow rates and both designs is the magnetic force. This is promising, as it shows that the magnetized MSCMA is able to exert enough force on the MT cells to draw cells into traps even with a high flow rate. Since the fluid velocity was relatively low at the low cell heights used for the simulation (*z*-direction), the fluid velocity did not significantly affect the drag force. The drag force is mainly affected by the velocity of the cell relative to the fluid. The velocity of the cell is dominated by the magnetic force (as this is the dominant force). Therefore, the drag force followed the magnetic force closely. It is also seen that the buoyancy and gravitational force remain constant throughout the simulation and are only significant when the cell is at a distance greater than 50 μm.

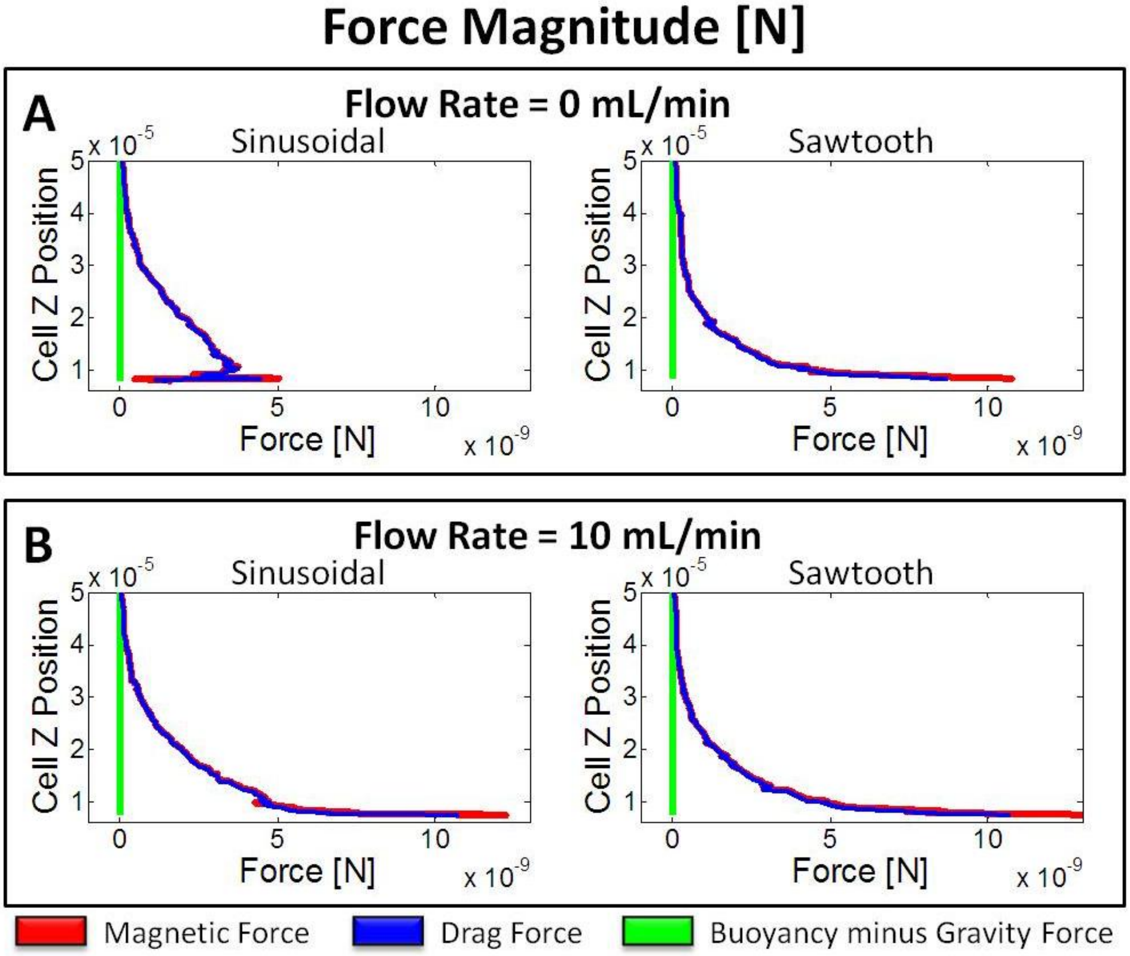

Figure 6.26: Force magnitude for the sinusoidal and sawtooth permalloy design for flow rate of (A) 0 *mL/min* and (B) 10 *mL/min*.

6.6 Simulation and FEM Results

The results from the FEM results and the predicted cell path simulation are used to optimize the CFS. This next section will outline the optimal CFS design and best experimental methodology.

6.6.1 Optimal CFS Design

To determine the best permalloy design, two main factors are considered, including the speed that the MSCMA is able to draw cells towards the trap, and the placement of cells in the traps. The sinusoidal design exhibits greater magnetic forces at a height greater than 18 μm from the substrate. Since the magnetic force is greater farther from the permalloy traps, MT cells will respond quicker to the sinusoidal trap compared to the sawtooth trap. This is also seen in the total time summarised in Table 6.13, where the total time is faster for the sinusoidal design for all flow rates.

Based on the cell path simulations, the sinusoidal design has the tendency to draw MT cells to three main locations, either side of the trap and to the centre of the trap. The sawtooth design on the other hand, only draws MT cells towards the centre of the trap. This implies that the sawtooth has a better chance of having a single cell in each trap. Although the sinusoidal design has the tendency to draw cells into the trap at a quicker rate, the overall time difference is not significant. The ability to draw a MT cells into the centre of the trap, and therefore increasing the probability of having a single cell per trap makes the sawtooth design preferable.

6.6.2 Optimal Experiment Methodology

There are two main methods that could be used for experimental testing: (i) deliver the cells over the traps, remove the cross flow to allow the cells to fall towards the traps due to gravity, then flush out any unwanted cells by applying the cross flow again, or (ii) apply a constant flow rate and allow the cells to become trapped by passing over the MSCMA.

Method (i) could increase the number of MT cells that can potentially become trapped since a greater percentage of cell will eventually settle towards the traps. However, this also increases the number of non-magnetically tagged (NMT) cells that could potentially become attached to the MSCMA chip. If the adhesion forces are high, a high flow rate would be needed to remove unwanted cells, which may also remove captured MT cells from the traps. The adhesion forces between the MSCMA and the cells are currently unknown and to minimize the number of NMT cells that become attached to the chip, method (ii) will be used.

Method (ii) can be optimized using the FEM models and this was done by considering several factors, including the effect of the cross flow on the cell path and the cell settling velocity. Since the magnetic force is negligible at a height greater than 50 *µm*, the only forces acting on both MT and NMT cell will be stokes drag, buoyancy force, and gravitational force. The cell will fall at a constant rate based on the settling velocity (U_s) (Equation 4.20) and this velocity will determine how quickly a cell will fall to a height of 50 *µm* from the MSCMA substrate. At this height the magnetic force will become dominant for MT cells, and will increase the rate that MT cells are falling, but NMT cells will continue to fall at the settling velocity. Using the constants found in Appendix D, a Jurkat cell that that is roughly 12 *µm* in diameter will have a settling velocity of 0.0047 *mm/s* (4.7 *µm/s*) (Equation 4.20).

The horizontal distance a cell will travel will depend on the settling velocity and the flow rate. Table 6.14 shows the horizontal distance a single cell will travel using different flow rates, assuming that the cell travels from a *z*-height of 1 *mm* to 50 *µm.* Using a settling velocity of 4.7*µm/s*, the time it takes a cell to fall a distance of 0.95 *mm* (1 *mm* to 50 *µm*) is approximately 202 *s*. In this time, the horizontal distance the cell will travel is estimated using the average flow velocity determined from the large scale fluid flow FEM model. A flow rate of 0.1 *mL/min* will cause the cells to travel a horizontal distance of 20.2 *mm*. Considering that the trap area is between 7.8 – 10.2 *mm* from the inlet, as can be seen in Figure 6.27, even a low flow rate of 0.1 *mL/min* will cause cells to overshoot the trap area.

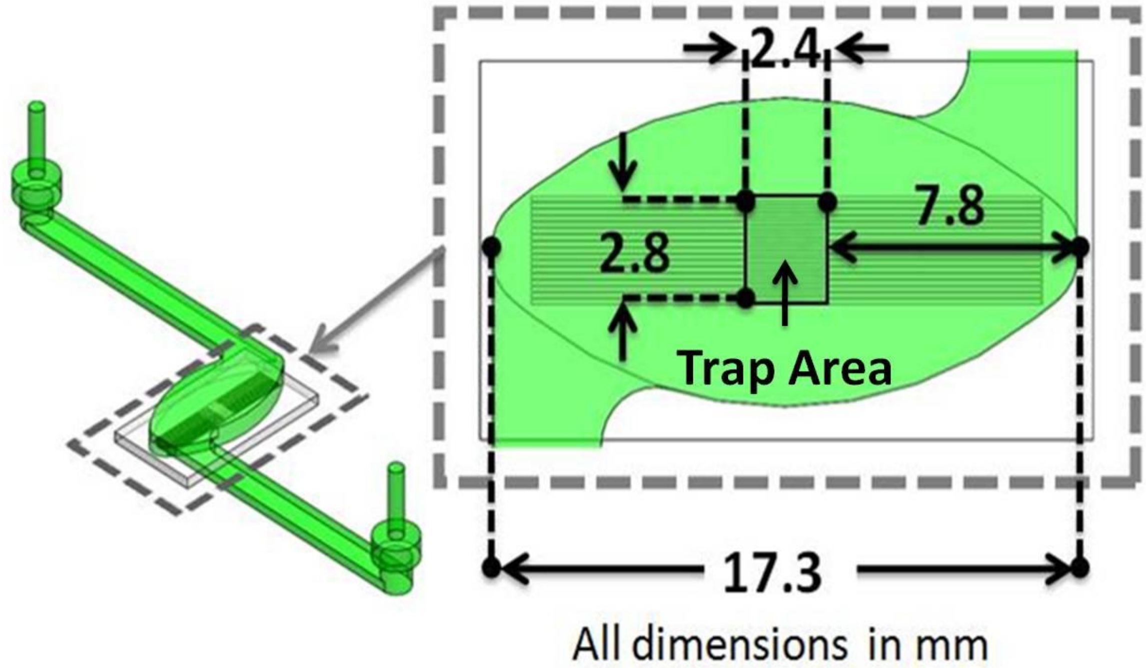

Figure 6.27: Flow over MSCMA with overall culture chamber dimensions and distance to traps.

Table 6.14: Horizontal distance a cell travels due to settling velocity.

Flow Rate [*mL/min*]	**0.01**	**0.10**	**1.00**	**10.0**
Average flow velocity (U_{avg}) [*mm/s*]	0.01	0.1	1	10
Time (t) to fall from a height (h) of 0.95 *mm* [*s*]	202 *s* = 3.4 min			
Horizontal distance (d) [*mm*]	2.02	20.2	202	2020

Note:
- The average flow velocity [*mm/s*] is approximately equal to the flow rate [*mL/min*] based on the large scale FEM model
- Time for cell to fall depends on the settling velocity $\boldsymbol{t = h/U_S}$
- Horizontal distance cell travels depends on average fluid velocity $\boldsymbol{d = U_{avg} \times t}$

The initial height of the cell over the MSCMA will be the main factor when determining an optimal flow rate. To determine the best flow rate, the flow rate was analyzed over a range of initial heights. The bottom culture chamber inlet is located 1 *mm* from the bottom of the culture chamber. A majority of the cells will then have an initial height between 1 to 2 *mm* (where 2 *mm* is the top of the chamber). Using these initial cell heights, the flow rate that would be needed to deposit a majority of the cells to the trap area was analyzed, as can be seen in Figure 6.28.

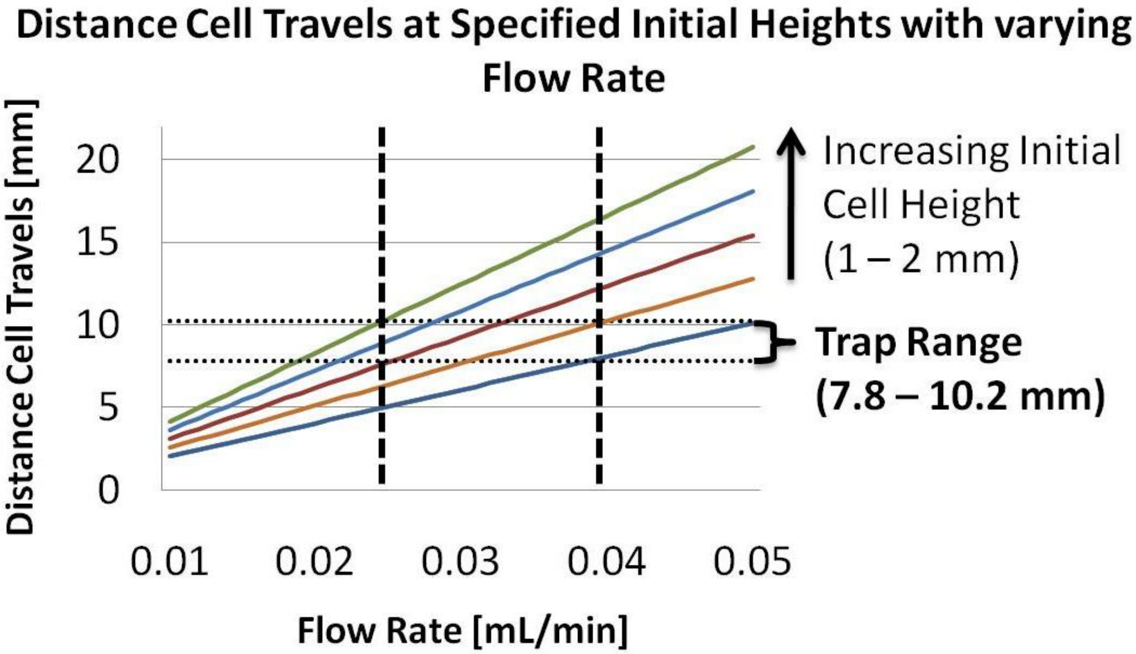

Figure 6.28: Distance cell travels at specified initial heights with varying flow rates

Since the trap area only covers 2.4 *mm*, it is not possible to have a single flow rate that can accommodate all initial cell heights, as can be seen in Figure 6.28. A flow rate of 0.025 *mL/min* will deposit cells starting from an initial height of 2 *mm* to the end of the traps (i.e. the farthest horizontal distance), whereas a flow rate of 0.04 *mL/min* is needed to deposit cells starting from an initial height of 1 *mm* to the beginning of the traps (i.e. the closest horizontal distance). The flow rate used to introduce MT cells into the culture chamber needs to deliver the MT cells to the trap area while also carrying the NMT cells towards the outlet. The adhesion force between the MSCMA surface and the cells are unknown, and if the NMT cells touch the chip they may attach permanently. Due to these two requirements, the lower (0.025 *mL/min*) and higher flow rate (0.04 *mL/min*) will be used initially in experimental testing to determine the best flow rate.

Along with the flow rate, another factor that will influence the capture rate is the concentration of cells. A high concentration will result in more cells passing over the trap area per unit volume. An increase in cells will increase the probability of MT cells being captured but also increases the number of NMT cells that become attached within the trap area. It is desirable to maximize the amount of MT cells that get trapped in cells, while minimizing the amount of NMT cells that become attached to the chip. Due to these two requirements, two cell concentrations, 10^4 *cells/mL* and 10^5 *cells/mL* will be used initially to determine the best cell concentration. The next chapter will outline the cross flow experiments conducted , which use the suggestions extracted from the FEM model and predicted cell path simulation discussed in this chapter.

Chapter 7: Cross Flow Experiment

A number of experiments are devised to determine the ability of the CFS to capture cells using various flow rates, various concentrations, and various ratios of MT cells to NMT cells. This chapter will discuss the experimental objective, procedure/setup and results of these tests.

7.1 Experimental Objective

All experiments conducted with the CFS have two main objectives. The first objective is to isolate and array single cells, motivated by the needs described in Chapter 1 and 2. The MSCMA chip with the sawtooth pattern is used for all experiments, since the analysis of Chapter 6 showed that they draw cells towards the centre of the chip. This will increase the probability of drawing single cells into each individual trap. The second objective is to capture rare cells from a heterogeneous population of cells. This is done to eliminate the need to process the cells to create a homogeneous population prior to arraying the cells. For a device to be classified as a rare cell detection device, it is generally considered to be capable of capturing rare cells that have a ratio less than 1 to 10^6 (MT Cells to NMT Cells) [97,98,99].

7.2 Experimental Setup and Procedure

To accurately compare all tests results, the same experimental setup and procedure is used. The tests are analyzed using images that are taken after each experiment. These images are captured using a camera integrated into a brightfield microscope that displays the images on a computer, as can be seen in Figure 7.1. The CFS was originally designed for integration with the RoboSCell system, which uses a

DIC microscope setup. However, it was found that the DIC Setup was not adequate for experimental verification of the CFS performance. This next section will discuss the reasons for using a brightfield microscope setup and the experimental setup/procedure used for experiments conducted with the brightfield microscope.

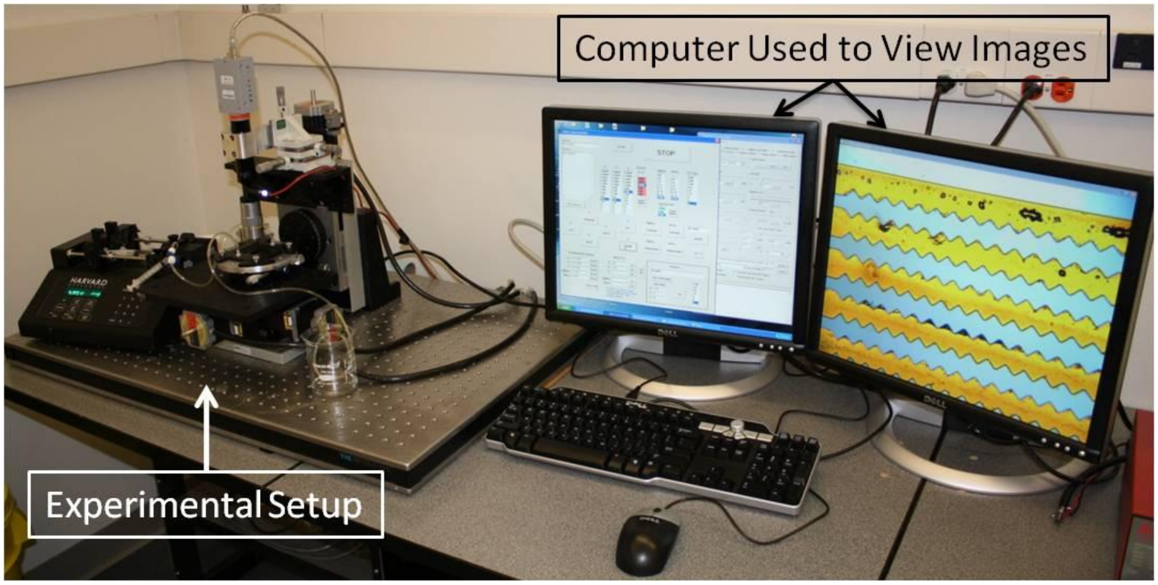

Figure 7.1: Experimental setup and computer used to view and extract images.

7.2.1 DIC versus Brightfield Setup

One of the initial design requirements for the CFS was to integrate the device with the RoboSCell system (requirement 12 in section 5.1). This limited the overall size of the CFS to physically fit within the system. It also defined the culture chamber size and dimensions, due to the occlusion of light at the edge of the culture chamber (parameter *x* shown in Figure 5.1). This also defined the overall design and materials used. In an inverted DIC microscope system, light passes through a transparent sample. The light source first passes through the condenser that is above the sample, then through the sample, then through the objective that is below the sample and finally onto the charge-coupled device (CCD) sensor. The CFS was designed to allow light to pass through the MSCMA, and this required that anything above or below the trap area to be transparent.

Preliminary experiments were conducted using the RoboSCell system as shown in Figure 7.2 (A), and images of cells using the DIC microscope can be seen in Figure 7.2 (B). Although the CFS was successfully integrated with the RoboSCell setup, cells could only be viewed when they are between the permalloy strips. This is shown in Figure 7.2 (B), where the black areas show the permalloy strips, the grey areas show the transparent glass substrate between the permalloy strips, and the shiny circles are the cells. Any cells that were on top of the permalloy (black regions) cannot be viewed using this setup.

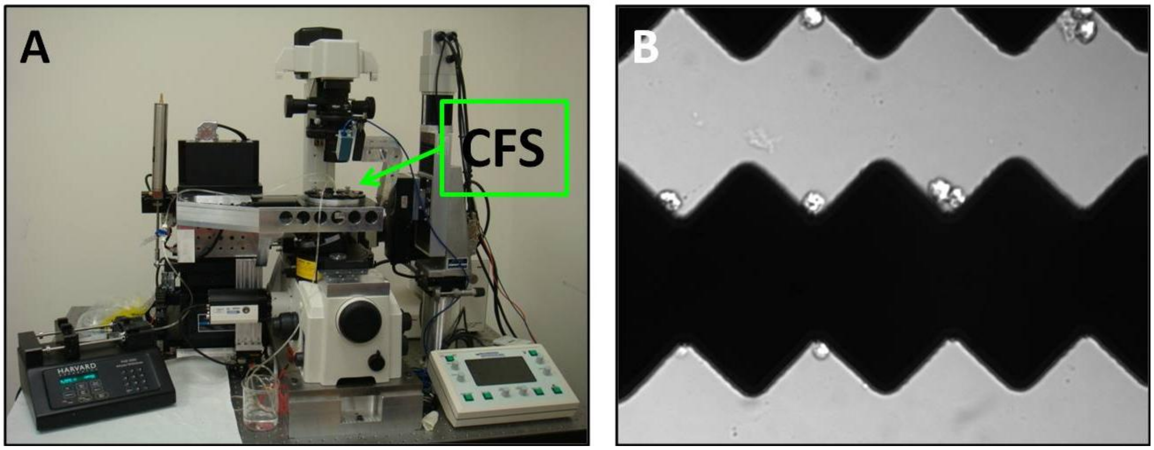

Figure 7.2: (A) RoboSCell Setup. (B) Cells viewed using DIC setup, where the black areas are the permalloy strips, and the shiny circles are cells.

The DIC microscope could be used to distinguish between MT cells and NMT cells using fluorescent dyes when conducting rare cell experiments. This can be seen in Figure 7.3, which shows a mixed population of MT cells and NMT cells, where the MT cells are also fluorescently dyed. The left image shows all the cells and the right image shows the same field of view, with only the cells that are fluorescently tagged (i.e. the MT cells only). These images show that the DIC microscope on the RoboSCell system worked well to distinguish fluorescently dyed MT cells from non-dyed NMT cells.

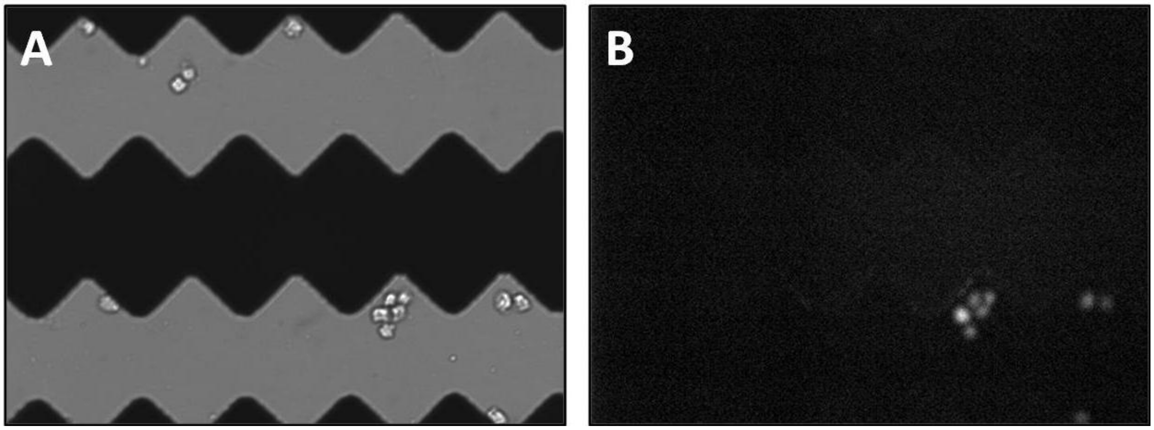

Figure 7.3: (A) Mixed population of cells viewed using the DIC setup. (B) Same image as (A), but only showing the fluorescently tagged cells.

One main goal of the CFS is to sort rare cells from a heterogeneous population. Since cells are free to flow over the entire chip, they are able to flow over both the glass substrate and the permalloy strips. To conduct this research, it is necessary to view the entire chip when analyzing the images, to account for all cells landing in all possible locations. This becomes very important when quantifying the devices ability to capture rare cells, as it is necessary to know if any unwanted cells are also being trapped. When NMT cells are flowed over the MSCMA, they land randomly on the chip and this means that some cells will land on top of the permalloy. As will be shown in section 7.4, it was not possible to remove all NMT cells from the chip. The ability of the brightfield setup to view the entire chip, including areas above the permalloy strips is a necessary advantage for all tests. Although the brightfield setup does not have the ability to view fluorescently tagged cells, it will be shown in section 7.5 that cells can be dyed to visually distinguish between MT and NMT cells. All future tests in this chapter are therefore conducted using the brightfield setup.

7.2.2 Brightfield Experimental Setup

The brightfield experimental setup can be seen in Figure 7.4 and consists of a syringe pump, the CFS, 3-way stopcock, 2 syringes, tubing, and a waste container. A 5 *mL* syringe is used in the syringe pump to flow medium through the CFS. The syringe is attached to a 3-way stopcock using 15 *cm* of tubing. The 3-way stopcock is used to control the origin of the flow with one port attached to the 5 *mL* medium syringe, the second port attached to a 3 *mL* syringe, which contains the cells, and the last port leads to the CFS via 25 *cm* of tubing. Changing the valve on the 3-way stopcock allows for either the medium to flow to the CFS via the syringe pump or it allows cells to be manually deposited towards the CFS. Once the fluid flows through the CFS, it exits via the outlet into the waste container.

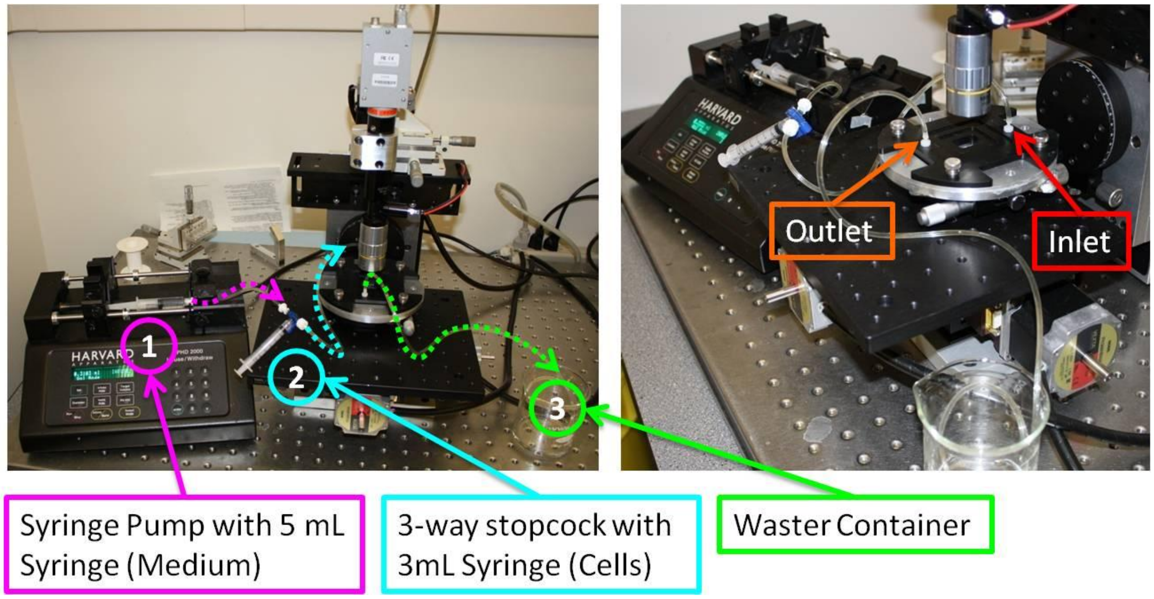

Figure 7.4: Experiment setup using a brightfield microscope. Dotted lines show the tubing and the direction of flow in the tubing. (1) A 5 *mL* syringe contains the medium, which is introduced into the CFS using the syringe pump. (2) The medium goes through tubing and a 3-way stopcock that also has a 3 *mL* syringe, which contain the cells and the cells/medium enter the CFS via the inlet. (3) Fluid exits out of the CFS via the outlet into the waste container.

7.2.3 Experimental Procedure

Each experimental set uses the same setup (lines, gasket, syringes, and MSCMA chip) with each set lasting a single day of testing (3 to 9 hours). The experimental procedure followed for all experiments is as follows:

1. Assemble the CFS by inserting the MSCMA, gasket assembly, magnets, magnet cover, and top plate into the base.
2. Install all fittings and tubing to the CFS as shown in Figure 7.4.
3. Secure the base to the microscope stage.
4. Using the 5 *mL* syringe, fill it with phosphate buffer solution (PBS) and tap the syringe to remove all bubbles and install it into the syringe pump.
5. Dilute cells to appropriate cell concentrations.
6. Using the 3 *mL* syringe, fill it with 1.0 *mL* of cell solution and tap the syringe to remove all bubbles and attach it to the 3-way stopcock.
7. Open the 3-way stopcock towards the 3 *mL* syringe (cell inlet) and saturate the 3-way stopcock, but do not deposit cells at this point.
8. Open the 3-way stopcock towards the 5 *mL* syringe (medium inlet) to saturate all lines using the syringe pump at a flow rate of 1.0 *mL/min*.
9. Turn the 3-way stopcock to allow for cell loading and manually deposit the cell solution towards the CFS.
10. Turn on the medium inlet by adjusting the 3-way stopcock valve. Turn on the syringe pump to specified flow-rate to run for a total volume of 1 *mL*.
11. Collect images of the entire chip for future analysis.

7.2.4 Post-Experimental Procedure

Steps 1 through 11 outlines the experimental procedure used for each test. After a single experiment is completed, the device is flushed and prepared for the next experiment using the following steps:

1. Empty lines using a large 25 *mL* syringe.
2. Flush distilled water through the device.
3. Cycle the distilled water over the chip to remove all cells and repeat several times.
4. Flush more distilled water through the device and empty all lines.

7.2.5 Cleaning Procedure

To minimize the number of chips and gaskets needed, everything is cleaned after each experimental set using the following procedure

1. Remove the lines (including the 3-way stopcock), syringes and barbed fitting attached to the top plate and dispose of them.
2. Remove the top plate and disassemble the gasket assembly and dispose of the glass cover slip.
3. Rinse the culture chamber and square gasket with distilled water.
4. Remove and clean the MSCMA chip by soaking it in a 1/500 concentration of Decon detergent for a minimum of 1 hour. Rinse the items with distilled water 4 times, then soak with ethanol for approximately 15 minutes and let the chip air dry.

7.2.6 Cell Preparation

All experiments are conducted using either fixed or live Jurkat cells. Fixed cells are previously live cells, which have been preserved in formaldehyde. They still retain the physical characteristics of live cells but they do not require nutrients and do not need to be kept at the optimal cell temperature, which is 35ºC for Jurkat cells. Each experiment uses either MT cells or NMT cells and cells can only be magnetically tagged if they are live. Cells are immunomagnetically labelled using an EasySep Human CD3+ Positive Selection Kit. This process involves the following steps [100]:

1. Starting with live cells, mix the cells with EasySep positive selection cocktail at 50 μL for every 1 mL of cells. Mix well and incubate at room temperature (15 – 25 ˚C) for 15 minutes.
2. Then add EasySep Magnetic Nanoparticles at 50 μL for every 1 mL of cells. Mix well and incubate at room temperature (15 – 25 ºC) for 10 minutes.
3. Bring the cell suspension to a total volume of 5 mL and gently mix the cells.
4. Place the tube into the magnet and let sit for 5 minutes.
5. Pick up the magnet and pour off the liquid in the tube. The MT cells will be attached to the side of the tube.
6. Repeat steps 4 – 5 several times (3 or 4 times).
7. Remove the tube from the magnet and re-suspend the cells in the appropriate volume and medium.
8. Formaldehyde is added at this point if fixed cells are desired.

7.2.7 Methods to Analyze Experimental Results

Images are taken of the MSCMA chip after each experiment. These images are used to determine the experimental results of each test. This section will discuss the methods used to analyze experimental results. This includes analyzing the images once experiments have been completed and the terminology used to quantify the efficiency of each test. For clarification, when referring to the “entire trap area”, this refers to all 16 permalloy lines, and therefore, all 1280 traps. However, when referring to a “trap region”, this refers only to one specific trap. These two definitions are further defined in Appendix F.

7.2.7.1 Image Analysis

All tests are analyzed using images taken of the entire trap area. Each image is visually analyzed and cells are classified as being on one of the following areas: on top of the permalloy, between the permalloy and in a trap region. Figure 7.5 (A) shows the three different regions where the cells could land, and Figure 7.5 (B) shows a sample of the cell count analysis that was performed for all results shown. For this particular image, it was found that 13 cells were on the permalloy, 4 cells in the traps region, and 3 cells between the permalloy. When counting cells found in the trap region, they are counted as being either a single cell, 2 cells or 3+ cells. When counting the cells seen, anything that looked misshapen (i.e. not spherical) or too small is not counted as a cell.

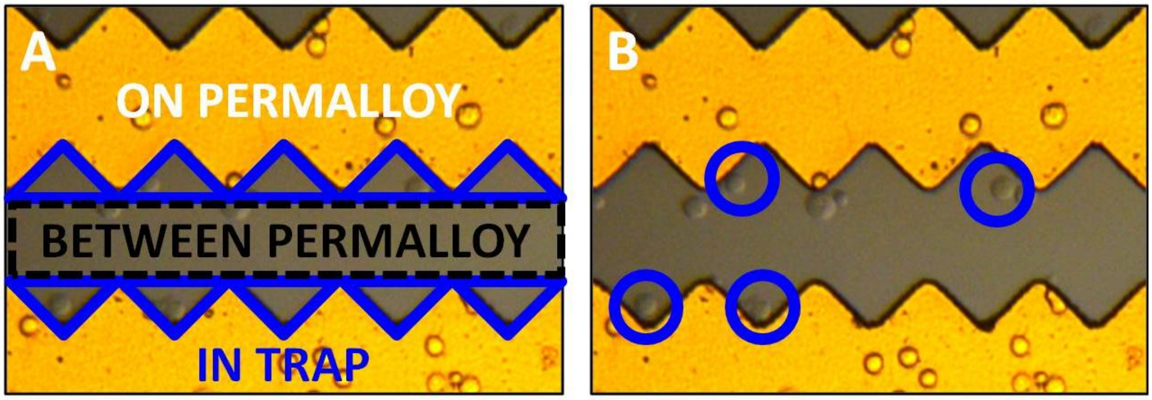

Figure 7.5: (A) Cells that were imaged were categorized as being on the permalloy, between the permalloy, or in traps. (B) This image shows a sample of the images used to analyze the device where the blue circles show cells that are considered to be in traps. The total cell count results in 13 cells on the permalloy, 4 cells in a trap, and 3 cells between the permalloy.

7.2.7.2 Efficiency Analysis

When analyzing images, two efficiencies are used to determine the success of each test. The first efficiency is the cell capture efficiency (CE%) and it can be quantified as follows:

$$\boldsymbol{NMT - CE\% = \frac{Number\ of\ NMT\ Cells\ Captured}{Cell\ Concentration\ \times Volume} \times 100} \tag{7.1}$$

$$\boldsymbol{MT - CE\% = \frac{Number\ of\ MT\ Cells\ in\ a\ Trap}{Cell\ Concentration\ \times Volume} \times 100} \tag{7.2}$$

This efficiency can be used for both NMT and MT cells, but will differ for each type of cell. For NMT cells, it shows the number of NMT cells found on the chip compared to the total number of NMT cells used. For MT cells, it shows the number of MT cells that were found in the trap region compared to the total number of MT cells used. For an ideal case, the NMT-CE% should be close to 0% and the MT-CE% should be close to 100%. This means that there are no NMT cells found on the chip but all the MT cells were captured in a trap region.

It is also important to know the ratio of cells captured in the traps region vs. the total number of traps, since one of the design objectives is to capture and isolate single cells. To quantify this, another efficiency used to analyze MT cells is a trapping efficiency (TE%) and single cell trapping efficiency (SCTE%) as follows:

$$\boldsymbol{TE\% = \frac{\#\ Traps\ with\ Cells}{Total\ Number\ of\ Traps} \times 100} \tag{7.3}$$

$$\boldsymbol{SCTE\% = \frac{\#\ Traps\ with\ a\ single\ cell}{Total\ Number\ of\ Traps} \times 100} \tag{7.4}$$

For these two efficiencies, an ideal experiment will have high TE% and SCTE%, and this means that a majority of the traps contained cells, but more importantly, that a majority of traps contained a single cell. To maximize the number of single cells that are captured an ideal case would also have the TE% equal the SCTE%.

7.3 Establishment of Experimental Parameters

To establish the experimental parameters for fluid flow rate and cell concentration, a series of parameter experiments are conducted. Using the values obtained from the predicted cell path simulation two flow rates (0.025 *mL/min* and 0.04 *mL/min*) and two concentrations (10^4 *cells/mL* and 10^5 *cells/mL*) are used. Each test is completed three times using 1.0 *mL* of cells and the results are averaged and are shown in Figure 7.6 and Figure 7.7. The summary and efficiency of each test is also shown in Table 7.1 and Table 7.2.

Both the NMT and MT cells showed similar trends. Increasing the concentration and increasing the flow rate results in an increase in cells, as can be seen in Figure 7.6. It also results in an increase in single MT cells being captured, as can be seen in Figure 7.7. Increasing the concentration results in more cells passing over the chip for any given flow rate. This is seen for both the MT and NMT cells where increasing the cell concentration increased the number of cells found on the chip. Increasing the flow rate also increased the number of cells found on the chip. This trend is not as expected, as it was expected that a higher flow rate would carry a majority of the cells away from the trap area. A reason for this trend is that the fluid velocity through the culture chamber might be lower than predicted. The lower flow rate of 0.025 *mL/min* may not actually be fast enough to deliver sufficient numbers of cells to the trap area.

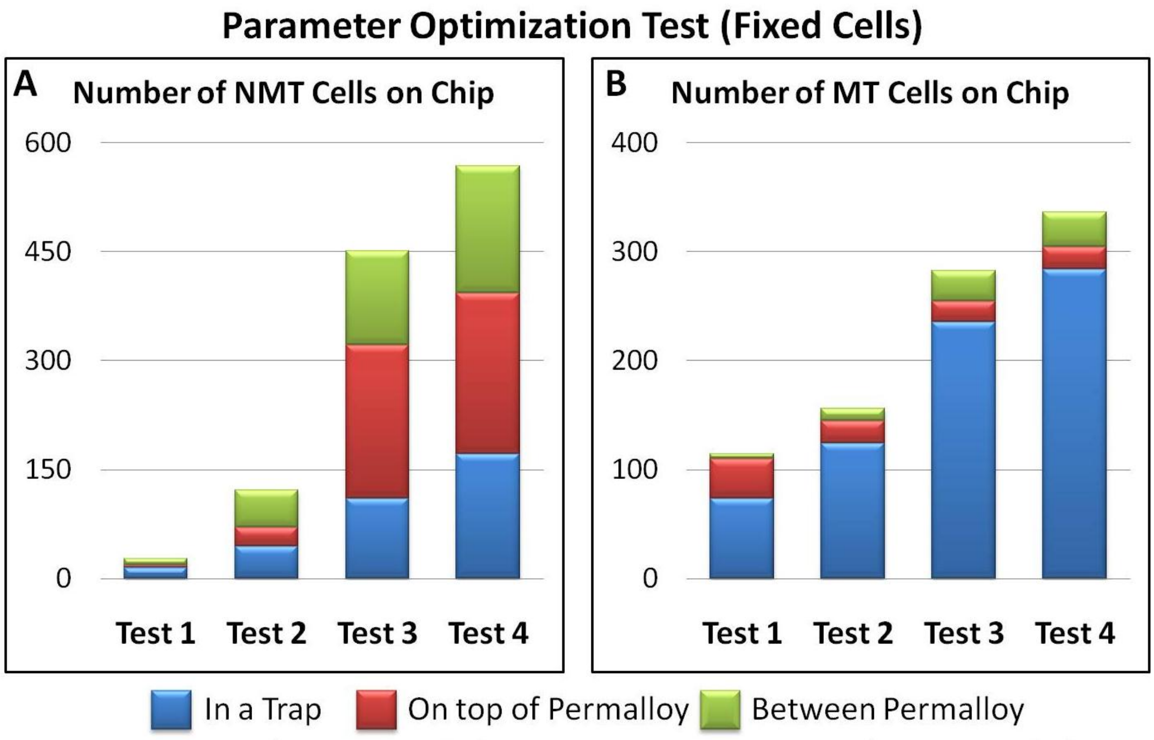

Test 1: 0.025 mL/min, 1e4 cells/mL
Test 2: 0.04 mL/min, 1e4 cells/mL
Test 3: 0.025 mL/min, 1e5cells/mL
Test 4: 0.04 mL/min, 1e5 cells/mL

Figure 7.6: Parameter establishment results using two flow rates and two concentrations. The graph shows the number of cells found on the permalloy, in a trap, or between the permalloy for (A) NMT Cells only and (B) MT cells only.

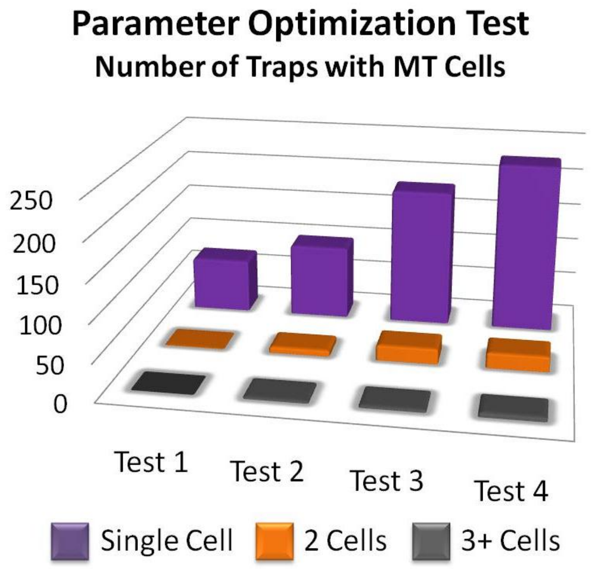

Test 1: 0.025 mL/min, 1e4 cells/mL
Test 2: 0.04 mL/min, 1e4 cells/mL
Test 3: 0.025 mL/min, 1e5cells/mL
Test 4: 0.04 mL/min, 1e5 cells/mL

Figure 7.7: Parameter establishment results with the number of traps with MT cells.

The results for the parameter establishment can be seen in Table 7.1, and the efficiency analysis can be seen in Table 7.2. The NMT - CE%, MT - CE%, TE% and SCTE% all tend to increases with increasing flow rates and increasing cell concentrations. The MT - CE% and TE% can be increased by increasing the number of cells that pass over the MSCMA chip. This can be done by either increasing the volume or concentration of cells used. A drawback to increasing both the volume and the concentration is that this will also result in an increase in the number of NMT cells that will become attached to the chip. The next section will look at methods to minimize the number of NMT cells that become attached to the chip.

Table 7.1: Parameter establishment test summary.

Parameter	**Test 1**	**Test 2**	**Test 3**	**Test 4**
Flow Rate [*mL/min*]	0.025	0.04	0.025	0.04
Concentration [*cells/mL*]	10^4	10^4	10^5	10^5
Number of NMT Cells	28	122	451	567
Number of MT Cells in Trap Region	74	124	236	284
Number of Traps with MT Cells	73	110	208	253
Number of Traps with a Single MT Cell	72	99	184	227

Table 7.2: Efficiency analysis for parameter establishment test.

Parameter	**Test 1**	**Test 2**	**Test 3**	**Test 4**
NMT - CE%	0.028 %	0.12 %	0.45 %	0.57 %
MT - CE%	0.074%	0.124%	0.2355 %	0.284 %
MT Cell TE%	5.70 %	8.59 %	16.25 %	19.73 %
MT Cell SCTE%	5.63 %	7.73 %	14.38 %	17.70 %

7.4 Methods to Minimize Non-magnetically Tagged Cells

The two flow rates tested are shown to successfully deliver cells to the entire trap area, with the higher flow rate being more successful. Although MT cells are successfully captured many NMT cells are also becoming attached to the MSCMA chip. To minimize the number of NMT cells that become attached to the MSCMA chip two methods are tested. The first method involves increasing the flow rate used to deliver the cells to the trap region. The second method uses a lower flow rate to deliver the cells to the trap region and then a higher flow rate is applied to remove unwanted cells.

7.4.1 High Initial Flow Rate Test

The first method tested to minimize the number of NMT cells that become attached to the chip is increasing the initial flow rate used to deposit cells to the trap region. A higher flow rate of 1.0 *mL/min* is used to deposit 1.0 *mL* of cells with a concentration of 10^5 *cells/mL*. These cells are completed with only one type of cell (all MT cells or all NMT cells). Each test is completed twice and the results are averaged and are shown in Figure 7.8, Table 7.3 and Table 7.4.

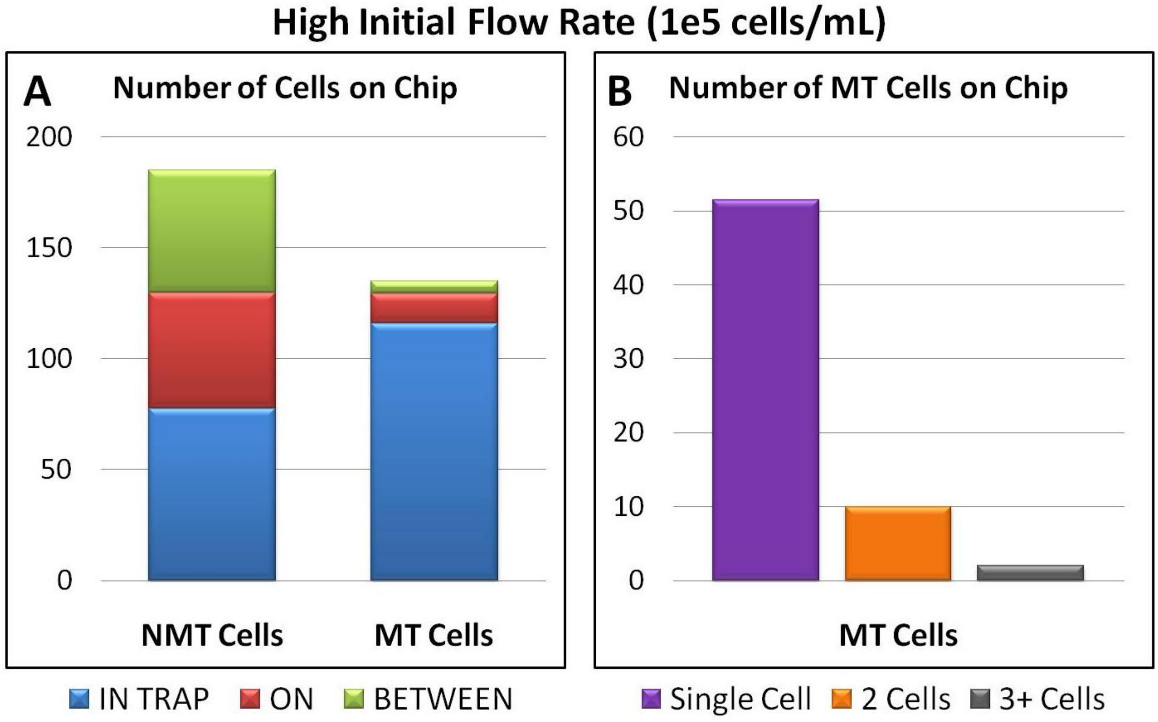

Figure 7.8: High initial flow rate tests using both MT and NMT cells. (A) Number of cells on chip. (B) Number of traps with MT cells.

Increasing the flow rate drastically decreases the number of NMT cells that are found on the chip, but this also reduces the number of MT cells that are captured. It is found that when using a higher flow rate the NMT - CE% is 0.19%. Although this is very promising, using a higher flow rate also results in a lower MT - CE% (0.12%), TE% (4.96%), and SCTE% (4.02%). This shows that increasing the flow rate to 1.0 *mL/min* or beyond is not a viable solution, as it drastically reduces the number of MT cells that are captured. Perhaps there is some intermediate value between the 0.04 *mL/min* used and the 1.0 *mL/min* value, where this approach may work.

Table 7.3: High initial flow rate test summary.

Parameter	High Flow Rate Test
Flow Rate [*mL/min*]	1
Concentration [*cells/mL*]	10^5
Number of NMT Cells	185
Number of MT Cells in Trap Region	116
Number of Traps with MT Cells	64
Number of Traps with a Single MT Cell	52

Table 7.4: Efficiency analysis for high initial flow rate test.

Parameter	High Flow Rate Test
NMT - CE%	0.19 %
MT - CE%	0.12 %
MT Cell TE%	4.96 %
MT Cell SCTE%	4.02 %

7.4.2 Cell Removal Tests

A second method was tested to attempt to minimize the number of NMT cells attaching to the chip. This was done by applying a higher flow rate at the end of the cell capture experiment. For these tests an initial flow rate of 0.04 *mL/min* is used to deliver the cells to the trap region for 25 minutes (which results in a volume of 1 *mL* of fluid passing over the chip). Once the cells are successfully delivered to the trap region, two additional high flow rates are applied to the chip: 1.0 *mL/min* for 10 minutes and 2.5 *mL/min* for 5 minutes (which results in an additional 20 *mL* of fluid passing over the chip). The cell removal tests are performed twice using only fixed NMT cells or only fixed MT cells. The result for the both the MT and NMT cell tests are averaged and are shown in Figure 7.9, Figure 7.10, Table 7.5, and Table 7.6.

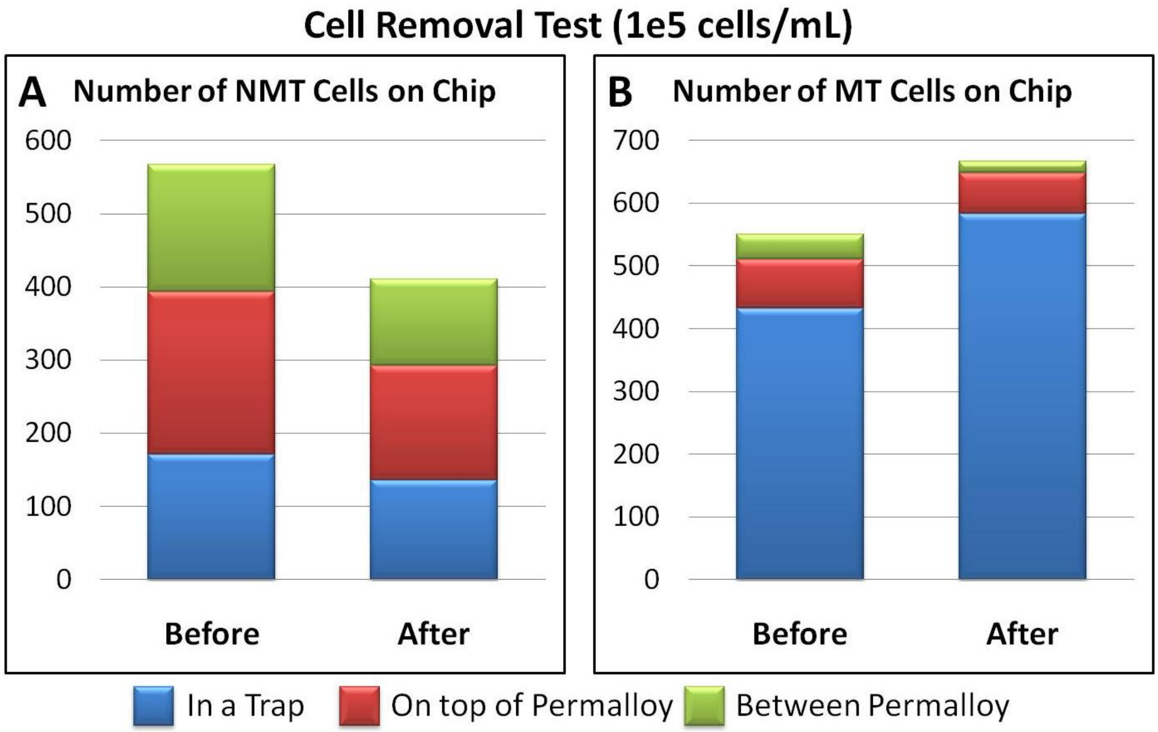

Figure 7.9: Number of cells on the chip for the cell removal test for (A) NMT and (B) MT cells using different flow rates to remove cells.

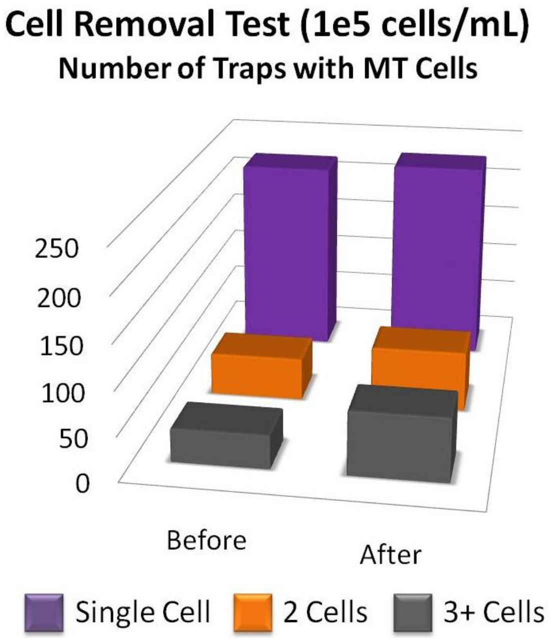

Figure 7.10: Cell removal tests showing the number of traps with a single cell, 2 cells, or 3+ cells before and after the cell removal test.

As the flow rate is increased, the NMT - CE% reduced from 0.57% to 0.41%. This shows that it is possible to remove some unwanted cells but not all of them. Most of the cells that are removed are either on the permalloy, or between the permalloy traps. The MT cell CE% increases from 0.55% to 0.67% and the total TE% increases from 24.10% to 28.98%. Also, the majority of MT cells that have been captured are not removed from their traps after the cell removal test. This is shown by the number of MT cells found in the traps increases after the cell removal test.

Table 7.5: Cell removal test summary.

Parameter	Before Cell Removal Test	After Cell Removal Test
Flow Rate [*mL/min*]	0.04	0.04
Concentration [*cells/mL*]	10^5	10^5
Number of NMT Cells	567	411
Number of MT Cells in Trap Region	433	40
Number of Traps with MT Cells	309	371
Number of Traps with a Single MT Cell	222	231

Table 7.6: Efficiency analysis for cell removal test.

Parameter	Before Cell Removal Test	After Cell Removal Test
NMT Cell CE%	0.57 %	0.41 %
MT Cell CE%	0.43 %	0.58 %
MT Cell TE%	24.10 %	28.98 %
MT Cell SCTE%	17.34 %	18.01 %

The distribution of MT cells after the cell removal test is shown in Figure 7.11, and the difference in traps is shown in Figure 7.12. These images show that a majority of the MT cells that are captured are not removed, and additional MT cells are captured when the higher flow rate is applied. For both tests the cells are randomly distributed throughout the trap region with a higher concentration of cells located towards the outer region of the entire trap area. This is to be expected since these traps are the closest to the magnet and they will exhibit the greatest *B*-field. A higher *B*-field will result in these traps exerting a higher magnetic force on a MT cell. The majority of MT cells that are captured before applying a higher flow rate are not removed, as can be seen in Figure

7.12. Originally there are 309 traps with MT cells, 53 of these traps have cells removed after applying a higher flow rate (17.2% of the original traps), and an additional 115 traps capture cells (37.2% of the original traps). This shows that there is a net benefit in performing the cell removal tests.

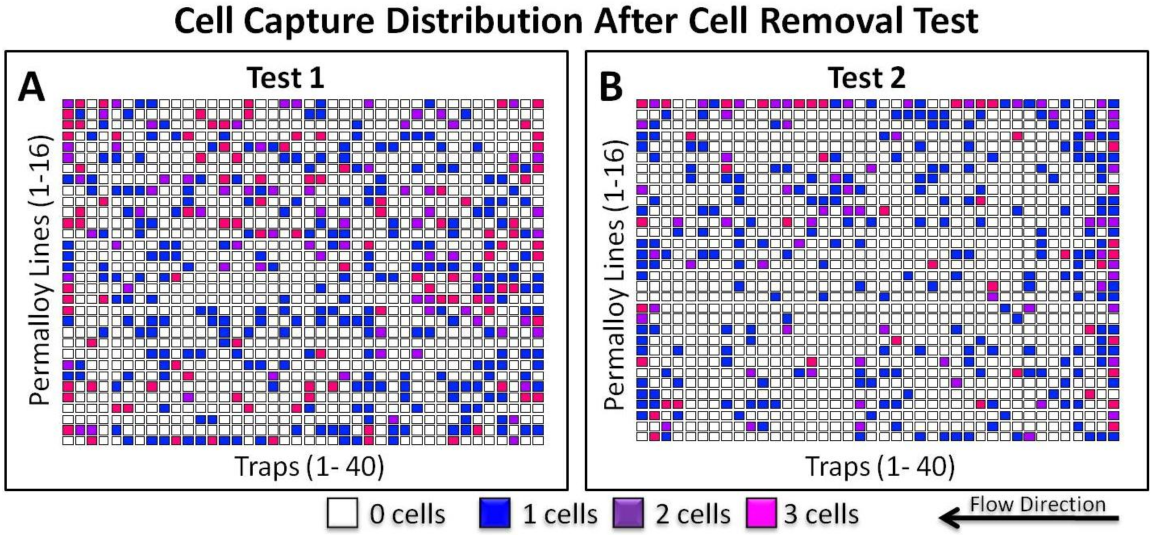

Figure 7.11: Distribution of captured MT cells before and after cell removal test for (A) Test 1 and (B) Test 2.

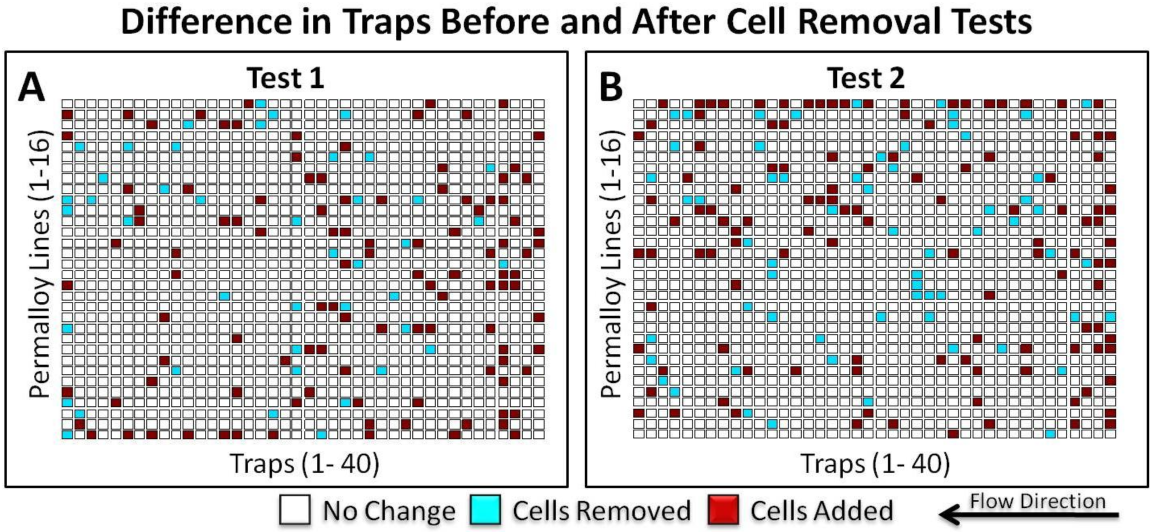

Figure 7.12: Traps that either had cells removed or added after cell removal tests for (A) Test 1 and (B) Test 2.

Table 7.7: Change in traps after cell removal tests shown in Figure 7.11.

Parameter	Test 1	Test 2	Average
Original Number of Traps	353	264	309
Number of Traps with MT Cells Removed	43	62	53
Number of Traps with MT Cells Added	110	120	115
Final Number of Traps with MT Cells	420	322	371

Of the two methods tested to remove NMT cells from attaching to the chip, the cell removal test was the most successful. This test was capable of removing 27.5% (156) NMT cells while 82.8% (256) of the occupied traps are unchanged and there was an increase in captured cells with a 37.2% (115) increase. Therefore, based upon the parameter establishment tests, and also the cell removal tests, all subsequent experiments described in this thesis have been conducted using the following methods:

- Perform steps 1 through 11 described in section 7.2.3.
- Apply a flow rate of 1 *mL/min* for a total of 10 minutes (total volume of 10 *mL*).
- Apply a flow rate of 2.5 *mL/min* for a total of 5 minutes (total volume of 10 *mL*).

7.5 Rare Cell Experiments

Rare cell detection experiments are conducted with the objective being to separate rare cells from a heterogeneous population of cells that contain both MT and NMT cells. These experiments are conducted using both fixed and live cells using the procedure outlined in sections 7.2.3 (experimental procedure) and section 7.4.2 (cell removal test procedure). Each test uses 1 *mL* of cells with a cell concentration of 10^5 *cells/mL*. A total of five experiments are completed using the following ratios of MT to NMT cells: 1 to 0 (only MT cells), 1 to 1, 1 to 10, 1 to 100, and 1 to 1000, as summarised in Table 7.8.

Table 7.8: Rare cell experiment parameters assuming a total cell concentration of 10^5 *cells/mL*.

Test	Ratio (MT:NMT Cells)	MT Volume [*mL*]	# MT Cells	NMT Volume [*mL*]	# NMT Cells
1	1:0	1	100,000	0	0
2	1:1	0.5	50,000	0.5	50,000
3	1:10	0.1	10,000	1	100,000
4	1:100	0.01	1,000	1	100,000
5	1:1000	0.001	100	1	100,000

7.5.1 Rare Cell Experiment Counting Procedure

Since the rare cell experiments will use a heterogeneous mix of MT and NMT cells, it is important to know which cells are which. MT and NMT cells appear visually identical, therefore an additional method is needed to 'visually mark' the cells. This is done by staining the MT cells so that they can be visually distinguished from the NMT cells using a brightfield microscope. Using a reflective (i.e. not transmissive) brightfield microscope also allows the top of the permalloy to be viewed. This is important feature of reflected brightfield microscopy, since many NMT cells land on top of the opaque permalloy.

Rare cell experiments are conducted with both fixed and live cells. The fixed MT cells dyed blue using trypan blue and the live MT cells are dyed with rhodamine b isocyanate. When using the fixed cells, the contrast between stained MT and un-stained NMT cells was always very visible and reliable, as shown in Figure 7.13 A. However, when using live cells, the contrast between the stained MT cells and un-stained NMT cells was not clearly visible, as shown in Figure 7.13 B, and tended to change based on the cell health and time.

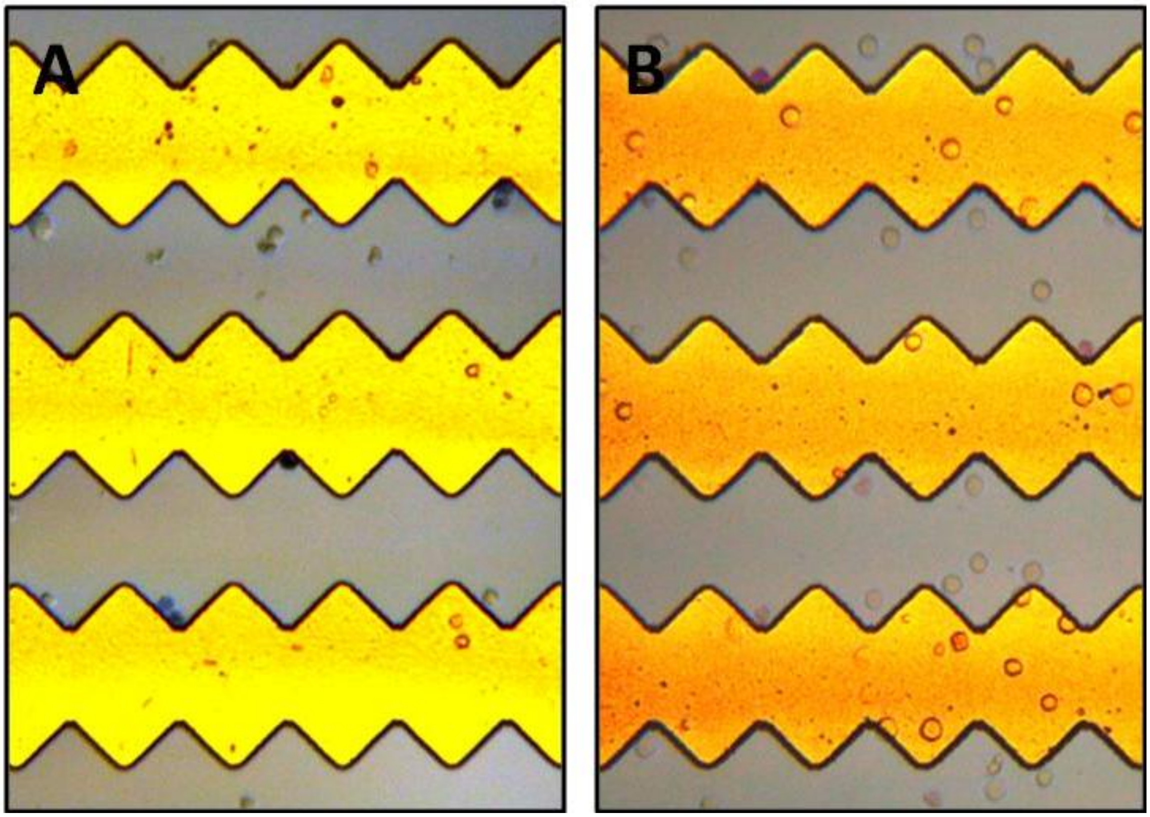

Figure 7.13: Heterogeneous population of cells showing the contrast between MT and NMT cells. (A) Fixed NMT cells were dyed using Trypan Blue

For the live rare cell experiments, the first experiments were performed with only MT cells. It was found that the majority of MT cells captured are found at the centre of the trap, touching the permalloy, as shown in Figure 7.14 A. When NMT cells are put through the CFS, they landed randomly on the chip and when they happened to land in traps, they are rarely seen at the centre of the trap touching the permalloy, as shown in Figure 7.14 B. Using this observation, when analyzing the images for the rare cell experiments, it is always assumed that if a cell showed a pink hue it was MT. It is also assumed that if a cell is not pink, but is found in the centre of the trap flush against the permalloy it is also a MT cell, as shown in Figure 7.15. This is done because not all the cells successfully took up the dye, and this is seen when only MT cells were used.

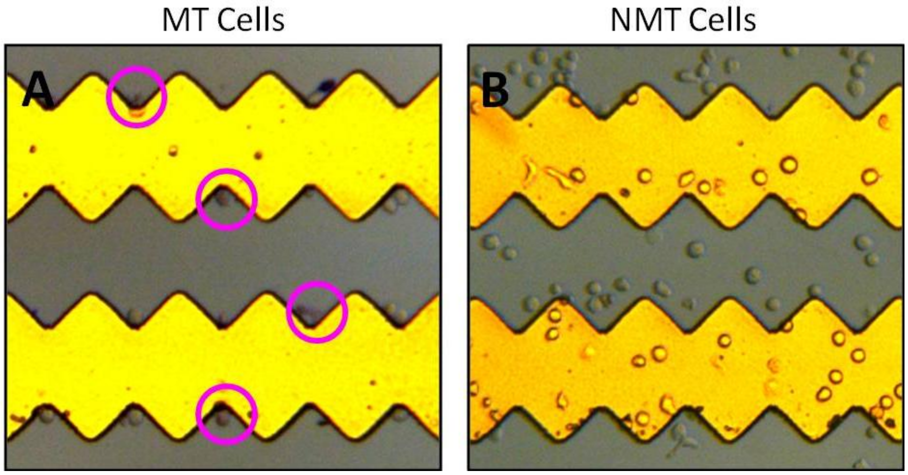

Figure 7.14: (A) MT Cells at a concentration of 3e5 *cells/mL*. (B) NMT Cells at a concentration of 3e5 *cells/mL*.

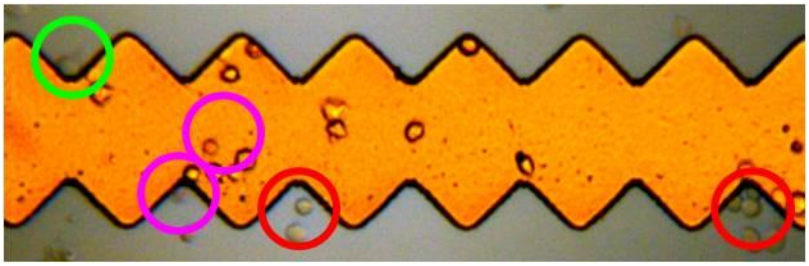

Figure 7.15: Cells that appear pink are shown in a pink circle and are known to be MT cells. Cells shown in a green circle are not pink, but are assumed to be MT due to position. Cells shown in a red circle are not assumed to be MT even though they are in a trap.

7.5.2 Rare Cell Experiment Results

Each rare cell test outlined in Table 7.8 is performed 4 times and the results are averaged and are shown in Figure 7.16, Figure 7.17, Figure 7.18 and Figure 7.19. The summary of results and efficiency analysis are also shown in Table 7.9, Table 7.10, Table 7.11 and Table 7.12. Figure 7.16 shows the number of MT and NMT cells found on the chip for all rare cell tests for both fixed and live cells. The total number of cells on the chip is constant for all tests, which is to be expected since the total cell concentration are the same for all tests, and therefore the total number of cells that pass over the chip is similar for all tests. The results show that it is possible to capture cells at all ratios, however it is not possible to remove all unwanted NMT cells from the chip.

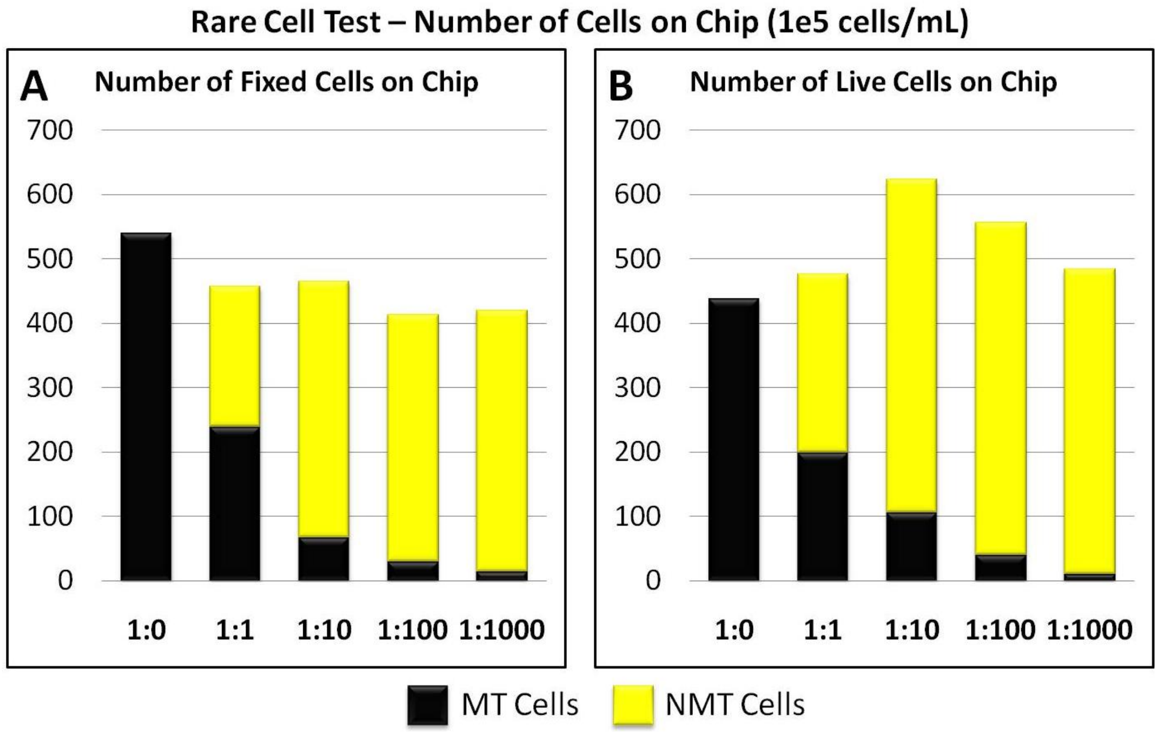

Figure 7.16: Comparison between MT and NMT cells for rare cell tests. (A) Using fixed cells and (B) live cells.

As the cell ratio decreases (MT to NMT Cells), the total number of MT cells that pass over the device decreases and the number of cells that are captured also decreases, as can be seen in Figure 7.17. A majority of the MT cells found on the chip are caught within traps, which shows that a majority of the MT cells are being successfully captured. Of the cells that are found in a trap, a majority of them are single cells and this is shown in Figure 7.18. Figure 7.19 shows that the number of NMT cells found on the MSCMA chip and the results are consistent for all tests. The second test (cell ratio of 1:1) has half the amount of NMT cells and this is to be expected since half the amount of NMT cells are used for this test. For all tests, the distribution of NMT cells on the chip is evenly distributed between all three regions: in the traps, on the permalloy, and between the permalloy lines.

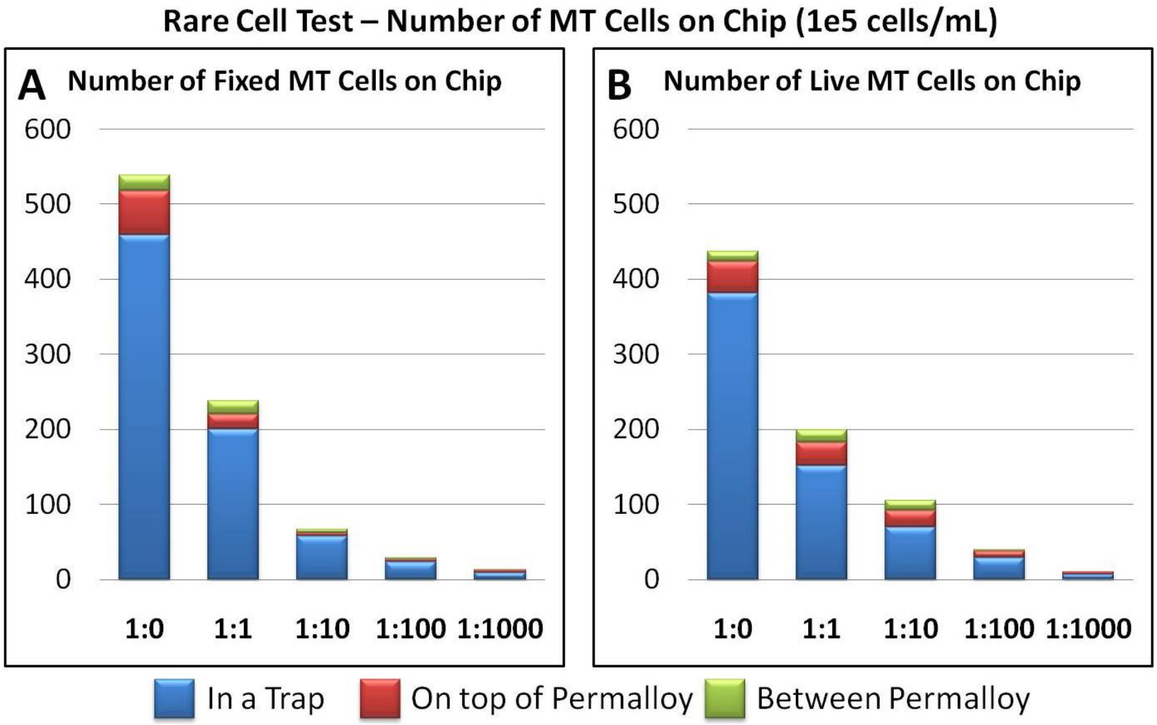

Figure 7.17: Rare cell test results showing the number of MT cells on the chip for (A) fixed cells and (B) live cells.

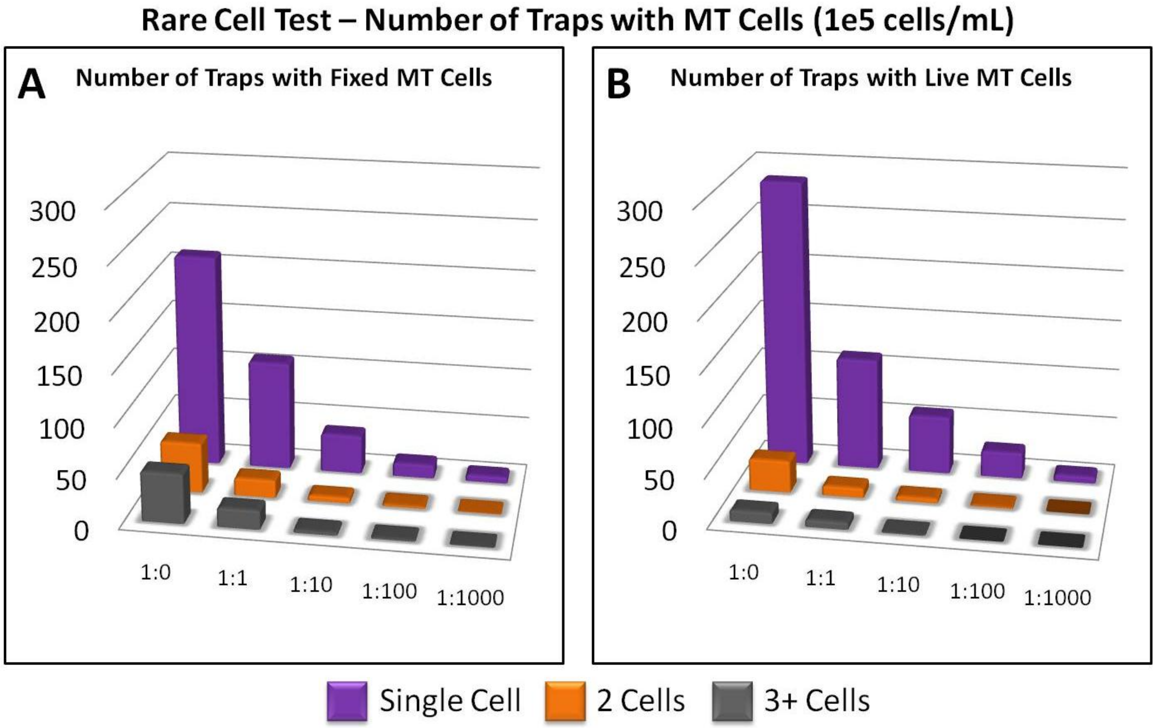

Figure 7.18: Rare cell test results showing the number of traps with a single cell, two cells, or 3+ cells for (A) fixed cells and (B) live cells.

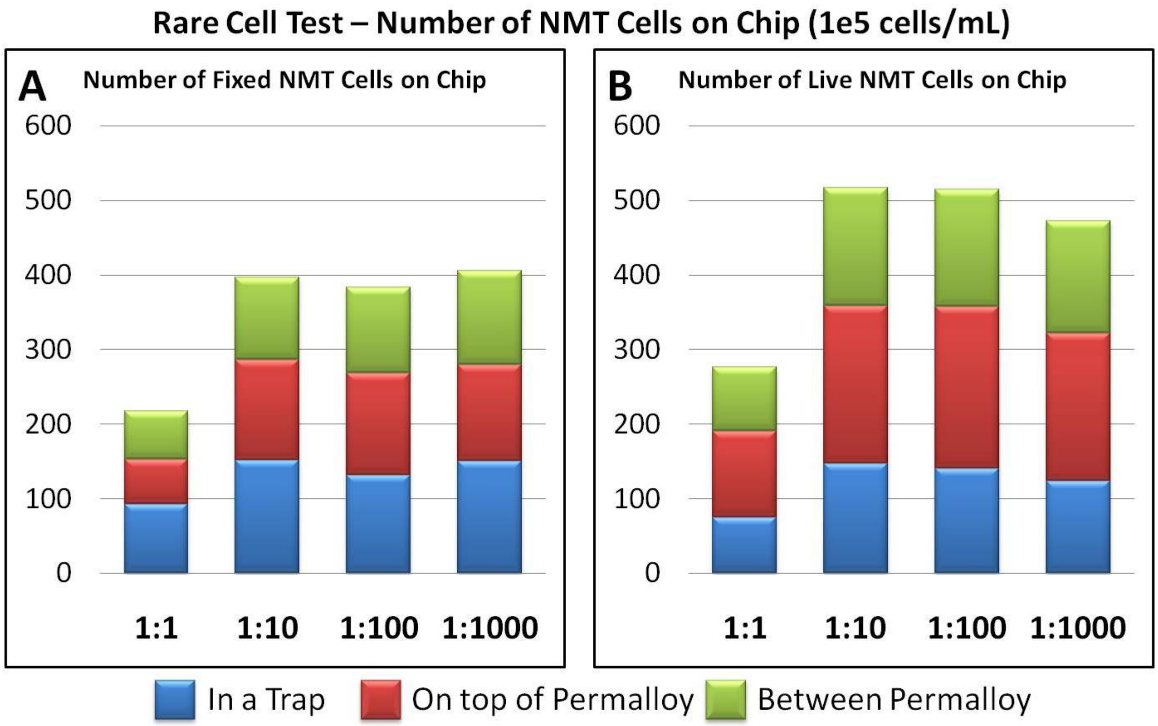

Figure 7.19: Rare cell test results showing the number of NMT cells on the chip for (A) fixed cell and (B) live cells.

The NMT cell CE% is similar for all ratios, and this shows that the number of NMT cells that become attached to the chip is related to the concentration of cells used. The MT cell CE% increases with each ratio, which look very promising. However, this might be happening since it is difficult to accurately obtain the smaller amounts of cell solution needed for each successive ratio. A ratio of 1:1000 requires 1 μL of cell solution, and the volume of MT cells actually present may be higher than predicted (i.e. a MT cell volume greater than 1 μL may have been used). The TE% and SCTE% decreases with each ratio, and this is to be expected since each ratio has a smaller number of MT cells available for capture. When comparing the results using fixed cells and live cells, the CE% were similar for both cells. This is promising, as it shows that the analysis used for fixed and live cells was comparable. When looking at the TE% and SCTE%, the live results were very similar to the fixed cells but always slightly higher. It was found that fixed cells tended to clump together, whereas single live cells tended to be separate.

Table 7.9: Rare cell test summary (fixed cells only).

Parameter	1:0	1:1	1:10	1:100	1:1000
Flow Rate [*mL/min*]	0.04	0.04	0.04	0.04	0.04
Concentration [*cells/mL*]	10^5	10^5	10^5	10^5	10^5
Number of NMT Cells	NA	218	397	383	406
Number of MT Cells	459	200	58	23	10
Number of Traps with MT Cells	310	145	47	18	8
Number of Traps with a Single MT Cell	211	109	39	14	6

Table 7.10: Rare cell test summary (live cells only).

Parameter	1:0	1:1	1:10	1:100	1:1000
Flow Rate [*mL/min*]	0.04	0.04	0.04	0.04	0.04
Concentration [*cells/mL*]	10^5	10^5	10^5	10^5	10^5
Number of NMT Cells	NA	276	517	515	473
Number of MT Cells	381	152	70	29	7
Number of Traps with MT Cells	328	128	64	26	7
Number of Traps with a Single MT Cell	285	112	58	26	7

Table 7.11: Efficiency analysis for rare cell test (fixed cells only).

Parameter	1:0	1:1	1:10	1:100	1:1000
NMT Cell CE%	NA	0.44 %	0.40 %	0.38 %	0.41 %
MT Cell CE%	0.46 %	0.40 %	0.58 %	2.33 %	9.50 %
MT Cell TE%	24.22 %	11.32 %	3.67 %	1.37 %	0.63 %
MT Cell SCTE%	16.48 %	8.52 %	3.05 %	1.09 %	0.47 %

Table 7.12: Efficiency analysis for rare cell test (live cells only)

Parameter	1:0	1:1	1:10	1:100	1:1000
NMT Cell CE%	NA	0.55 %	0.52 %	0.52 %	0.47 %
MT Cell CE%	0.38 %	0.30 %	0.70 %	2.90%	6.50 %
MT Cell TE%	25.59 %	10.03 %	4.96 %	2.15 %	0.51 %
MT Cell SCTE%	22.25 %	8.75 %	4.53 %	2.03 %	0.51 %

7.5.3 Summary of Cross Flow Experiments

A variety of tests were completed using the CFS to determine the capability of the device. Parameter establishment tests were first conducted to determine the best flow rate and concentration to use. It was found that NMT cells became attached to the chip, so tests were conducted to determine ways to minimize the number of adherent NMT cells. With the information obtained from these parameter establishment and cell removal tests, rare cell experiments were conducted using a heterogeneous population of cells. It was shown that the CFS could capture cells with a frequency of 1 in 1000 but it was not possible to remove many NMT cells that became adhered during the experiment. The next chapter will discuss in length the experimental results and how they relate to the FEM and simulation analysis previously conducted. Also, several recommendations will be made to increase the MT CE% and SCTE%.

Chapter 8: Discussion and Recommendation

Several experiments were conducted to test the performance of the CFS design. These experiments were developed based upon FEM models created of the CFS and a predicted cell path simulation. This next section will outline the key findings from the experiments and how they relate to the FEM models, as well as some recommendations to improve the overall CFS design and the predicted cell path simulation.

8.1 Key Findings

After conducting several experiments, it was shown that the CFS is capable of capturing MT cells from a heterogeneous population of cells, with ratios up to 1:10^3 (MT:NMT cells) using a cell concentration of 10^5 *cells/mL*. Although this number is very promising, there are a number of other methods currently available that are capable of capturing MT cells at ratios of 1:10^6 [97,98,99]. It was also found that results using fixed cells showed similar results to tests completed with live cells. This section will outline some key findings found from the experimental tests and where applicable, how they relate to the FEM models.

8.1.1 MT Cells

It was possible to capture MT cells for all tests completed, even up to a ratio of 1:1000 (MT cell to NMT cell). This section will discuss the experimental results, concentration on MT cells, and how they relate to the FEM and simulation analysis. This will include the MT cell capture trends, MT cell interaction with the fluid flow and the effectiveness of the permalloy traps.

8.1.1.1 MT Cell Capture Trends

For all tests completed approximately 85% of the MT cells were found in a trap, with a majority of these cells found in the centre of the trap flush against the permalloy. This was predicted by the smaller boundary fluid/magnetic FEM model (section 6.4) where the maximum *B*-field was found in the centre of the trap. This was also shown in the predicted cell path simulation when the final position of the cell was generally located in the centre of the traps, as seen in Figure 8.1. Since the direction and magnitude of the magnetic force was always towards the maximum *B*-field, the fact that the cells are generally found at the centre of the traps shows that this prediction was correct.

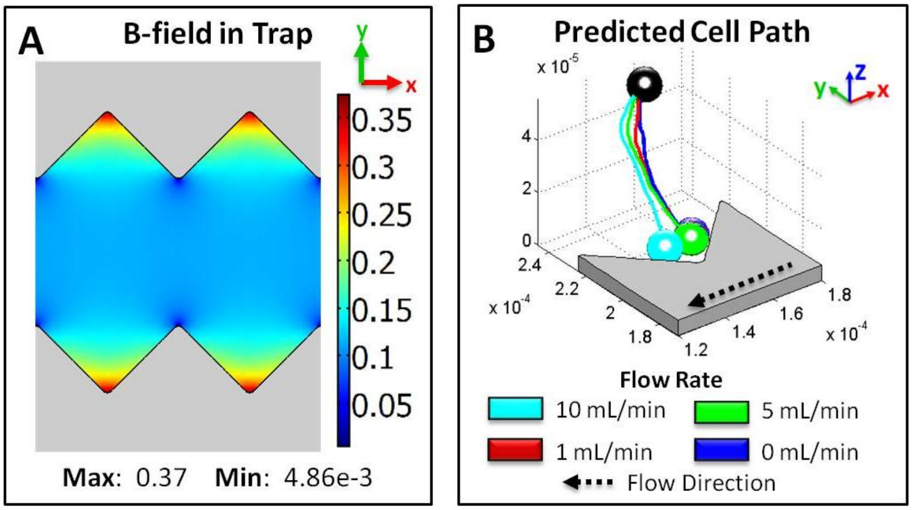

Figure 8.1: (A) *B*-field in traps. (B) predicted cell path results.

Another result seen from the FEM models was that the *B*-field along the permalloy lines was highest for portions of the MSCMA chip that were closest to the magnet, as shown in Figure 8.2 (A). This implies that the *B*-field would be strongest at the traps closer on either side of the MSCMA. Therefore, a higher number of captured cells are expected as traps with stronger *B*-field. This expectation is verified by observing Figure 8.2 (B), which shows the actual distribution of captured cells on the MSCMA after an experiment. It can be seen that there is indeed a greater number of cells captured at the left and right edges of the MSCMA, which are closer to the magnets and have a higher *B*-field. This result is also emphasized by Figure 8.3, which shows the capture distribution along a single permalloy line (yellow structure), from one end of the chip to the other end using a cell concentration of $3\text{x}10^6$ *cells/mL*. The traps that are closest to either end (denoted as inlet and outlet) appear to have a higher number of captured cells.

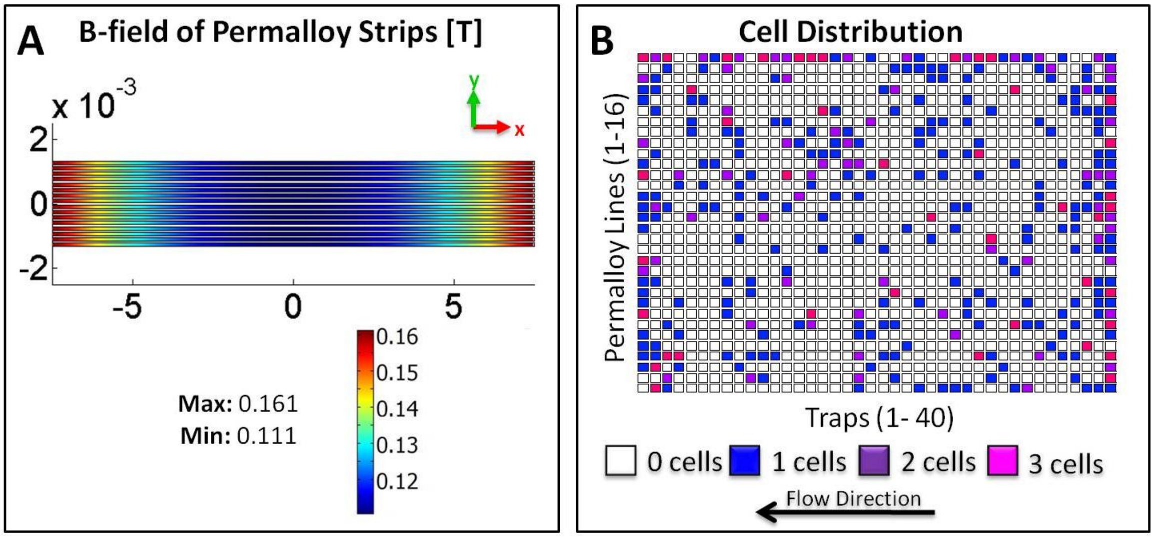

Figure 8.2: (A) *B*-field along permalloy strip. (B) Cell capture distribution.

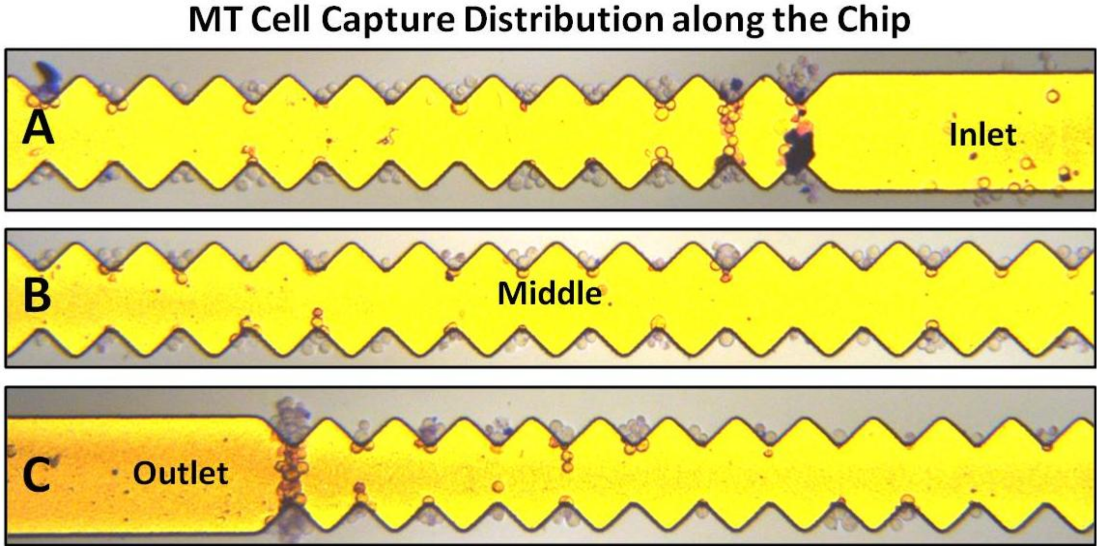

Figure 8.3: Live MT cell capture distribution along the chip showing (A) the side closest to the inlet, (B) the middle of the chip, and (C) the side closest to the outlet.

8.1.1.2 MT Cell interaction with the Fluid Flow

Fluid flow rates were increased at the end of some experiments, in an attempt to remove unwanted NMT cells that became adhered to the chip. It was found that captured MT cells were well secured, and higher flow rates did not remove a significant number of cells, as seen in Figure 8.4. Although 17.2% cells captured are removed from traps, 37.2% of additional traps were filled when the higher flow rates were applied, which shows that there is a net benefit to using the higher flow rates. This shows that the magnetic force exerted on the MT cells by the permalloy is strong enough that high flow rates (up to 2.5 *mL/min*) cannot remove them. These results were predicted in the smaller boundary magnetic/fluid FEM model previously discussed (section 6.4). The sawtooth model was shown to exert a high magnetic force on a cell when the cell was in the centre of the trap.

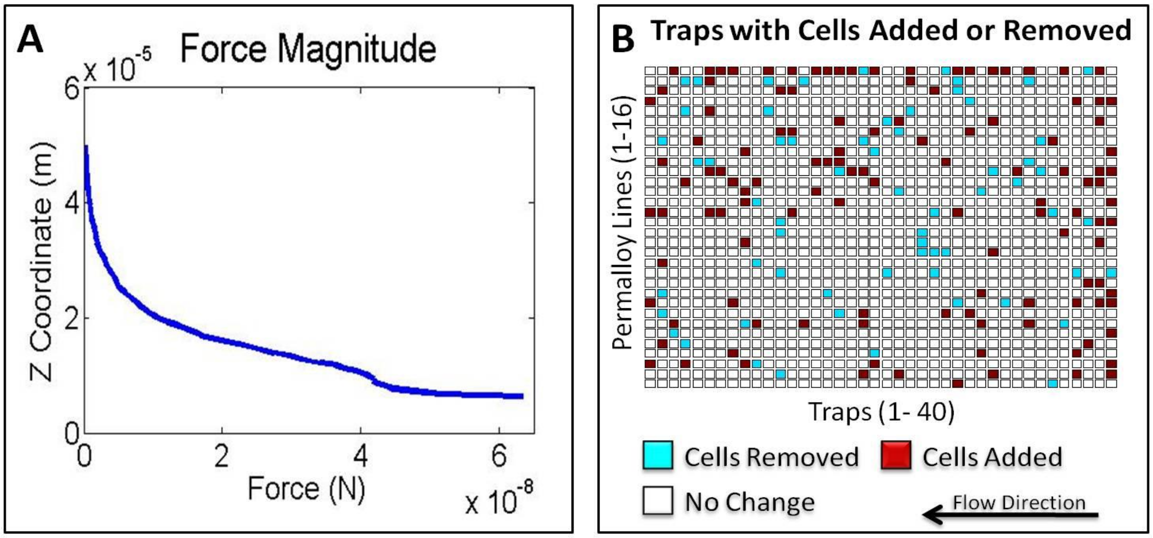

Figure 8.4: (A) Force magnitude for the sawtooth design. (B) Test showing traps with cells added or removed.

Four different flow rates were used in the predicted cell path simulation ranging from no flow rate up to 10 *mL/min*. It was found that the MSCMA was capable of capturing cells for all flow rates assuming that the cell started 50 *μm* above the substrate.

The cell path simulation also predicted the time it takes a cell to be captured, when the cell starts within 50 *μm* zone above the substrate, for various cross flow rates. However, it was difficult to determine the time it takes to capture a cell, since the initial z-axis height above the substrate is difficult to determine, using the microscopy setup of the experiment. Generally, it was qualitatively observed that when the cells were being captured, they were always captured within 1 - 5 seconds. Also, the cell path simulation predicted that if cells are within 50 *μm* from the substrate, MT cells can still be captured using flow rates up to 10 *mL/min* (section section 6.5). Although the highest flow rate was not tested, MT cells were successfully captured using an initial flow rate of 1.0 *mL/min*, resulting in a MT-CE% of 0.12%.

8.1.1.3 Permalloy Trap Effectiveness

A major result from the FEM analysis and cell path simulation was that the magnetized permalloy lines would only influence MT cells when they were within 50 *μm* from the substrate. This was difficult to experimentally validate, since it was difficult to determine the height that cells were being successfully captured using the microscopy setup. The low efficiency percentages shown in Table 7.11 and Table 7.12 indicate that many of the cells that flowed over the device are not being affected. When tests were completed using only MT cells, the TE% ranged from 24 – 26 % , SCTE% ranged from 17 – 25%, and the MT-CE% ranged from 0.40 – 0.46%. This implies that although a promising number of traps are occupied with cells and majority of traps contained a single cell, only a very small percentage of cells were actually captured from the total volume of cells that passed over the MSCMA chip. This low MT cell CE% means that only a small percentage of cells are being captured, whereas a majority of the cells are either being flushed away or are not landing in the trap area. The low MT cell CE% may have to do with the large culture chamber size.

The culture chamber dimensions are roughly 17 *mm* long and 8 *mm* wide, whereas the trap region of the MSCMA only occupies 2.4 x 2.8 mm^2 of that area, as seen in Figure 6.27. Therefore, it is possible for many cells suspended in the fluid to flow around the trap region, instead of above it. In addition, the simulations predicted that cells can only be captured if they are within 50 μm from the substrate. Since the height of the chamber is 2 *mm*, many cells in suspension will flow right over top the MSCMA without being magnetically attracted to it. Therefore, the useful cell capture zone above the MSCMA is roughly 2.4 x 2.8 x 0.05 mm^3, which is equivalent to 0.336 mm^3. In comparison, the total volume of the culture chamber is 210 mm^3, therefore, the useful capture zone only occupies 0.16% of this volume.

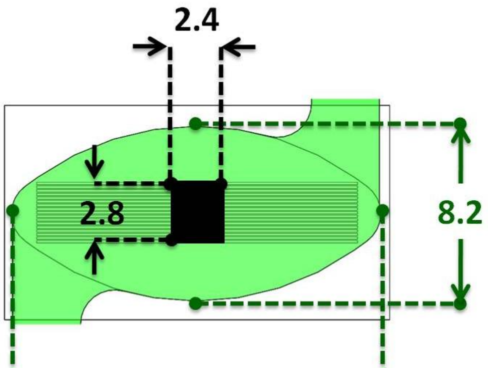

All dimensions in mm

Figure 8.5: Dimensions of trap area (black) versus culture chamber (green)

It has been experimentally observed that cells are evenly distributed throughout the chamber, as shown in Figure 8.6, this means that at any one time only 0.16% of all cells are passing by the capture zone. For all tests, a total of 1 *mL* of cells was used and since the culture chamber can only accommodate 0.21 *mL* at any one time, the duration of the test will have an equivalent of 4.5 full chambers. Assuming that all the cells that pass through the capture zone are successfully captured and all other cells outside the capture zone are flushed out of the CFS, this means in theory, 0.72% (0.16% x 4.5) of all cells can be successfully captured.

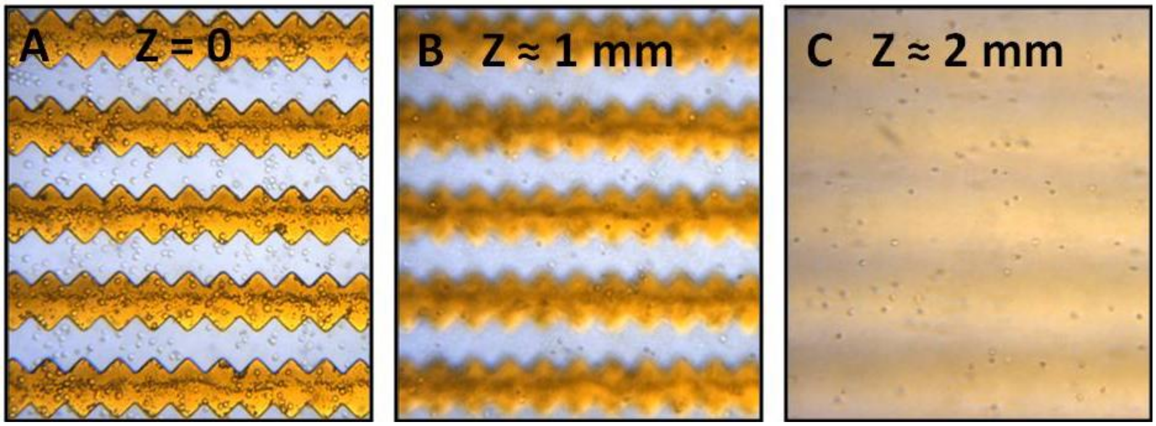

Figure 8.6: Images taken at various z-heights. (A) Starting at the substrate where z = 0. (B) z ≈ 1 *mm*. (C) z ≈ 2 *mm*.

Experimentally, it was found that the MT-CE% for tests completed with only MT cells was roughly 0.4 – 0.5%. This experimental percentage is comparable to the theoretical percentage of cells that pass through the capture zone. This demonstrates that a majority of cells are being successfully captured once they are within the capture zone. Further, it was experimentally found that the cell CE% increased with decreasing ratios (i.e. using less MT cells results in a better cell capture efficiency). This could be a result of the volume of MT cells actually used for experiments may have been higher than what the ratios show (i.e. a ratio of 1:1000 should have a 1 μL volume of MT cells, but the actual tests may have had a higher volume of MT cells). It is difficult to accurately obtain the smaller volumes of cells needed for experiments with low ratios, and as a result, a larger volume of MT cells may have been used. To make the CFS a competitive rare cell detector, several changes to the design need to be made, as outlined in section

8.3. These changes will address the low cell capture efficiency, which will improve the devices ability to trap single rare cells.

8.1.2 NMT Cells

When conducting the rare cell experiments it was not possible to remove all NMT cells as the NMT cells land randomly on the MSCMA chip. This next section will discuss the experimental results, concentrating on the NMT cells cell adhesion and where the NMT cells land.

8.1.2.1 NMT Cell Adhesion

A significant problem that occurred during testing was the adhesion of NMT cells to the MSCMA chip. Further, these adhered cells were not easily removed. This is an important issue as it is directly related to how effective the CFS is as a rare cell device. An optimal rare cell device should only capture desired cells, and this includes not having any undesired cells present on the chip. The presence of undesired cells, in our case NMT cells, significantly decreases the effectiveness of the CFS. A couple of methods were attempted to minimize the NMT cell adhesion problem encountered, including: (i) applying a higher flow rate to flush away the NMT cells after the MT cells were successfully captured, and (ii) using a higher initial flow rate to deposit the cells over the MSCMA. Both of these methods were successful in reducing the number of NMT cells, but neither method was capable of completely removing all NMT cells.

The first method was used for all rare cell experiments conducted. It was found that applying two consecutive flow rates, first 1.0 *mL/min* and then 2.5 *mL/min* was capable of reducing the number of NMT cells attached to the chip by 27.5% (567 initially to 411 after high flow rates were applied). This can also be seen in the NMT-CE% which decreased from 0.57% to 0.41%. Although these low numbers do seem promising, as a comparison, tests completed using only MT cells showed similar CE% of 0.67%. This indicates that cells that are in close proximity to the chip will have two likely outcomes: (i) MT cells will become magnetically captured towards a trap, and (ii) NMT cells will become attached to the chip. This is also emphasized when looking at the results for the rare cell experiments. The NMT-CE% were consistent for all ratios, with values ranging from 0.41% to 0.55%. Since the cells are evenly distributed throughout the culture chamber (as was shown in Figure 8.6), consistent NMT cell CE% shows that regardless of the volume of cells used, cells that are close to the MSCMA chip will become adhered to the surface. Methods to potentially minimize this problem will be discussed in depth in a later section.

8.1.2.2 Cell Landing

When analysing experiments that included NMT cells, it was found that the cells always landed randomly on the chip. This was seen for all graphs showing the number of NMT cells that landed on chip, where equal amounts of cells were found in the traps, on the permalloy, and between the permalloy. Although the number of cells on each area was similar for NMT cells, the area that the traps physically occupy is significantly smaller than the other two areas (on and between the permalloy). If the cells were truly landing on the chip randomly, one would expect to see a smaller number of cells within the traps since the traps occupy less space. Figure 8.7 shows two images side by side of the same area of the chip before and after the cell removal test <u>using only NMT cells</u>. The yellow regions represent the permalloy layer, while the grey regions are the glass substrate, and the lighter circles are the cells. The cells are actually landing on the chip randomly. When the higher flow rate is applied to flush the system, many of the cells move around, however, those that are closer to, or within the trap region exhibit little/no movement, as seen in Figure 8.7.

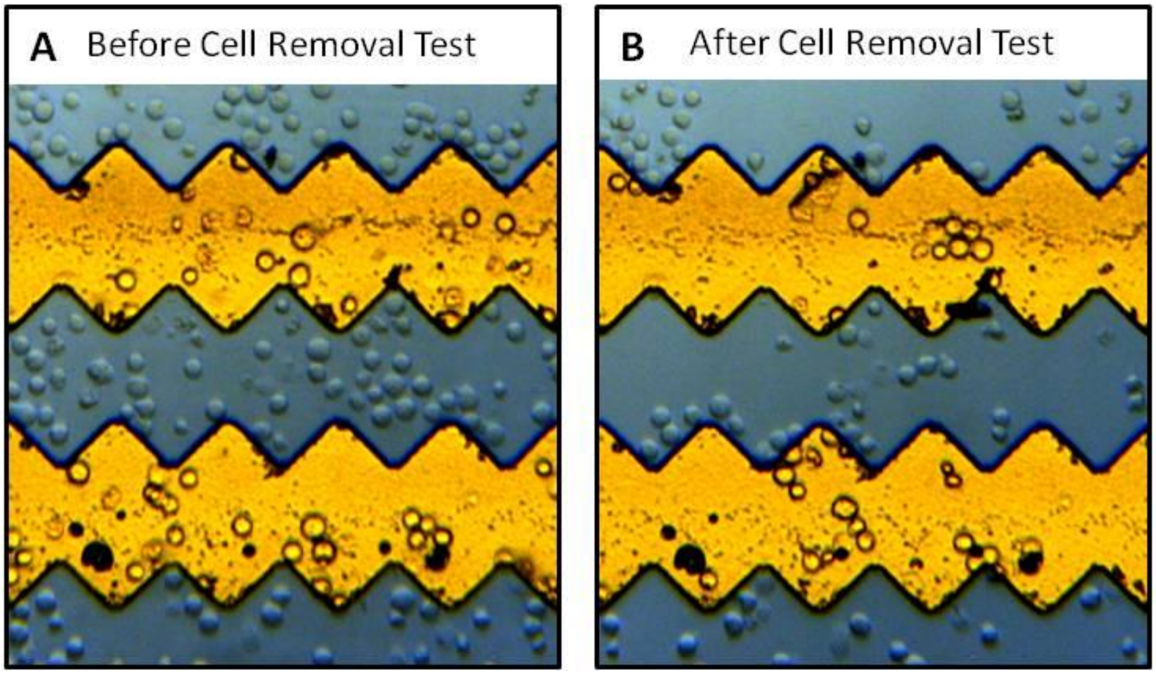

Figure 8.7: (A) Image of chip after initial cell deposit using a flow rate of 0.04 *mL/min*. The cells land randomly on the chip. (B) Image of chip after cell removal test using flow rates of 1.0 *mL/min* and 2.5 *mL/min*.

The higher number of NMT cells that remain close to or within the trap region after the flushing operation is most likely due to the physical shape of the trap. The permalloy layer is 6 μm higher than the substrate, which creates a physical valley with zigzag sides. When a NMT cell lands in a valley or trap, the fluid force exerted on the cell during when higher flow rates are not large enough to overcome the adhesion force experienced between the cell and the chip. Also, FEM simulations predicted that the flow rate within the traps was shown to be significantly lower than the flow rate in the valley, or on top of the permalloy, as seen in Figure 8.8. Therefore, it can be concluded that it is difficult to 'flush out' a NMT cell with higher flow rates, after it lands randomly within a trap, due to the surface adhesion to the surface.

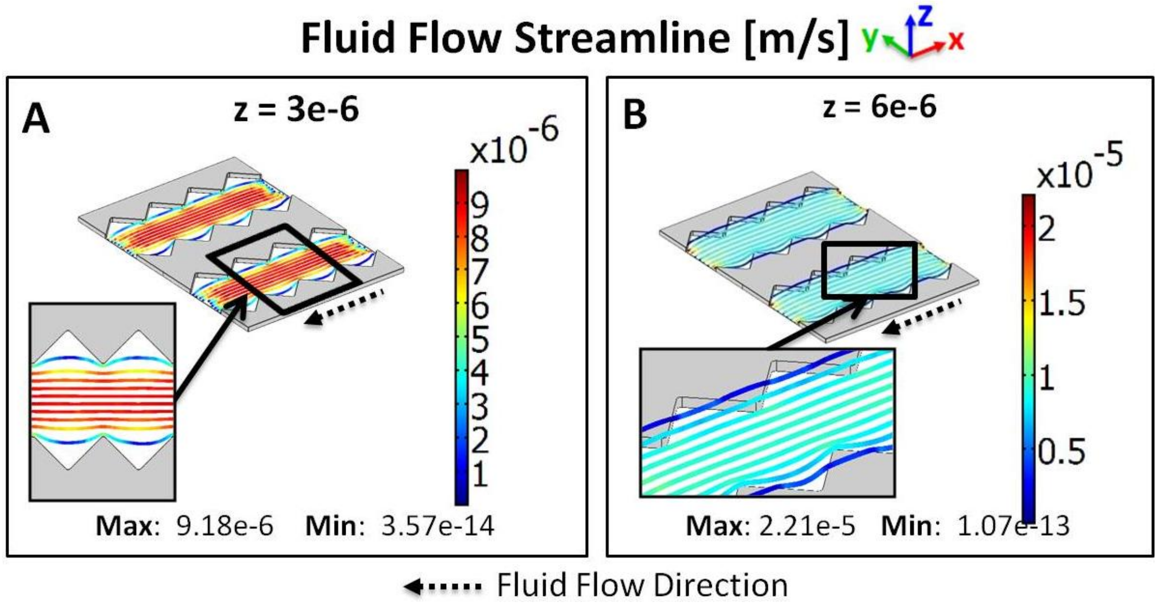

Figure 8.8: FEM model showing flow rate around the traps

8.2 Predicted Cell Path Recommendations

The predicted cell path simulation was an iterative process that extracted information from a COMSOL FEM model to determine the magnetic and fluid forces exerted on a single cell. This section will outline methods to verify the current simulation, and improvements for future simulations.

8.2.1 Verifying Current Simulation

Although the simulation was capable of showing the path a MT cell follows due to magnetic and fluid forces, several improvements can be made. Prior to improving the current simulation, methods need to be investigated to verify this simulation. The simulation can be verified using two methods: (i) tracking the position of the cell in 3D space and (ii) determining the forces exerted on a single cell.

The predicted cell path simulation predicts the position of the cell in the x, y, and z directions. Although it is possible to easily track the cell in the x and y direction using the microscope setup, it is difficult to track the cells z position. The microscope used has a low depth of focus (approximately 3 μm) in the z-direction, and as the cell moves away from the focal plane, the cell becomes blurry. For example, if the top of the permalloy traps is in focus, anything above or below that z-plane, will be slightly blurry. As the distance away from the focal plane increases, the object becomes progressively more blurry until at about 30 μm away, it becomes impossible to see. Therefore, to verify the simulation by tracking the cells position, three main pieces of information need to be obtained: (i) the initial position (x, y, and z) of the cell relative to a trap, (ii) initial velocity of the cell and (iii) time it takes the cell to reach the trap. If this information can be obtained, the simulation can be easily verified.

The second method that could be used to verify the simulation is by determining the forces that are exerted on the cell, more specifically, the magnetic force and Stokes drag. The Stokes drag can be easily identified if the velocity of the cell relative to the fluid flow is known. The fluid velocity could be measured by injecting dye into the culture chamber, and observing the rate that it flows through the culture chamber. Obviously there will be diffusion affects at work, so this would also have to be accounted for. The magnetic force can be verified by determining the number of magnetic particles that are attached to the surface of the cell, or physically measuring the magnetic force of a MT cell in response to a known situation that can be easily modelled using COMSOL. Determining the number of magnetic particles attached to the surface of the cell will be difficult due to the small size of the particles relative to the cell. Therefore, measuring the magnetic force exerted on a MT cell in a known situation would be ideal. This could be completed by potentially using optical tweezers to measure the magnetic force between a cell and a trap when the cell is at the centre of the trap [101]. This situation can be easily modelled in COMSOL to verify the numbers that are obtained. Once the simulation has been verified, several things can be done to improve the simulation.

8.2.2 Methods to Improve the Current Simulation

Several assumptions were used to simplify this simulation and are outlined in section 6.5.2. These assumptions need to be addressed to improve the simulation. The current simulation solves the COMSOL model once, where the model does not physically include the cell. This eliminates the interaction between the cell and the fluid. A simulation should be conducted which investigates the effects of adding the cell to the model, especially once the cell gets close to the permalloy traps. This could easily be done by comparing two separate FEM models, one with the cell close to the permalloy traps, and another with the cell far away from the permalloy trap.

One of the main assumptions used, was that the entire cell was a magnetic particle and only 1% of this force was actually acting on the cell. This assumption was used for simplicity, but needs to be changed to improve this simulation. The effects of the number and distribution of magnetic particles on the cell should be investigated. A sensitivity study can be done to show the difference between the entire surface of the cell being coated with magnetic particles, or only 10% of the surface containing magnetic particles. A simulation should be conducted showing the effects of the distribution of the magnetic particles. This will show the potential rotation of the cell as the magnetic particles attempt to align with the *B*-field and migrate towards areas of higher *B*-fields.

8.3 Cell Experiment Recommendations

It was shown that the CFS is capable of capturing cells from a heterogeneous population of cells. Although the ideal "rare cell ratio" of 1:10^6 (MT:NMT cells) was not achieved, there is still potential for the CFS to become a more powerful rare cell detection device. In order to make this a reality, several changes need to be made to the CFS. This next section will outline methods to increase the MT cell CE%, methods to decrease the NMT cell CE%, general improvements to the CFS, and finally a summary of methods to optimize the CFS.

8.3.1 Methods to Increase the MT Cell Capture Efficiency

An optimized CFS will have a high MT cell CE%, TE%, and SCTE%. The TE% and SCTE% should be equal to one another to increase the number of single cells captured. This next section will discuss methods to increase the MT cell CE% and will include cell cross flow improvements, MSCMA improvements, and increasing the cell concentration used.

8.3.1.1 Cross Flow System Improvements

The CFS design is simple and can effectively and reliably flow cells over the MSCMA chip. The flow rate can easily be controlled using a syringe pump and the cells were easily viewed using either a DIC microscope, or a brightfield microscope setup. To increase the cell trapping efficiency, the size of the culture chamber needs to be reduced to only include the capture zone. The ideal solution would be to have a culture chamber that measures 2.4 x 2.8 x 0.05 mm^3, which is also referred to as the “cell capture volume”. Reducing the culture chamber to only include the trap region would also decrease the number of cells that become attached to other parts of the chip. Figure 8.9 shows two parts of the chip that are part of the current culture chamber where MT cells easily become attached.

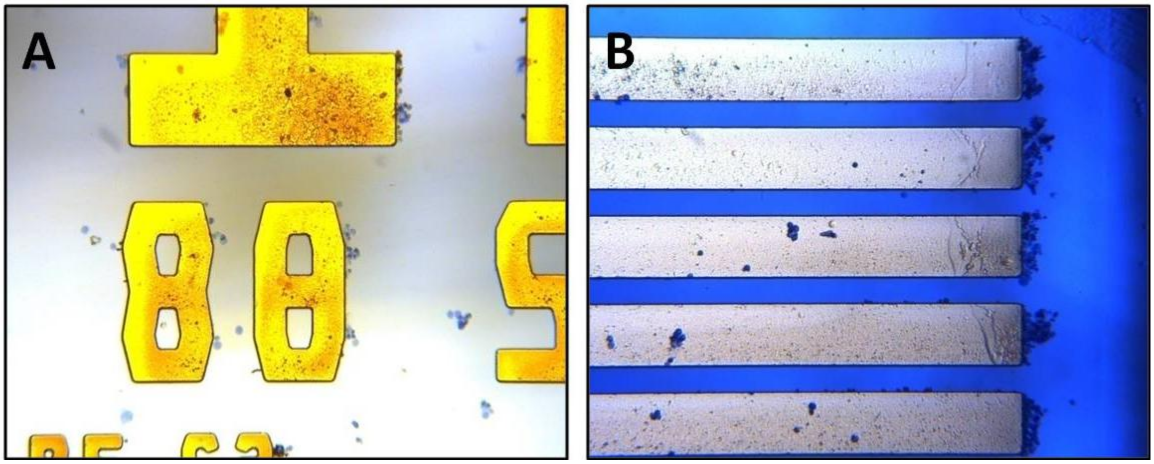

Figure 8.9: Cells attached to (A) features found on the trap and (B) to the end of the permalloy strips.

Decreasing the chamber size would also ensure that all cells have to pass through the capture zone, which would increase the TE. Changing the dimensions would require a significant change to the gasket assembly. The current gasket assembly design is made up of the culture chamber gasket, a microscope cover slip and a square gasket. This assembly allows flows fluid over the MSCMA chip, while minimizing leaks and allowing adequate light to pass through the chamber. The light that passes through the chamber is necessary to allow for the microscope platforms to properly view the cells.

Changing the chamber depth to 0.05 *mm* from the original 2 *mm* will also require a major change in the gasket assembly. The culture chamber gasket has two depths: the first depth extends 1 *mm* from the top and includes the inlet and outlet arms, the second depth extends through the entire gasket and includes the culture chamber, as seen in Figure 8.10. This two depth gasket was made to minimize leaks and to ensure biocompatibility since the base is made of aluminum and can be toxic to cells.

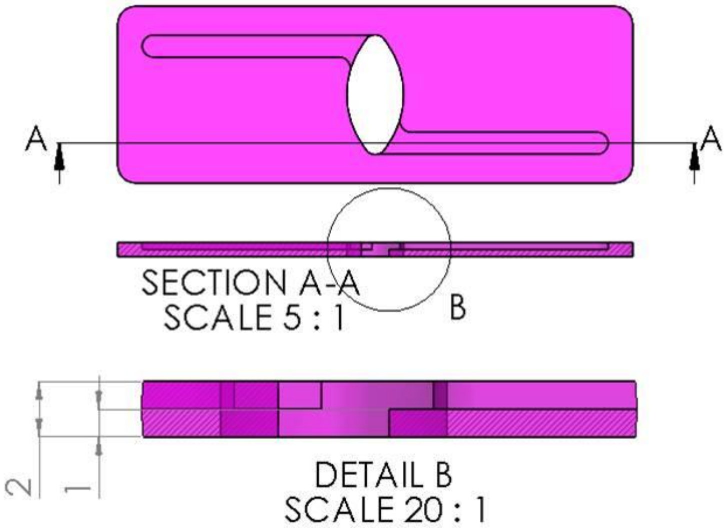

Figure 8.10: Culture chamber gasket

To obtain features on a micron scale, using microfluidic techniques to make the gasket may be necessary. Microfluidic devices are generally made of PDMS using contact photolithography [43]. A CAD file is printed onto a photomask that is used to expose certain parts of a photoresist material that is on a silicon wafer to UV light. This creates a master mould that can be used with PDMS. Due to the micron sized features, the gaskets are generally several centimetres thick to ensure the integrity of the channels and chamber.

This poses the following two problems: (i) this might degrade the optical clarity and (ii) it becomes more difficult to have an open chamber. The first problem can be resolved by properly preparing the PDMS. Figure 8.11 shows two images of the same spot on the MSCMA. The left image shows the chip viewed without anything on top and the right images shows the chip viewed through 2 cm of PDMS. The PDMS used for this test was prepared by de-gassing the PDMS several times to remove any bubbles. Although the image on the right is not perfect, it is still very clear.

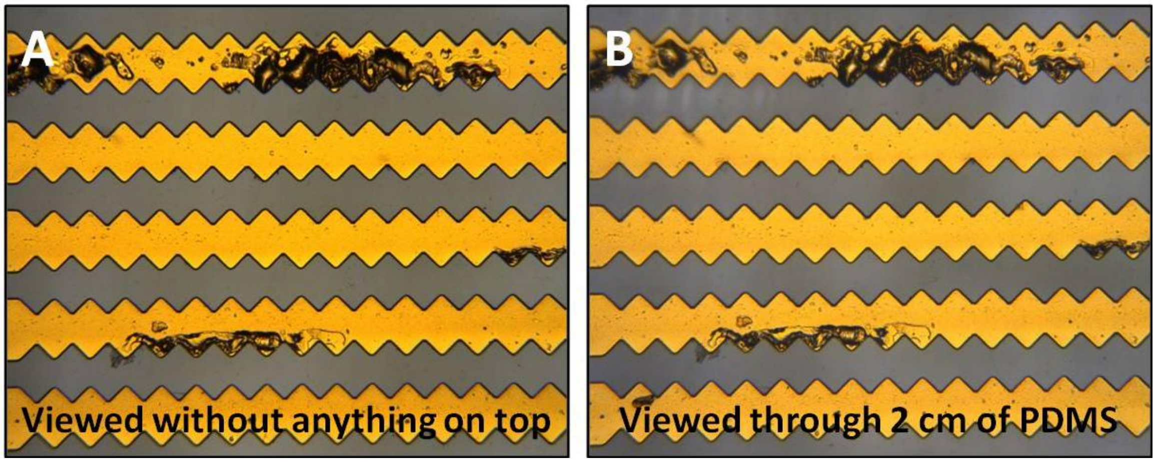

Figure 8.11: MSCMA viewed (A) normally and (B) through 2 cm of PDMS.

One benefit to using a smaller chamber size is that a higher flow rate could be used for experiments. A higher flow rate would minimize the number of NMT cells that become attached to the chip. As was shown in the predicted cell path simulation, cells can be captured using a flow rate up to 10 *mL/min* using the current chamber size. One reason that cells could be captured at such high flow rates is that since the chamber height was large, this caused the fluid velocity closer to the permalloy to be low due to the no slip conditions that were applied. A smaller chamber would result in higher pressure and also a higher change in pressure throughout the chamber and as a result higher fluid velocities would be seen.

These higher velocities may cause the stokes drag on the cell to become dominant and would overcome the magnetic force exerted from the permalloy traps if the same high flow rate is used. The flow rate would have to be adjusted to accommodate for the change in chamber size. Although the flow rate would need to be decreased, the fluid velocity through the chamber could be kept consistent. A flow rate that yields a high fluid velocity through the chamber could still be used to both capture the MT cells and limit any NMT cells that become attached to the chip.

8.3.1.2 MSCMA Improvements

Another way to increase the efficiency of the MSCMA is to use a different chip design. MT cells were successfully captured using the sawtooth design and cells were generally drawn to the centre of the trap. One major drawback to this design is the overall size of the trap itself. The sawtooth trap measures 60 μm peak to peak and has a lateral depth of 30 μm. The diameter of a Jurkat cell is roughly 12 μm, which is significantly smaller than the trap. Due to the large size of the trap, it is possible for multiple cells to be captured in a single trap and this is commonly seen when using a high concentration of cells. One way to address this is to use a chip with smaller traps that have a peak to peak length of 30 μm and a lateral depth of 15 μm. A magnetic FEM simulation of proposed MSCMA with smaller trap size can be seen in Figure 8.12 and Figure 8.13.

The B-field predicted within these smaller traps (at height $z = 0$), in comparison to the original traps, can be seen in Figure 8.12. The maximum B-field is slightly lower than the larger traps but it is still located at the centre of each trap. Since the distance between each trap is smaller, there would be an increase in maximum B-field points seen per unit area. This would result in a higher capture success rate since cells that flow by have more traps that can be readily accessed. A lower B-field will also result in a lower force being exerted on a cell when it is in a trap, which has two implications. Firstly, a MT cell that is successfully captured might be removed by the fluid cross flow if the flow is too high, and secondly, the speed that a MT cell will be drawn towards the trap will be slower. Figure 8.13 shows a FEM simulation that predicts the B-field above the proposed MSCMA with smaller trap sizes. It can be seen that the B-field starts to lose distinction (no *B*-field gradient) at a distance of 30 μm above the substrate. This means that the smaller traps can magnetically influence cells only within 30 μm above the substrate, which is almost half the distance compared to the larger traps that will influence cells that are within 50 μm of the substrate.

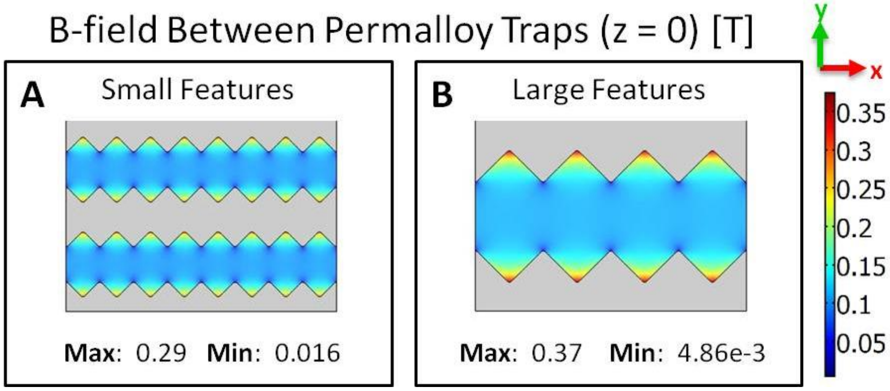

Figure 8.12: Magnetic flux density between the permalloy (z = 0). Comparison between (A) Sawtooth with small features and (B) Sawtooth with large features.

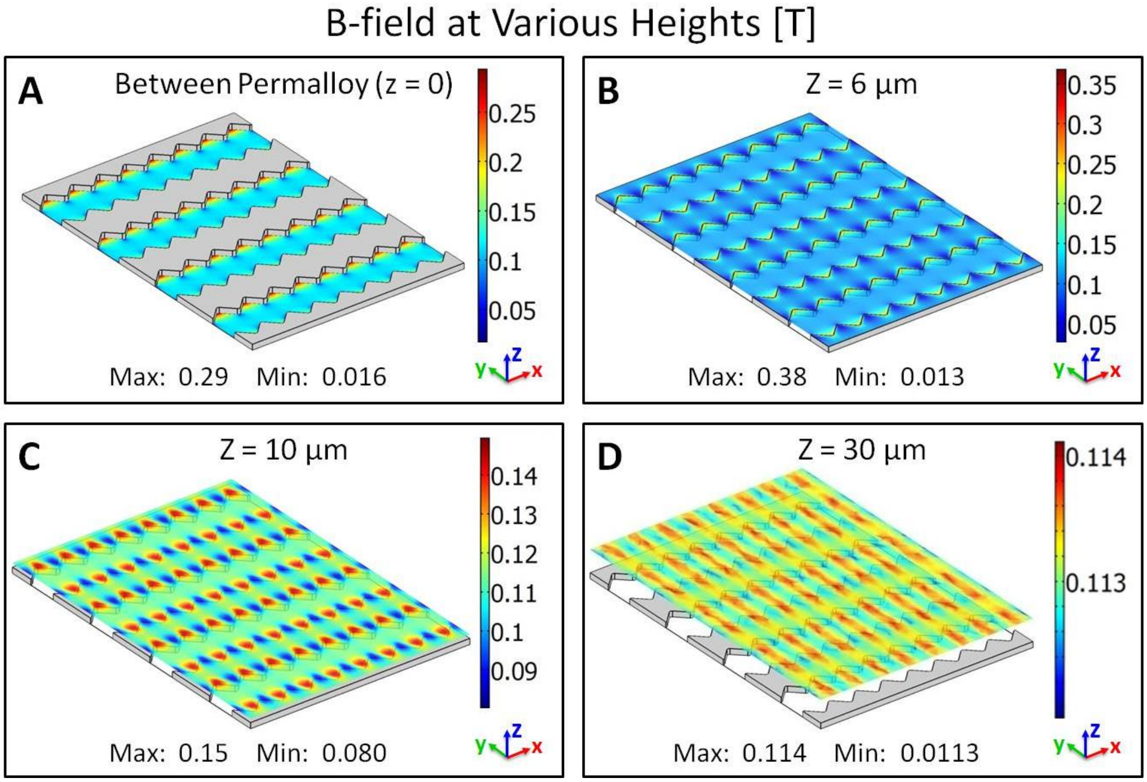

Figure 8.13: Magnetic flux at various heights. (A) Between the permalloy z = 0. (B) z = 6 μm. (C) z = 10 μm. (D) z = 30 μm.

Since the smaller traps can physically accommodate less cells compared to the larger traps, this would increase the number of traps that contain a single cell. One drawback to the smaller design is that the B-field for these traps does not extend as far in the z-direction. This means that MT cells need to be closer to the trap before they can be trapped. To accommodate for this, the culture chamber could be made smaller but this poses one problem. The cell diameter is roughly 12 μm, which would be half the size of a chamber with a 30 μm depth. Having features this size could potentially harm cells and this would mean decreasing the flow rate to ensure that cells are not harmed. However, a lower flow rate could potentially increase the number of NMT cells that become attached to the chip.

8.3.1.3 Cell Concentration

One simple way to increase the SCTE% is to increase the concentration of cells used. A higher cell concentration will have a greater number of MT cells per unit volume and therefore increase the number of MT cells that are available for capture. The rare cell experiments conducted for this thesis only used a concentration of $1\text{x}10^5$ *cells/mL*. Tests were completed with live cells with three different concentrations and the results are shown in Figure 8.14, Table 8.1 and Table 8.2. Tests completed with the three concentrations had similar MT cell CE% ranging from 0.10 – 0.44%. The lower CE% value is likely due to the analysis procedure that was followed. If any trap was seen to have more than 3 cells, that trap was categorized as a 3+ trap. When counting the actual number of cells, the 3+ traps were multiplied by 3 to give the total number of cells in that trap. This method worked well when working with a concentration of $1\text{x}10^5$ *cells/mL*, since there were only a small number of traps that contained more than three cells. When performing analysis for 3x10^{6} *cells/m*L on the other hand, this was no longer the case where a majority of the traps contained more than 3 cells.

A concentration of 3x10^{5} *cells/mL* has the best results with a SCTE of 43.03% (553) and a TE of 56.33% (721). A concentration that is 10 times greater (3x10^{6} *cells/mL*) results in a low SCTE of 18.12% (232) but a high TE of 95.55% (1223). This is also emphasized by the cell capture distribution image shown in Figure 8.15. This shows that the concentration of cells needs to be optimized for each device. Using a cell concentration higher than the optimal value will result in an increase in the TE%, but a significant decrease in the SCTE%. On the other hand, using a smaller concentration than the optimal value will result in a decrease in both the TE% and the SCTE%. Several factors will influence the optimal cell concentration, including the culture chamber size, MSCMA chip design, and volume of cells used for each experiment. If any of these parameters are altered, a new optimal cell concentration needs to be found.

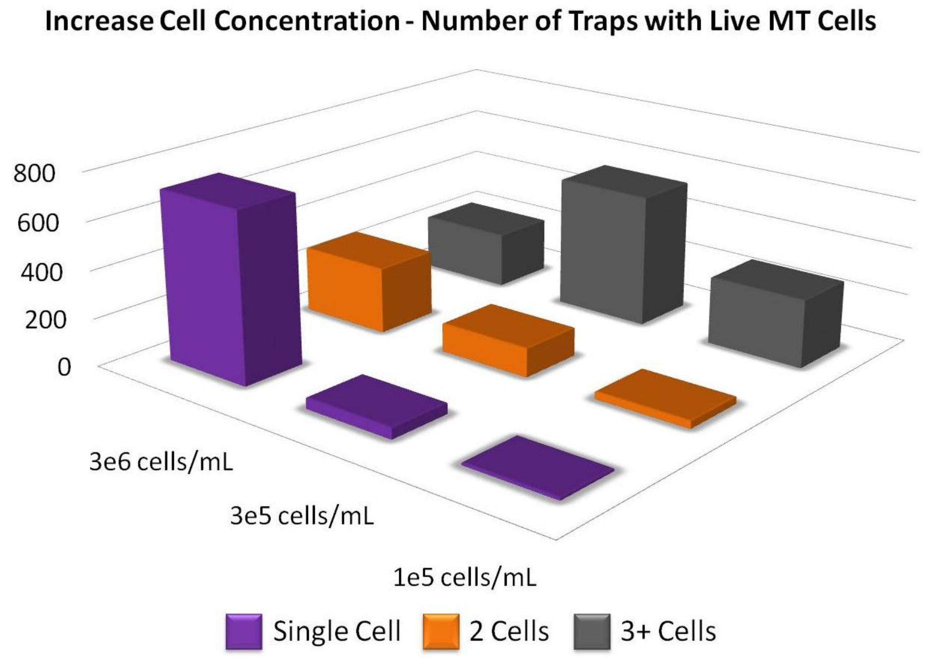

Figure 8.14: Number of traps with live MT cells with increasing cell concentrations.

Table 8.1: Increasing cell concentration test summary.

Parameter	**Test 1**	**Test 2**	**Test 3**
Flow Rate [*mL/min*]	0.04	0.04	0.04
Concentration [*cells/mL*]	10^5	30^5	10^6
Number of MT Cells	437	963	3021
Number of Traps with MT Cells	328	721	1223
Number of Traps with a Single MT Cell	285	553	232

Table 8.2: Efficiency analysis for increasing cell concentration.

Parameter	**Test 1**	**Test 2**	**Test 3**
MT Cell CE%	0.44 %	0.32 %	0.10 %
MT Cell TE%	25.59 %	56.32 %	95.55%
MT Cell SCTE%	18.13 %	43.20 %	22.25 %

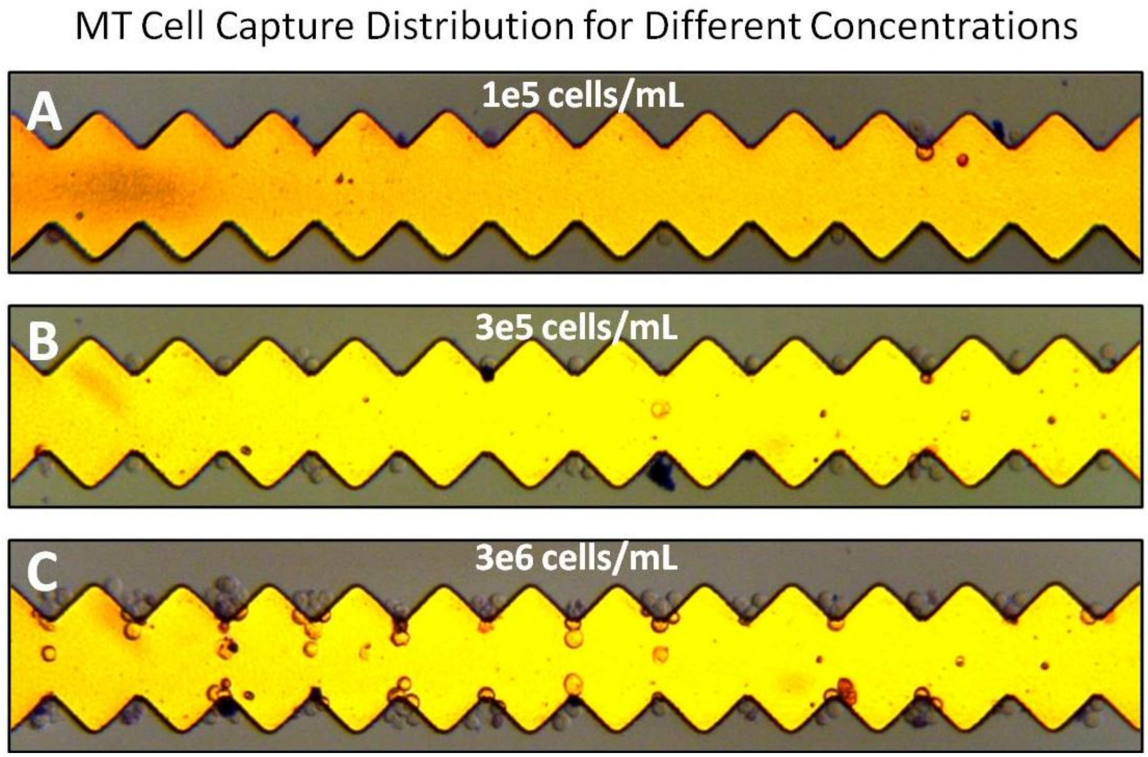

Figure 8.15: Live MT cell capture distribution for different concentrations. (A) 1e5 *cells/mL*. (2) 3e5 *cells/mL*. (3) 3e6 *cells/mL*.

This optimal cell concentration also needs to account for the number of NMT cells that are captured. Although increasing the concentration increases the number of MT cells that are captured, it also increases the number or NMT cells that become attached to the chip. As was seen with all experiments NMT cells became attached to the chip even when using a low concentration of cells. This is emphasized in Figure 8.16, which shows the distribution of cells on the chip with varying concentrations. Applying a high flow rate to remove cells was not successful in removing all unwanted NMT cells. As was discussed in section 8.1.2.1, the NMT cell CE% was fairly constant for all tests completed. Therefore, decreasing the concentration of NMT cells used will reduce the adhesion seen, but as long as the core problem of the adhesion is not solved, NMT cell will always become attached to the chip. The cell adhesion problem needs to be addressed, and methods to minimize this problem will be discussed in the next section.

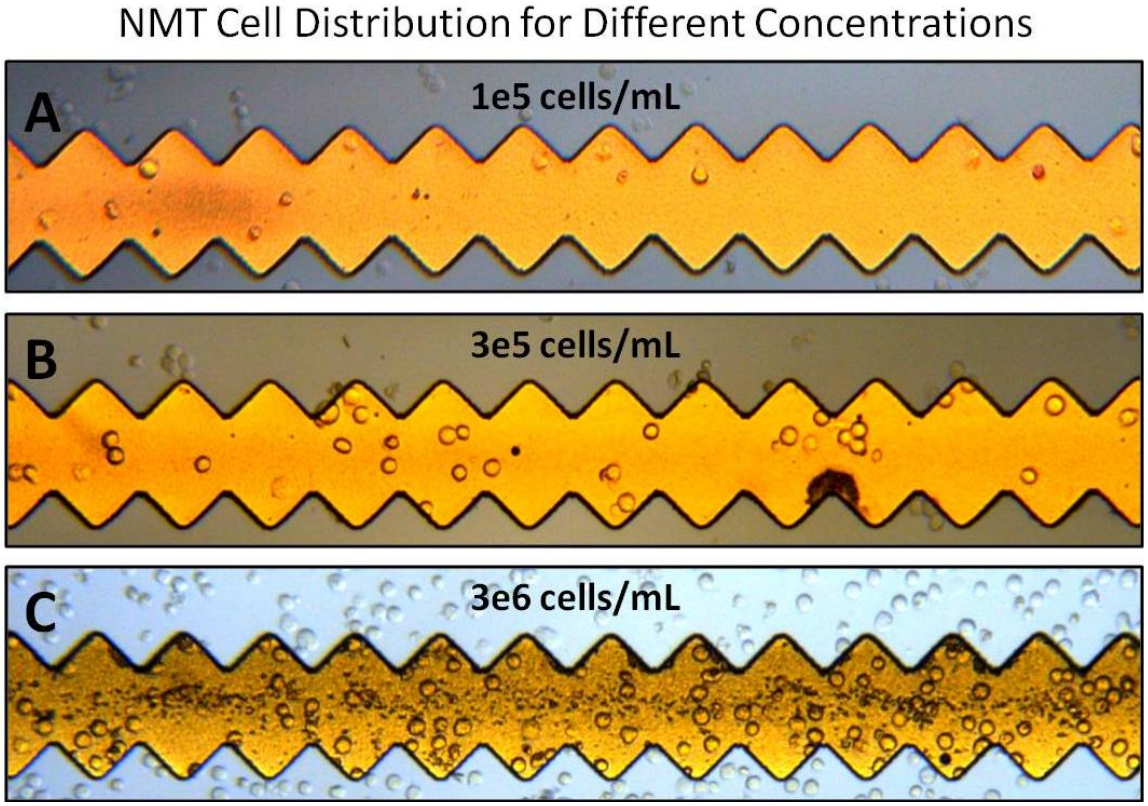

Figure 8.16: Live NMT cell distribution for different concentrations. (A) 1e5 *cells/mL*. (B) 3e5 *cells/mL*. (C) 3e6 *cells/mL*.

8.3.2 Methods to Decrease the NMT Cell Capture Efficiency

As was shown in previous sections, the NMT adhesion is a major problem for the CFS. This section will discuss possible methods to decrease the NMT Cell CE%

including improvements to the cell environment, MSCMA chip, and potentially increasing the flow rate.

8.3.2.1 Cell Environment and MSCMA Chip

The optimal temperature for a Jurkat cell is 37ºC since they are human cells. Although live cells were used for all experiments, they were not kept at the optimal temperature for the duration of the experiment. When conducting rare cell tests, both fixed and live cells were used. Although results using both cells were similar, it was found that there were more NMT live cells found on the chip for all ratios. The live NMT cells are in the process of dying during the test, since they are not at the optimal cell temperature. During this process, the live cells may be emitting a reagent that makes them more adherent to the MSCMA, or a surface molecule on the cell surface that is adherent to the MSCMA could become activate. Incorporating a culture chamber that is at the correct temperature may help to reduce the adhesion problem.

Along with maintaining the cells at the optimal temperature, keeping the cells in the optimal medium could also be beneficial. When magnetically tagging the Jurkat cells, they are taken out of their culture medium and put into PBS for the tagging process. Jurkat cells are generally cultured in solution that contains Dulbecco’s Modified Eagle Medium (DMEM), L-glutamine, sodium pyruvate, penstrep, and fetal bovine serum (FBS). Keeping the cells in this solution might also minimize any cell excretions of molecules that could cause the cell to adhere to the chip.

All experiments were conducted using the MSCMA chip that is fabricated using the method described in Appendix A. The NMT cells landed randomly on the chip and were seen to attach to the entire chip, not just the trap area, as shown in Figure 8.17.

Cells were not seen to attach to the PDMS gaskets or the upper surface of the culture chamber which was made of glass. Although the probability of cells becoming attached to these regions are lower. The PDMS generally makes up vertical surfaces of the culture chamber and any horizontal PDMS surfaces were subject to a higher fluid velocity.

This suggests that there may be a coating on the MSCMA which is adherent to the cells. The entire MSCMA chip is coated with a thin layer of gold, as gold is non-toxic to cells. Perhaps cells are adhering to the gold layer, or some other portion of the MSCMA is leaching through the gold and causing the cell adhesion. This could be solved by applying a protein that is known to be non-adherent to cells to the culture chamber. Generally these proteins are used when the medium is at 37°C (optimal cell temperature). This problem could also be solved by changing the materials used when fabricating the MSCMA. This could be easily verified by flow cells over a variety of surfaces to see which surfaces the cells become attached to.

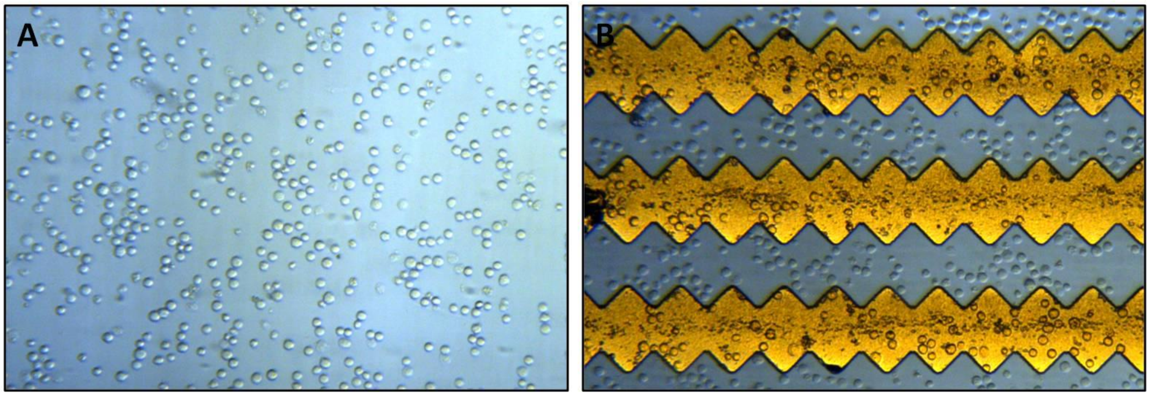

Figure 8.17: NMT cells become attach to entire surface of the MSCMA. (A) Above the trap area. (B) In the trap area.

8.3.2.2 Increase the Fluid Velocity

Along with changing the cell environment and MSCMA chip, another potential method to decrease the NMT cell CE% is by using a higher fluid velocity through the culture chamber. One method tested to minimize the number of NMT cells that become attached to the chip, was by increasing the initial flow rate used. This method was successful in reducing the number of NMT that became attached to the MSCMA, with a NMT cell CE% of 0.19%. This method was not used for tests, as it also drastically reduced the number of MT cells that were successfully captured. Therefore, this option is only viable if the culture chamber size is reduced to only include the cell capture volume as described in section 8.3.1.1.

8.4 Summary of CFS Findings and Recommendations

Overall the cell experiments showed consistent results with both the FEM models and the predicted cell path simulation. Several recommendations were made to improve the predicted cell path simulation and they include:

1. Experimentally tracking the x, y, and z path of a MT cell as it is being captured.
2. Experimentally determining the forces exerted on a MT cell.
3. Performing several additional simulations to determine the effects of magnetic particle distribution on the cell, and the fluid interaction with the cell.

To optimize the CFS, the NMT cell CE% needs to be significantly decreased. Also, the MT cell CE% and SCTE% should be increased. Several recommendations were suggested to improve the MT-CE% and they include:

1. Changing the culture chamber size to only include the effective cell capture volume, which measures roughly 2.4 x 2.8 x 0.05 mm^3.
2. Using a different MSCMA design that contains traps that are half the size of the original traps (30 μm peak to peak, and 15 μm in lateral depth).
3. Finding the optimal cell concentration that will not only yield a high SCTE% and MT cell CE%, but will also yield a low NMT cell CE%.

Several recommendations were also made to possibly reduce the NMT cell capture and they include:

1. Maintaining the cells in an optimal cell environment, including temperature and culture medium.
2. Using a new material to fabricate the MSCMA.
3. Coating the culture chamber and MSCMA with a protein that is non-adherent to Jurkat cells.
4. Increasing the fluid velocity (must be coupled with recommendations 1 for MT cells).

Chapter 9: Conclusion

This thesis showed the design, analysis and testing of a the cell cross flow system (CFS). The main objective of the CFS is to capture and array single rare cells from a heterogeneous population of cells. This was done by using an MSCMA chip that contains permalloy strips with a sawtooth design. By applying an external magnetic field, via a permanent magnet, it was possible to magnetize the permalloy strips and create magnetic traps at the centre of each sawtooth. Jurkat cells were immunomagnetically tagged, suspended in a fluid, and the fluid was passed over the MSCMA using the CFS. Some of these magnetically tagged (MT) cells were then drawn into traps due to the magnetic attraction. The CFS contained several parts that all worked together, and to allowed for the cells to be viewed clearly within a the microscope platform.

Several FEM models were developed to simulate the CFS, and predicted both the fluid and magnetic interactions of the device. From larger scale FEM models, a smaller model was created, which clearly showed the interaction of a single cell with the fluid flow and the magnetic traps. This model was used to predict the path a MT cell would follow due to the buoyancy force, gravitational force, Stokes drag, and magnetic forces that were exerted on the cell.

Using the FEM model, the optimal sawtooth trap design was selected for testing. This design contained a single maximum at the centre of each trap that had the potential to draw cells into the trap from a distance of 50 μm. The predicted cell path simulation was also used to determine the best flow rate. Two flow rate of 0.025 *mL/min* and 0.04

mL/min were selected for use, as these rates were predicted to deliver a majority of the cells to the trap region.

With this information, a variety of experiments were conducted to determine the performance of the CFS. In addition, experiments to test the capability of the CFS as a rare cell capture device were conducted. The first tests conducted were to establish the parameters to be used for future tests. This included testing the two flow rates with two different cell concentrations. These tests were conducted with both fixed MT and non-magnetically tagged (NMT) cells. It was found that increasing the concentration and flow rate resulted in more MT being captured, but also more NMT cells become attached to the chip.

To reduce the number of NMT cells that were attached to the MSCMA chip, two methods were tested. This included: (i) using a higher initial flow rate, and (ii) applying a high flow rate after the cells had been captured. Using a higher flow rate did drastically decrease the number of NMT cells that were attached to the chip, but it also decreased the number of MT cells that were successfully captured. The second method yielded better results with some of the NMT cells being removed once two high flow rates of 1.0 *mL/min* and 2.5 *mL/min* were applied after the cells were captured. Applying the higher flow rates also increased the total number of MT cells that were captured.

After conducting the NMT cell removal tests, rare cell experiments were then conducted to determine if the CFS could be used as a rare cell capture device. Using live or fixed cells, it was found that it was possible to capture MT cells from a heterogeneous cell mixtures with ratios of up to $1:10^3$ (MT:NMT cells). Although it was possible to capture MT cells, it was not possible to remove all the NMT cells that became attached to the chip. Tests using live or fixed cells showed similar results where a higher percentage of single cells being captured when using live cells.

The CFS shows potential of being a useful rare cell detection device. Before this can happen, several changes need to be made to the design. Firstly, the culture chamber volume needs to be reduced to include only the areas where cells are likely to be captured. This includes the entire trap area extending above the MSCMA surface up to about 50 μm. This will increase the number of cells that pass by the magnetic capture range of the chip, which will increase the number of cells that become captured. This could be accomplished by making the gasket using microfluidic techniques, which will allow for micron sized features to be made. Secondly, the MSCMA chip design could be altered to include smaller traps. These smaller traps can physically hold a smaller number of cells and this should increase the single cell loading. One drawback to using traps that are smaller is that the vertical reach of the traps is only 30 μm, thus reducing the capture volume.

The parameters of the CFS need to be further refined to increase the functionality of this device. The MSCMA is shown to quickly and effectively draw in MT Jurkat cells whether they are live of fixed. This is the heart of the device, and optimizing everything around it will result in this device being capable of capturing and arraying cells with a ratio of at least $1:10^6$ (MT:NMT cells).

When this device is optimized, it has the potential to be used for a wide range of applications. The ability to capture and array single cells allows this device to be used to obtain valuable single cell information. Also, arraying the cells make automatic detection of cells for applications such as electrophoresis simpler and more effective. Since the

MT cells are firmly held by the permalloy traps a high flow rate can be applied to introduce media. This allows the CFS to be used to culture cells if the culture chamber is integrated with a temperature control unit.

Applications in single cell analysis continue to grow due to its wide applications and future potential. The common method to extract cellular behavioural and characteristic information is through bulk experiments such as cells grown on a Petri dish. It has been shown that bulk data does not accurately represent the single cells behaviour and it does not capture dynamic cell information correctly. The ability to capture single cells in an array format allows for single cell behaviours and dynamics to be observed while exposing cells to the same environment.

The ability to capture rare cells from a heterogeneous population of cells also has many applications. Positive cell selection could be completed to capture rare cells of interest such as stem cells. Stem cells have huge potential if they can be successfully captured and cultured for application such as tissue engineering. Another use for the rare cell detection is to detect cells that decrease the health of an individual, such as cancer or birth defects. The CFS has potential to become a very powerful tool with future iterations that can optimize the device so that it can be used at its full potential.

References

[1] H. M. Davey and D. B. Kell, "Flow Cytometry and Cell Sorting of Heterogeneous Microbial Populations: The Importance of Single-Cell Analyses," *Microbiological Reviews*, vol. 60, no. 4, Dec. 1996.

[2] H.A. Svahn and A. Van Der Berg, "Single cells or large population?," *Lab on a Chip*, vol. 7, no. 5, pp. 544-546, 2007.

[3] D. D. Carlo and L. P. Lee, "Dynamic single - cell analysis for quantitative biology," *Analytical Chemistry*, vol. 23, no. 78, pp. 7918-7925, 2006.

[4] M. E. Lidstrom and D. R. Meldrum, "Life-on-a-Chip," *Nature*, vol. 1, no. 2, pp. 158-165, November 2003.

[5] R. H. Templer and O. Ces, "New frontiers in single-cell analysis," *J. R. Soc. Interface*, vol. 5, pp. S111-S112, July 2008.

[6] G. Vunjak-Novakovic, M. Radisic, and B. Obradovic, "Cardiac tissue engineering: effects of bioreactor flow environment on tissue constructs," *Journal of Chemical Technology and Biotechnology*, vol. 81, pp. 485-490, October 2006.

[7] F. C. Heidhardt, "Effects of Environment on the Composition of Bacterial Cells," *Annual Review Microbiology*, vol. 17, pp. 61-86, 1963.

[8] Y. Jin, "Human Embryonic Stem Cells Create Their Own Niche," *Cell Research*, vol. 17, pp. 744-745, 2007.

[9] D. Chen and D. McKearin, "Gene Circuitry Controlling a Stem Cell Niche," *Current Biology*, vol. 15, pp. 179-184, January 2005.

[10] H. M. Davey and D. B. Kell, "Flow Cytometry and Cell Sorting of Heterogeneous Microbial Populations: The Importance of Single-Cell Analyses," *Microbiological Reviews*, vol. 60, no. 4, pp. 641-696, Dec. 1996.

[11] B. F. Brehm-Stecher and E. A. Johnson, "Single-Cell Microbiology: Tools, Technologies, and Applications," *Microbiology and Molecular Biology Reviews*, vol. 68, no. 3, pp. 538-559, Sept. 2004.

[12] T. Graf and M. Stadtfeld, "Heterogeneity of Embryonic and Adult Stem Cells,"

Cell Stem Cell, vol. 3, pp. 480-484, November 2008.

[13] T. J. Strovas, L. M. Sauter, X. Guo, and M. E. Lidstrom, "Cell-to-cell Heterogeneity in Growth Rate and Gene Expression in Methylobacterium extorquens AM1," *Journal of Bacteriology*, vol. 189, no. 19, pp. 7127-1733, July 2007.

[14] H. J. Worman, I. Lazaridis, and S. D. Gerogatos, "Nuclear Lamina Heterogeneity in Mammalian Cells," *The Journal of Biological Chemistry*, vol. 263, no. 24, pp. 12135-12141, March 1988.

[15] Institute of Health Resource for Stem Cell Research. (2010, November) Stem Cell Basics. [Online]. http://stemcells.nih.gov/info/basics/basics6.asp

[16] M. Shackleton, E. Quintana, E. R. Fearon, and S. J. Morrison, "Heterogeneity in Cancer: Cancer Stem Cells versus Clonal Evolution," *Cell*, vol. 138, pp. 822-830, September 2009.

[17] M. C. Lanasa et al., "Single cell analysis reveals oligoclonality among low count monoclonal B-cell lymphocytosis," *Leukemia*, vol. 24, pp. 133-140, 2010.

[18] E. Leclerc et al., "Study of osteoblastic cells in a microfluidic environment," *Biomaterials*, vol. 27, pp. 586-595, July 2006.

[19] E. Cimetta, E. Figallo, C. Cannizzaro, N. Elvassore, and G. Vunjak-Novakovic, "Micro-bioreactor arrays for controlling cellular environments: Design principles for human embryonic stem cell applications," *Methods*, vol. 47, pp. 81-89, October 2009.

[20] Z. Zhang et al., "Microbioreactors for Bioprocess Development," *JALA*, pp. 143-151, June 2007.

[21] W. Liu et al., "A novel permalloy based magnetic single cell micro array," *Lab on a Chip*, vol. 9, no. 16, 2009.

[22] W. Liu, "Development of a Novel Magnetic Single Cell Micro Array," University of Victoria, Victoria, Thesis 2008.

[23] K. Sakaki et al., "RoboSCell: an automated single cell arraying and analysis instrument," *Biomedical Micordevices*, vol. 11, 2009.

[24] J. P. Desai, A. Pillarisetti, and A. D. Brooks, "Engineering approaches to biomanipulation," *Annual Review Biomedical Engineering*, vol. 9, 2007.

[25] R. F. Probstein, *Physiochemical hydrodynamics: an introduction*, 2nd ed. New York, New York: John Wiley and Sons, Inc., 1994.

[26] E. Oosterbroek, "Modeling, design and realization of microfluidic components," University of Twente, Enschede, PhD thesis ISBN, 1999.

[27] V. Studer, A. Pepin, Y. Chen, and A. Ajdari, "An integrated AC electrokinetic pump in a microfluidic loop for fast and tunable flow control," *The Analyst*, vol. 129, pp. 944-949, 2004.

[28] A. R. Wheeler et al., "Microfluidic Device for Single-Cell Analysis," *Analytical Chemistry*, vol. 75, pp. 3581-3586, 2003.

[29] W. H. Wright, G. J. Sonek, Y. Tadir, and M. W. Berns, "Laser trapping in cell biology," *IEEE Journal of Quantum Electron*, vol. 26, no. 12, 1990.

[30] I. Sraj, A. C. Szatmary, D. W. M. Marr, and C. D. Eggleton, "Dynamic ray tracing for modeling optical cell manipulation," *Optics Express*, vol. 18, no. 16, August 2010.

[31] W. M. Arnold and U. Zimmermann, "Electro-rotation: development of a technique for dielectric measuremtns on individual cells and particles," *Journal of Electrostatics*, vol. 21, no. 2-3, 1988.

[32] M. Washizu, Y. Kurahashi, H. Iochi, O. Kurosawa, and S. I. Aizawa, "Dielectrophoretic measurement of bacterial motor characteristics," *IEEE Transactions on Industry Applications*, vol. 29, no. 2, 1993.

[33] J. Voldman, "Electrical Forces for Microscale Cell Manipulation," *Annual Review Biomedical Engineering*, vol. 8, pp. 425-454, March 2006.

[34] F. H. C. Crick and A. F. W. Hughes, "The physical properties of cytoplasm: a study by means of the magnetic particle method," *Exp. Cell. Res.*, vol. 1, no. 4, 1949.

[35] C. Wilhelm, F. Gazeau, and J. C. Bacri, "Magnetic manipulation in the living cell," *Europhysics News*, vol. 36, no. 3, 2005.

[36] M. Guthold, M. R. Galvo, W. R. Mathews, S. Paulson, and W. Washburn,

"Controlled manipulation of molecular samples with the nanomanipulator," *IEEE/ASME Transactions of Mechatronics*, vol. 5, no. 2, 2000.

[37] J. P. Nolan and L. A. Sklar, "The emergence of flow cytometry for sensitive, real-time measurements of molecular interactions," *Nature Biotechnology*, vol. 16, no. 7, 1998.

[38] P. O. Krutzik and G. P. Nolan, "Fluorescent cell barcoding in flow cytometry allows high-throughput drug screening and signaling profiling," *Nature Methods*, vol. 3, pp. 361-368, 2006.

[39] A. Darzynkiewicz, E. Bedner, X. Li, W. Gorczyca, and M. R. Melamed, "Laser-Scanning Cytometry: A New Instrumentation with Many Applications," *Experimental Cell Research*, vol. 249, pp. 1-12, 1999.

[40] M. H. Harnett, "Laser Scanning Cytometry: understanding the immune system in situ," *Nature Reviews*, vol. 7, pp. 897-906, November 2007.

[41] C. Conrad and D. W. Gerlich, "Automated microscopy for high-content RNAi screening," *JCB: Review*, vol. 188, no. 4, pp. 453-461, 2010.

[42] Z. E. Perlman et al., "Multidimensional Drug Profiling By Automated Microscopy," *Science*, vol. 306, pp. 1194-1196, November 2004.

[43] J. C. McDonald et al., "Fabrication of microfluidic systems in poly(dimethylsiloxane)," *Electrophoresis*, vol. 21, no. 1, 2000.

[44] A. Daridon et al., "Microfluidic Device for Single-Cell Analysis," *Analytical Chemistry*, vol. 75, no. 14, 2003.

[45] R. N. Zare and S. Kim, "Microfluidic Platforms for Single-Cell Analysis," *Annual Review Biomedical Engineering*, vol. 12, pp. 187-201, April 2010.

[46] E. H. Turner, D. Cohen, and H. R. Puglsey, "Chemical cytometry: the chemical analysis of single cells," *Anal Bioanal Chem*, vol. 390, pp. 223-226, 2008.

[47] S. Mitra, *Sample Preparation Techniques in Analytical Chemistry*. Hoboken, New Jersey: John Wiley & Sons, 2003.

[48] D. Cohen et al., "Chemical Cytometry: Fluorescence-based Single-cell Analysis," *Annual Reviews of Analytical Chemistry*, vol. 1, pp. 165-190, January 2008.

[49] S. H. Krylov et al., "Instrumentation for Chemical Cytometry," *Analytical Chemistry*, vol. 72, pp. 872-877, 2000.

[50] H. Wang and C. Lu, "Microfluidic chemical cytometry based on modulation of local field strength," *Chemical Communication*, no. 33, 2006.

[51] J. R. Retting and A. Folch, "Large-scale single-cell trapping and imaging using microwell arrays," *Analytical Chemistry*, vol. 77, no. 17, 2005.

[52] K. Smistrup et al., "On-chip magnetic bead microarray using hydrodynamic focusing in a passive magnetic separator," *Lab on a Chip*, vol. 5, no. 11, 2005.

[53] B. Kim et al., "Thermalloy actuated probe arrays for manipulation and characterization of individual bio-cell," , Boston, 2003.

[54] I. Safarik and M. Safarikova, "Use of magnetic techniques for the isolation of cells," *Journal of Chromotography B*, vol. 722, no. 1, 1999.

[55] J. Choi, T. M. Liakopoulos, and C. H. Ahn, "An on-chip magnetic bead separator using spiral electromagnets with semi-encapsulated permalloy," *Biosensors & Bioelectronics*, vol. 16, no. 1, 2001.

[56] H. Lee, A. M. Purdon, V. Chu, and R. M. Westervelt, "Controlled assembly of magnetic nanoparticles from magnetotactic bacteria using microelectromagnets arrays," *Nano Letters*, vol. 4, no. 5, 2004.

[57] K. Ino et al., "Cell culture arrays using magnetic force-based cell patterning for dynamic single cell analysis," *Lab on a Chip*, vol. 8, no. 1, 2008.

[58] D. C. Pregibon, M. Toner, and P. S. Doyle, "Magnetically and Biologically Active Bead-Patterned Hydrogels," *Langmiur*, vol. 22, no. 11, 2006.

[59] J. D. Adams, U. Kim, and H. T. Soh, "Multitarget magnetic activated cell sorter," *Proceedings of the National Academy of Sciences*, vol. 105, no. 47, 2008.

[60] Q. A. Pankhurst, J. Connolly, S. K. Jones, and J. Dobson, "Applications of magnetic nanoparticles in biomedicine," *Journal of Physics D: Applied Physics*, vol. 36, no. 1, 2003.

[61] T. L. Chow, *Electromagnetic Theory: A modern perspective*. Boston: Jones and Bartlett, 2006.

[62] S. B. Palmer and M. S. Rogalski, *Advanced University Physics*. Boca Raton: Taylor & Francis Group, 2006.

[63] B. D. Cullity and C. D. Graham, *Introduction to Magnetic Materials*, 2nd ed. Hoboken, New Jersey: John Wiley & Sons, 2009.

[64] G. P. Hatch and R. E. Stelter, "Magnetic design considerations for devices and particles used for biological high-gradient magnetic separation (HGMS) systems," *Journal of Magnetism and Magnetic Materials*, vol. 225, no. 2, 2001.

[65] K. E. McCloskey, J. J. Chalmers, and M. Zborowski, "Magnetic cell separation: characterization of magnetophoretic mobility," *Analytical Chemistry*, vol. 75, no. 24, 2003.

[66] K. E. McCloskey, J. J. Chalmers, and M. Zborowski, "Magnetophoretic Mobilities Correlate to Antibody Binding Capacity," *Cytometry*, vol. 40, no. 2, 2000.

[67] K. Davis, B. Abrams, S. Iyer, R. Hoffman, and J. Bishop, "Determination of CD4 antigen density on cells: role of antibody valency, avidity, clones, and conjugation," *Cytometry*, vol. 33, pp. 197-205, 1998.

[68] U. K. Veeramachaneni and Dr. R. L. Carroll, "Magnetic particle motion in a gradient field," , Boston, 2007.

[69] Nicole Pamme, "Magnetism and microfluidics," *Lab on a Chip*, vol. 6, no. 1, 2006.

[70] S. T. Wereley and Ngyuen N, *Fundamentals and Applications of Microfluidics*. Norwood: Artech House, Inc., 2002.

[71] W. M. Deen, *An Analysis of Transport Phenomena*. UK: Oxford University Press, 1998.

[72] F. M. White, *Fluid Mechanics*. New York: Mcgraw-Hill, 2003.

[73] G. K. Batchelor, *An Introduction to Fluid Dynamics*.: Cambridge University Press, 1967.

[74] J. P. Holman, *Heat Transfer*.: McGraw Hill.

[75] D. B. Dusenbery, *Living at Micro Scale*. Massachussetts: Harvard University Press, 2009.

[76] C. Rands, B. W. Webb, and D. Maynes, "Characterization of transition to

turbulence in microchannels," *International Journal of Heat and Mass Transfer*, vol. 49, no. 17-18, 2006.

[77] H. Lamb, *Hydrodynamics*.: Cambridge University Press, 1994.

[78] H. Eugene and A. Zajac, *Optics*, 4th ed.: Pearson Higher Education, 2003.

[79] WebElements. Home of the periodic table. [Online]. http://www.webelements.com/

[80] J. E. Hatch, *Aluminum Properties and Physical Metallurgy*.: American Society for Metals, 1984.

[81] Dupont. Delrin. [Online]. http://plastics.dupont.com

[82] G. Elert. Density of Glass. [Online]. http://hypertextbook.com/facts/2004/ShayeStorm.shtml

[83] J. E. Mark, *Polymer Data Handbook*, 2nd ed., J. E. Mark, Ed.: Oxford University Press, 1999.

[84] D. R. Lide and W. M. Haynes, *CRC Handbook of Chemistry and Physics*., 2010.

[85] J. C. Mester and J. M. Lockhart, "Remanent magnetization of instrument materials for low magnetic field applications," , Prague, 1996.

[86] British Stainless Steel Association. Magnetic Properties fo Stainless Steel. [Online]. http://www.bssa.org.uk/cms/File/SSAS2.81-Magnetic%20Properties.pdf

[87] M. C. Wurz, D. Dinulovic, and H. H. Gatzen, "Invesitgation of permeability on electroplated and sputtered permalloy," , Honolulu, 2004.

[88] W. P. Taylor, M. Schneider, H. Baltes, and M. G. Allen, "Electroplated Soft Magnetic Materials for Microsensors and Microatuators," , Chicago, 1997.

[89] D. Lim, T. Young, and Y. Fang, "Studies on the effect of surface properties on the biocompatability of polyurethane membranes," *Biomaterials*, vol. 22, pp. 1521-1529, 2001.

[90] A. Nakahira, M. Tamai, S. Miki, and G. Pezzotti, "Fracture behavior and biocompatibility evaluation of nylon-infiltrated porous hydroxapatite," *Journals of material Science*, vol. 37, pp. 4425-4430, 2002.

[91] J. S. Fister, V. A. Memoli, J. O. Galante, W. Rostoker, and R. M. Urban,

"Biocompatibility of Delrin 150: a creep-resistent polymer for total joint prostheses," *Journal of Biomedical Material*, vol. 19, no. 5, pp. 519-533, May-June 1985.

[92] R. Shukla et al., "Biocompatibility of Gold Nanoparticles and Their Endocytotic Fat Inside the Cellular Compartment: A Microscopic Overview," *Langmuir*, vol. 21, pp. 10644-10654, 2005.

[93] COMSOL, "AC/DC Modele User's Guide," 2008.

[94] COMSOL, "COMSOL Multiphysics Modeling Guide," 2008.

[95] George Mizzell. About Magnet Ratings and Terminology. [Online]. http://www.supermagnetman.net/information.php?info_id=10

[96] J. E. Schiel and D. S. Hage, "Density measurements of potassium phosphate buffer from 4 to 45C," *Talanta*, vol. 65, no. 2, 2005.

[97] D. Recktenwald and A. Radbruch, "Detection and isolation of rare cells," *Current Opinion in Immunology*, vol. 7, no. 1, 1995.

[98] R. T. Krivacic et al., "A rare-cell detector for cancer," *Proceedings of the National Academy of Science*, vol. 101, no. 29, 2004.

[99] MetaSystems. Rare Cell Detection. [Online]. http://www.imagingassociates.co.uk

[100] StemCell Technologies. StemCell Technologies. [Online]. http://www.stemcell.com

[101] M. Anderssonn et al., "Using optical tweezers for measuring the interaction forces between human bone cells and implant surfaces: System design and force calibration," *Review of scientific instrumentation*, vol. 78, pp. 074302-1 - 074302-8, 2007.

[102] C. Liu, *Foundations of MEMS*. New Jersey: Pearson Education Inc., 2006.

[103] K. Park et al., "'Living cantilever arrays' for characterization of mass of single cells in fluid," *Lab on a Chip*, vol. 8, no. 7, 2008.

Appendix A: Magnetic Single Cell Micro Array Fabrication Process

The MSCMA is fabricated using a mask electroplating process. The procedure is as follows, and can also be seen in Figure A.1 [23]:

1. Fabrication process starts with a 1.1 *mm* thick square microscope slide (substrate).
2. The substrate is sputtered with 20 *nm* / 130 *nm* thick Cr/Au seed layer.
3. PMGI SF series resist is then spun onto the substrate with a thickness of 120 *nm* and baked for 2 minutes at 180°C.
4. An 8 *µm* photoresist (AZ-9260) is then spin coated onto the substrate (3000 *rpm* for 30 *s*). Slide sits at room temperature for 5 minutes followed by soft baking at 110°C for 5 minutes to remove remaining solvent in the photoresist. Once slide is cooled to room temperature it is soaked in Deionised Water (DW) for 10 minutes to hydrate the film.
5. The photoresist layer is patterned by exposing the substrate with ultraviolet light at nominal doses of 1.8 *J* with a contact mask aligner.
6. The photoresist and underlying adhesion layers are then developed in a 4:1 DW:AZ-400 *K* developer for approximately 5 minutes. The slide is then rinsed in DW and blown dry with N_2.
7. Slide is then reactive ion etched to clean the now exposed gold surface.
8. Slide submerged in an electroplating bath (recipe found in Table A.1) with a current density of 9 – 10 mA/cm^2 for 1 hour rotating 180º every 30 minutes to obtain a 6 *µm*

thick permalloy layer. Slide is then removed from bath rinsed with DW and blown dry with N_2.

9. Mould material removed by flood exposing the slide in the mask aligner with a dose of 3.6 *J* and then removing the rest of the layers in a sequence of developers. Slide then rinsed in DW and blown dry with N_2.
10. Seed layer removed in a two-step etching process. (1) Gold layer removed in TFAC gold etchant. (2) Chromium layer removed using Transene 1020 Cr etchant.
11. MSCMA permalloy channels coated in gold to ensure biocompatibility. Gold layers were deposited using Transene Bright Electroless Gold. This electroless plating process was carried out at 90±5 ºC for 8 minutes to achieve a gold layer 200 *nm* thick.
12. Slide is then diced into individual MSCMA using a wafer saw.

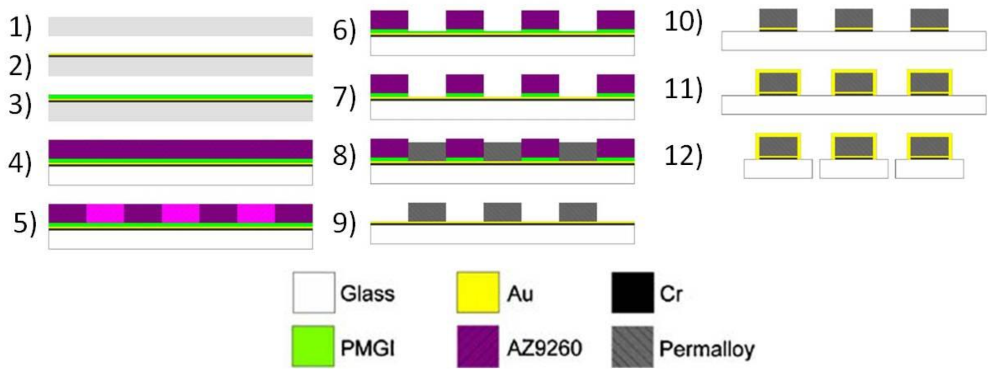

Figure A.1: MSCMA fabrication steps [23].

Table A.1: Electroplating bath recipe [102].

Name (Chemical Name)	**Amount Used [*g/L*]**
Nickel(II) chloride hexahydrate ($NiCl_2\ 6 \cdot H_2O$)	39
Nickel sulphate ($NiSO_4\ 6 \cdot H_2O$)	16.3
Boric-acid powder (Fisher A74-500) (H_3BO_4)	25
Sodium saccharin, for stress adjustment	1.5
Sodium chloride ($NaCL$)	25
Ferrous sulphate crystal ($FeSO_4\ 7 \cdot H_2O$)	1.4
Note: • The solution should have a pH value between 2.7 and 2.8. • To lower pH, drop in a small amount of diluted HCl. • Ideal current density is: 8 – 12 *mA/cm*^{2}	

Appendix B: Magnetic Information for Permalloy Strips

Table A.2: Magnetic information for permalloy strips [88]

Magnetic Induction [*T*]	Applied Field [*A/m*]	Relative Permeability
-1.03	-47746.48293	1
-1.03	-15915.49431	51.5
-1.03	-15119.71959	54.21052632
-1.03	-14323.94488	57.22222222
-1.03	-13528.17016	60.58823529
-1.03	-12732.39545	64.375
-1.025	-11936.62073	68.33333333
-1.02	-11140.84602	72.85714286
-1.015	-10345.0713	78.07692308
-1.0125	-9549.296586	84.375
-1.01	-8753.52187	91.81818182
-1.0075	-7957.747155	100.75
-1.005	-7161.972439	111.6666667
-1	-6366.197724	125
-0.99	-5570.423008	141.4285714
-0.98	-4774.648293	163.3333333
-0.97	-3978.873577	194
-0.96	-3183.098862	240
-0.94	-2387.324146	313.3333333
-0.91	-1591.549431	455
-0.8	-795.7747155	800
-0.79	-716.1972439	877.7777778
-0.76	-636.6197724	950
-0.73	-557.0423008	1000
-0.7	-477.4648293	1000
-0.62	-397.8873577	1000
-0.55	-318.3098862	1000
-0.45	-238.7324146	1000
-0.35	-159.1549431	1000
-0.2	-79.57747155	1000
0	79.57747155	1000
0.2	159.1549431	1000
0.275	238.7324146	1000
0.36	318.3098862	1000
0.44	397.8873577	1000

Magnetic Induction [*T*]	**Applied Field [*A/m*]**	**Relative Permeability**
0.5	477.4648293	1000
0.55	557.0423008	1000
0.65	636.6197724	1000
0.7	716.1972439	777.7777778
0.75	795.7747155	750
0.85	1591.549431	425
0.9	2387.324146	300
0.915	3183.098862	228.75
0.93	3978.873577	186
0.94	4774.648293	156.6666667
0.95	5570.423008	135.7142857
0.955	6366.197724	119.375
0.96	7161.972439	106.6666667
0.965	7957.747155	96.5
0.97	8753.52187	88.18181818
0.975	9549.296586	81.25
0.98	10345.0713	75.38461538
0.985	11140.84602	70.35714286
0.99	11936.62073	66
0.995	12732.39545	62.1875
1	13528.17016	58.82352941
1	14323.94488	55.55555556
1	15119.71959	52.63157895
1	15915.49431	50
1	47746.48293	1

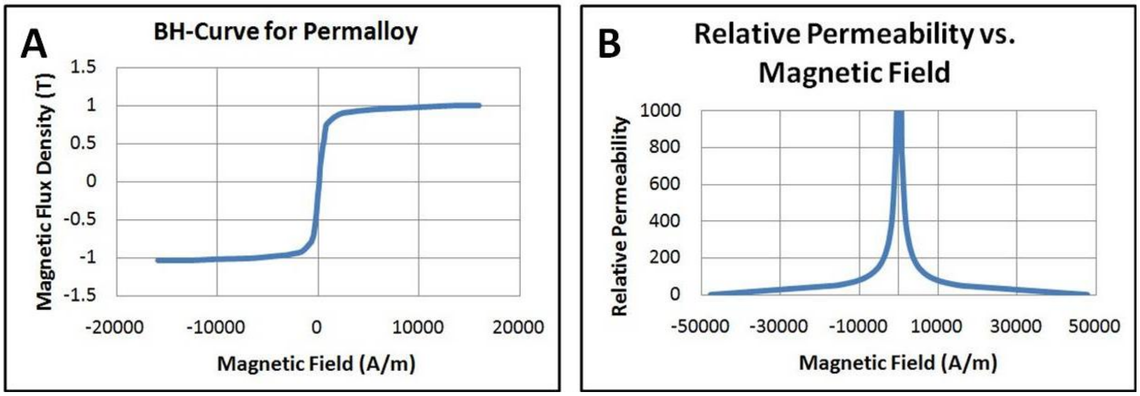

Figure A.2: Permalloy magnetic information (A) Relative permeability vs. magnetic field. (B) BH curve.

Appendix C: Dimensions for Large Scale Fluid Flow Model

The large scale fluid flow model assumes that the volumetric flow rate through the entire volume is constant. To determine the fluid velocity at the inlet, the following dimensions were used to compare the fluid at the culture chamber compared.

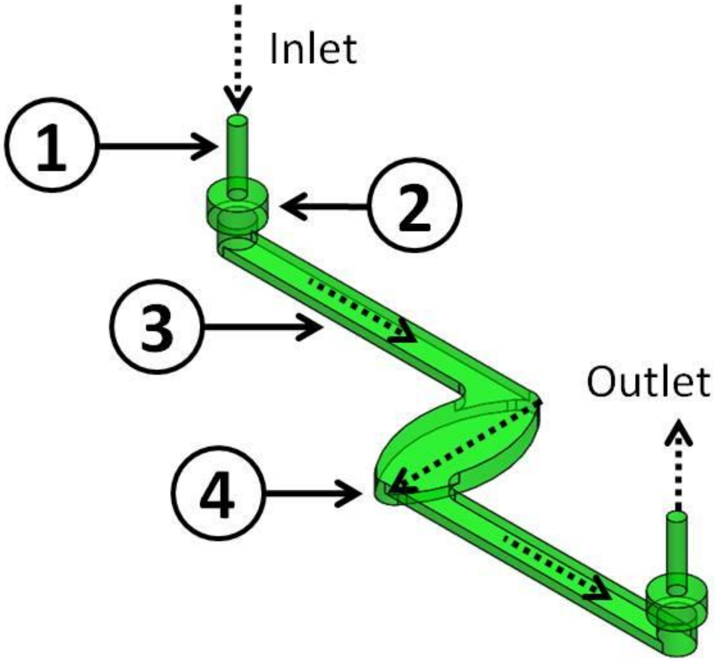

Figure A.3: Large scale fluid flow model. (1) Barbed fitting. (2) Top plate after the fluid exits the barbed fitting. (3) Inlet/Outlet arms. (4) Culture chamber.

Table A.3: Area perpendicular to flow and volume according to Figure A.3. For Area D (culture chamber) was taken at the largest part of the culture chamber, which is at the centre.

Section (Figure A.3)	**1**	**2**	**3**	**4**
Length [$\times 10^{-3}$ *m*]	NA	NA	3.18	8.16
Width [$\times 10^{-3}$ *m*]	NA	NA	1	2
Radius [$\times 10^{-3}$ *m*]	0.584	2.41	NA	NA
Area [$\times 10^{-4}$ m^2]	1.0722	18.292	3.175	1.631
Volume [*mL*]	0.0153	0.0836	0.229	0.209
TOTAL VOLUME [*mL*]	**0.537**			

Appendix D: Predicted Cell Path Simulation Steps

The following steps were used when conducting the predicted cell path simulation.

1. Setup, define, mesh and solve the COMSOL model via Matlab.
2. Define all constants as shown in Table A.4.

Table A.4: Constants used in predicted cell path simulation.

Symbol	Description	Value
χ_m	Volume magnetic susceptibility of medium (water)	-9.035x10^{-6}
χ_c	Volume magnetic susceptibility of magnetic particle	1.6 (**Appendix E**)
Mass	Mass of a single Jurkat cell	2.88x10^{-22} *kg* **[103]**
G	Gravitational force	9.80665 m/s^2
ρ_m	Density of the fluid (water)	1x10^{3} kg/m^3
ρ_c	Density of the Jurkat cell	1.06x10^{3} kg/m^3 **[103]**
η	Dynamic fluid viscosity (water)	1x10^{-3} *Pa·s*
r	Radius of the cell	6 *µm*
V_m	Volume of the cell $\frac{4}{3}\pi r^3$	4.714x10^{-15} m^3
μ_o	Relative permeability of free space	4 π x 10^{-7} N/A^2

3. The initial position of the cell ($P_{c,i=1}$) is defined by the user and all simulation use the same initial position.

$$P_{c,i=1} = \begin{cases} x = 160\ \mu m \\ y = 240\ \mu m \\ z = 50\ \mu m \end{cases} \qquad \textbf{A.1}$$

4. Define where the edge of the permalloy is located.
5. If the cell comes in contact with the edge of the permalloy, STOP the simulation. If the cell does not come in contact with the permalloy edge, continue to next step.
6. Extract the *H*-field at the surface of the cell and determine the maximum value, this point will determine the direction of the magnetic force.
7. Extract the *B*-field data at the edges of the cell to determine the square of the *B*-field gradient and determine the magnetic force on the cell.

$$\boldsymbol{\nabla(B^2)_{\mathrm{i}} = \frac{\partial B_i^2}{\partial x} + \frac{\partial B_i^2}{\partial y} + \frac{\partial B_i^2}{\partial z}} \tag{A.2}$$

$$\boldsymbol{F_{m,i} = \frac{V_m(\chi_m - \chi_c)}{2\mu_o}\, \nabla(B^2)_{\mathrm{i}}} \tag{A.3}$$

8. Extract the fluid velocity at the cell position and determine the Stokes drag on the cell (where $u_{m,i}$ is the velocity of the fluid and $u_{co,i}$ is the initial velocity of the cell for each step). It is assumed that the cell had the same velocity as the fluid for the first simulation step. The initial velocity for every other step is the same as the final velocity from the previous step.

$$\boldsymbol{F_{d,i} = 6\pi\eta r(u_{m,i} - u_{co,i})} \tag{A.4}$$

$$\boldsymbol{u_{co,i} = \begin{cases} u_{m,i=1} & (i = 1) \\ u_{cf,(i-1)} & (i \neq 1) \end{cases}} \tag{A.5}$$

9. Sum up all forces to determine the total force on the cell in the x, y, and z direction.

$$\boldsymbol{F_{tot,i} = F_{m,i} + F_{d,i} + F_g + F_b} \tag{A.6}$$

10. Using the total force on the cell, determine the acceleration and final velocity of the cell in the x, y, and z direction.

$$\boldsymbol{F_{tot,i} = Mass \times a_i} \tag{A.7}$$

$$\boldsymbol{u_{cf,i} = u_{co,i} + a_i t} \tag{A.8}$$

11. Determine the distance travelled by the cell in the x, y, and z direction and the final position of the cell.

$$\boldsymbol{d_i = \frac{u_{cf,i}^2 - u_{co,i}^2}{2a_i}} \tag{A.9}$$

$$\boldsymbol{P_{c,(i+1)} = P_{c,i} + d_i} \tag{A.10}$$

12. Repeat steps 5 through 11.

Appendix E: Dynabead Magnetic Characteristics

Dynabeads in general are made of highly cross-linked polystyrene with an even dispersion of magnetic material (gamma Fe_2O_3 and Fe_3O_4). To encase the magnetic material and provide a defined smooth surface the beads are further coated with a thin polymer shell. The derivatization of surface happens on the top of polymer shell.

As Dynabeads consist of a combination of various ferromagnetic iron oxides, this means by definition, that their properties are dependent on both temperature and flux density (B). Further, due to the small size of the iron domains, the particles are superparamagnetic and in theory the coercivity and remanence should equal to zero.

The core sizes are less than 15 *nm* but we have no information on how monodisperse they are. The amount of ferrites varies in beads of different size. Included is the hysteresis curves plus typical values for saturation magnetization, magnetic susceptibility and ferrite content for our products with different sizes in below. We have not measured the magnetic moments for our beads yet

NOTE:

- DS stands for Dried Beads
- Please note that the values for magnetic susceptibility and saturation magnetization are given in SI system.
- To transform to the CGS system use the following formula: CGS: SI $\div(4\,\pi\,x\,10^{-3})$.

Table A.5: Magnetic characteristics of Dynabead magnetic nanoparticles

Type of Dynabead	MyOne	M-280	M-270	M-450
Size [*μm*]	1	2.8	2.8	5.4
Ferrite Content [%]	37	17	17	29
Density [gDs/cm]	1.8	1.4	1.6	1.6
Magnetic Susceptibility (mass) [x10^{-4} m^3/kg]	8	5	6	10
Magnetic Susceptibility (volume)	1.4	0.7	1	1.6
Saturation Magnetization (mass) [Am^3/kg]	24	10	13	19
Saturation Magnetization (volume) [*kA/m*]	43	14	20	30

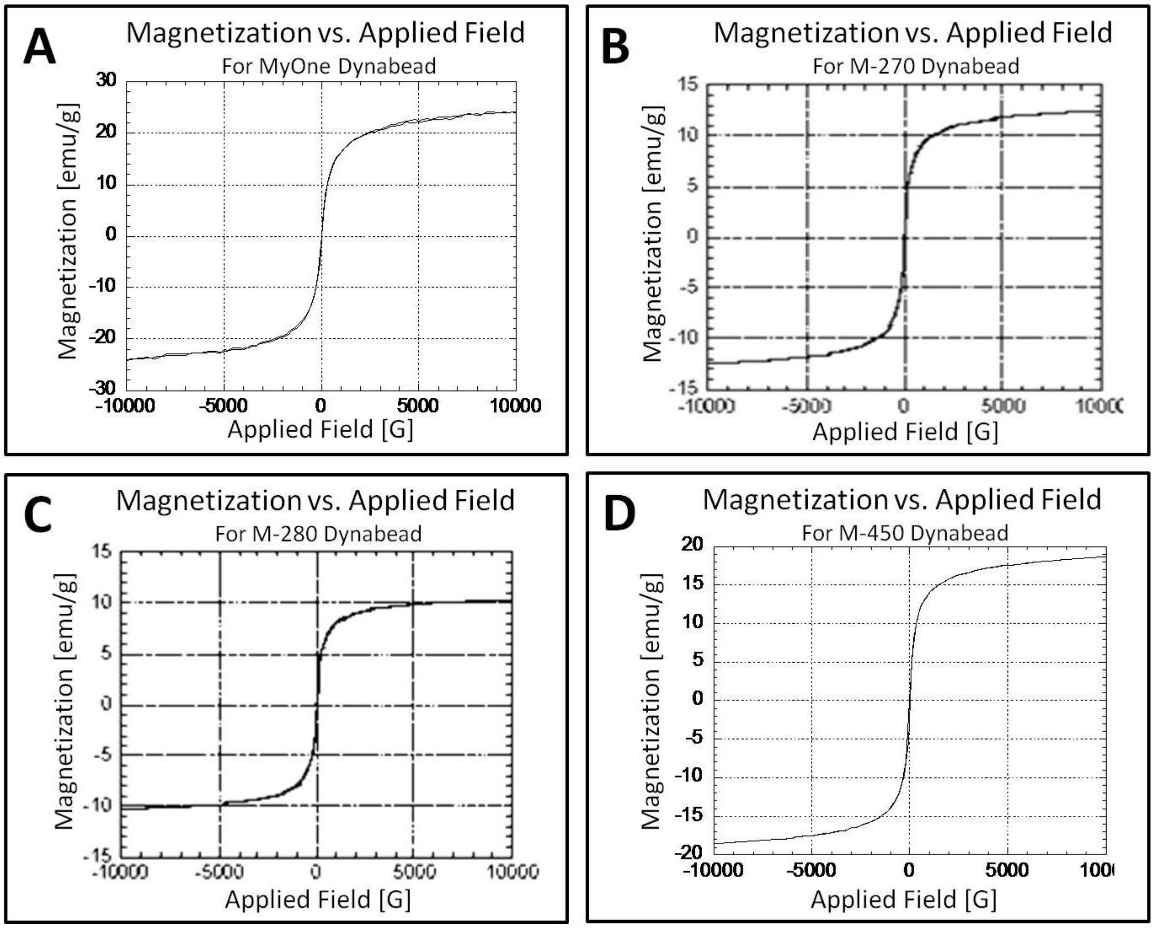

Figure A.4: Magnetization versus Applied Field for magnetic Dynabead particles. (A) MyOne Dynabead (B) M-270 Dynabead (C) M-280 Dynabead (D) M-450 Dynabead

Appendix F: Entire Trap Area vs. Trap Region

Two trap areas are commonly discussed in Chapter 7, and include the "Entire Trap Area" and the "Trap Region". The "Trap Region" is shown in Figure A.5 and only includes the green triangle. The trap region is commonly referred to when discussing where MT cells are captured on the chip. The second area is the "Entire Trap Area", which is shown in Figure A.6 using 15 images of the MSCMA chip. When analyzing each experiment, The same 15 images of the entire chip were used. This area includes 2 ½ permalloy strips (1a and 1b) and 15 full permalloy strips (2 - 16). Each ½ permalloy strip contains 40 traps and each full permalloy strip contains 80 traps. When referring to the "Entire Trap Area", it refers to all 1280 traps that are on the MSCMA.

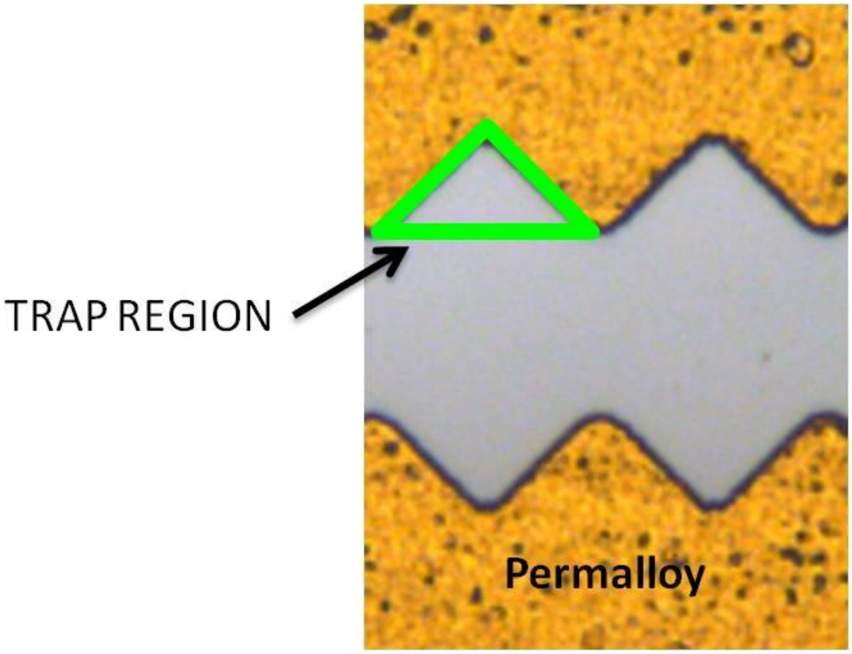

Figure A.5: Trap region which only includes the green triangle shown.

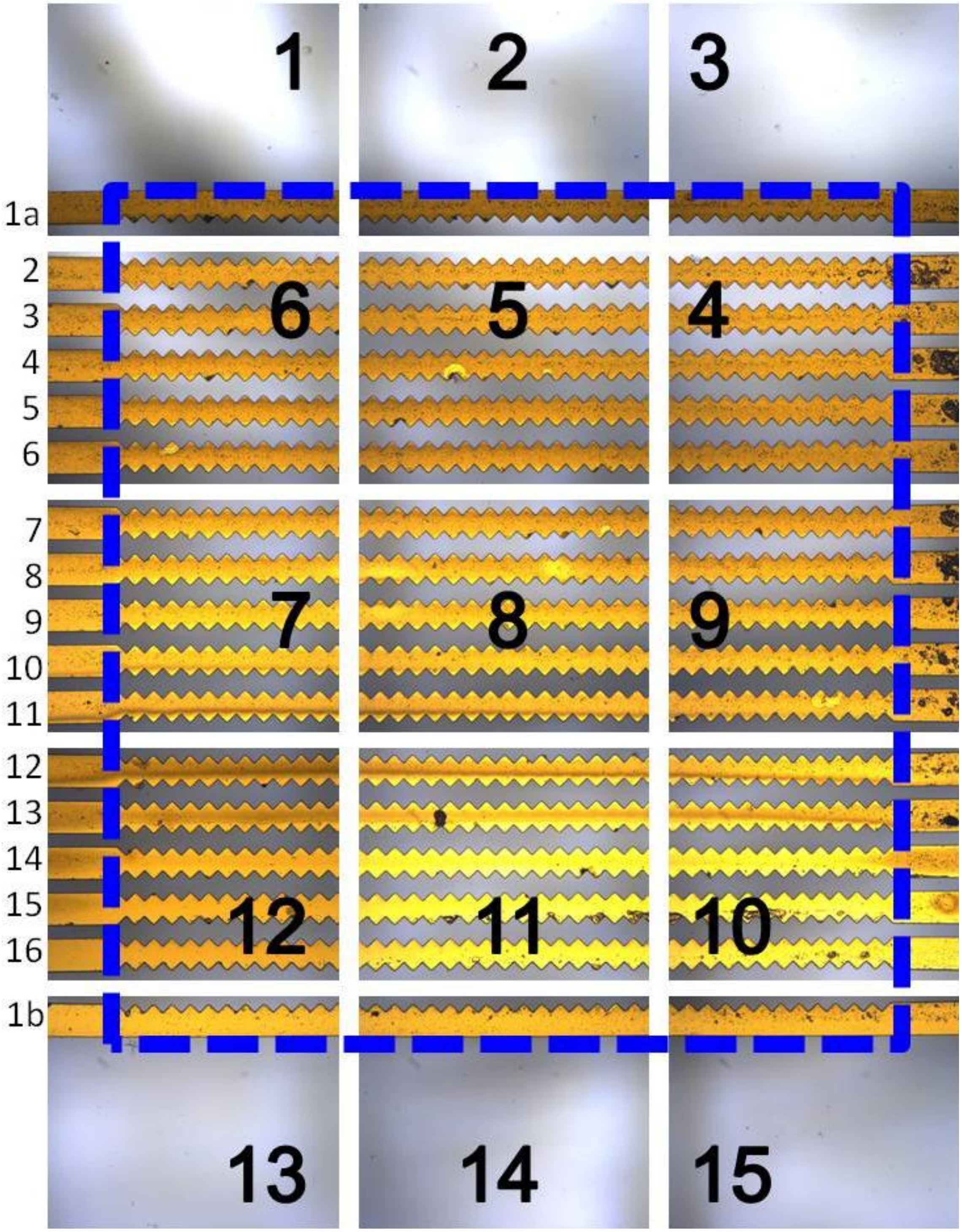

Figure A.6: Image analysis used 15 images of the entire chip. Entire trap area which includes 2 ½ strips (1a and 1b) and 15 full strips (2 - 16). Each ½ strip contains 40 traps, and each full strip contains 80 traps for a total of 1280 traps.